

Solid-State NMR Investigations and MD Simulations of Lipid Bilayers in Interaction with Amphiphilic and Polyphilic Molecules

Dissertation

zur Erlangung des Doktorgrades der Naturwissenschaften
(Dr. rer. nat.)

der
Naturwissenschaftlichen Fakultät II
Chemie, Physik und Mathematik

der Martin-Luther-Universität
Halle-Wittenberg

vorgelegt von

Ruth Bärenwald
geboren am 28. September 1987 in Dessau

Halle (Saale), den 07.05.2018

Gutachter:

1. Prof. Dr. Kay Saalwächter (Martin-Luther-Universität Halle-Wittenberg)
2. Prof. Dr. Alfred Blume (Martin-Luther-Universität Halle-Wittenberg)
3. Prof. Dr. Daniel Huster (Universität Leipzig)

Öffentliche Verteidigung: 07.11.2018

Contents

1	Introduction	1
2	Lipid Membrane Systems	3
2.1	Amphiphilic and Polyphilic Molecules	3
2.2	Lipid Bilayers	4
2.3	Biological Membranes	8
2.4	Model Membranes	10
3	Basics of NMR Spectroscopy	13
3.1	The Nuclear Spin	13
3.2	The Density Operator	16
3.3	The NMR Experiment	18
3.3.1	Theoretical Considerations	18
3.3.2	Practical Aspects	19
3.4	NMR Interactions	21
3.4.1	Chemical Shift	21
3.4.2	Dipolar Coupling	23
3.4.3	J -Coupling	26
3.5	Relaxation Processes	26
4	Description of Molecular Dynamics in Lipid Bilayers	29
4.1	The Order Parameter	29
4.2	Correlation Function and Spectral Density	30
4.3	Molecular Motions in Lipid Bilayers	32
5	NMR Methods for the Investigation of Membrane Systems	35
5.1	Standard Methods of Solid-State NMR	35
5.1.1	Magic Angle Spinning (MAS)	35
5.1.2	Heteronuclear Dipolar Decoupling	36
5.1.3	Homonuclear Dipolar Decoupling	37
5.2	^1H MAS Spectra	37
5.3	^{13}C MAS Spectra	39
5.3.1	Direct Polarization	39
5.3.2	Methods for Signal Enhancement	40
5.4	Determination of T_1 Relaxation Times	43
5.5	The NOESY Experiment	45
5.6	Order Parameters Determined from Dipolar Couplings	51
5.6.1	The DIPSHIFT Experiment	52
5.6.2	The R-PDLF Experiment	55
5.6.3	C–H Order Parameters of DMPC	58
5.6.4	H–H Order Parameters determined by the BaBa-xy16 Experiment	60

6	MD Simulations and Results for Pure Lipid Bilayer Systems	65
6.1	Introduction	65
6.2	Order Parameters	66
6.3	R_1 Relaxation Rates	68
7	Lipid Bilayers and Amphiphilic Triblock Copolymers	71
7.1	Amphiphilic Triblock Copolymers	71
7.2	Polymers Interacting with Lipid Bilayers	72
7.3	Samples	75
7.4	Polymer and Lipid-Polymer Systems Simulated	76
7.5	DSC Results	83
7.6	^{13}C Spectra	86
7.7	Cross-Relaxation Rates	87
7.8	Order Parameter S_{CH} of Lipid Molecules	92
7.9	Relaxation Rates R_1 of Lipid Molecules	94
7.10	Polymer Configuration and Dynamics	95
7.10.1	Analysis of the DQ build-up curve	95
7.10.2	Order Parameters Determined from MD Simulations	97
7.10.3	Relaxation Rates R_1 of Polymers	101
7.10.4	Comparison of Different Sample Preparation Methods	104
7.10.5	Influence of the Polymer Architecture	105
7.10.6	Temperature Dependence	109
7.10.7	Variation of the Lipid Molecules	111
7.10.8	Addition of Cholesterol	113
7.10.9	Concentration Dependences	114
7.11	Summary of Results for the Lipid/Polymer Systems	115
8	Systems of Lipid Bilayers and Anion Transporters	117
8.1	Samples and ^1H Spectra	117
8.2	Results from the NOESY Experiment	118
9	X-shaped Bolapolyphiles in Interaction with Lipid Bilayers	121
9.1	Sample Systems and Previous Results	121
9.2	^1H Spectra	123
9.3	^1H - ^{13}C Dipolar Couplings from the DIPSHIFT Experiment	125
9.4	^1H - ^1H Dipolar Couplings from DQ Sideband Spectra	127
10	Summary	129
A	Spin State Representation by Wave Functions	133
B	Experimental Details	135
B.1	Sample Preparation	135
B.2	NMR Measurements	135

C	Description of NMR Experiments and Data Analysis	137
C.1	Determination of the Peak Volume Matrix from a 2D NOESY Spectrum	137
C.2	Relaxation Rate Matrix of POPC	137
C.3	Analytical Fit Functions for DIPSHIFT Curves	138
C.4	Results from the R-PDLF Experiment for DMPC	141
C.5	The Basic DQ Experiment	142
D	Results from MD Simulations of Lipid/Polymer Systems	145
E	Results from NMR Experiments on Lipid/Polymer Systems	147
E.1	Lipid Order Parameters	147
E.2	Results from the R-PDLF Experiment for a Polymer Resonance	148
	References	164

1 Introduction

As boundaries of cells and subcellular organelles, biological membranes are essential for all living matter. They provide a barrier function and are site of many biochemical events. Consequently, the study of membrane structure and dynamics is important to obtain a better understanding of many biological processes. Every biological membrane shows a distinct and very complex composition of many different proteins and lipids which stands in relation to its function. The basic membrane structure is given by the phospholipids forming a bilayer in water. Due to the complexity of cell membranes, simplified model membrane systems consisting of only one or a few phospholipid species are often used for investigations. Here, we study lipid bilayers in water which form vesicles.

Many properties of a phospholipid bilayer, for example its flexibility or its permeability, can be modified by the addition of guest molecules which could attach to the surface or penetrate deeply into the membrane. By systematically varying the structural properties of the guest molecules, their influence on the interaction with the membrane can be investigated in detail. Molecular structures, which influence membrane properties in a specific, well-defined way may find medical or pharmaceutical application in the future.

In this work, we investigate three different types of guest molecules in mixture with lipid bilayers. The first class are amphiphilic triblock copolymers. Mainly, we here investigated Pluronics, which find wide-ranging applications in pharmacy and medicine, for example for the healing of wounds [1, 2] or in cancer therapy [3]. Pluronics are non-toxic, commercially available and depending on the specific block lengths, they interact with lipid membranes in a variety of ways. As a second system, we investigated a number of urea and thiourea compounds capable of mediating the transport of anions across the membrane, and a third project part deals with lipid bilayers in interaction with X-shaped bolapolyphiles which consist of a rigid aromatic core, flexible aliphatic side chains and polar end groups. Being incorporated in the bilayer in transmembrane orientation, these molecules can self-assemble into supramolecular structures and change the phase behavior of the lipids [4–6]. It is the aim of this thesis to get a detailed understanding of structure and molecular dynamics of membrane-guest molecule systems. This includes the localization of the guest molecules inside the membrane and the characterization their mobility as well as the detection of their possible influence on lipid order and dynamics.

Generally, a vast number of techniques are available for the investigation of lipid bilayer systems [7–9]. Thermodynamic methods like calorimetry or densitometric measurements can be used to study thermotropic phase transitions [10]. Fluorescence microscopy allows for the visualization of lipid bilayers forming giant vesicles [4, 5] and for the investigation of the membrane permeability and heterogeneity [11]. However, in most cases labeling with a fluorescent dye is necessary, which could disturb the system and alter its behavior [12]. Using transmission electron microscopy, high resolution images approaching molecular resolution of lipid vesicles can be taken [4, 7]. From X-ray or neutron scattering experiments, structural parameters like the bilayer repeat distance (small angle scattering) [4, 13] or the packing density within the membrane (wide angle scattering) [4] can be determined and also the electron density profile across bilayer can be measured [14]. Additionally, studies on Langmuir monolayers are commonly used [15–17]. In this case, the lipid is spread over an air-water interface the size of which can be reduced so that the lipid monolayer gets compressed. Further structural and dynamic information can be gained

from different spectroscopic methods, like infrared, Raman or EPR spectroscopy [17, 18].

In this study, we apply solid-state Nuclear Magnetic Resonance (NMR) spectroscopy which is well suited to determine structure and dynamics of the model membrane/guest molecule systems [8, 19]. The NMR technique is non-invasive, allows for chemical resolution and offers a number of experiments from which structural and dynamical observables can be determined. NMR experiments were already used for a long time for the study of lipid bilayer systems [20]. In the 1960s, first high-resolution NMR studies on small unilamellar liposomes were performed [21]. In the following time, static solid-state ^2H NMR was commonly applied to determine lipid order parameters [22, 23] and ^{31}P NMR was used to study the behavior of the lipid headgroups [24]. In the 1980s, Magic-Angle sample-Spinning (MAS) NMR was shown to yield well-resolved spectra of liquid-crystalline lipid samples [25], which allowed for the development of many different NMR techniques in the recent decades [20].

Here, we studied lipid sample systems by applying various ^1H and ^{13}C MAS NMR experiments. Firstly, simple spectra were acquired which contain information about molecular dynamics and for example allow for the investigation of the phase behavior of the lipid sample systems which can be rather complex, like in the case of the lipid/bolapolyphile mixtures. With the help of the NOESY experiment, the deep insertion of the polymers and the anion transporters into the membranes of the respective systems was proven and the guest molecule position inside the membrane was estimated. Furthermore, we measured relaxation rates which depend on molecular dynamics, and dipolar coupling constants, from which the order parameters can be calculated which in turn contain information about the motional geometry. With this, lipid ordering and dynamics can be investigated and potential changes due to the guest molecules can be detected. Additionally, the restricted mobility of the guest molecules in the membrane can be characterized. For the lipid/polymer systems, we are able to draw conclusions on the polymer configuration inside the membrane by comparison of our experimental values with results from MD simulation. Using dipolar NMR experiments, it is also possible to determine the fraction of polymer that deeply enters into the membrane while the rest is dissolved in the water phase showing nearly isotropic mobility. For systematic investigations of all the different systems, we varied the structure of the guest molecules, for example the lengths of the polymers, the type of lipid and further conditions, like the temperature, the concentration or the way of sample preparation.

In the first three sections of the thesis, basic concepts about lipid membranes and solid-state NMR are introduced. Subsequently, we explain the specific NMR methods used and show results for order parameters and relaxation rates determined from pure lipid bilayer samples. Then, the MD simulations are introduced. We analyze a pure lipid bilayer system simulated with regard to the quantities determined from the NMR measurements. In the last sections, results from NMR experiments and MD simulations for the different lipid bilayer/guest molecule systems are presented and summarized in the end.

2 Lipid Membrane Systems

In the following section, amphiphilic and polyphilic molecules in general and lipid bilayer systems specifically will be introduced. Explanations are mainly based on the textbooks of Evans and Wennerström [7], Marsh [9] and Winter and Noll [26].

2.1 Amphiphilic and Polyphilic Molecules

An amphiphilic molecule is composed of topologically separated hydrophilic and hydrophobic building blocks. While the hydrophilic molecular regions induce water solubility, the hydrophobic units are insoluble in water. In apolar liquids, however, the hydrophobic molecular parts induce solubility. Typical examples for amphiphilic molecules are surfactants, lipids, certain block copolymers or peptides.

Polyphilic molecules represent an extension of the amphiphilic molecules as they contain special units like mesogenic (liquid crystal forming) parts, fluorinated regions or covalently-bonded nanoparticles in addition to the amphiphilic moiety. With this additional part, specific properties of the molecule and its interaction with the surrounding can be tuned [27].

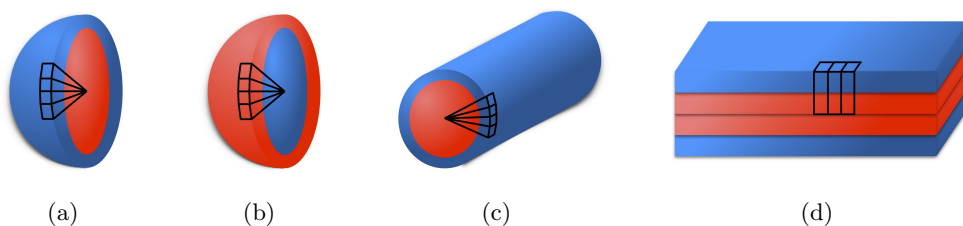


Figure 1: Schematic drawing of a few aggregate architectures: (a) micelle, (b) inverse micelle, (c) cylindrical micelle, (d) lamella. Hydrophilic parts are shown in blue and hydrophobic parts in red. Black lines denote the space that one molecule occupies.

Molecules containing blocks of different philicities that repel each other generally show special behavior like the tendency for aggregation and surface activity [7]. Particularly for biological systems, the molecular self-association of amphiphilic molecules in an aqueous medium is of utmost importance [28]. Referred to as the hydrophobic interaction, aggregation is a consequence of unfavorable contacts between hydrophobic parts of the molecule and water [29, 30]. For example, alkyl chains induce an ordering of the water molecules lowering the entropy of the system. Consequently, aggregates are formed in a way that interactions between the hydrophobic molecular parts and water are minimized while the contacts between hydrophilic parts and water are maximized. The overall molecular arrangement is generally optimized to achieve a minimal total free energy of the system. For this, not only the amphiphile-water contacts play a role, but also the interactions between the amphiphilic molecules within an aggregate. Among hydrophilic groups, there can be electrostatic or steric repulsions and also the formation of hydrogen bonds is possible. Van der Waals forces act between hydrophobic groups.

At high dilution, amphiphiles usually occur as unimers in water. By increasing their concentration, the molecules start to aggregate at some point. For example, surfactants or certain amphiphilic block copolymers form micelles when the critical micelle concentration (cmc) is

reached. A similar behavior can be observed with rising temperature at a fixed amphiphile concentration. Micelles appear at the critical micelle temperature (cmt). At high amphiphile concentrations or at high temperatures, a dynamic equilibrium between micelles and unimers exists in the ideal case with an unimer concentration corresponding to the cmc. Further increase of the concentration causes changes of the aggregate shapes and the appearance of superstructures of aggregates.

In general, a large variety of self-assembled structures can be found for amphiphilic molecules, for example spherical or cylindrical micelles in solution, lamellar structures composed of stacks of bilayers, vesicles in solution, or more complicated arrangements like bicontinuous cubic structures. A few examples are shown in Figure 1. The form of an aggregate is critically influenced by the shape of its molecular components [31] and can be explained roughly using a phenomenological model that accounts for the sizes of the different molecular parts. According to this model, cylindrical amphiphiles consisting of hydrophobic and hydrophilic parts with similar cross-sectional area develop lamellar structures. Cone-shaped amphiphilic molecules that have a hydrophilic part with a higher cross-sectional area than the hydrophobic part, form normal micelles and vice versa, cone-shaped molecules with a hydrophilic part with a smaller cross-sectional area than the hydrophobic part show inverse micelles. The cross-sectional areas are influenced in turn by a number of conditions like temperature, ionic strength of the solvent and pH.

In many cases, amphiphilic molecules form liquid crystalline structures that show a certain order on the one hand and partial disorder and mobility on the other hand. Furthermore, these systems can be lyotropic and thermotropic, that is, their phase behavior depends on the water concentration and/or the temperature, respectively.

2.2 Lipid Bilayers

In this work, we examine phospholipids which are a major component of biomembranes. They consist of a hydrophilic head group containing a phosphate group and usually two hydrophobic alkyl chains. The specific structure of the hydrophilic and hydrophobic groups depends on the lipid type. Here, we investigate phosphatidylcholines which belong to the group of glycerophospholipids and account for more than half of the phospholipids in eukaryotic cells [32]. They consist of a choline headgroup and a glycerol backbone to which two saturated or unsaturated hydrocarbon chains are attached via an ester bond. At physiological conditions, these molecules are zwitterionic because of the negatively charged phosphate group and the positively charged choline group [30].

In Table 1, some important features of the different phosphatidylcholines used in this work are summarized. The three lipids dilauroylphosphatidylcholine (DLPC), dimyristoylphosphatidylcholine (DMPC) and dipalmitoylphosphatidylcholine (DPPC) only differ in the length of the saturated acyl chains consisting of 16 carbons for DPPC, 14 carbons for DMPC and 12 carbons for DLPC. Palmitoyloleoylphosphatidylcholine (POPC) has a double bond in the middle of one acyl chain and dioleoylphosphatidylcholine (DOPC) comprises two unsaturated chains. While saturated hydrocarbon chains of DPPC and POPC have the same length, the unsaturated chain of POPC contains two more carbons. Due to the double bond, a POPC molecule occupies a larger cross sectional area than a molecule of DPPC [33].

Besides the phosphatidylcholines, other glycerophospholipids with different head groups are

also relevant for biological membranes. Examples are phosphatidylethanolamines, which have a single amine group, or phosphatidylserines and phosphatidylinositol, which have ionic head groups. In addition to the group of glycerophospholipids, other lipid groups like sphingophospholipids (for example sphingomyelins), glyceroglycolipids and sphingoglycolipids also play an important biological role.

Steroids are also commonly referred to as lipid molecules. The most prominent example is cholesterol which is the predominating sterol in mammalian cells [32]. It consists of a rigid, relatively planar and stiff ring system with a flexible aliphatic side chain and a polar part formed by a single OH group (see Figure 2).

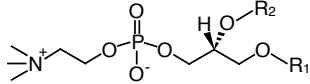
lipid	M_w / g/mol	T_m / °C	
DLPC	622	-2	$R_1 = R_2 = \text{CO}-(\text{CH}_2)_{10}-\text{CH}_3$
DMPC	678	24	$R_1 = R_2 = \text{CO}-(\text{CH}_2)_{12}-\text{CH}_3$
DPPE	734	41 - 41.5	$R_1 = R_2 = \text{CO}-(\text{CH}_2)_{14}-\text{CH}_3$
POPC	760	-3.5	$R_1 = \text{CO}-(\text{CH}_2)_{14}-\text{CH}_3$ $R_2 = \text{CO}-(\text{CH}_2)_7-\text{CH}=\text{CH}-(\text{CH}_2)_7-\text{CH}_3$
DOPC	786	-17.5	$R_1 = R_2 = \text{CO}-(\text{CH}_2)_7-\text{CH}=\text{CH}-(\text{CH}_2)_7-\text{CH}_3$

Table 1: Molecular weight M_w , main phase transition temperature T_m and chemical structure of the lipids investigated in the framework of this thesis. The values for T_m were taken from Reference [9] and refer to the fully hydrated lipid bilayer.

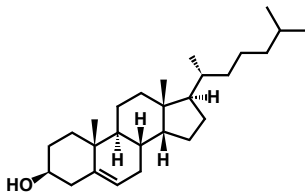


Figure 2: Chemical Structure of Cholesterol.

Depending on the lipid type and on the solution conditions, lipid molecules can form different kinds of aggregates. Here, we consider phosphocholines that assemble into bilayers when dispersed in water. Such a bilayer consists of two layers (or leaflets) of lipid molecules having their headgroups positioned at the interfaces in contact with the aqueous environment. The lipid alkyl chains are located in the center of the bilayer and therefore have minimal water contact (see Figure 3). They interact with each other via van der Waals forces which are stronger for longer chains [34]. Between the lipid headgroups, steric repulsions and interactions between the positive and negative groups are present [26]. In general, the heads of the lipid molecules are bent, that is, in time-average, a connection line from the choline to the phosphate group lies approximately perpendicular to the bilayer normal [35,36]. Furthermore, water molecules associate with the lipid head groups forming a hydration shell that stabilizes the bilayer [37]. Depending on the size of the lipid molecules and on solution conditions like the temperature, a lipid bilayer has

a thickness of a few nanometers. For example, at 30 °C, bilayers of DLPC and POPC exhibit an overall thickness of about 3.3 and 3.9 nm, a hydrocarbon region thickness of about 2.2 and 2.9 nm, and an area per lipid molecule of 60.8 Å² and 64.3 Å², respectively [33].

While on a length scale of a few nanometers, a lipid bilayer is a planar sheet, the whole membrane system can exhibit many different morphologies on larger length scales of about hundreds of nanometers to tens of micrometers. Most simply, lamellar stacks of bilayers separated by water films can be formed. This morphology can be used to create samples of oriented bilayer stacks on thin glass plates which, for example, allow for the investigation water or lipid diffusion in specific directions [37, 38]. However, experiments on oriented bilayer stacks are complicated due to problems like a low signal-to-noise ratio and poor mechanical stability. Also a sufficient and homogeneous sample hydration is difficult to achieve.

Another potential morphology is represented by the lipid bicelles which are small bilayer patches formed from a mixture of short and long chain saturated phospholipids. Due to their ability to align themselves when brought into a magnetic field, they are frequently used for NMR experiments [39–41]. Additionally, there exist more complicated structures like a bicontinuous phase of cubic symmetry or a sponge phase. As a general rule for this, bilayers tend to curve back on themselves to avoid contacts between water and the hydrophobic regions at the edges.

The simplest form of such a closed structure is given by the lipid vesicles, also called liposomes. Exhibiting different forms and sizes, they represent the most important lipid morphology. Due to their biocompatibility, biodegradability and ability to enclose both hydrophilic and lipophilic drugs, liposomes are applied as carriers for many different molecules for example in pharmaceutical industry [42]. However, it must be kept in consideration, that liposomes usually do not resemble the equilibrium state. But in most cases, they are stable long enough for certain applications or to conduct NMR experiments.

Unilamellar vesicles (ULVs) constitute one class of liposomes. They are only stable in very dilute solutions and can be produced with sizes of about 20 nm (small unilamellar vesicles) [42] to about 100 µm (giant unilamellar vesicles) [43].

In course of this project, all investigations were conducted on a second class of liposomes, the multi-lamellar vesicles (MLVs) which form spontaneously when a phospholipid like DPPC is prepared with a water content of around 30 wt% or more. As illustrated in Figure 3, MLVs consist of several bilayers which are arranged onion-like, being separated from each other by water films which are a few nanometers thick. The size of an entire MLV varies between 0.1 and 5 µm depending on the preparation method [42].

Between two neighboring bilayers of an MLV, different interactions occur, for example van der Waals attraction, electrostatic repulsion, hydration repulsion, interactions due to thermal bilayer undulations and steric repulsion. The strength of the interaction forces depends on the lipid type, the stiffness of the bilayer and on the thickness of the water layer in-between, which in turn strongly depends on the degree of hydration [44].

Phospholipid samples, like DMPC, exhibit a certain thermotropic phase behavior which will be explained in the following. At a water content above 30 wt%, all phase transitions are concentration-independent as can be seen in the phase diagram, shown in Figure 4, which was compiled originally in 1979 by Janiak et al. [45]. Already a few years before, Tardieu et al. [46] gave a comprehensive characterization of the phases of a lecithin-water system.

After prolonged incubation at low temperature, lipid bilayers exhibit the crystal L_c phase

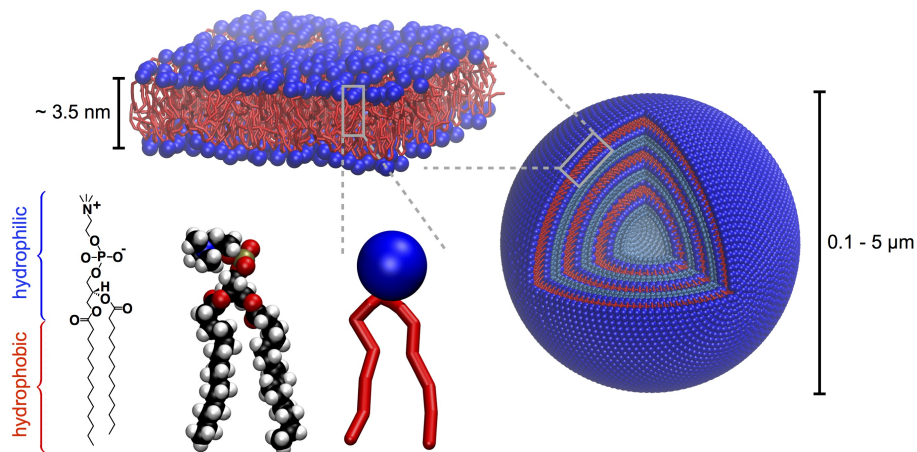


Figure 3: Schematic structure of a DMPC lipid molecule, a lipid bilayer and an MLV. Pictures were created using the molecular visualization program VMD. The thickness of the DMPC bilayer in the liquid-crystalline phase at 50 °C and the general size of MLVs are given in References [33] and [42], respectively.

which is characterized by low molecular mobility. In this phase, the lipids are arranged on a two-dimensional orthorhombic lattice, their alkyl chains being stretched in an all-trans conformation. When heated to the subtransition temperature T_s , the system transforms into a gel phase, in which the lipid alkyl chains still exhibit the stretched all-trans conformation and consequently show low mobility. They are packed with rotational disorder in a two-dimensional quasi-hexagonal lattice [26]. In contrast to the L_c phase, the water in-between the bilayers in the gel phase is liquid-like and the lipid head groups are highly mobile [7]. Special bilayer structures, which exhibit for example tilted chains, bilayer ripples or chain interdigitation, occur allowing for the compensation of a potential mismatch between the cross-sectional areas of the lipid tails and the head groups and therefore ensure a more dense packing. As an example, the $L_{\beta'}$ phase is characterized by chains that are inclined by an angle of about 30° with respect to the bilayer normal. At the temperature T_p (about 11 °C for DMPC), a broad, low enthalpy pretransition takes place. Above this temperature, the two-dimensionally ordered metastable $P_{\beta'}$ ripple phase appears, which is characterized by a periodically oscillating wave structure of the bilayers. However, many lipids, for example phosphocholines with unsaturated chains, do not exhibit a pretransition and a $P_{\beta'}$ phase.

By further heating the sample, the main phase transition takes place when the respective transition temperature T_m (24 °C for DMPC) is reached. For pure lipid samples, this phase transition occurs over a small temperature range reflecting the high cooperativity of the lipid molecules. It is a first-order process during which the lipid acyl chains melt and fast rotational reorientation of the lipid molecules about their molecular long axis sets in. In Table 1, the main phase transition temperatures of the lipids, used in this work, are listed. It can be seen that lipids with unsaturated chains exhibit a lower temperature T_m than lipids with saturated chains because the double bonds cause a higher disorder of the chains in the gel phase [47]. Lipids with longer chains generally show higher phase transition temperatures due to the stronger van der Waals interaction in-between the chains.

The liquid-crystalline L_α -phase is characterized by fluid bilayers, that is, the lipid molecules can diffuse within the bilayer plane and besides the lipid head groups, also the acyl chains are highly mobile and disordered switching rapidly between trans- and gauche $^\pm$ conformations. Nevertheless, a certain residual order remains keeping the chains in average aligned perpendicular to the bilayer normal. With rising temperature, the disorder of the lipid chains increases further and the bilayer thickness decreases accordingly.

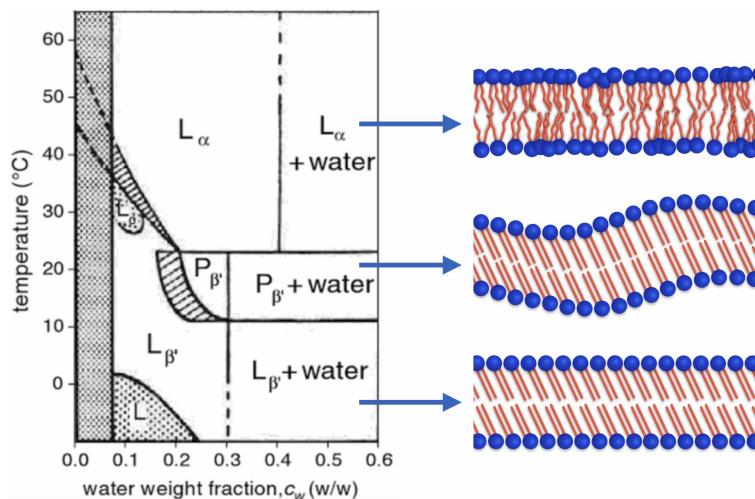


Figure 4: Phase diagram of DMPC from [9, 45] and schematically drawn bilayer structures in the $L_{\beta'}$, $P_{\beta'}$ and L_α phase.

For sample systems consisting of more than one phospholipid, the phase behavior is often more complex than for a single lipid, as immiscibility and phase separation can occur. However, we will not explain these cases here, as all the systems investigated in this work only contain a single phosphocholine or a mixture of one phosphocholine and an amphiphilic or polyphilic molecule.

2.3 Biological Membranes

Biological membranes play an important role in living matter. They surround the cytoplasm of cells and additionally can be found within eucaryotic cells, where they enclose cell organelles like mitochondria, are part of the endoplasmatic reticulum or form a loose membrane network around the nucleus. Having a very complex structure (see Figure 5), biological membranes at different positions fulfill versatile functions. For a general description of their hierarchical structure and dynamics, a wide range of time and spatial scale is needed.

The present understanding of the biological membrane was developed within the past hundred years [49]. In the beginning, Overton described the membrane as a 'fatty oil' rich in cholesterol and phospholipids ([49], and references therein). By studying lipid extracts of membranes from red blood cells, Gorter and Grendel recognized in 1925 that the basic structure of biological membranes is formed by a lipid bilayer [50]. In 1972, Singer und Nicolson introduced their famous fluid mosaic model [29], in which the membrane is described as a fluid phospholipid bilayer that provides a two-dimensional solution environment for other membrane components, like proteins,

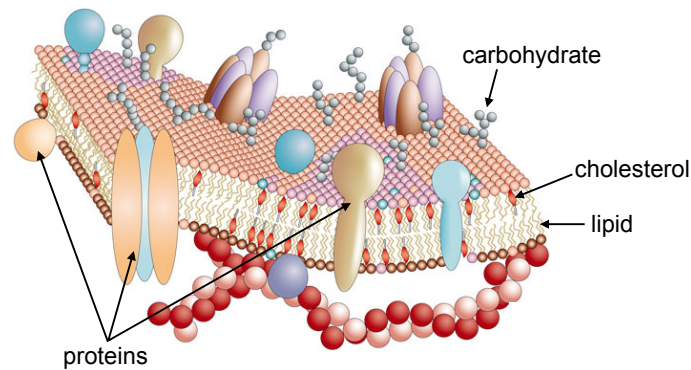


Figure 5: Biological membrane, from [48].

which are mobile and randomly distributed within the membrane. Afterwards, this model was refined frequently to be in line with newer research results [51–53], for example about membrane heterogeneity, mobility restrictions or the interaction of components.

Biological membranes mainly consist of a mixture of lipids, proteins and carbohydrates [52,53], with the specific composition depending on its particular function and thus on the type of the living species, the organ, the particular location in the organ and the cell type, where the membrane can be found. Also the cell plasma, and the extracellular region influence structure and dynamics of the membrane.

The basic bilayer structure is mainly formed by glycerophospholipids, sphingolipids and glycolipids [7]. Most of them have two hydrocarbon chains of a typical length of 14 to 24 carbons [30]. These lipid tails can be saturated, thus having a higher resistance against oxidation, or unsaturated which increases the membrane fluidity. A single cell contains about hundred different lipid species [7]. While in plants, more glycolipids can be found, there are more phospholipids in animal cells. Membranes of higher organisms additionally contain cholesterol and other sterols. For example the membrane of red blood cells or of the eye lens exhibit a high content of cholesterol [7, 54]. It increases the order of the lipid molecules and thus functions as a control of the membrane fluidity and permeability.

Besides the lipids, also proteins are of major importance for biological membranes. They can be attached to the surface, be deeply inserted or span the membrane. Due to their high concentration, protein crowding occurs. Consequently, there are many protein-protein contacts and the proteins also strongly interact with lipid molecules influencing the physical properties of the lipid bilayer, for example increasing its stability.

It is the main task of a membrane to separate and with this to protect the cell interior or a cell organelle from its environment. Forming a selective permeability barrier, the membrane allows for a controlled exchange of material and information between the two separated regions. For the transfer of molecules from one side of the membrane to the other, different mechanisms exist, for example endocytosis and exocytosis for the uptake and release of substances, respectively. Furthermore, molecular transport can be mediated by proteins, which can act as active carriers or form channels for example for ions [55,56]. Besides this, the biological membrane is site of many biochemical processes, like hormone action, energy production, immune response and neuronal signaling [48]. Hereby, the proteins act as receptors and transporters. Additionally, the

membrane stabilizes the cell and creates certain connections to the surrounding, for example to the cytoskeleton or to neighboring cells.

Complexity and heterogeneity with regard to molecular composition, membrane architecture and phase state are major characteristics of biological membranes. For example, membranes commonly show transmembrane asymmetry, that is the two leaflets of the bilayer have different chemical composition [53]. Also the lateral heterogeneity of biological membranes is remarkable. Of major relevance is the formation of domains with different chemical composition and size (from smaller than 100 nm to 1 μm) which provide specific functions [52]. While the phase of the biological membrane can mostly be described as liquid-crystalline, initiated by cholesterol and proteins there are also domains in the liquid-ordered phase [52]. One example are the so-called lipid rafts, which were extensively discussed within the last two decades [52, 57, 58]. Lipid rafts are small (several tens of nanometers), reversibly-formed, highly mobile membrane domains enriched in cholesterol, sphingolipid and certain proteins. Besides the lateral heterogeneity, also the membrane thickness, which normally amounts to about 10 nm [30], can locally vary significantly. Additional heterogeneity comes from non-lamellar phases which can occur alongside the mostly lamellar structures and play a role for certain processes like membrane fusion or fission. Normally, a biological membrane is constantly under reconstruction and not in a state of thermal equilibrium. This metastability makes the membrane more sensitive, allowing for a reaction to small stimuli.

In a number of serious illnesses, the functioning of membranes plays an important role. For example cystic fibrosis and epilepsy are promoted by a perturbation of certain ion channels [48]. However, the membrane can also be used as a location for pharmaceutical treatment. Drugs that should reach the cell interior need specific design to be able to pass the membrane, for example by passive diffusion or with the help of proteins [59].

2.4 Model Membranes

As outlined in the last section, the study of cell membranes on the molecular scale is a major research goal because it can improve the understanding of many biological processes. However, the high complexity of biological membranes renders these investigations difficult. Due to the presence of many different molecules and structures in a membrane, it is hard to extract the reaction of distinct components on certain conditions or substances from measured data. Therefore, model membranes often just consisting of only one or a few phospholipid species are used for simplification. Results from experiments on such model membranes cannot directly explain the behavior of biological membranes, but they can at least yield a very basic understanding. The model systems used in this work consist of phosphocholine MLVs which can be prepared easily and, due to the relatively high lipid concentration, provide a good signal-to-noise ratio in the NMR spectrum. Specifically, we investigate the interaction of lipid bilayers with amphiphilic or polyphilic guest molecules which can attach to the membrane surface or get embedded in the bilayers possibly forming a homogeneous distribution or assemble in clusters. As a result, membrane properties, like flexibility or permeability, or the membrane phase behavior can change.

Amphiphilic molecules are suited particularly well for the interaction with lipid bilayers. While the hydrophilic parts can interact with the lipid head groups or stay in the surrounding water, the hydrophobic molecule part can be incorporated into the lipid acyl chain region which

works especially well when its dimensions fit the bilayer core. These interactions can be tuned further by using polyphilic molecules. Their additional molecular units can, for instance, cause self-assembly of the guest molecules or the formation of a composite structure with the lipids. The intensity with which a guest molecule influences membrane properties depends on its membrane affinity and simultaneously on its ability to disturb the bilayer [60]. By systematically varying the chemical structure of the guest molecule, we search for a correlation to the form and strength of its interaction with the lipid membrane.

Probably the most intensely investigated model membrane/guest molecule system is the phospholipid bilayer with incorporated cholesterol, which is localized just underneath the lipid head group region with its hydroxy group pointing towards the water phase positioned near the glyceryl-fatty acid ester bonds and the rings immersed in the hydrocarbon region, preferentially aligned parallel to the lipid tails [23, 35]. Structure and dynamics of the polar lipid head groups are only slightly influenced by cholesterol [61]. Specifically, the tilt of the head group and the dynamics of the glycerol backbone can change [35, 62]. However, cholesterol has a considerably higher impact on the lipid hydrocarbon chains. While it increases the chain fluidity when the bilayer is in the gel phase, it decreases the chain fluidity when incorporated into a bilayer in the liquid-crystalline phase [23, 63]. This condensing effect arises from a stretching of the lipid chains [25, 61] that partially align next to the planar cholesterol rings [64]. As a consequence, the membrane thickness [65], impermeability [37, 66] and viscosity [67] are increased. In some cases, lateral phase separation is observed. For example, in bilayers of lipids with fully saturated acyl chains, e.g DPPC or sphingomyelin, domains with disordered lipid chains (liquid disordered phase) and regions with lipid tails that show enhanced stretching (liquid ordered phase) were found [64, 68]. Additionally, phase separation can occur in bilayers made of different lipid species and cholesterol because cholesterol interacts more favorably with saturated chains possibly expelling unsaturated lipids to separated domains [64].

Besides cholesterol, a large variety of other molecules in interaction with lipid membranes were investigated intensely. A few examples are given by numerous relatively small molecules [69] that incorporate in a bilayer, like ethanol [70, 71], glycerol [9], or various drugs [10]. Furthermore, there are many investigations on other sterols than cholesterol [25, 72] and on molecules with a size of a few nanometers that are able to form pores or channels in the bilayer [73, 74]. Also membrane systems with large additional molecules, like polymers [60], polypeptides [75] and proteins [10, 76] are studied widely in literature. Here, we specifically investigate lipid bilayers in interaction with amphiphilic triblock copolymers, which can assume different configurations inside the membrane. Furthermore, we study partially fluorinated urea and thiourea compounds capable of transporting anions through the membrane and X-shaped bolapolyphiles that can self-assemble into supramolecular structures in the bilayer.

3 Basics of NMR Spectroscopy

NMR is a well-established method for the investigation of molecular structure and dynamics in wide variety of samples. In this work, it is applied specifically for the study of lipid membranes. The basic concepts of NMR spectroscopy are introduced in the following section. The description is based on the textbooks of M. H. Levitt [77] and M. J. Duer [78]. Details about the specific NMR experiments used in this project are presented in Section 5. Before that, molecular dynamics in the lipid bilayer systems investigated are described in Section 4.

3.1 The Nuclear Spin

The basis of the NMR experiment is given by the intrinsic property of an atomic nucleus to have a spin which is a form of angular momentum. The net nuclear spin results from the spins of all the protons and neutrons forming the nucleus. Its ground state is described by the nuclear spin quantum number I which can take the values $0, \frac{1}{2}, 1, \frac{3}{2}, \dots, 6$. Within the framework of this work, we only conducted NMR experiments on the nuclei ^1H and ^{13}C , which both feature a spin quantum number of $I = \frac{1}{2}$. For NMR investigations on biological or model membrane systems in general, also the spin-1/2 nuclei ^{31}P , ^{15}N and ^{19}F are important [19, 76]. Furthermore, the isotope ^2H with $I = 1$ is frequently used to determine molecular order and dynamics in lipid bilayer systems [22, 23]. However, the naturally abundant nuclei ^{12}C and ^{16}O , which constitute a major part of many organic molecules, have a spin quantum number of $I = 0$ and consequently are not detectable by NMR.

The angular momentum of a spin is represented by the operator $\hat{\mathbf{I}}$ which is a vector describing its strength and direction. The vector components are given by the hermitian operators \hat{I}_x , \hat{I}_y and \hat{I}_z . The following eigenequations apply:

$$\hat{\mathbf{I}}^2 |I, m\rangle = I(I + 1) |I, m\rangle \quad (1)$$

$$\hat{I}_z |I, m\rangle = m |I, m\rangle \quad (2)$$

Herein, the reduced Planck constant \hbar , which actually should appear as a factor on the right side of both equations, is assumed to be a part of the operator. The eigenfunctions $|I, m\rangle$ are called Zeeman eigenstates. They are determined by the spin quantum number I and the magnetic quantum number m which can take the values $I, I - 1, \dots, -I$. Correspondingly, there exist $(2I + 1)$ eigenfunctions. As apparent from the Equations 1 and 2, the absolute value of the spin angular momentum and one of its components, which we have chosen to be the z -component, are quantized.

The total angular momentum P of a nucleus can be calculated from the square root of the eigenvalue of $\hat{\mathbf{I}}^2$:

$$P = |\mathbf{P}| = \hbar\sqrt{I(I + 1)} \quad (3)$$

and the z component of the angular momentum \mathbf{P} results from the eigenvalue of \hat{I}_z :

$$P_z = m\hbar \quad (4)$$

As any quantum mechanical state, the nuclear spin state can be described by a wave

function $|\Psi(t)\rangle$ which generally can be expanded into a series of a complete, orthonormal set of eigenfunctions $|\psi_j\rangle$:

$$|\Psi(t)\rangle = \sum_j c_j(t) |\psi_j\rangle \quad (5)$$

Herein, the superposition coefficients c_j are complex numbers that can be calculated from $c_j = \langle \psi_j | \Psi \rangle$. Normalization yields the relation $\langle \Psi | \Psi \rangle = \sum_j |c_j|^2 = 1$. Equation 5 can be used to describe the state of a nuclear spin or a system of coupled spins as a superposition of the $(2I + 1)$ eigenfunctions $|\psi_j\rangle = |I, m_j\rangle$. The resulting formulas are given in the Supplementary Section A.

In a next step, we want to predict the result of a measurement on a quantum mechanical system defined by a certain quantum state. To calculate a measured physical quantity Q , the associated quantum mechanical operator \hat{Q} is needed, the eigenvalues of which resemble the possible experimental results. As already described above, the state of a nuclear spin can be described mathematically by a superposition of states where the actual state is unknown. Hence, it is not clear which eigenvalue will be measured at a particular time. But the probability for measuring a specific eigenvalue can be determined and thus, also an expectation value, which resembles the average result of many observations, can be calculated:

$$Q = \langle \hat{Q} \rangle = \langle \Psi | \hat{Q} | \Psi \rangle \quad (6)$$

The magnetic moment of the nucleus is one example for such a physical quantity. It is proportional to the spin angular momentum and can be described using the operator:

$$\hat{\boldsymbol{\mu}} = \gamma \hat{\mathbf{I}} \quad (7)$$

The proportionality constant is given by the gyromagnetic ratio γ which is a nucleus-specific constant. The gyromagnetic ratio of ^1H is about four times higher than the gyromagnetic ratio of ^{13}C

$$\begin{aligned} \gamma(^1\text{H}) &= 267.522 \cdot 10^6 \text{ rad s}^{-1} \text{ T}^{-1} \\ \gamma(^{13}\text{C}) &= 67.283 \cdot 10^6 \text{ rad s}^{-1} \text{ T}^{-1} \approx \frac{1}{4} \gamma(^1\text{H}) \end{aligned}$$

which is the reason for the higher sensitivity of ^1H NMR experiments compared to ^{13}C NMR experiments. According to Equation 6, the expectation value of the nuclear magnetic moment can be calculated from

$$\boldsymbol{\mu} = \langle \Psi | \hat{\boldsymbol{\mu}} | \Psi \rangle. \quad (8)$$

The sum of all nuclear magnetic moments yields the measurable macroscopic magnetization

$$\mathbf{M} = \sum_i \boldsymbol{\mu}_i. \quad (9)$$

For a sample in equilibrium without external influences, this macroscopic magnetization is zero, due to the isotropic orientation distribution of the nuclear magnetic moments.

The evolution of a spin state $|\Psi\rangle$ over time can be examined by using the time dependent

Schrödinger equation:

$$i \frac{d}{dt} |\Psi(t)\rangle = \hat{H} |\Psi(t)\rangle \quad (10)$$

The Hamiltonian \hat{H} is a Hermitian operator, given here in natural units ($\hbar = 1$), which describes the energy of the spin system. It depends on external influences and interactions within the system.

For an NMR experiment, the sample is brought into a constant external magnetic field \mathbf{B}_0 which we choose to be aligned along the z -axis of our laboratory coordinate system: $\mathbf{B}_0 = B_0 \mathbf{e}_z$. The interaction of this field with the magnetic moments of the spins is described by the Zeeman Hamiltonian

$$\hat{H}_0 = -(\hat{\boldsymbol{\mu}} \cdot \mathbf{B}_0) = -\gamma B_0 \hat{I}_z = -\omega_0 \hat{I}_z \quad (11)$$

which in turn is characterized by the Larmor frequency $\omega_0 = \gamma B_0$. Considering additionally, that a sample does not only contain one kind of nuclear spins but various different spins with different Larmor frequencies, the Zeeman Hamiltonian can be written as the sum of these single contributions:

$$\hat{H}_0 = - \sum_i \omega_{0,i} \hat{I}_{iz} \quad (12)$$

The eigenequations of the Zeeman Hamiltonian are given by

$$\hat{H}_0 |I, m_j\rangle = E_j |I, m_j\rangle \quad (13)$$

with the Hamiltonian eigenstates or energy eigenfunctions $|I, m_j\rangle$ being equal to the already introduced eigenfunctions of \hat{I}_z . The eigenvalues are real numbers representing the energy levels E_j of the spin system. They can be calculated from

$$E_j = -m_j \omega_0. \quad (14)$$

As for the quantum number m_j , there exist $(2I + 1)$ values for E_j enumerated by the index j . In the absence of an magnetic field, these sublevels are degenerate. The splitting of the nuclear spin ground state, also called Zeeman effect, only appears under influence of an external magnetic field. The energy difference between two subsequent sublevels with m_j and $m_j \pm 1$ is called Zeeman splitting and given by the Larmor frequency $\Delta E = \omega_0$.

For example, for a system of isolated spin-1/2 nuclei, the ground level splits into two energetically different sublevels characterized by the eigenvalues $E_{|\alpha\rangle/|\beta\rangle} = \mp 0.5 \omega_0$ for the eigenstates $|\alpha\rangle$ und $|\beta\rangle$. The difference of the two energy levels is small ($\hbar \omega_0 \approx 2.65 \cdot 10^{-25}$ J for protons in a field of 9.4 T) in comparison to the thermal energy ($k_B T \approx 4.1 \cdot 10^{-21}$ J at room temperature). However, because the energy of the spin state $|\alpha\rangle$ is a slightly lower than the energy of state $|\beta\rangle$, there is a slightly higher probability for a spin to assume the state $|\alpha\rangle$ in thermal equilibrium causing a small measurable macroscopic magnetization which points in the direction of the external magnetic field.

3.2 Description of a Spin Ensemble by the Density Operator

Until here, only a single-spin system was considered. A real sample, however, contains a huge amount of spin systems. In the following, we will therefore introduce the density operator $\hat{\rho}(t)$ which allows for the description of the quantum state of a whole ensemble of spin systems and simultaneously avoids the need to deal with single spin states. Instead, the density matrix only contains the average contribution of each ensemble member. The spin density operator is given by

$$\hat{\rho}(t) = \langle |\Psi(t)\rangle \langle \Psi(t)| \rangle \stackrel{\text{Eq.5}}{=} \sum_{i,j} \langle c_i(t)c_j^*(t) \rangle |\psi_i\rangle \langle \psi_j|. \quad (15)$$

The angular brackets indicate the averaging over all members of the spin ensemble. The spin density operator is Hermitian, normalized so that its trace equals one, and all its eigenvalues are positive. As for the spin states, also the density operator can be written as a matrix consisting of the elements

$$\rho_{ij}(t) = \langle \psi_i | \hat{\rho} | \psi_j \rangle = \langle c_i(t)c_j^*(t) \rangle. \quad (16)$$

For an ensemble of non-interacting equivalent spin-1/2 nuclei, the density matrix contains four elements.

The diagonal elements ρ_{ii} represent the populations of the eigenstates associated. They are real numbers between zero and one that altogether sum up to one. A difference in the populations indicates that there is a macroscopic magnetization parallel to the external magnetic field, which is called longitudinal magnetization.

The non-diagonal elements ρ_{ij} ($i \neq j$) of the density matrix are referred to as coherences. They describe the relation between the two eigenstates $|\psi_i\rangle$ and $|\psi_j\rangle$ and can be characterized by the coherence order $o_{ij} = m_i - m_j$, calculated from the difference of the z -angular momentum of the two associated states. The presence of coherences with order $o_{ij} = -1$ is a hint for partially aligned transverse spin polarizations that cause transverse magnetization, that is measurable macroscopic magnetization in the xy -plane which is perpendicular to the external magnetic field. Coherences of higher order can appear, for example, for an ensemble of systems consisting of two or more coupled spins. These multi-quantum coherences do not represent a macroscopic magnetization and therefore are not directly detectable. They can be imagined as polarization correlations within a group of interacting spins.

By help of the density matrix, the expectation value of an operator \hat{Q} , that is, a macroscopic observable Q , can be determined easily. Using Equations 5 and 6, we get:

$$\langle \hat{Q} \rangle = \sum_{ij} c_i c_j^* \langle \psi_i | \hat{Q} | \psi_j \rangle = \sum_{i,j} \rho_{ij} Q_{ij} = \text{Tr}(\hat{\rho} \hat{Q}) \quad (17)$$

Using this equation, we can conclude, that only longitudinal magnetization is present, when the spin density operator can be expressed by an \hat{I}_z -term alone, and accordingly, when the density operator contains $\hat{I}_{x,y}$ -terms, transverse magnetization occurs.

The evolution of the density operator over time under influence of different interactions represented by a Hamiltonian \hat{H} , given in natural units, can be described by help of the

Liouville-von Neumann equation

$$\frac{d}{dt}\hat{\rho}(t) = -i \left[\hat{H}, \hat{\rho}(t) \right], \quad (18)$$

which is calculated from the Schrödinger equation using the definition of the density operator given in the Equations 10 and 15, respectively. In case of a time-independent Hamiltonian that commutes with the density operator, the solution of the differential equation can be written as

$$\hat{\rho}(t) = e^{-i\hat{H}t}\hat{\rho}(0)e^{i\hat{H}t}. \quad (19)$$

However, when the Hamiltonian changes during time, the solution is more complex. In this case, one possible approach is to split the examined time frame in smaller time intervals on which the Hamiltonian is constant or assumed to be constant. With this, a solution can be obtained in the same manner as before:

$$\hat{\rho}(t_1 + t_2 + \dots + t_n) = e^{-i\hat{H}_n t_n} \dots e^{-i\hat{H}_2 t_2} e^{-i\hat{H}_1 t_1} \hat{\rho}(0) e^{i\hat{H}_1 t_1} e^{i\hat{H}_2 t_2} \dots e^{i\hat{H}_n t_n} \quad (20)$$

To calculate the outcome of a complex NMR experiment, the average Hamiltonian theory is a common tool. In this context, the development of a spin system over time is described by an effective time-independent Hamilton operator, which has the same influence on the spin system as all single, possibly time-dependent Hamiltonians together. Generally, the average Hamiltonian includes contributions from interactions within the spin system as well as external manipulations.

When a sample is kept undisturbed in the magnetic field for a long time, then the spin system reaches thermal equilibrium which is the usual starting point for an NMR experiment. In this case, the ensemble of spin states can be described by a diagonal density matrix with populations that can be calculated using the Boltzmann distribution with the Boltzmann constant k_B and the temperature T :

$$\hat{\rho}^{\text{eq}} = \frac{\exp\left[-\sum_j^J \frac{\hat{I}_{jz} \hbar \omega_{0,j}}{k_B T}\right]}{\text{Tr}\left\{\exp\left[-\sum_j^J \frac{\hat{I}_{jz} \hbar \omega_{0,j}}{k_B T}\right]\right\}}. \quad (21)$$

As the lower energy eigenstates are more populated than the higher ones, a macroscopic magnetization arises, which is smaller for nuclei with smaller gyromagnetic ratios γ . Equation 21 can be approximated well by a Taylor series as the value of the energy quotient in the exponent is very small. The result is the so called high-temperature approximation:

$$\hat{\rho}^{\text{eq}} = \frac{1}{J} \hat{1} + \frac{1}{J} \frac{\hbar \omega_0}{k_B T} \hat{I}_z \quad (22)$$

The term with the unity matrix is usually abolished because it does not cause detectable magnetization. Similarly, the prefactors are in most cases not of interest. Therefore, only the term

$$\hat{\rho}^{\text{eq}} \sim \hat{I}_z \quad (23)$$

is left over to describe the spin ensemble at the starting point of the NMR experiment.

3.3 The NMR Experiment

3.3.1 Theoretical Considerations

During an NMR experiment, a radio frequency (r.f.) pulse is applied, that is, a magnetic field B_1 oscillating with a frequency ω_{ref} close to the Larmor frequency is irradiated on the sample, consequently, disturbing the equilibrium state of the spin system. In the density matrix, populations change and coherences appear and as a result measurable magnetization can be created. To describe the effects of a pulse on the spin ensemble mathematically, the system is transferred to the rotating frame which is a reference frame that rotates around the z -axis with the frequency of the applied field ω_{ref} . In this case, the Schrodinger equation and the Liouville-von Neumann relation (Equations 10 and 18) can be used as before taking additionally into account that they now comprise the rotating-frame wave function and Hamiltonian. The rotating-frame Zeeman Hamiltonian contains the offset frequency $\Omega_0 = \omega_0 - \omega_{\text{ref}}$ in place of the Larmor frequency ω_0 . The r.f. Hamiltonian is time independent in the rotating frame. For a short, ideal r.f. pulse applied in an angle of 90° to the static magnetic field, the r.f. Hamiltonian can be written as

$$\hat{H}_{\text{rf}} = -\gamma B_1 (\hat{I}_x \cos \phi_p + \hat{I}_y \sin \phi_p). \quad (24)$$

As before, for describing a system of several coupled spins, we use the sum of the components $\sum_i \hat{I}_{ix}$ and $\sum_i \hat{I}_{iy}$. In Equation 24, the angle ϕ_p determines the irradiating direction of the pulse in the xy -plane. For example for $\phi_p = 0$, the pulse is directed parallel to the x -axis. A pulse antiparallel to the x -axis we mark with \bar{x} . Analogously, pulses with $\phi_p = \pi/2, 3\pi/4$ in $\pm y$ direction are indicated by y and \bar{y} .

By solving the Liouville-von Neumann equation, the influence of an x -pulse on a spin system in thermal equilibrium ($\hat{\rho}(0) \sim \hat{I}_z$) can be determined to be

$$\hat{\rho}(t) \sim e^{-i\gamma B_1 \hat{I}_x t} \hat{I}_z e^{i\gamma B_1 \hat{I}_x t} = \hat{I}_y \cos(\gamma B_1 t) - \hat{I}_z \sin(\gamma B_1 t) \quad (25)$$

From this equation, we can see that besides the fast rotation about the direction of the static magnetic field $B_0 \mathbf{e}_z$, the spin polarization additionally rotates about the axis given by the B_1 field of the pulse. This double rotation motion is also called nutation and defined by the nutation frequency

$$\omega_1 = \gamma B_1. \quad (26)$$

The flip angle $\beta_p = \omega_1 t_p$ specifies how far the direction of spin polarization is rotated by the pulse during the irradiation time t_p . A 90_x° pulse, which is a pulse in x direction with $\beta_p = 90^\circ$, transforms the states of a spin ensemble from equilibrium $\hat{\rho}^{\text{eq}} \sim \hat{I}_z$ to $\hat{\rho} \sim \hat{I}_y$, where macroscopic magnetization in y direction can be measured. A 180° pulse causes an inversion of the populations resulting in $\hat{\rho} \sim -\hat{I}_z$. However, in NMR experiments using induction coils, only transverse magnetization can be detected.

After subsequently reversing the transformation to the rotating frame, we get a macroscopic magnetization vector that precesses about the direction of the irradiated magnetic field as the end result. However, the system does not stay in this state, but tends back to its equilibrium value due to relaxation processes which arise from the interaction of the spins with their environment causing a decrease of the transverse magnetization and a rebuilding of the longitudinal magnetization

with the characteristic time constants T_2 and T_1 , respectively. Alternatively, the relaxation rates $R_2 = T_2^{-1}$ and $R_1 = T_1^{-1}$ are used. A simple mathematical description of these relaxation processes using exponential functions can be gained from the phenomenological approach of Bloch.

Generally, the effect of an r.f. pulse can also be described easily in a classical way using the vector model. Hereby, we just consider length and direction of the magnetization vector, which, for example is rotated by a pulse about its irradiation axis.

For the explanation of more complex NMR experiments, the Product Operator Formalism (POF) is used frequently. In this case, the spin density operator is expressed as a linear combination of base operators (\hat{I}_x , \hat{I}_y , \hat{I}_z and combinations of them, so-called product operator terms) and its time development under influence of couplings and pulses is calculated using given rules which partly allow for a geometric visualization [79].

3.3.2 Practical Aspects

The NMR experiment needs to fulfill the demanding task of measuring a very small signal with high sensitivity and frequency resolution. Prerequisite is a strong, static and very homogeneous magnetic field \mathbf{B}_0 which is achieved by using superconducting coils cooled with liquid helium. At present time, NMR magnets producing fields up to 23.5 T are offered commercially [80]. With additional shim coils, the field homogeneity can be fine-tuned.

To bring the sample in the region of the homogeneous field, it is put in a probe head which is inserted in the magnet through a bore. Appropriate equipment in the probe allows for sample rotation and the setting and stabilizing of the sample temperature. However, the most important function is the sending of r.f. pulses on and the detection of the following emission from the sample which is all operated by the pulse program on the computer.

For the r.f. pulse, an electric signal $s \sim \cos(\omega_{\text{ref}}t + \phi)$ is generated by the transmitter section of the spectrometer. This signal is sent through a pulse gate, which sets the pulse duration t_p . Subsequently, it is amplified and directed to a coil wound around the sample where it causes an oscillating magnetic field \mathbf{B}_1 . Ideally, this r.f. field is perpendicular to the main magnetic field and spatially homogeneous. A shorter pulse with a larger r.f. amplitude is less frequency selective and therefore allows for a reasonably uniform manipulation of all spin states of a specific type of nucleus in the sample, even when they show slightly different Larmor frequencies.

Transverse magnetization created by the r.f. pulse is very small but nevertheless detectable because it oscillates with a well-defined frequency. After switching off the pulse, the precessing magnetization vector from the sample generates a voltage in the surrounding coil which in turn gives rise to an oscillating electric current. To maximize the signal transmission, the resonance frequency of the circuit containing the coil with the sample can be tuned to the pulse frequency and its impedance can be matched to the connections by adjusting additional capacitors. For NMR experiments on different nuclei, for example ^1H and ^{13}C , the probe head contains different resonance circuits, called frequency channels.

By using a duplexer, only the weak NMR signal is sent in the sensitive signal detection path, while the strong pulse is blocked. Nevertheless, there is a dead time of some microseconds between the decaying pulse and the start of signal acquisition. Subsequently, the NMR signal is further amplified by the receiver. Using quadrature detection, we can monitor the time evolution

of the magnetization in the rotating frame from two perpendicular directions. For this, the signal of the sample is mixed with two reference waves oscillating with ω_{ref} , that are shifted by 90° to each other. The resulting signal oscillates with an offset frequency of $\Omega_0 = \omega_0 - \omega_{\text{ref}}$ which is slow enough to be processed by an analogue-to-digital converter. Representing the two perpendicular directions, we obtain two output signals that can be interpreted as real and imaginary part of a complex signal. When we combine the two signals and also consider an exponential decay accounting for the relaxation process, we get

$$s(t) \propto e^{i\Omega_0 t} e^{-tR_2} e^{-i\phi_{\text{rec}}}. \quad (27)$$

By doing a phase correction, the user defined receiver phase ϕ_{rec} is set to zero which allows for a so-called absorptive measurement. This signal intensity measured over time is referred to as Free Induction Decay (FID). As an example, a curve calculated from Equation 27 is presented in Figure 6. In the more general case, one sample can yield many different signal contributions with different relaxation times and frequencies. The total signal arises from the superposition of all part-signals:

$$s(t) = \sum_l a_l e^{(-i\Omega_{0,l} - R_{2,l})t} \quad (28)$$

Using the Fourier transform analysis

$$S(\Omega) = \int_0^\infty s(t) e^{-i\Omega t} dt \quad (29)$$

the time dependent signal intensity is converted into a frequency dependent function. In practice, an FID is usually processed by performing a discrete Fourier transformation using the Fast Fourier Transformation (FFT) method, which yields the same result as the analytical formula. In an absorptive measurement, the NMR spectrum is represented by the real part of $S(\Omega)$. The imaginary part has a dissipative form and is mostly not of interest. For a simple exponential signal decay like shown in Equation 27, we get a spectrum with a Lorentzian peak:

$$\text{Re}[S(\Omega)] = A(\Omega) \propto \frac{R_2}{R_2^2 + (\Omega - \Omega_0)^2} \quad (30)$$

In the more general case of a sum of different signals as given in Equation 28, the spectrum contains the respective peaks of all contributing components. The peak position in the spectrum is determined by the offset frequency Ω_0 and the peak width by the relaxation rate R_2 (see Figure 6), when only homogeneous broadening is present. However, due to additional inhomogeneous broadening caused by variations of macroscopic magnetic fields over the sample or by spin interactions, experiments often yield spectra with broader peaks. A faster decay of the FID generally results in a broader peak in the spectrum.

The spectral width depends on the dwell time, that is the time distance between two acquired points and the center of the spectrum is defined by the reference frequency. The acquisition time is the total duration over which the signal is sampled, which ideally equals the time at which the signal is decayed to the noise level. When, however, distinct signal intensity is left at the end of the acquisition period, the whole signal can be multiplied by a window function that accelerates its decay and therefore suppresses so-called wiggles in the spectrum. With subsequent zero filling

the number of points in the spectrum can be increased. To enhance the signal-to-noise ratio, the experiment is usually performed several times and the results are averaged. A single experiment is called one scan and the time in-between two scans is the recycle delay. Phase cycles, that is different pulse phases in different scans of one experiment, can be used to select or suppress specific NMR signals and to eliminate artifacts caused by pulse or receiver imperfections.

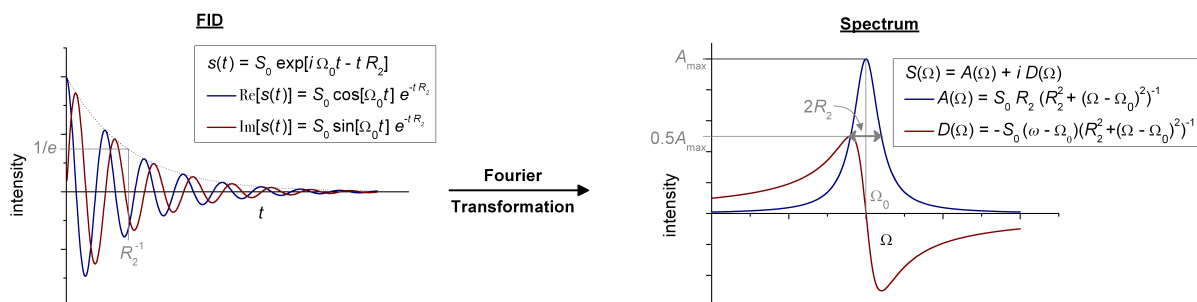


Figure 6: FID and spectrum calculated from Equation 27 and 30, respectively.

3.4 NMR Interactions

The Zeeman effect is the dominating interaction for nuclear spins in a magnetic field. However, also a variety of internal interactions influence the spin system. For solid-state NMR, the chemical shift and the dipolar coupling are most important. The J -coupling in solid samples is only small in comparison, but it is relevant for liquid-state NMR. The quadrupolar interaction only plays a role for nuclei with $I > \frac{1}{2}$ and therefore will not be considered in this work. Mathematically, it can be described in a similar way as the dipolar coupling. All these interactions give rise to a deviation of the spin resonance frequency from the Larmor frequency. Hence, they provide relevant molecular-level information and therefore form the basis for the NMR experiments.

An internal interaction can be represented by a Hamilton operator \hat{H}_{int} . When different spin interactions are present, the total Hamiltonian of the system arises from the sum of the Zeeman and all other Hamiltonian. Because the local fields produced by internal interactions are small in comparison to the high external magnetic field, their influence can be described mathematically in a facilitated manner as a first order perturbation of the dominating Zeeman effect. In this so-called secular approximation or high-field truncation, the Hamiltonian \hat{H}_{int} is simplified by only considering the parts that are time-independent (also in the rotating-frame) and commute with the Zeeman Hamiltonian \hat{H}_0 . All other, non-secular, terms are neglected. They play a role, however, for the relaxation processes. Fast molecular dynamics allow for further simplification of the Hamiltonian by approximating it by its motional average thereby removing the time dependence.

3.4.1 Chemical Shift

The chemical shift is caused by the indirect interaction of the nuclear spins with the magnetic field via their electronic surrounding. More precisely, the external magnetic field \mathbf{B}_0 induces currents in the electron cloud of a molecule and mixes electronic states. The electrons, in turn,

generate secondary magnetic fields \mathbf{B}_{ind} which cause a variation of the local magnetic fields $\mathbf{B}_{\text{local}}$ on a submolecular distance scale:

$$\mathbf{B}_{\text{local}} = \mathbf{B}_0 + \mathbf{B}_{\text{ind}} \quad (31)$$

Consequently, also the resonance frequency of a nucleus is influenced. The induced frequency shift is called chemical shift because it depends on the chemical surrounding of the nucleus such as the directly bonded or other neighboring atoms from the same or a different molecule. The resonance frequency of a nucleus can be determined by its position in the molecule, the solvent or even secondary molecular structures. For example, an aromatic ring in the vicinity of the nucleus investigated, can induce a shift of its resonance frequency due to ring-current effects.

Generally, the induced field and therefore also the resonance frequency of a nucleus is proportional to the external magnetic field. However, in solid samples, we need to consider additionally the Chemical Shift Anisotropy (CSA). This means that depending on the molecular form, the external magnetic field can point in a different direction than the induced magnetic field:

$$\mathbf{B}_{\text{ind}} = \boldsymbol{\sigma} \cdot \mathbf{B}_0 \quad (32)$$

Herein, the chemical-shift tensor $\boldsymbol{\sigma}$ is a 3×3 matrix with real elements.

The general Hamiltonian describing the chemical shift interaction is given by

$$\hat{H}_{\text{CS}}^{\text{full}} = -\gamma \hat{\mathbf{I}} \cdot \boldsymbol{\sigma} \cdot \mathbf{B}_0, \quad (33)$$

and for the secular part we get

$$\hat{H}_{\text{CS}} = -\gamma B_0 \sigma_{zz} \hat{I}_z \quad (34)$$

which is analogous to the Zeeman Hamiltonian, only containing the zz -component of the shielding tensor as an additional factor which depends on the angles that transfer the chemical shift tensor from its principle axis system to the laboratory frame defined by \mathbf{B}_0 .

In a powder sample, all tensor orientations occur and all of them give rise to a different resonance frequency $\omega_{\text{CS}} = \gamma B_0 \sigma_{zz}$ in the NMR spectrum. The superposition of all these sharp peaks yields a spectrum with a typical powder pattern form.

For lipid molecules in a fluid bilayer, the CSA tensor is uniaxial due to the fast reorientation of the lipids about their long axis. In this case, the resonance frequency can be calculated from

$$\omega_{\text{CS}} = \omega_0 (\sigma_{\text{iso}} + \langle \delta \rangle P_2(\cos \vartheta)), \quad (35)$$

where σ_{iso} is the isotropic chemical shift, $\langle \delta \rangle$ the anisotropy parameter of the time-averaged CSA tensor, and $P_2(\cos \vartheta) = \frac{1}{2} (3 \cos^2 \vartheta - 1)$ refers to the second Legendre polynomial taken of the cosine of the angle ϑ which describes the long-axis orientation of the lipid molecule with respect to \mathbf{B}_0 . For $\vartheta = 0^\circ$ and $\vartheta = 180^\circ$, the maximum value of $P_2(1) = P_2(-1) = 1$ is assumed, and for a molecular long-axis perpendicular to the magnetic field ($\vartheta = 90^\circ$), the minimum value of $P_2(0) = -0.5$ is reached. The powder spectrum resulting for a sample of liposomes, is characterized by a high-field peak and a low-field shoulder that originate from lamellar normal orientations perpendicular and parallel to the magnetic field, respectively [81]. Experimentally, such a spectrum can be acquired for ^{31}P , which is an isolated spin-1/2 nucleus.

For fast-tumbling molecules in solution, there is no orientation dependence and each chemically different nucleus in general gives rise to a separate resonance line with a characteristic isotropic chemical shift frequency

$$\omega_{\text{CS}} = \omega_0 \sigma_{\text{iso}} \quad (36)$$

which is of high importance for the determination of molecular structure and dynamics in chemistry.

As a standard, the position of a resonance line in the NMR spectrum is given by the field-independent expression

$$\delta = \frac{\omega_0 - \omega_{0,\text{ref}}}{\omega_{0,\text{ref}}} \quad (37)$$

which is called chemical shift although it can be used to describe all kinds of change in the resonance frequency. It is a dimensionless quantity calculated by using the frequency $\omega_{0,\text{ref}}$ of a reference compound (for example TMS) and is usually given in ppm (parts per million).

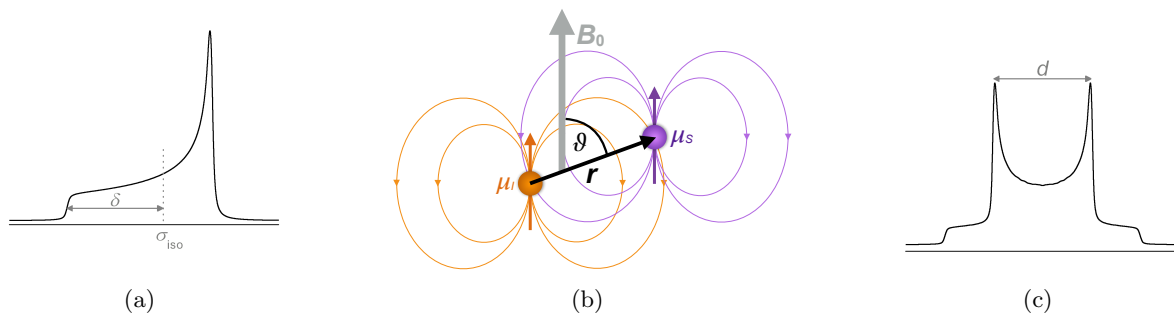


Figure 7: (a) NMR spectrum resulting of the chemical shift interaction from one chemical site in a molecular group performing fast uniaxial reorientations calculated from Equation 35. (b) Schematic drawing of the dipolar interaction of two nuclei with the magnetic moments μ_I and μ_S , and (c) Pake pattern calculated using Equation 42.

For determining the spectra, a line shape according to Equation 30 is assumed for the signal of one orientation and the powder distribution is calculated from $S_{\text{powder}}(\omega) = \int_0^\pi d\vartheta \sin(\vartheta) S(\omega)$. The x -axis is normalized by ω_0 .

3.4.2 Dipolar Coupling

Besides the CSA, another main reason for line broadening in solid-state NMR is the dipole-dipole coupling which is the direct magnetic interaction through space between nuclear spins possibly intermolecular or intramolecular. Specifically, a nuclear spin possessing a magnetic dipole moment μ generates a local magnetic field which influences the magnetic moment of a second nucleus close by. In turn, also the first spin interacts with the magnetic field produced by the second spin (see Figure 7(b)). The Hamilton operator for the dipolar interaction between two spins I and S can be derived analogously to the classical description of the interaction energy of two point magnetic dipoles and results as

$$\hat{H}_D^{\text{full}} = d \left(\hat{\mathbf{I}} \cdot \hat{\mathbf{S}} - \frac{3(\hat{\mathbf{I}} \cdot \mathbf{r})(\hat{\mathbf{S}} \cdot \mathbf{r})}{r^2} \right). \quad (38)$$

The amplitude is given by the dipolar-coupling constant

$$d = \frac{\mu_0 \gamma_I \gamma_S \hbar}{4\pi r^3} \quad (39)$$

which depends on the magnetic constant μ_0 and the distance r between the two spins. For a complete treatment of a system with many spins, one needs to sum up the contributions of all interacting spin pairs, which, particularly for solid samples, can be a bigger number. This is also the case for all secular Hamiltonians derived later on.

Alternatively, the dipolar Hamiltonian for a two-spin system can also be written as

$$\hat{H}_D^{\text{full}} = -2\hat{\mathbf{I}}\mathbf{D}\hat{\mathbf{S}} \quad (40)$$

by using the dipolar coupling tensor \mathbf{D} . Determination of the eigensystem of \mathbf{D} yields a principal axis frame with a unique axis pointing along the interconnection vector of the spins I and S . In this frame, the axially symmetric and traceless tensor is defined by its principal values $-d/2$, $-d/2$ and d .

The dipolar Hamiltonian can be further simplified in several steps. After expanding it by writing the interconnection vector \mathbf{r} in spherical coordinates and using the shift operators to describe the spin angular momenta, the transition in the rotating frame is performed and secular approximation applied. Hereby, we distinguish between the homonuclear case, where spins of the same isotopic species are coupled and the heteronuclear interaction between spins of different isotopic species. In the homonuclear case, rotation matrices are applied on both spins and in the heteronuclear case only on one of the two spins. Commonly, the dipolar Hamiltonians are also expressed in terms of spherical tensor operators and spherical tensor functions simplifying further calculations like many rotations. However, we will not do this here. We now firstly consider the heteronuclear interaction. For this work, the most relevant example is the coupling between ^1H and ^{13}C nuclei (spins I and S). The secular Hamiltonian only consists of one term

$$\hat{H}_D^{\text{hetero}} = -2P_2(\cos \vartheta)d\hat{I}_z\hat{S}_z. \quad (41)$$

It contains the second Legendre polynomial P_2 of the cosine of the angle ϑ which lies between the connection vector of the two spins and the external magnetic field (see Figure 7(b)). The eigenfunctions of this Hamiltonian are equal to the Zeeman product states. and the energy levels, given by the corresponding eigenvalues, depend, among other things, on the polarization of the two spins to each other. The dipolar interaction of two spins with parallel polarization yields a positive and with antiparallel polarization a negative contribution resulting in a line splitting in the NMR spectrum. Therefore, the spectrum recorded for the rare spin S shows a line doublet at

$$\omega = \omega_0 \pm dP_2(\cos \vartheta) = \omega_0 \pm \omega_D \quad (42)$$

due to the dipolar coupling to spin I . The transition frequency of spin S without dipolar interaction is given by ω_0 .

As for the CSA, the dipolar spectrum of a powder sample follows from the superposition of the signals from spin pairs in all orientations to the magnetic field. Due to the identical positive and negative contributions we get a spectrum with the typical form of a Pake pattern consisting

of two mirror images with identical isotropic frequency (see Figure 7(c)). The two maxima correspond to signals from spin pairs oriented perpendicular to the external magnetic field and appear in a distance that equals the coupling constant d . However, the spectrum of real samples often only features a washed-out form of the Pake pattern due to additional interactions with other nuclei and molecular motions.

The homonuclear dipolar interaction occurs in-between abundant nuclei like ^1H . For two coupled spins I_1 and I_2 , the secular Hamiltonian is given by

$$\hat{H}_D^{\text{homo}} = -P_2(\cos \vartheta)d \left(3\hat{I}_{1z}\hat{I}_{2z} - \hat{\mathbf{I}}_1 \cdot \hat{\mathbf{I}}_2 \right). \quad (43)$$

Besides the first term that already appeared for the heteronuclear interaction, it contains a second term which expresses a possible 'flip-flop' mechanism meaning that the two interacting spins can induce spin state transitions to each other because they precess with similar frequencies. This effect can be seen from the eigenfunctions of the Hamiltonian, given by $|\alpha\alpha\rangle$, $|\beta\beta\rangle$ and two linear combinations of $|\alpha\beta\rangle$ and $|\beta\alpha\rangle$. In time evolution, these two functions result in a mixing of the states $|\alpha\beta\rangle$ and $|\beta\alpha\rangle$ cancelling out their degeneracy. Also for a many-spin system, eigenfunctions are generally given by linear combinations of the degenerate Zeeman levels.

For an ensemble of non-interacting spin pairs, the resulting spectrum has a similar form as in the heteronuclear case

$$\omega = \omega_0 \pm \frac{3}{2}dP_2(\cos \vartheta) = \omega_0 \pm \frac{3}{2}\omega_D. \quad (44)$$

Due to the second term in the Hamiltonian, the splitting is increased by a factor of $\frac{3}{2}$.

For a many-spin system however, we have multiple splittings of originally degenerate Zeeman levels causing many transition frequencies and therefore broad lines with width of several tens of kHz in the NMR spectrum. For large spin systems, the line form is nearly Gaussian which is generally the case in organic solids, where strong multiple homonuclear couplings between ^1H nuclei are present.

A phenomenon caused by dipolar couplings is spin diffusion. This is a quantum-mechanical exchange process which in case of non-uniform magnetization distribution in a sample can cause polarization transfer between neighboring spins allowing for an equilibration of the differences. This transfer, however, only works efficiently, when the dipolar coupling between the nuclei exceeds the difference of their resonance frequencies in the NMR spectrum, that is lines need to overlap. Spin diffusion can occur between protons in more rigid systems and influence experimental results.

As for the chemical shift, also the dipolar interaction is influenced by molecular dynamics. Averaging of the dipole-dipole coupling occurs when spin pair orientations change due to molecular motions that are fast compared to the inverse of the coupling strength. In liquids, fast isotropic molecular dynamics lead to a complete averaging of dipolar couplings. In the NMR spectrum, only sharp peaks appear at the isotropic chemical shift because of

$$\int_0^\pi (3 \cos^2 \vartheta - 1) \sin \vartheta d\vartheta = 0. \quad (45)$$

In liquid-crystalline systems and also in solids, usually a partial averaging occurs which can be

expressed mathematically by the time and ensemble average of the coupling strength

$$\langle \omega_D \rangle = \frac{\mu_0 \gamma_I \gamma_S \hbar}{4\pi} \frac{1}{2} \left\langle \frac{3 \cos^2 \vartheta - 1}{r^3} \right\rangle \quad (46)$$

and can be seen as a reduced splitting in the NMR spectrum. This residual dipolar coupling can be determined from experiments and used to describe the molecular order in various sample systems.

3.4.3 *J*-Coupling

The scalar coupling or *J*-coupling or indirect dipole-dipole interaction is the magnetic interaction of two nuclear spins mediated by the electrons of the connecting chemical bond. Although this interaction is described by a *J*-coupling tensor, its anisotropy is much smaller than the one of the direct dipolar coupling and therefore can be neglected in most cases. In an isotropic liquid, the *J*-coupling tensor is averaged and unlike in the case of the direct dipolar coupling, a certain interaction remains which can be described by the Hamiltonian

$$\hat{H}_J = -2\pi J \hat{I}_z \hat{S}_z \quad (47)$$

for the heteronuclear case. For example, for a $^1\text{H} - ^{13}\text{C}$ spin pair, the field-independent *J* coupling constant amounts to about 140 Hz [82]. In the NMR spectra of samples where motional averaging occurs, the *J*-coupling causes a line splitting which can be very useful in chemistry as it contains information about the nuclei connected by bonds.

3.5 Relaxation Processes

After perturbation of a spin system, a relaxation process takes place converting the excited state of the system back to the state of thermal equilibrium (see Section 3.3.1). Reason for this relaxation process are thermal motions which induce changes in the molecular orientations. This in turn results in variations of the orientation-dependent interactions of the nuclear spins, like the dipolar coupling or the CSA interaction, causing fluctuations of the microscopic magnetic fields at the nuclear sites. Correspondingly the Larmor frequencies of the nuclei are influenced which finally cause changes of the nuclear spin states towards the thermal equilibrium state of the system.

Longitudinal relaxation (also called spin-lattice relaxation or T_1 relaxation) refers to the build-up of macroscopic magnetization, when an external magnetic field is switched on abruptly or alternatively it refers to the magnetization decay to zero when the magnetic field is switched off again. Accordingly, in the NMR experiment, it describes the rebuilding of longitudinal magnetization after a perturbation like a 90° pulse.

In the quantum-mechanical representation, the longitudinal relaxation is defined as the drift of the populations in the density matrix back to their value of thermal equilibrium. In the easiest case, the build-up or decay of magnetization or populations can be described by an exponential function containing just a single characteristic time constant T_1 . This relaxation time is short for molecular segments showing fast motions with rates near the Larmor frequency. These dynamics cause fast changes of the nuclear spin interactions and accordingly fast fluctuations

of the transverse components of local effective fields and therefore allow for an effective energy transfer between the spin system and the surroundings (also called “lattice”). Hence, strong relaxation results. On the opposite, for molecular segments showing motional rates that are considerably larger or smaller than the Larmor frequency, there is no efficient coupling of spins and lattice and accordingly, the relaxation is slower and T_1 higher. Because protons have a higher magnetic moment than carbons, they generally also show shorter T_1 relaxation times.

The T_2 relaxation, which is also called transverse relaxation or spin-spin relaxation, describes the non-reversible decay of transverse magnetization to zero, for example after a 90° pulse. In the mathematical description, this is the decay of the coherences in the density matrix. The relaxation is caused by spin-spin interactions. Again, it is influenced by slight fluctuations in strength and orientation of local magnetic fields which in this case cause the precessing nuclei to lose their phase coherence. Additionally, the limited life time of a certain spin state plays a role. When all phases are distributed randomly, the transverse magnetization is zero. An exchange of energy does not occur during this relaxation process, but the entropy of the spin system increases. The process of transverse relaxation is described by the transverse relaxation time T_2 which is generally smaller than the T_1 relaxation time.

Another relaxation process takes place during r.f. irradiation over a longer time in an NMR experiment. It is characterized by the rotating frame relaxation time $T_{1\rho}$.

From the considerations above, it can be concluded that measurements of nuclear spin relaxation times in an NMR experiment can be used to investigate molecular motions. In principle, the measurement of T_1 times at different magnetic fields or for a number of different temperatures, can yield valuable information on geometry and rates of motional processes and allow for their separation. However, the precise mathematical description of relaxation phenomena is difficult. Secular and motional approximations cannot be used, as non-secular parts of the interaction Hamiltonian also play a role. In most cases the magnetization decay cannot be described by a single exponential function thus rendering the determination of a relaxation time more difficult.

4 Description of Molecular Dynamics in Lipid Bilayers

4.1 The Order Parameter

Molecular dynamics are generally characterized by their geometry and their motional rate. For the theoretical description presented here, we will consider the motions of a vector which can refer to certain molecular parts, for example the molecular long axis, a C-H bond, or a connection vector of two atoms. Amplitude and direction of the motion of this vector can be characterized using the order tensor, also called Saupe ordering matrix:

$$S_{\alpha\beta} = \frac{1}{2} \langle 3 \cos \vartheta_\alpha \cos \vartheta_\beta - \delta_{\alpha\beta} \rangle \quad (48)$$

The indices α and β denote the three dimensions x , y and z in space, $\delta_{\alpha\beta}$ is the Kronecker symbol and the angle between the vector and the respective axis is given by ϑ . The angle brackets indicate the time average when the motion of a single vector is described. For a system of many vectors, the average also can be taken over the results from all vectors at one point of time yielding a matrix which describes the ordering of the system. In ergodic systems, the average over all particles and the time average are identical. Experimental results usually arise from simultaneous averaging over all particles in the sample and a certain time interval.

Of special interest for this work is the description of uniaxial motions which play a role, for example, for lipid molecules in a bilayer in the liquid crystalline phase where they perform fast reorientations of about their molecular long axis. A principle axis system (PAS) with one axis (here we chose the z axis) parallel to the rotation axis can be defined, in which the order tensor is given by the traceless diagonal matrix

$$\underline{S} = S \begin{pmatrix} -\frac{1}{2} & 0 & 0 \\ 0 & -\frac{1}{2} & 0 \\ 0 & 0 & 1 \end{pmatrix}. \quad (49)$$

Two of its elements are identical. The position of the third element defines the direction of the motional axis its value given by the order parameter S which is the only quantity necessary for describing the geometry of this system or motion. With Equation 48, it becomes apparent that the order parameter is given by

$$S = \langle P_2(\cos \vartheta) \rangle \quad (50)$$

with ϑ being the angle between the vector and the z axis. Equation 50 gives a general definition of the order parameter, also for systems without uniaxial symmetry.

For a stiff system where only motions of small amplitude occur, an order parameter approaching unity can be determined. Isotropic molecular dynamics are described by an order parameter of zero, and an order parameter of $S = -\frac{1}{2}$ is calculated for isotropic molecular motions in a plane perpendicular to the z axis. A C-H bond of an hydrocarbon chain in all-trans conformation performing fast motions about its chain axis is an example yielding such an order parameter [83].

The order parameter of specific molecular segments, for example in a lipid bilayer sample, can be determined from various NMR experiments. Hereby the influence of molecular motions on nuclear spin interactions is used, for example the orientation dependence (anisotropy) of the

dipolar coupling (see Equation 46 in Section 3.4.2). Such experiments determining the dipolar coupling constant are particularly well suited for the investigation of molecular motions with rates exceeding the range of dipolar couplings that a vector can assume. In this case of fast limit, all possible vector positions are explored during the time interval of $\omega_D^{-1} \approx 50 \mu\text{s}$ (determined for a system performing large amplitude motions) over which the time average is taken and consequently, the result depends exclusively on the geometry of motion. For vector of a fixed length (for example a C-H bond), the order parameter is given by the ratio of the experimentally determined residual coupling constant $\langle \omega_D \rangle = \omega_{D,\text{res}}$ and the rigid-lattice value ω_D

$$S = \frac{\omega_{D,\text{res}}}{\omega_D}. \quad (51)$$

Depending on the molecular system investigated, it reveals specific features of the motional geometry. When the general form of movement is known, for example, when a vector performs uniaxial reorientations or distinct jump motions, then the average angle between the vector and rotational axis can be determined from the order parameter. When on the opposite, an angle of reorientation can be reasoned with regard to the molecular structure, then conclusions on the shape of motion can possibly be drawn. Various motion's patterns and the corresponding order parameters can be found in Reference [84]. However, without any knowledge about the geometry of motion, the order parameter alone is difficult to analyze. Additionally, from most experiments, only absolute values of order parameters are measured rendering the interpretation even more complicated.

Further difficulties arise when a system exhibits a distribution of dipolar couplings or when several distinct motional patterns are superimposed. Generally, the total order parameter of a system showing superimposed motions that are independent of one another can be calculated from the product of the order parameters of the separate motions. However, it can happen that equal order parameters are determined for systems with completely different distributions and conformations [83].

4.2 Correlation Function and Spectral Density

Besides, the geometry of molecular dynamics, also the time scales will be described. In membrane systems, a variety of molecular motions occur over a broad time window from picoseconds to hours or even days [8, 9]. For the following theoretical considerations, we firstly introduce a general functional value $f(t)$, which is assumed to be a real number that can refer to any motion dependent quantity. Using this observable, a stochastic motion can be described mathematically by the auto-correlation function given by [77]

$$g(\tau) = \langle f(t) \cdot f(t + \tau) \rangle. \quad (52)$$

As for the order parameter, the average is taken over time and over all particles. For the two limiting cases of zero and infinite time τ , we get $g(0) = \langle f(t)^2 \rangle$ and $g(\tau \rightarrow \infty) = \langle f(t) \rangle^2$. At two time points t and $t + \tau$ enclosing an interval τ that is small compared to the time scale of the motional fluctuations, the motion dependent quantity f shows two similar values, mostly with the same sign yielding a positive product close to $\langle f(t)^2 \rangle$. For a time interval τ that is long in comparison with the motional time scale, there is no consistent relationship between the two

values $f(t)$ and $f(t + \tau)$. They can have the same sign or opposite ones and correspondingly yield a positive or negative product with a random value. The ensemble average over all products amounts to a value close to zero and the system is said to “have lost its memory”.

In the following, we will consider reorientation dynamics of the unit vector $\boldsymbol{\eta}$ referring to a C–H bond with normalized length and the motion dependent quantity will be the dipolar coupling constant influencing for example relaxation times of the system. In this case, the specific auto-correlation function is given by the second Legendre polynomial calculated from the scalar product of the vector $\boldsymbol{\eta}$ at two different time points τ and $\tau + t$ which equals the angle between the respective vectors [85]:

$$g(\tau) = \langle P_2(\boldsymbol{\eta}(t)\boldsymbol{\eta}(t + \tau)) \rangle \quad (53)$$

This correlation function is equivalent to $g_1(\tau) = \langle P_2(\cos \vartheta(t)) \cdot P_2(\cos \vartheta(t + \tau)) \rangle$ with ϑ being the angle between $\boldsymbol{\eta}$ and the external magnetic field, when the vector $\boldsymbol{\eta}$ performs uniaxial reorientations.

For a C-H vector only performing isotropic dynamics, the correlation function is simply represented by an exponential decay $g(\tau) = g(0) e^{\tau/\tau_c}$ which contains the correlation time τ_c that is a measure for the time scale of the motion and thus for the time interval needed to randomize the vector orientation. Fast motions induce fast fluctuations of the dipolar coupling consequently causing a fast decay of the auto-correlation function which is described by a small correlation time τ_c . Slow motions, on the contrary, result in a slow decay and a long correlation time τ_c , accordingly. As molecular motion generally gets faster with rising temperature, also the correlation time decreases. In case of restricted molecular motions, some correlation of the bond orientations to their initial state remains even after infinite long time and consequently, the correlation function does not decay to zero.

In Figure 8(a), a correlation function describing the dynamics of a C–H bond in a lipid bilayer sample is shown. It can be represented by a two-step model as:

$$g(t) = (1 - S_{\text{CH}}^2) g_f(t) + S_{\text{CH}}^2 g_s(t) \quad (54)$$

The correlation function g_f describes the fast rotational anisotropic diffusion of the molecular segments. Often, its decay is more complicated than a simple exponential function, but it can generally be modeled by a superposition of exponential functions with different correlation times. Equation 54 contains a second term accounting for the fact that these fast motions are not sufficient to completely randomize the bond orientations. Despite the great disorder in a bilayer in the liquid crystalline phase, in average, a lipid molecule stays aligned parallel to the membrane normal keeping a certain residual order characterized by the order parameter S_{CH} . Additionally, a second correlation function g_s is introduced which describes slower isotropic motions, which, for example, result from the diffusion of lipids on the vesicle surface. However, on short time scales, g_s can be considered as equal to one, that is the total correlation function decays on a plateau value given by S_{CH}^2 .

Fourier transformation of the auto correlation function $g(\tau)$ yields the spectral density $J(\omega)$.

$$J(\omega) = 2 \int_0^{\infty} g(\tau) \exp(-i\omega\tau) d\tau \quad (55)$$

An example is shown in Figure 8(b). Fast fluctuations with short correlation times result in a broad spectral density function and slow fluctuations with long correlation times are characterized by a sharp spectral density function.

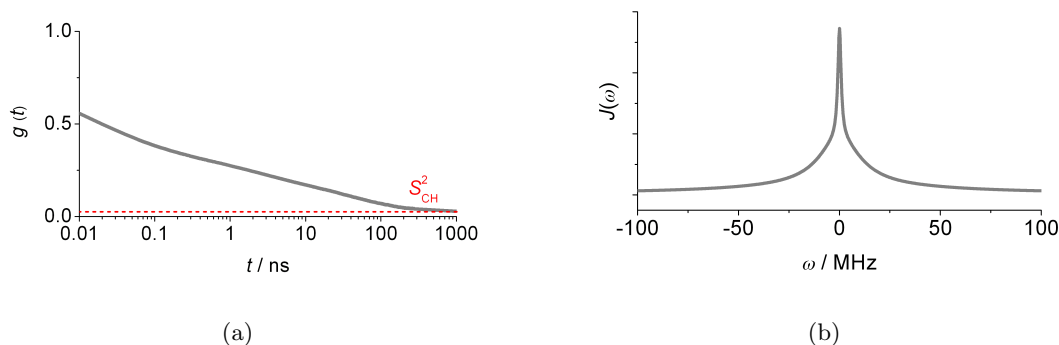


Figure 8: Schematic representation of (a) an autocorrelation function of a C–H bond in a lipid bilayer and (b) the respective spectral density.

4.3 Molecular Motions in Lipid Bilayers

Lipid membranes exhibit a broad variety of molecular dynamics that occur on a wide range of timescales. Most of these motions can be detected using NMR spectroscopy hereby covering a time range from picoseconds to seconds [77].

Molecular motions with correlation times smaller than microseconds, we define as fast dynamics which firstly include the fast oscillations or librations of the nuclei about their average position occurring on a time scale of picoseconds or shorter [77]. Also segmental motions like gauche/trans isomerizations of the lipid alkyl chains exhibit short correlation times in a range of $\tau_c \approx 0.1$ ns [9]. Furthermore, some motions of the entire molecule belong to the group of fast dynamics although they are slightly slower than segmental dynamics. This includes for example, the diffusional reorientation of the lipids about their molecular long axis and local lateral movements of the molecules which occur on a timescale of nanoseconds. The wobbling or tumbling motion of the lipid long axis, also described as a fluctuation in a cone, is slower by about one order of magnitude [9, 69].

Because correlation times of fast rotational diffusive motions are below the spectral time-scale, they cause an averaging of nuclear spin interactions therefore influencing the results of NMR experiments, for example by narrowing the spectral lines. This can be used to determine motional geometries in a lipid bilayer in the liquid crystalline phase. Fast dynamics with correlation times much smaller than the inverse dipolar coupling constant of a few kHz (for ^{13}C – ^1H) cause an averaging of the dipole–dipole couplings, from which the order parameter can be determined (see Section 4.1). Furthermore, as already explained in Section 3.5, motions occurring on the Larmor time scale ($|\omega_0\tau_0| \sim 1$), like atomic vibrations and fast local rotations of molecular groups, influence the T_1 relaxation time from which information about motional geometry as well as correlation times can be obtained with some effort [8, 86, 87]. Accordingly, the T_1 relaxation time can also be used to investigate the influence of guest molecules on a lipid bilayer. For example in presence of cholesterol, $T_1(^1\text{H})$ of the lipid glycerol backbone is reduced due to a slow down of

the fast molecular dynamics [88, 89].

Molecular dynamics with correlation times in the range of microseconds to milliseconds are here referred to as intermediate motions. For example, reorientational motions of lipid molecules due to bilayer undulations occur on an intermediate time scale [62]. They arise from elastic properties of the bilayer, which in turn can be studied using microscopic methods. Because intermediate motions occur on the spectral time-scale, they cause spectral line shape perturbations [77] which in turn can be utilized to study the motional process. For example, the reorientations of lipid molecules can be investigated by the help of the transverse relaxation time T_2 of ^{31}P [90, 91] or ^2H [92]. Hereby, motion-induced changes of the CSA or the quadrupolar coupling are used, respectively. Additionally, molecular motions on a time scale of microseconds influence the rotating frame relaxation time $T_{1\rho}$ [62].

Slow motions exhibit correlation times longer than milliseconds. These include collective motions like slow membrane undulations [8, 69]. Also reorientation motions of lipid molecules due to their lateral diffusion on the vesicle surface belong to this group. For a bilayer in the fluid phase, a diffusion coefficient of $D \approx 10^{-11} \text{ m}^2/\text{s}$ can be measured by pulsed-field-gradient NMR [41, 93].

Ultraslow motions comprise the tumbling of the whole vesicle and flip-flop motions of the lipids between the two leaflets of the bilayer, which are also referred to as transversal lipid diffusion. Because this requires the energy-intensive movement of the hydrophilic lipid head group through the hydrophobic bilayer core, flip-flop motions only rarely occur in pure lipid bilayers [7]. The respective correlation times range from many milliseconds up to hours or even days depending on the type of lipid and on the temperature [9, 94]. In biological membranes however, the flip-flop process is mediated by enzymes and therefore occurs more frequently and in regulated manner [59]. Also for the lipid bilayer/guest molecule systems investigated here, the lipid flip-flop motions can be crucial, possibly allowing for the transport of a guest molecule from one side of the membrane to the other.

Although slow motional processes do not influence the spectral line form or relaxation processes, they can be detected by specific NMR experiments. For example, flip-flop motions were studied by exchange NMR techniques [41, 94].

5 NMR Methods for the Investigation of Membrane Systems

Solid-state NMR techniques are well suited for the investigation of membrane systems allowing for the determination of molecular structure and dynamics with atomic resolution [95]. For example, conformations, averaged distances between molecular segments or the main characteristics of motional processes, that is amplitude, geometry and correlation times, can be obtained.

In the following section, some basic concepts of solid-state NMR and the specific methods used in this work are introduced, and to illustrate their application, some results for pure lipid bilayer samples are presented. The related experiments were set up and conducted specifically for demonstration purposes, and the larger part of this section has been published as a methodological review article [96]. The NMR techniques presented are also highly applicable for the study of model membrane/guest molecule systems, for example allowing for the detection of possibly changed lipid dynamics or for investigating position and mobility of the guest molecules in the membrane.

5.1 Standard Methods of Solid-State NMR

In solid-state NMR we have to deal with broad spectral lines caused by strong anisotropic interactions such as the dipolar coupling or the chemical shielding. However, several methods were developed to obtain good spectral resolution for solid or liquid crystalline powder sample, like lipid MLVs in water [78,95].

5.1.1 Magic Angle Spinning (MAS)

Magic angle spinning (MAS) is probably the most relevant possibility to enhance spectral resolution in solid-state NMR. It affects anisotropic spin interactions in a similar way as the isotropic tumbling of molecules in solution [78]. To explain this effect, we firstly note that the secular Hamiltonians of the chemical shift and the heteronuclear dipolar coupling both show an orientation dependence of the form $P_2(\cos\vartheta)$ with ϑ being the angle between the magnetic field \mathbf{B}_0 and the orientation of the spin interaction tensor (see Equations 35 and 41 in Section 3.4). In case of lipid MLV samples, the fast reorientation motion of the lipid molecules leads to averaged spin interaction tensors exhibiting a symmetry axis along the lipid long-axis and consequently, ϑ is the angle between the membrane normal and magnetic field.

For the MAS experiment, the sample is contained in a cylindrical NMR rotor which rapidly rotates about an axis inclined by the magic angle of $\beta_m = 54.74^\circ$ with respect to the static magnetic field. This causes the molecular orientation to change periodically over time. When the rotation is fast enough, the orientation dependence of the spin interactions can be described by its time average written as

$$\langle P_2(\cos\vartheta) \rangle = P_2(\cos\theta)P_2(\cos\beta). \quad (56)$$

Here, θ is the angle between the principal axis of the shielding tensor, which is the bilayer normal in case of lipid samples, and the spinning axis of the rotor. In a powder sample it can assume all values between 0° and 180° . The angle β is in-between the spinning axis of the rotor and the magnetic field (see Figure 9(a)). Choosing $\beta = \beta_m$, the second Legendre Polynomial of the cosine

of this angle vanishes ($P_2(\cos \beta_m) = 0$) and so does the whole orientation dependent term of the anisotropic interaction ($\langle P_2(\cos \vartheta) \rangle = 0$). However, the averaging only works optimally, when the spinning frequency is about three times or more greater than the anisotropic interaction. In this case the powder pattern is reduced to a single line at the isotropic value and consequently the chemical-shift resolution is regained, comparable to what is common in solution-state NMR. In case of a spinning speed less than or comparable with the size of the anisotropic interaction, a sideband spectrum is observed with a central resonance at the isotropic chemical shift and sidebands spaced with a distance equal to the rotor frequency. Although, spinning frequencies of more than 100 kHz can be reached currently [97], sample preparation for such fast-spinning rotors is difficult and increased pressure due to large centrifugal forces can cause undesirable structural changes [20]. Therefore, moderate spinning frequencies of about 5 to 10 kHz are used for the investigation of lipid samples. Examples for ^1H spectra of DPPC acquired under static conditions and under MAS can be seen in Figure 9(b).

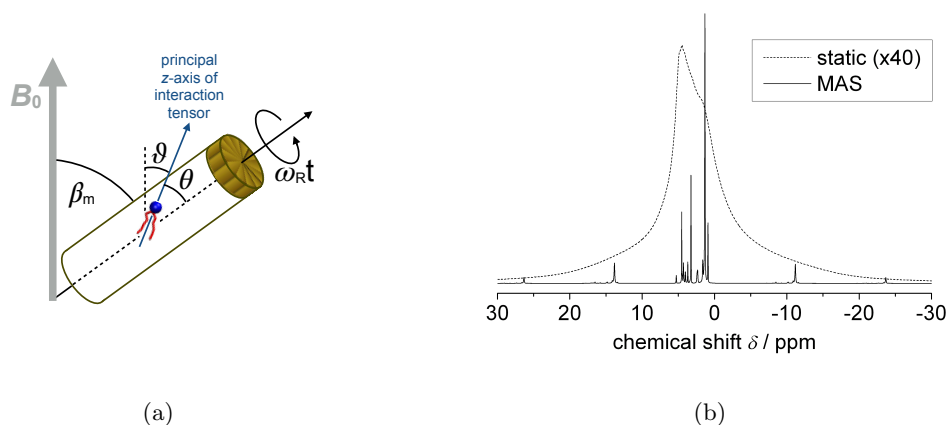


Figure 9: (a) Principle of the MAS experiment. Anisotropic spin interactions are averaged because of rapid rotation of the sample about an axis inclined by the magic angle to the magnetic field. (b) ^1H spectra of DPPC acquired at 50°C under static conditions and under MAS with a spinning rate of 5 kHz .

5.1.2 Heteronuclear Dipolar Decoupling

In solid-state NMR, the resonances of often dilute, low- γ nuclei such as ^{13}C or ^{31}P are usually broadened due to strong heteronuclear dipolar interactions with the surrounding abundant ^1H nuclei. MAS at moderate spinning speeds cannot average these interactions completely, To achieve nevertheless well-resolved ^{13}C spectra, high-power heteronuclear decoupling [77, 78] is applied during signal acquisition, that is an r.f. field with an amplitude ω_1 and a frequency close to the proton resonance frequency is continuously irradiated on the ^1H channel (continuous-wave (CW) decoupling). This causes repeated transitions of the ^1H spins between the two states $|\alpha\rangle$ and $|\beta\rangle$, which in turn averages the ^1H - ^{13}C coupling to zero when the transition rate ω_1 is fast in comparison to the coupling constant $\omega_{\text{D,res}}$. Consequently, effects of the heteronuclear dipolar interaction and the J -coupling are absent, yielding a ^{13}C spectrum with sharp, not split lines which is easier to interpret due to less peak overlap and crowding. Although, the CW

decoupling technique is quite effective, it needs a relatively high r.f. power, possibly causing sample heating, which is especially relevant for lipid samples containing high amounts of water. Therefore, different phase-modulated decoupling sequences are applied allowing for more effective decoupling with less power. A widely used decoupling scheme is the Two Pulse Phase Modulation (TPPM) sequence [98]. It consists of a continuous repetition of two pulses slightly shorter than 180° (for example 165° [99]) with different phases (-10° and -10°). Another standard decoupling scheme is the Small Phase INcremental Alternation with 64 steps (SPINAL-64) [99]. It contains the basic two-pulse step of the TPPM sequence but with an additional stepwise variation of the phase angle improving the broadband decoupling performance of the sequence for liquid crystals and solids. Both, the TPPM and the SPINAL-64 sequence, are widely used in NMR experiments on lipid bilayer samples [100]. Due to the relatively high molecular mobility, a decoupling power of 50 kHz is usually sufficient for lipid bilayers in the liquid-crystalline phase.

5.1.3 Homonuclear Dipolar Decoupling

Like the heteronuclear dipolar coupling, also the homonuclear dipolar interaction between abundant nuclei like ^1H is too strong to be averaged by MAS alone. Therefore, different techniques for the suppression of homonuclear dipolar interactions were developed. We apply them here in some instances in combination with other methods for the determination of heteronuclear dipolar couplings.

As one possibility for homonuclear decoupling in the indirectly-detected dimension, a number of multipulse sequences, like WAHUA, MREV-8, BLEW-12 and BR-24, can be used [101]. Another approach is given by the Lee-Goldburg (LG) scheme [102] and its variants [101, 103]. These sequences involve the continuous irradiation of 360° pulses which are applied off-resonant by $\pm\omega_1/\sqrt{2}$ causing an effective magnetic field in the rotating frame that is tilted away from the \mathbf{B}_0 field by the magic angle. Averaging of the dipolar interaction is reached when a nutation frequency ω_1 is chosen that exceeds the dipolar coupling $\omega_{D,\text{res}}$. In the Frequency-Switched Lee-Goldburg (FSLG) sequence, the offset frequency is switched rapidly between the positive and the negative LG condition and at the same time the pulse phase is shifted by π [101]. This sequence has a high tolerance to pulse errors and also works well at low pulse power. Like the pure LG scheme, also the FSLG sequence exhibits a scaling factor of $\kappa = 1/\sqrt{3} = 0.577$ which defines by how much the chemical-shift and heteronuclear dipolar interactions are reduced during the pulse sequence.

5.2 ^1H MAS Spectra

Valuable information about molecular composition and dynamics in lipid samples can directly be gained from simple ^1H MAS spectra. For example the gel-to-liquid crystalline phase transition of lipid bilayers is reflected in changes of peak intensities near the respective temperature. As can be seen in Figure 9(b) in Section 5.1, the ^1H spectrum of a DPPC MLV sample acquired under static conditions only shows broad and overlapping peaks. However, ^1H MAS spectra of fluid lipid bilayer systems above the phase transition temperature are well resolved even at moderate spinning frequencies of 5–10 kHz [25, 104, 105]. Besides the center peaks, also spinning sidebands can be seen, their peak intensities depending on the strength of residual homonuclear dipolar interactions.

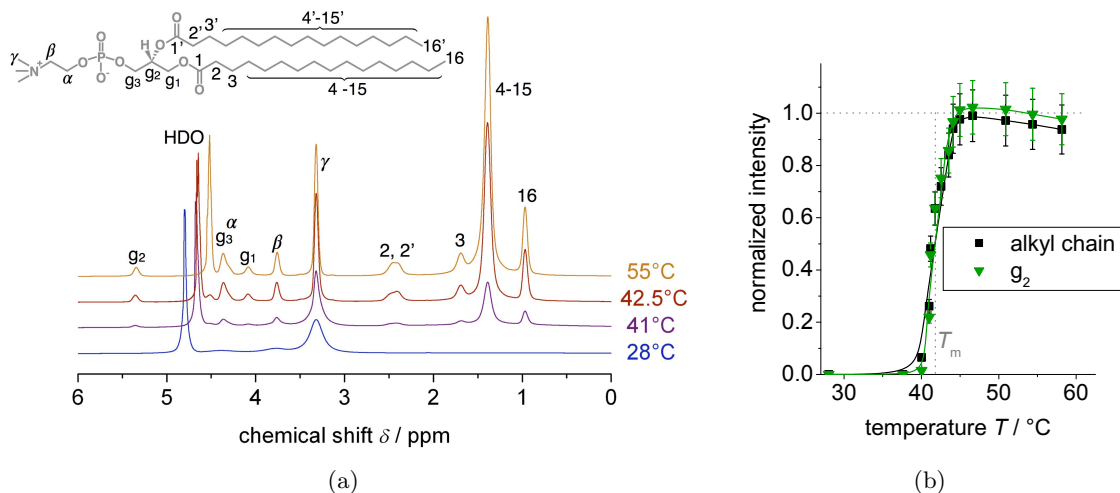


Figure 10: (a) ^1H spectra of DPPC at different temperatures recorded with a spinning frequency of 5 kHz; and (b) temperature dependence of the acyl chain peak intensity, normalized such that it reaches unity at high temperatures. From variations of the baseline for some points, we determined an uncertainty of 10%.

^1H spectra of DPPC at 5 kHz MAS acquired at different temperatures are shown in Figure 10(a). The peak assignment is well-known from literature [25, 106]. The signals in the range of 3 to 6 ppm originate from the lipid glycerol backbone and the choline group and peaks of the lipid acyl chain appear between 0 and 3 ppm. The signal of carbon 2 shows two maxima reflecting the different conformations of the two lipid chains in the upper region. Despite the use of D_2O , a water signal, mainly originating from HDO, appears in the spectrum. As the position of the water signal shows a significant temperature dependence, it was used for verification of the temperature calibration [82, 100].

Spectra recorded at temperatures below the phase transition of DPPC only show low resolution ($T = 30^\circ\text{C}$ in Figure 10a). This can be explained by the well-defined packing and comparably low mobility of the lipid acyl chains inducing strong inter- and intra-molecular ^1H - ^1H dipole-dipole couplings, which cause line broadening down to baseline level [25, 104, 105]. Consequently, the aliphatic and glycerol resonances are not visible, at least when a moderate spinning frequency is used. Only some peaks of the lipid headgroup can be seen due to the increased mobility of these molecular segments even in the gel phase.

When the sample is heated to temperatures near the phase transition temperature, the lipid signals increase over a range of about 5°C before reaching a maximal value which they keep subsequently at all higher temperatures. Such a transition temperature range instead of the expected sharp transition is caused by a temperature gradient over the sample in the rotor and by sample inhomogeneity. We assign the phase transition temperature to the inflection point of the sigmoidal trend.

At high temperatures, the bilayer is in the liquid crystalline phase which is characterized by high molecular mobility. ^1H - ^1H dipolar interactions still exist, but due to dynamic averaging, they are sufficiently weak and rendered inhomogeneous, leading to well-resolved peaks with high intensities in the ^1H spectrum ($T = 55^\circ\text{C}$ in Figure 10(a)). In this phase, the signal intensities are proportional to the number of protons at the peak-specific chemical site. Consequently, the peak integrals can be considered as an estimate of the number of mobile lipid molecules and

therefore allow for the observation of the main phase transition.

To determine meaningful peak intensities, quantitative ^1H spectra need to be acquired which is achieved by using weight-controlled samples, a recycle delay ($d_1 = 8\text{ s}$) much larger than the T_1 relaxation time, and Curie correction for the temperature dependence of the intensity (see Equation 22 in Section 3.2). Especially for temperatures below or near the phase transition, baseline correction is necessary to eliminate contributions from underlying broad signals of immobile protons. For this, a linear or a parabolic function can be used depending on the spectral region. Subsequently, the signal intensities are determined by integration over the respective centerband peak as well as over the spinning sidebands. Especially for signals from the glycerol group and the upper chain region, the spinning sidebands contain significant intensity because these segments have the lowest molecular mobility and therefore the highest residual dipole-dipole coupling. Contrary, the sideband intensity of signals from the choline head group and the tail ends is negligibly small due to high molecular dynamics [107]. In Figure 10(b), results are shown for the temperature dependence of the normalized signal intensity from the alkyl chains and from the glycerol backbone. As expected, the phase transition of DPPC occurs at a temperature of about 42°C (see Table 1). The slight intensity decrease with rising temperature above the phase transition can possibly be explained by shimming issues.

5.3 ^{13}C MAS Spectra

While a ^1H spectrum has a chemical shift dispersion of only about 10 ppm, a ^{13}C spectrum spans beyond 200 ppm allowing for a better ^{13}C spectral resolution. This difference can be explained by the higher mass of the carbon atom as compared to the proton [77]. Similar to the case of ^1H , information about molecular composition, dynamics and packing can be gained from peak intensities and positions in the ^{13}C spectrum.

5.3.1 Direct Polarization

In the most simple experiment, referred to as Direct Polarization (DP), a ^{13}C spectrum is recorded after applying a single 90° hard pulse. Additionally, MAS at 5 kHz and heteronuclear decoupling are applied to remove effects from CSA and heteronuclear ^1H - ^{13}C couplings. Homonuclear dipolar interactions are not relevant for a dilute spin such as ^{13}C . Under these conditions, well-resolved spectra can be gained for lipid bilayer systems especially in the liquid-crystalline phase. Furthermore, for DP spectra recorded with a recycle delay long enough to allow for complete T_1 relaxation, the area under each resonance line is proportional to the number of nuclei at the respective chemical site. The width of the resonance lines depends on magnetic field homogeneity, the MAS rate, the efficiency of the ^1H decoupling and the ^{13}C transverse relaxation time.

Figure 11(b) shows DP spectra of DPPC for a temperature below and a temperature above the main phase transition. The peak assignment was done according to literature [25, 106]. Due to the high mobility of the choline lipid headgroup in the liquid crystalline phase as well as in the gel phase, the signals from the α , β and γ carbon are unchanged by temperature and correspond to the resonance of an average conformation. In contrast, segmental dynamics of the glycerol backbone and the acyl chains are considerably more restricted in the gel phase than in the liquid crystalline phase resulting in broader peaks of these molecular groups at temperatures below the

phase transition temperature. For example the peak of carbon 1 of the COO group is very broad at 30 °C and clearly resolved with high intensity at 50 °C.

Furthermore, the positions of the peaks from the acyl chain region differ between the two spectra. The largest signal from the center-chain CH₂ groups is shifted downfield by about 3 ppm in the gel phase vs. the liquid-crystalline phase. This can be explained the γ -gauche effect [108] which characterizes the influence of chain conformation on the chemical shift. In this case, the hydrocarbon chains of a lipid show an increased population of all-trans conformation in the gel phase. In the liquid crystalline-phase however, they are disordered and change rapidly between trans and gauche conformation.

As in the case of ¹H, some alkyl resonances are split in two because the signals for the two individual acyl chains are partially separated. This is the case for the upper chain region, for example carbon 1 and 3, where the two lipid tails differ in conformation [82].

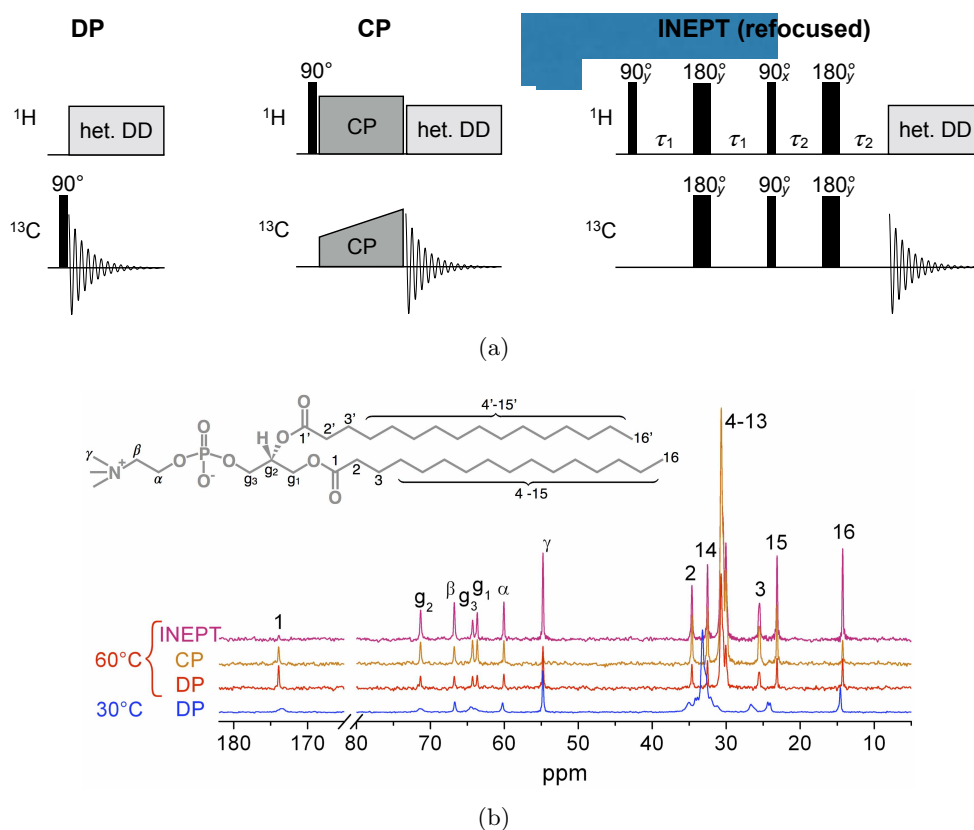


Figure 11: (a) Pulse sequences for the excitation of transverse ¹³C magnetization; (b) ¹³C MAS spectra of DPPC. Results for the temperatures 30 °C and 60 °C and for the excitation schemes DP, CP and INEPT are compared. Note that the spectrum at 30 °C is measured with a considerably higher number of scans to compensate for the broader lines. For the CP spectrum a contact pulse of 5 ms was used.

5.3.2 Methods for Signal Enhancement

Although a ¹³C spectrum shows a broad chemical shift dispersion, the lower spin density and gyromagnetic ratio of ¹³C as compared to ¹H also results in a reduced sensitivity. As a consequence, more scans need to be accumulated, rendering the acquisition of a ¹³C spectrum more time

consuming. To improve this, several signal enhancement methods were developed, which are based on magnetization transfer from ^1H to ^{13}C , thus exploiting the higher signal intensities and the shorter recycle delay of ^1H . They enable the recording of a spectrum with higher sensitivity but also render the peak intensities non-quantitative.

Cross-polarization (CP) transfer is one of these techniques used by default in solid-state NMR. This method is most effective for rigid samples or regions in samples where the dipolar coupling is not averaged by molecular dynamics, because the polarization transfer is mediated by through-space dipolar interactions. The pulse sequence is shown in Figure 34 (a) in the middle. It starts with a $\pi/2$ pulse on the proton channel which creates transverse magnetization. Subsequently, a contact pulse is applied, that is, two r.f. fields on-resonant with the Larmor frequencies are irradiated simultaneously on the ^1H and ^{13}C channel over a few milliseconds. The ^1H r.f. field is aligned to the direction of the transverse ^1H magnetization sustaining it at least to a certain degree.

During the contact pulse, polarization transfer occurs. We will refrain here from an exact explanation of this process using average Hamiltonian theory and instead give a brief illustration by firstly introducing a doubly rotating frame [78], given by the magnetic fields exerted on the spins during the contact pulse. Specifically, the $B_1(^1\text{H})$ field acts as quantization axis for protons in the rotating frame and the $B_1(^{13}\text{C})$ field for the carbons. The energy gaps of the two rotating frame spin states are equal for the two nuclei when the amplitudes of the contact pulses are chosen to fulfill the Hartmann-Hahn condition

$$|\gamma_{\text{H}}B_1(^1\text{H})| = |\gamma_{\text{C}}B_1(^{13}\text{C}) \pm n\omega_{\text{r}}| \quad (57)$$

with $n = 1, 2, 3, \dots$ and ω_{r} being the MAS rotation frequency. In this case, energy can be redistributed between ^1H and ^{13}C spins, mediated by the heteronuclear dipolar coupling. However, because the spin quantization axes are perpendicular to the B_0 field, the net energy and the net spin polarization of the system need to be conserved. This means that every change of polarization of one spin (^1H) needs to be compensated for by the transition of a second spin polarization (^{13}C) in the opposite direction. Energy and polarization flow from ^1H to ^{13}C spins finally occurs because the initial magnitude of the transverse ^1H magnetization, given by the equilibrium z -magnetization in the B_0 field, is too large to be sustained by the spin lock field and on the contrary, the initial transverse ^{13}C magnetization is zero. The transfer process proceeds over a longer time period because homonuclear dipolar couplings allow for continuous further transport of spin polarization between the protons.

Generally, a longer contact pulse gives more time for the magnetization transfer which results in better signal in the spectrum acquired directly afterwards. However, due to $T_{1\rho}$ relaxation of the spin-locked magnetization, the CP transfer also becomes less efficient for longer times and the peak intensities decay again. Thus, a suitable medium contact time needs to be chosen.

For rigid samples exhibiting strong heteronuclear dipolar couplings ($d \approx 15 - 22$ kHz), a short contact time τ_{CP} is sufficient due to the fast CP transfer rate. For samples with weaker dipolar interactions, for example sample systems showing a high molecular mobility, longer contact pulses need to be used and the sequence is generally less efficient. The optimal recycle delay is $5T_1(^1\text{H})$.

When using the CP sequence in combination with MAS, it is advantageous to apply variable amplitude contact pulses to increase the transfer efficiency and reduce the sensitivity to small

missettings of the Hartmann–Hahn match. Here, we used the ramped-amplitude (RAMP) CP method in which the proton or carbon spin-lock field in the rotating frame is gradually increased. This sequence reduces the signal sensitivity on pulse amplitude and B_1 field inhomogeneities and it ensures that also in complex systems the Hartmann–Hahn condition can be satisfied for all spins [109, 110]. It has proven to be useful for the investigation of lipid samples before [62]. However, a potential disadvantage of the CP method in general, are the long r.f. irradiation times, possibly causing sample heating which is especially relevant for the aqueous lipid samples.

For magnetization transfer in solution-state NMR, the refocused Insensitive Nuclei ENhanced by Polarization Transfer (INEPT) method is applied frequently. This technique uses the through-bond J -coupling between nuclei to induce magnetization transfer and is therefore most effective for ^{13}C atoms of mobile molecules in solution, which show sharp lines in the NMR spectrum with homogeneous widths smaller than the J -coupling constant [111]. Independently of the bond orientation, the magnetization is transferred from a proton defined by the spin operator \hat{I} to a directly bonded carbon that has the spin operator \hat{S} .

Here, we use the refocused INEPT method, which was developed by Burum and Ernst [112]. It includes the INEPT transfer introduced by Morris and Freeman [113] and simultaneously allows for heteronuclear decoupling during acquisition [77]. The pulse sequence is shown in Figure 11(a) on the right. By the first 90° pulse, transverse ^1H magnetization is created. During the time intervals $2\tau_1$ and $2\tau_2$, ^1H and ^{13}C magnetization precess under the influence of the heteronuclear J -coupling allowing for the magnetization transfer to occur. To refocus off-resonance effects, there is a 180° pulse in the center of each time period. Using the product operator formalism, the dominant term of the spin density matrix can be calculated to develop from $\hat{\rho}_1 \propto \hat{I}_x$ after the first pulse, over $\hat{\rho}_2 \propto 2\hat{I}_z\hat{S}_z$ after the first time interval $2\tau_1$ to $\hat{\rho}_3 \propto \hat{S}_y$ at the beginning of signal acquisition. The signal enhancement of this sequence is given by [114]

$$F(\tau_1, \tau_2) = N_{\text{H}} \frac{\gamma_{\text{H}}}{\gamma_{\text{C}}} \sin(2\pi J_{\text{CH}}\tau_1) \cdot \sin(2\pi J_{\text{CH}}\tau_2) \cdot \cos^{(N_{\text{H}}-1)}(2\pi J_{\text{CH}}\tau_2) \quad (58)$$

with N_{H} being the number of directly bonded protons. By choosing $\tau_1 = \frac{0.25}{J_{\text{CH}}}$ and $\tau_2 = \frac{0.25}{J_{\text{CH}}}$ or $\tau_2 = \frac{0.20}{J_{\text{CH}}}$, we obtain maximal signal intensity for the resonance of a CH_2 or a CH_3 group, respectively. However, these criteria are not strict under experimental conditions due to additional influence from distributions of J -couplings and relaxation effects. Additionally, for an efficient application of the INEPT sequence under MAS, the evolution delays need to be rotor-synchronized, that is τ_1 and τ_2 need to be chosen as integer multiples of the rotor period [111, 115]. Assuming a coupling constant of $J_{\text{CH}} \approx 140$ Hz, we used time delays of $\tau_1 = 1.94$ ms and $\tau_2 = 0.97$ ms at a spinning frequency of 5.15 kHz [82].

As the lipid bilayer itself represents a system in-between solid and liquid, both signal enhancement methods might be applicable. Furthermore, besides the purpose of intensity enhancement, also information on molecular mobility can be gained from the CP and INEPT signal intensities due to their influence on the sequence efficiency. Nowacka et al. [116] found out that under typical experimental conditions, there is nearly no INEPT signal and maximal CP signal for molecules performing slow and/or anisotropic motions with $\tau_c > 10$ μs and/or $S > 0.5$. In contrast, for molecules showing fast isotropic motions with $\tau_c < 0.01$ μs and $S < 0.05$, the CP signal is very small and the INEPT signal is maximal and when intermediate molecular motions with a τ_c in the order of microseconds are present, only a small polarization transfer can be

reached with both methods [116].

With these in mind, the molecular mobility of a lipid bilayer and also the association of a guest molecule with the membrane can be investigated by simply comparing peak intensities in the CP and INEPT spectra. As an example, Figure 11(b) shows a DP, a CP and a refocused INEPT spectrum of DPPC at 60 °C in comparison. Because the lipid molecules perform fast motions with $\tau_c < 0.01 \mu\text{s}$ and $0 < S < 0.3$ in the fluid state, the refocused INEPT sequence generally enhances the ^{13}C signal more efficiently than the CP method [117]. In this regime, the ratio between CP and INEPT intensity can be used as a measure of the order parameter S [116]. For example, the methyl groups at the chain ends and the γ carbons in the head group are very mobile having small order parameters. Accordingly, the INEPT spectrum shows a much higher signal for these peaks than the CP spectrum. On the contrary, the CP spectrum shows a resonance of higher intensity for the large peak of the acyl chain middle region which is motionally restricted.

Comparison of signal intensities from the two different enhancement methods can also be used to examine model membrane/guest molecule systems. For example, a guest molecule that is incorporated into a bilayer is motionally constrained and will therefore give rise to larger CP and smaller INEPT signals than a molecule that moves isotropically in the surrounding water.

5.4 Determination of T_1 Relaxation Times

For the determination of the longitudinal relaxation time T_1 , we used the SATuration RECOVERY (SATREC) pulse sequence and a ‘‘Torchia-like’’ experiment. All experiments were applied under MAS to achieve chemical resolution.

The SATREC sequence starts with a 90° pulse (or a train of 90° pulses) by which longitudinal magnetization is removed. The magnetization that is partly recovered during the following time period τ , is then flipped back in the transversal plane by help of another 90° pulse. The detection of ^{13}C signal is conducted under simultaneous heteronuclear dipolar decoupling. Fourier transformation yields a spectrum with chemical resolution. After repeating the experiment for a number of waiting times τ and determining the peak intensity $I(\tau)$ of the chemical site of interest from each spectrum, the relaxation time can be determined from

$$I(\tau) = I_0 \left(1 - e^{-\frac{\tau}{T_1}} \right). \quad (59)$$

The Torchia sequence was introduced in 1978 by D. A. Torchia for the determination of $T_1(^{13}\text{C})$ relaxation times. Here, we used a modified version of this sequence (see Figure 12(a)) [87], replacing the initial CP unit by an INEPT sequence (see Section 5.3.2) to create transverse ^{13}C magnetization. The subsequent 90° pulse on the ^{13}C channel flips this magnetization alternately in positive and negative z -direction. Because of the INEPT unit in the beginning, the resulting longitudinal magnetization is enhanced compared to the equilibrium value. During the following waiting time τ , the magnetization relaxes back approaching its equilibrium value I_0 for $\tau \rightarrow \infty$. Another 90° pulse on the ^{13}C channel flips the magnetization back to the transversal plane and subsequently the signal is detected under proton decoupling. Using an alternating receiver phase, the difference signal of the positive and the negative magnetization is recorded.

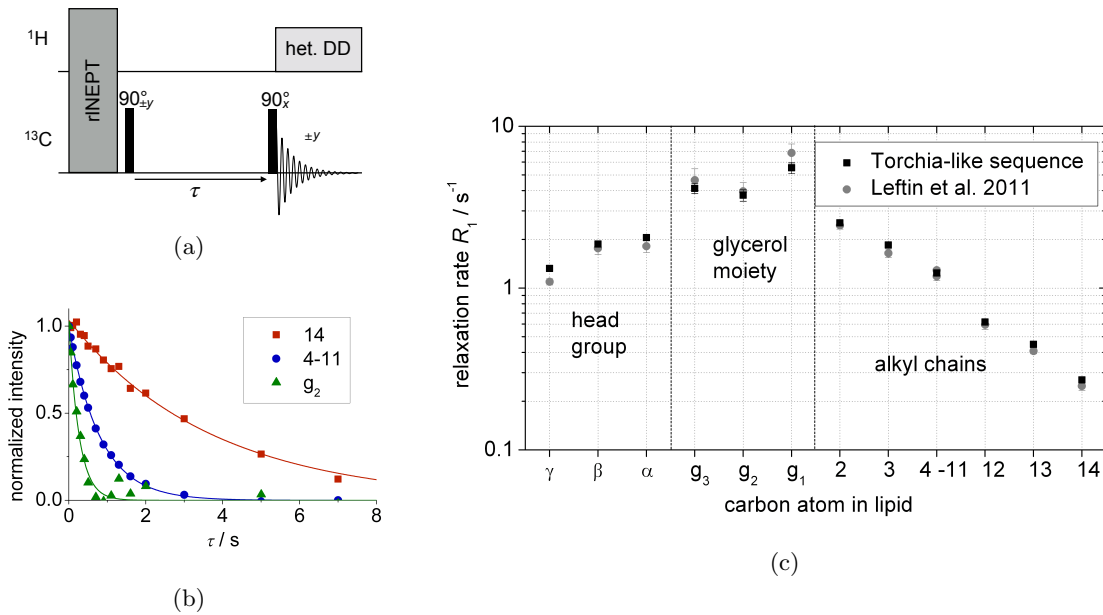


Figure 12: (a) “Torchia-like” pulse sequence and (b) intensity decay curves determined from this experiment at a carbon Larmor frequency of $\omega_0 = 100.59$ MHz for three resonances of DMPC at 47 °C. The symbols represent the measured data and the lines correspond to the exponential fit functions. The resulting R_1 relaxation rates are shown in (c) as black symbols. The grey symbols represent literature values for sonicated DMPC vesicles at 50 °C measured at a carbon Larmor frequency of $\omega_0 = 90.80$ MHz [8]

The relaxation time T_1 of a specific chemical site can be determined from the respective peak integrals determined for a number of different waiting times τ :

$$I(\tau) = 2I_{\text{INEPT}}e^{-\frac{\tau}{T_1}} \quad (60)$$

The SATREC sequence was applied to determine relaxation times $T_1(^1\text{H})$ and for $T_1(^{13}\text{C})$ relaxation times, both sequences were used yielding similar results. Compared to the SATREC sequence, the “Torchia-like” experiment has the advantage that in the long-time limit the signal intensities tend to zero, rendering the fit more stable.

In Figure 12, intensity decay curves and results for R_1 relaxation rates determined for DMPC at 47 °C using the “Torchia-like” experiment are shown. For all peaks, we obtain a single exponential signal decay as assumed in Equation 60, although in some cases segments with potentially different relaxation times contribute to one signal. Similar results were found in literature for example for protons [88, 107]. However, this does not mean that all contributing nuclei exhibit the same relaxation time. Instead, also the superposition of a number of functions decaying with different time constants, can result in an exponential-like function [88].

The R_1 profile of the lipid molecule represents the segmental mobility confirming the motional gradient extending from the glycerol backbone in both directions. As can be seen in Figure 12(c), our measured data resembles the literature values very well and also literature results for R_1 of ¹H and ²H show similar characteristic profiles [23, 62]. Due to the increasing mobility of the lipid tails towards the middle of the membrane, the relaxation rates decrease in this direction.

The glycerol moiety exhibits the largest R_1 values because in this molecular region less motions are present that induce T_1 relaxation and the relaxation rates of the choline group are slightly smaller again.

From literature results, it can be concluded that molecular motions with rates higher than the Larmor frequency contribute to the longitudinal relaxation because relaxation rates decrease with rising temperature [8, 62]. Furthermore, in literature, the lipid dynamics were studied more in detail by measuring T_1 relaxation times of ^2H or ^{13}C for different magnetic field strengths and describing the results assuming certain motional models. It was concluded that although fast motions (like gauche-trans isomerisations) contribute as the major part, also slower collective whole molecule motions influence T_1 [8, 86, 118].

Besides being used for the investigation of molecular motions in pure lipid bilayers, the measurement of T_1 relaxation times can also be used to study the influence of a guest molecule on lipid dynamics [75].

Assuming that the longitudinal relaxation of ^{13}C magnetization of CH, CH_2 and CH_3 groups in lipid samples is mainly caused by fluctuating dipolar interaction of the carbon with the directly bonded protons [119], a relation between the R_1 relaxation rates and the rotational correlation times τ_i of the molecular segments can be established applying appropriate quantum theoretical treatments [77]. The NMR relaxation rate can be expressed by help of the spectral density $J(\omega)$ [120]:

$$R_1 = \frac{d_{\text{CH}}^2 N_{\text{H}}}{20} [J(\omega_{\text{H}} - \omega_{\text{C}}) + 3J(\omega_{\text{C}}) + 6J(\omega_{\text{C}} + \omega_{\text{H}})] \quad (61)$$

The dipolar coupling constant d_{CH} is given in Equation 39 in Section 3.4.2, the carbon and proton Larmor frequencies are denoted as ω_{C} and ω_{H} and N_{H} is the number of bound protons. A general expression for the correlation function describing rotational dynamics of a C-H bond vector in a lipid molecule is already given in Equation 54 in Section 4.2. We assume a multi-exponential function for describing the fast decay [87] and the slow decay we omit. From the resulting correlation function

$$g(t) = (1 - S_{\text{CH}}^2) \sum_i a_i e^{-t/\tau_i} \quad (62)$$

we calculate a spectral density of

$$J(\omega) = 2(1 - S_{\text{CH}}^2) \sum_{i=1}^N a_i \frac{\tau_i}{1 + \omega^2 \tau_i^2} \quad (63)$$

which can be inserted in Equation 61. From this, we see that the relaxation rate depends on amplitudes and rates of the motion, described by order parameter and correlation time.

5.5 The NOESY Experiment

A powerful method to determine the atomistic resolution structure of lipid bilayer systems is the two-dimensional Nuclear Overhauser Enhancement (2D NOESY) experiment. Most commonly, the NOESY experiment is used in solution-state NMR to determine fixed intramolecular distances in organic chemical structures [77]. However, conducted in combination with MAS, the NOESY experiment can also be applied to investigate more rigid sample systems like liposome dispersions.

In this case, the interest lies in the temporary spatial proximity of nuclei of different molecules.

The first NOESY MAS spectra of DMPC were recorded about 30 years ago [104], followed by a number of further investigations on pure lipid samples [107, 121]. Furthermore, the NOESY experiment was used to detect the most favorable location and orientation of various guest molecules in fluid lipid bilayers [69]. Various small molecules in lipid bilayers were found to show a high mobility and with this a broad spatial distribution [69]. For example, the location distribution of different aromatic compounds such as flavonoids [122], indole [123], multidrug transporter substrates [124] or a cannabinoid ligand [125], was determined. The penetration capability of water [69, 121] and the interaction of the membrane with ethanol [70, 71] was investigated. Also, peptides in interaction with model membranes were studied by the NOESY experiment and precise structural information were obtained [126].

Due to the good resolution of ^1H MAS NMR spectra and the long spin-lattice relaxation times, the ^1H - ^1H NOESY experiment is generally well-suited for the investigation of lipid samples [107, 127]. For an even better separation of spectral lines, we used a relatively high spinning rate of about 10 kHz. Additionally, the spectral width was chosen to be a multiple of the spinning frequency to avoid problems with spinning side bands.

Typically, a simple three-pulse sequence in the phase-sensitive mode is used (see Figure 13) [77, 128]. To explain its mode of operation, we consider a homonuclear ensemble of spins that are not directly bonded but can approach each other on a small distance. In thermal equilibrium, the initial state can be characterized by $\hat{\rho}_0 \sim \sum_n \hat{I}_{nz}$. The index n counts the distinguishable spins of one system. The first 90° pulse creates transverse magnetization, which evolves under the influence of the isotropic chemical shift during the waiting time t_1 . In this way, each spin is labeled with its characteristic resonance frequency Ω_{n0} . The phase of the second 90° pulse is chosen in a way, that after the pulse the magnetization is aligned along the z -direction again. Omitting the T_2 decay for simplicity, the spin density operator of the system is now given by $\hat{\rho} \sim \sum_n \hat{I}_{nz} \cos(\Omega_{n0}t_1)$. Mediated by the dipolar interaction of neighboring spins, magnetization exchange can take place during the following mixing time τ_{mix} . This process can be described using the Solomon equations [77]:

$$\frac{d}{d\tau_{\text{mix}}}\hat{\mathbf{I}}_z = \mathbf{R}\hat{\mathbf{I}}_z \quad (64)$$

Here, the cross-relaxation matrix or exchange matrix is denoted by \mathbf{R} . It will be discussed in more detail later. The z components of the spin operators of the different spins are written in one vector:

$$\hat{\mathbf{I}}_z = \begin{pmatrix} \langle \hat{I}_{1z} \rangle \\ \langle \hat{I}_{2z} \rangle \\ \vdots \end{pmatrix} \quad (65)$$

The solution of Equation 64 is given by

$$\hat{\mathbf{I}}_z(\tau_{\text{mix}}) = \exp\{(-\mathbf{R}\tau_{\text{mix}})\}\hat{\mathbf{I}}_z(0). \quad (66)$$

With the last 90° pulse, detectable transverse magnetization is produced and subsequently, the spin system once again evolves under the influence of the chemical shift during the acquisition

time t_2 . The final magnetization can then be written as

$$\mathbf{M}(t_1, \tau_{\text{mix}}, t_2) = - \sum_n \sum_m e^{i\Omega_n t_2} [\exp(\mathbf{R}\tau_{\text{mix}})]_{nm} \text{Re} [e^{i\Omega_m t_1}] \mathbf{M}_0. \quad (67)$$

By repeating the experiment for a number of equally spaced t_1 times, a data matrix $s(t_1, t_2)$ is obtained and from this a two-dimensional spectrum $S(\Omega_1, \Omega_2)$ can be calculated by double Fourier transformation. When the States-TPPI (Time-Proportional Phase Incrementation) procedure is used for data acquisition and analysis, the resulting spectrum is characterized by pure absorption lineshapes [77]. It contains in the first dimension the resonance frequencies of the protons before and in the second dimension the frequencies after the mixing time, i.e. after a possible polarization transfer. A cross peak will appear when polarization transfer occurred between two protons with respective chemical shifts. Valuable information about the spatial proximity of different nuclei can be gained from the cross peaks in the spectrum. Generally, a NOESY spectrum acquired with a short mixing interval τ_{mix} in the sequence, only contains diagonal peaks. With rising τ_{mix} , cross peaks appear and get more intense while the diagonal peaks get weaker. In spectra acquired with long mixing times the peak intensities decrease again due to spin-lattice relaxation [77, 121].

In Figure 13(c), a 2D NOESY spectrum recorded for POPC with a mixing time of $\tau_{\text{mix}} = 300$ ms at a temperature of 25 °C is shown. Cross peaks for nearly all lipid resonances are visible, also for signals of protons that are far apart from each other within one lipid molecule, like protons of the head group and the tail ends. According to literature [127], these peaks are created by direct contacts (distance smaller than 5 Å) of neighboring molecules which emphasizes the great molecular disorder in lipid bilayers in the fluid phase [107]. From NOESY experiments on samples of DMPC and partially deuterated DMPC in a number of different mixing ratios, Huster et al. [107] concluded, that most cross peaks come from intermolecular interactions. Intramolecular magnetization exchange, in contrast, only occurs between neighboring protons [129] or between the two tails of one lipid [107].

For a quantitative description of the NOESY spectrum, the peak intensities given by their peak volumes need to be determined. The intensities of all peaks determined for one spectrum are collected in a matrix \mathbf{A} referred to as peak volume matrix. Details about the determination of \mathbf{A} are given in the Supplementary Section C.1.

From Equation 67, it can be concluded that the volume matrix \mathbf{A} shows the following dependence on the mixing time τ_{mix} :

$$\mathbf{A}(\tau_{\text{mix}}) = \exp\{(-\mathbf{R}\tau_{\text{mix}})\} \mathbf{A}(0) \quad (68)$$

The relaxation rate matrix can be written out as [107]

$$\mathbf{R} = \begin{pmatrix} \rho_{11} & \sigma_{12} & \dots & \sigma_{1N} \\ \sigma_{21} & \rho_{22} & \dots & \sigma_{2N} \\ \vdots & \vdots & \ddots & \vdots \\ \sigma_{N1} & \sigma_{N2} & \dots & \rho_{NN} \end{pmatrix}$$

with N being the number of peaks in the spectrum. For a lipid/guest molecule system, we

typically have a matrix with about 15×15 elements. The cross-relaxation rates σ_{nm} describe the magnetization transfer from a spin m to another spin n . The relaxation rate matrix \mathbf{R} is not symmetric, but its elements fulfill the relation

$$k_m \sigma_{nm} = k_n \sigma_{mn} \quad (69)$$

with k_n being the number of spins contributing signal to resonance n . The effective relaxation rates ρ_{nn} of the diagonal peaks can be calculated from the spin lattice relaxation rates R_{nn} of the respective peaks and the cross-relaxation rates σ_{nm}

$$\rho_{nn} = R_{nn} - \sum_{m=1}^n \sigma_{mn}. \quad (70)$$

From the volume matrix dependence on the mixing time, cross-relaxation rates can be determined by using different methods, such as the single mixing time approach, the spin-pair interaction model or the full matrix approach [107].

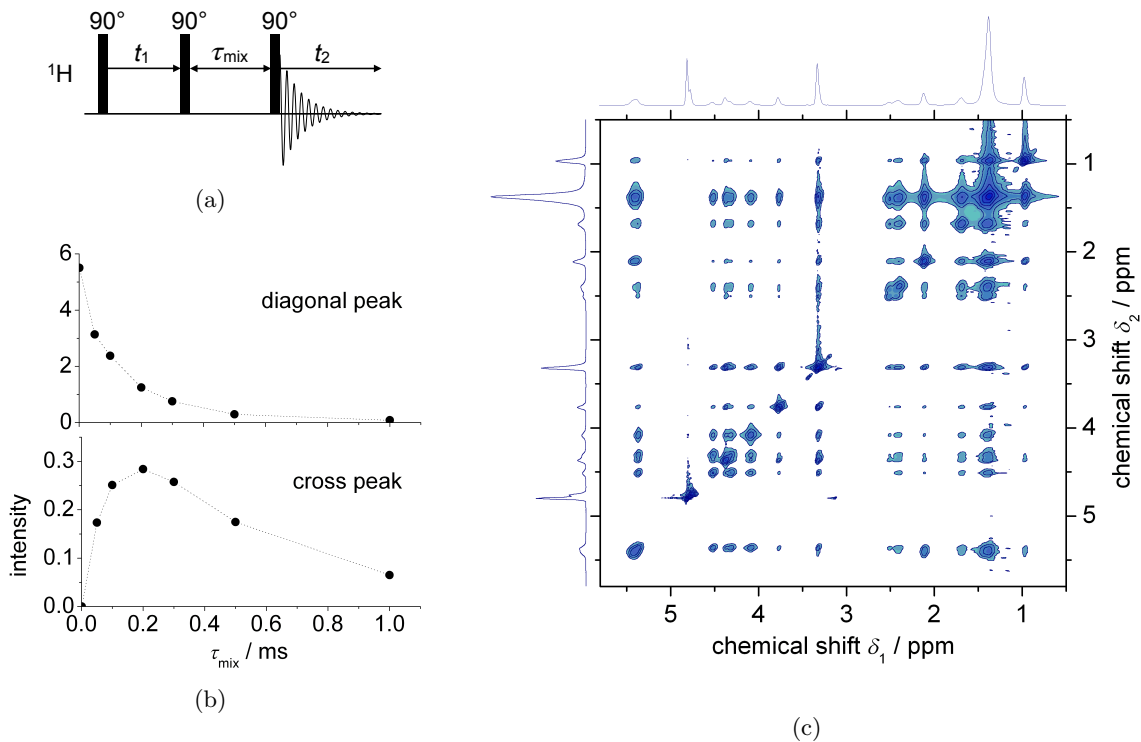


Figure 13: (a) Pulse sequence of the 2D NOESY experiment and results for POPC at 25 °C: (b) Mixing time dependence of the diagonal peak intensity from carbon 3 and of the cross peak intensity between the resonances of carbon 2 and 3 in the upper acyl chain region, and (c) 2D spectrum from an experiment with a mixing time of $\tau_{\text{mix}} = 300$ ms. An MAS frequency of 10 kHz was used and the experiments were conducted for 512 t_1 times.

Single-Mixing Time Analysis: Among the three methods, the single-mixing time analysis represents the easiest way to determine cross-relaxation rates [107]. It relies on the approximation of Equation 68 by the first two terms of the Taylor expansion of the exponential function, which is valid for short mixing times. Rearranging the resulting equation yields the following expression

$$\sigma_{nm} = \frac{a_{nm}(\tau_{\text{mix}})}{a_{mm}(\tau_{\text{mix}})\tau_{\text{mix}}} \quad (71)$$

from which a cross-relaxation rate σ_{nm} can be calculated by solely using the volumes a_{mm} and a_{nm} of the respective diagonal and cross peak determined at one specific short mixing time τ_{mix} . However, as this method is very simplistic, the results are not very reliable and should only be considered as qualitative. Especially, results for systems with different T_1 (^1H) cannot be compared because different systematic errors can occur [107].

Spin-Pair Interaction Model: Another way to obtain cross-relaxation rates from peak intensities is the spin-pair interaction model which reduces the multi-spin system to an isolated spin pair assuming that the spin system is reasonably well decoupled [69, 107]. In this case, the intensity of the cross peak of interest and the corresponding diagonal peak intensity need to be determined from NOESY spectra acquired for different mixing times. For lipid samples, we choose several mixing times between 1 ms and 1 s to have data points over the whole range including the initial increase and the subsequent decrease of the cross peaks (see Figure 13(b)). This makes the data analysis fast and easy but requires a certain experimental time. The fit function describing the mixing time dependence of the cross peak intensities

$$|a_{nm}(\tau_{\text{mix}})| = 0.5a_{mm}(0) [1 + e^{-2\sigma_{nm}\tau_{\text{mix}}}] e^{-\tau_{\text{mix}}/T_{nm}} \quad (72)$$

is taken from Reference [107]. In the last factor, spin lattice relaxation is considered. The peak volume $a_{mm}(0)$ at mixing time $\tau_{\text{mix}} = 0$ can be determined from back extrapolation of the respective diagonal peak intensities or it is measured directly. To stabilize the fitting process, $a_{mm}(0)$ enters as a fixed value and only T_{nm} and σ_{nm} are determined from the fit. This procedure yields good results for high and medium-high cross-relaxation rates. However, for weakly-interacting spin pairs, magnetization transfer to other spins is not negligible anymore and the cross-relaxation rates determined using the spin pair approach are systematically too small [107]. Especially for investigating the interaction between lipids and mobile guest molecules that might move in and out of the membrane, the precise determination of small cross-relaxation rates is relevant.

Full-Matrix Approach: As the last method, we introduce the full-matrix approach which is a more elaborate method yielding the most reliable results, also for small cross-relaxation rates [107]. Basically, the cross-relaxation rate matrix is determined by using the function given in Equation 68 as a fit function to describe the experimental data. For this, the entire peak volume matrices $\mathbf{A}(\tau_m)$ for a few different mixing times are needed and also the matrix $\mathbf{A}(0)$ approximated from a measurement with $\tau_{\text{mix}} = 1$ ms, which is more precise than a measurement with back-to-back pulses at mixing time zero [107], has to be determined. Additionally, the spin lattice relaxation rate R_{nn} is obtained for every peak using the SATREC pulse sequence (see Sec-

tion 5.4) on the ^1H channel. After rearranging Equation 68 and diagonalizing the volume matrix, the cross-relaxation matrix \mathbf{R} can be calculated from the volume matrix of one two-dimensional spectrum at any mixing time and the relaxation rates R_{nn} of all peaks, or from two volume matrices determined for any two different mixing times. The result was used as a starting value for the fit. Furthermore, the peak volumes were normalized in a way that all intensity curves $a_{nm}(\tau_{\text{mix}})$ reached a maximal value of about 1.0 at some point τ_{mix} . This ensures that during the fit all peaks have similar relevance, also potentially small lipid-guest molecule cross peaks.

The fit is carried out on the entire peak volume matrices, that is all curves $a_{nm}(\tau_{\text{mix}})$ are used simultaneously. To stabilize this procedure, several conditions are used. Firstly, the elements of $\mathbf{A}(0)$ are fixed to equal the experimental values. Considering Equation 69 and using that the ratio k_n/k_m equals the ratio of the relative peak intensities $a_{nn}(0)/a_{mm}(0)$, it can be concluded that only one half of the cross-relaxation matrix needs to be determined by fit. With this, the volume matrices calculated from the fit function are enforced to be symmetric. Also the diagonal values of \mathbf{R} are not determined by fit, but calculated from Equation 70 using the relaxation rates R_{nn} determined from the SATREC experiment. Although positive cross peaks, measured in all experiments here, result in negative cross-relaxation rates, in the fit some of them could become positive because volumes of small peaks can show a high scattering. Therefore, all cross-relaxation rates are enforced to be smaller than zero. Considering all these conditions, a stable fit can be obtained even when some volumes of small cross peaks are not determined very precisely.

The whole procedure was set up as a MATLAB routine and tested successfully for a sample of pure POPC and another one of pure DLPC. The results for POPC are given in the supplementary material. Generally, the matrix approach yields very accurate results [107]. However, the main disadvantage of this method is that the volumes of all peaks in the spectrum need to be determined. This is time consuming and can be rather imprecise for small and/or overlapping peaks.

NOESY cross-relaxation rates simultaneously contain information about molecular structures and dynamics. Specifically, they are influenced by molecular dynamics changing length and orientation of the vector connecting the interacting protons [121, 129].

In a similar way as already explained for the longitudinal relaxation rates R_1 (see Section 5.4), the cross-relaxation rates σ_{nm} can be calculated from the spectral density [129, 130] which results from the respective cross correlation function given by

$$C_{nm}(t) = \frac{4}{5} \sum_i \sum_j \left\langle \frac{Y_{20}(\mathbf{r}_{ij}(0))}{r_{ij}^3(0)} \frac{Y_{20}(\mathbf{r}_{ij}(t))}{r_{ij}^3(t)} \right\rangle, \quad (73)$$

where the two sums include the results of all protons contributing to the two peaks designated as n and m with the individual protons being referred to by the indices i and j , respectively. The spherical harmonic $Y_{20}(\mathbf{r}_{ij}) = \sqrt{\frac{5}{16\pi}}(3 \cos^2 \vartheta_{ij} - 1)$ is calculated using the angle ϑ_{ij} between the internuclear connection vector \mathbf{r}_{ij} and the membrane normal. Fourier transformation of the the cross correlation function yields the spectral density J_{nm} (see Equation 55 in Section 4) from which the cross-relaxation rate can be calculated using

$$\sigma_{nm} = (2\pi/5)\gamma^4 \hbar^2 (\mu_0/4\pi)^2 [3J_{nm}(2\omega_0) - 0.5J_{nm}(0)]. \quad (74)$$

When the cross correlation function can be described by a sum of exponential functions $C_{nm}(t) = \sum_l a_l e^{-t/\tau_l}$, then the Fourier transformation can be done analytically and the resulting cross-relaxation rate is given by

$$\sigma_{nm} = \frac{\gamma^4 \hbar^2 \mu_0^2}{40\pi} \sum_i \sum_j \sum_l a_l \tau_l \left\{ -1 + \frac{6}{1 + 4\omega_0^2 \tau_l^2} \right\}. \quad (75)$$

From this formula, conclusions about the sign of the cross-relaxation rate can be drawn [77]. For short correlation times, the last term becomes dominant and the resulting cross correlation rates positive. Consequently, the cross peaks are negative. One example are the cross peaks between resonances of lipid choline or glycerol groups and water molecules, which are highly mobile causing correlation times for the interaction in the order of 100 ps [69, 121].

For the interaction of larger molecules, like two lipids or a lipid and a larger guest molecule, longer correlation times in the nanosecond range play a role. In this case, the last term in Equation 75 is smaller than the first one, the NOESY cross-relaxation rates are negative and the cross peaks positive.

In our investigations, we mainly want to exploit the strong distance dependence of the correlation function (see Equation 73) and consequently the cross relaxation rate, which is contained in the prefactors $a_l = a_l(1/r_{ij}^6)$ in Equation 75. This means, that only proton pairs with an internuclear distance smaller than 5 Å contribute considerably [107]. Due to the high mobility, flexibility and disorder of the lipid molecules, the internuclear distances change constantly and consequently, the cross-relaxation rates become a measure of the probability of close approach of the respective nuclei [69], that is, the cross-relaxation rates depend on the number of close contacts and their duration [71]. However, this contact probability can only be deduced from the cross-relaxation rate when the rotational correlation time of the internuclear vector is equal for all contacts. From a direct comparison of results from NOESY experiments and MD simulations, Feller et al. concluded that the cross-relaxation rates are not directly and not in all cases proportional to contact probabilities [129]. Nevertheless, they can help to localize a guest molecule in a bilayer.

Besides the direct magnetization transfer considered here, also spin diffusion could occur, possibly transporting the magnetization for example along a lipid hydrocarbon chain. In this case the mathematical treatment shown above would not be valid. However, from measurements on partly deuterated samples, Huster et al. concluded that spin diffusion does not play a role in fluid lipid samples [107, 127].

5.6 Order Parameters Determined from Dipolar Couplings

A valuable source for the study of structure and dynamics in lipid bilayer samples is the dipolar coupling, which can be determined with atomic detail by various well-established NMR experiments. Besides being used for the investigation of internuclear distances, also the order parameter can be calculated from the dipolar coupling constant exploiting the fact that fast molecular dynamics ($\tau_c \ll \omega_D^{-1} \approx 50 \mu\text{s}$) average and, consequently, reduce the dipolar interaction (see Equation 51 in Section 4.1). In this case of fast dynamics, the time scale of the molecular motion is inaccessible from an experiment for determining the dipolar coupling. However, for motions

with intermediate correlation times of $\tau_c \approx \omega_D^{-1}$, the phase coherence of the spin polarization is lost during an NMR experiment with a typical time scale of several microseconds and the resulting T_2 relaxation contains information about the motional rates. Slow motions with correlation times $\tau_c \gg \omega_D^{-1}$ do not influence the experiment and consequently a coupling constant equal to the rigid coupling is measured.

Order parameters determined from coupling constants are very useful for the study of lipid bilayer/guest molecule systems. When the molecule is deeply incorporated in the membrane performing anisotropic and restricted dynamics, a coupling constant different from zero is determined. On the opposite, a guest molecule that does not attach to the bilayer but is dissolved in the surrounding water shows nearly isotropic mobility that averages all couplings to about zero. Additionally, a guest molecule can enhance or decrease the mobility restrictions of the lipid molecules.

As molecular dynamics average quadrupolar couplings in a similar way as dipolar interactions, order parameters for lipid membrane systems were usually determined from the measurement of quadrupolar couplings applying classical static ^2H NMR experiments for a long time [8, 22, 23, 34, 131]. Because, the quadrupolar coupling is larger than the dipolar coupling constant, the accuracy of the ^2H NMR experiment is generally increased and the time range of the fast limit is smaller [83]. However, isotope labeling is required due to the low natural abundance of ^2H . As selective deuteration approaches are cumbersome, in many ^2H NMR studies fully- or per-deuterated phospholipid molecules are used instead and specific methods of data analysis like the “de-packing” procedure [23, 132] are applied or special higher-dimensional MAS experiments [133, 134] are used which allow for the site-specific detection of quadrupolar couplings and thus order parameters.

In this work, we refrain from the ^2H NMR techniques and consider experiments to detect homonuclear ^1H - ^1H and heteronuclear ^{13}C - ^1H dipolar couplings instead. For chemical resolution, MAS is needed, which, however, is combined with the loss of precious information contained in the anisotropic interactions such as the CSA or the dipolar coupling. Nevertheless, order parameters can be extracted either from residual dipolar couplings which are not completely averaged by MAS or by the help of so-called recoupling methods. These are special pulse sequences that selectively and temporarily bring back anisotropic interactions under MAS. Examples are the frequently used REDOR sequence [135], which consists of 180° pulses applied at every half rotor period, or the symmetry-based sequences of Levitt [136]. Here, we apply so-called Separate Local Field (SLF) experiments which yield 2D spectra containing the isotropic chemical shift site specificity in the direct dimension, and the structural or dynamic information from the dipolar interaction in the indirect dimension [137]. In the following section, we will introduce the two SLF experiments DIPSHIFT and R-PDLF, with which ^{13}C - ^1H dipolar coupling constants can be determined. Subsequently, we explain the Double-Quantum (DQ) experiment which provides analogous ^1H - ^1H coupling constants.

5.6.1 The DIPSHIFT Experiment

The DIPolar chemical SHIFT correlation (DIPSHIFT) pulse sequence is an SLF technique commonly applied to measure residual dipolar couplings [137, 138]. Additionally, it can be used to determine correlation times of motions on the intermediate scale [139].

The DIPSHIFT technique detects the evolution of the rare ^{13}C spins under the influence of

all dipolar local fields produced by the surrounding protons. However, due to the strong distance dependence of the dipolar coupling (see Section 3.4.2, Equation 39), in most cases, the dominant contributions come from covalently bound protons, which therefore, will be considered solely in the calculations following later in this section. Instead of reintroducing heteronuclear dipolar interactions, in the basic DIPSHIFT experiment, only remaining dipolar sideband intensities are exploited [82,140]. Consequently, low or medium MAS frequencies are required.

The specific DIPSHIFT pulse sequence applied in this project is shown in Figure 14(a) [141]. In the beginning, transverse ^{13}C magnetization is excited by using CP or just a 90° pulse. During the following evolution time t_1 , a ^1H - ^1H homonuclear decoupling sequence applied allowing the system to develop under the influence of the heteronuclear dipolar interaction and the resonance offsets only. Here, we used the simple LG and the FSLG sequence. Subsequently, a heteronuclear decoupling sequence, like SPINAL64, is applied and consequently the influence of the C-H dipolar coupling on the ^{13}C spin evolution is stopped. Signal loss due to chemical shift of the carbons is refocused by a 180° pulse on the ^{13}C channel applied after half of the rotation period $\tau_r/2$ after the excitation sequence, that is in the middle of the sequence. Heteronuclear decoupling is continued during the acquisition time t_2 which starts after a total time interval of τ_r after excitation. Subsequent Fourier transformation yields a ^{13}C spectrum with chemical resolution. The whole experiment is repeated for a number of t_1 times which are incremented from zero to the full rotor period τ_r . Because the pulse sequence has the same length for all t_1 steps, the DIPSHIFT experiment is a so-called constant-time experiment. This means special attention must be paid to possible signal loss due T_2 relaxation, which might affect some parts of the sample more than others [142].

For data analysis, the peak intensities are determined by integration and plotted as a function of t_1 yielding a characteristic DIPSHIFT curve $I(t_1)$ for each chemical site that can be distinguished within the spectrum. For $t_1 = 0$, we have maximal signal intensity. With increasing t_1 the influence of the heteronuclear dipolar interaction rises and the signal intensity decreases until half the rotor period $\tau_r/2$ is reached. The influence of the dipolar interaction is reversed during the second half of the rotation period and a second maximum, a so-called rotor echo, appears after τ_r . However, due to T_2 effects, which are caused by molecular motions on the intermediate time scale affecting the decoupling performance or by imperfections of the pulse sequence, this second maximum does not necessarily reach the initial intensity again [139,141]. Information about the dipolar coupling is contained in the characteristic minimum of the DIPSHIFT curve, which is lower for higher coupling constants.

The DIPSHIFT curves $I(t_1)$ can be described by specific fit functions which allow for the determination of dipolar coupling constants from fitting the experimentally obtained curves which resemble an FID signal only influenced by the dipolar coupling [143,144]. The resulting functions that describe the DIPSHIFT curves of CH, CH_2 and CH_3 groups are given in the Supplementary Section C.3. When determining the dipolar coupling constant using any of these formulas, the characteristic scaling factor of 0.577 introduced by the homonuclear decoupling sequence, needs to be considered additionally (see Section 5.1). Deviations from the typical curve form can occur when a short CP is used for excitation. In this case the magnetization distribution in the sample might depend on bond orientations rendering the resulting DIPSHIFT curve asymmetric [145].

Using the basic DIPSHIFT experiment introduced here, coupling constants down to 4 kHz

can be measured when an MAS frequency of 5 kHz is applied. Smaller spinning frequencies result in DIPSHIFT curves with lower minima allowing for the extraction of smaller coupling constants. However, with the spinning speed also the spectral resolution decreases which possibly results in peak overlap and consequently renders the data analysis difficult. Therefore, a modified version of the DIPSHIFT experiment was introduced which allows for the determination of small coupling constants of a few kHz which are typical for mobile lipid molecules in fluid bilayers.

In the T_2 -recDIPSHIFT experiment from Cobo et al. [141], the basic DIPSHIFT experiment is applied in combination with rotor-synchronized 180° pulses to recouple heteronuclear dipolar couplings averaged by MAS. The pulse sequence is shown in Figure 14(b). Compared to the DIPSHIFT experiment, a mostly longer t_1 time of $t_1 = N\tau_r$, with $N = 1, 2, 3, \dots$, is chosen. During this time period, additional 180° pulses are applied on the ^{13}C channel at each half rotor period except of at the $N\tau_r/2$ position which allows for a full refocusing of isotropic and anisotropic chemical shifts. As a consequence, the recDIPSHIFT curve shows a greater modulation depth than the DIPSHIFT curve.

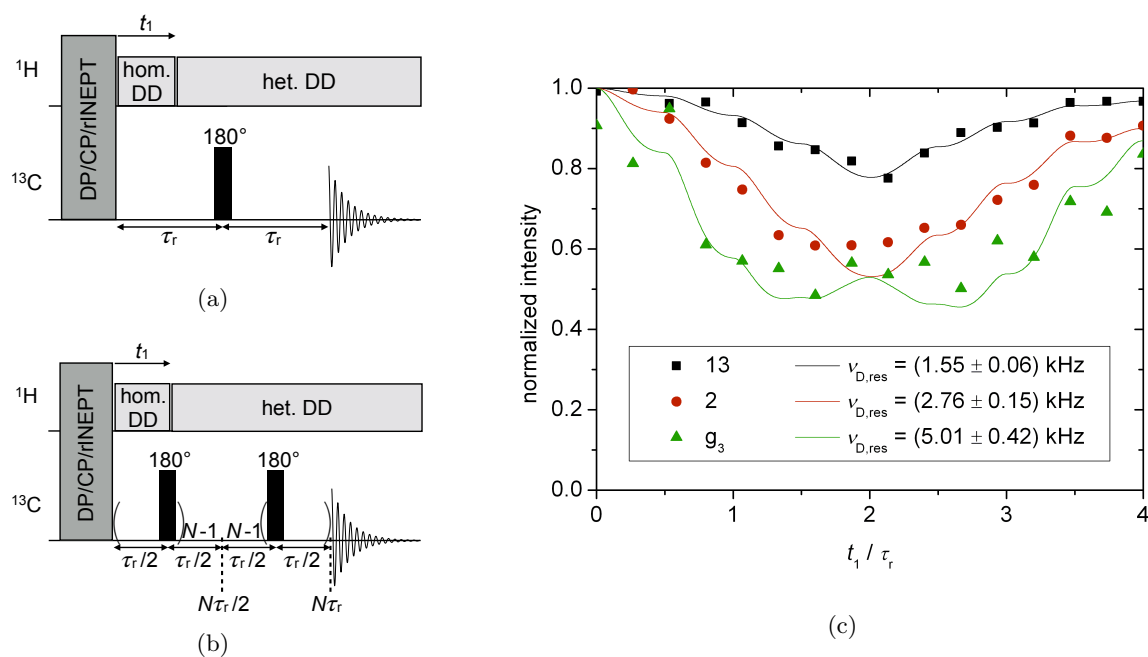


Figure 14: Pulse sequence of (a) the DIPSHIFT experiment and (b) the recDIPSHIFT experiment. In (c) modulation curves of selected resonances determined from the recDIPSHIFT experiment for DMPC at 47°C are shown. The symbols represent the measured data points and the lines are fit functions given by the respective equations in the Supplementary Section C.3 additionally considering an exponential T_2 decay.

Both DIPSHIFT-based methods described above are rather easy to set-up and robust with respect to pulse imperfections. They allow for the measurement of a wide range of dipolar couplings from about 1 to 22 kHz. Hereby, the DIPSHIFT sequence should be used to determine coupling constants bigger than 5 kHz and the recDIPSHIFT sequence for coupling constants smaller than 5 kHz.

However, by using the DIPSHIFT experiment only one averaged dipolar coupling constant can be determined for each modulation curve, that is for each peak in the ^{13}C spectrum. This can be an important drawback rendering data analyzation imprecise in cases like CH_2 groups having two distinct C–H dynamical order parameters, for crowded regions containing overlapping peaks from different molecular segments or for heterogeneous samples where one chemical site shows different dipolar couplings.

From literature, the wide application of the DIPSHIFT method, also for the investigation of lipid membrane systems, can be recognized. Besides for the study of pure lipid bilayers, DIPSHIFT experiments were used for the investigation of lipid bilayer/guest molecule systems [144]. For example, Middleton et al. determined the influence of added peptides, proteins and drug molecules on the dipolar coupling of DMPC lipids forming MLVs [146]. Also the motional geometry of various guest molecules in a membrane, like oligocholate macrocycles [73], peptide [75], cannabinoid ligand [125], were investigated by using the DIPSHIFT techniques.

Here we present exemplary the results of the recDIPSHIFT experiment for a sample of pure DMPC in water in the liquid-crystalline phase at 47°C . The resulting modulation curves of some resonances are shown in Figure 14(c). For the carbon g_3 and 13, the fit functions describe the data rather well. However, for carbon 2 the theoretical function has slightly a different form than the experimentally determined curve. The reason is, that for calculating the fit function, we assume identical coupling constants for all C–H bond contributing to the modulation curve. For the resonance of carbon 2, this is, however, not valid because the two bonds of one CH_2 group and the bonds in the two different tails show different coupling constants [144]. The results for all distinguishable resonances are summarized in Figure 17.

5.6.2 The R-PDLF Experiment

Proton-Detected Local Field (PDLF) NMR, is another method for the determination of heteronuclear dipolar coupling constants. In this experiment, the dipolar field induced by a ^{13}C spin on its neighboring ^1H spins is probed at the abundant ^1H nuclei rather than at the rare ^{13}C nuclei like it is done using the DIPSHIFT method. Therefore, PDLF spectra are governed by simple two-spin interactions which renders data analysis easier. One example for an PDLF experiment is the Dipolar Recoupling On-axis with Scaling and Shape preservation (DROSS) sequence, which has been applied to study the effect of cholesterol [147] and of oxidized lipids [148] on lipid bilayers. Besides the determination of absolute values of order parameters $|S_{\text{CH}}|$, a modified version of the DROSS experiment also allows for the detection of the sign of the order parameter [140].

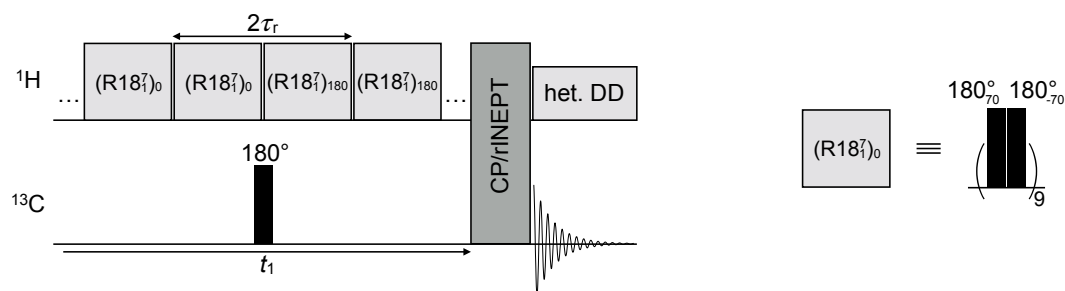


Figure 15: R-PDLF experiment.

Here, we use the R-PDLF sequence, which provides a better resolution than the DROSS experiment [82]. It contains a combination of R-type recoupling blocks, developed from Levitt's symmetry based sequences [136], and the PDLF method and was used by Dvinskikh et al. for the first time [115]. It is suitable for slow to intermediate MAS frequencies.

In Figure 15, the pulse sequence of the R-PDLF experiment is shown. It starts with the irradiation of rotor-synchronized $R18_1^7$ blocks on the proton channel over a total time of t_1 which is incremented by increasing the number of $R18_1^7$ blocks. Such an R block causes the suppression of homonuclear dipolar interactions among the ^1H spins and simultaneously reactivates the heteronuclear dipolar coupling between ^1H and ^{13}C nuclei and the ^1H CSA interaction. The $(R18_1^7)_0$ block, applied in the beginning of the sequence, contains nine pairs of 180° pulses. One pulse of the pair has a phase of 70° and the other one of -70° . Each pulse has a length of $1/18$ of the rotor period.

After the first set of $(R18_1^7)_0$ blocks applied for a time $t_1/2$, a second set with a phase shift of 180° is used. These $(R18_1^7)_{180}$ blocks contain pairs of two pulses with the phases 70° and 290° . Additionally, a 180° pulse is irradiated on the ^{13}C channel at $t_1/2$. This allows for a partial suppressing of the ^1H CSA interaction [115]. Hence, during the t_1 interval, ^1H polarization modulated by the ^{13}C - ^1H dipolar interaction is produced [82] and can be transferred to ^{13}C spins in the next step. Depending on the method applied for this, the selection of certain spin pairs is possible [115].

The CP transfer is used when interest lies in the signals of stiff molecular segments for example of cholesterol in a lipid bilayer [61]. However, only a short CP contact time should be used to avoid redistribution of ^1H polarization via spin diffusion. To determine the order parameters of very mobile molecular segments, for example of lipids in the liquid crystalline phase, the R-PDLF experiment with a rotor-synchronised refocused INEPT polarization transfer can be applied [61]. In this case, polarization transfer occurs almost exclusively between directly bonded carbons and protons, facilitating the measurement of one-bond dipolar interactions [115].

During the subsequent acquisition time t_2 , the ^{13}C magnetization evolves under influence of the chemical shift interaction [82]. After processing the measured data $s(t_1, t_2)$ by 2D Fourier transformation, we get a 2D spectrum $S(\omega_1, \omega_2)$ with the ^{13}C chemical shift in one dimension (ω_2) and a dipolar spectrum for each chemical site in the second dimension. As an example, a part of an R-PDLF spectrum recorded for DMPC is shown in Figure 16. Due to the influence of the R blocks, the dipolar spectra do not resemble the typical form of a Pake pattern but they show $n = 2$ rotary-resonance lineshapes instead [82]. The splitting $\Delta\nu$ between the two horns is proportional to the residual dipolar coupling constant $\nu_{\text{D,res}} = \omega_{\text{D,res}}/(2\pi)$:

$$\Delta\nu = \pm 0.315 \nu_{\text{D,res}} = 0.315 |S_{\text{CH}}| \cdot 22 \text{ kHz} \quad (76)$$

Deviations from the spectrum form can come from incomplete suppression of ^1H - ^1H interactions [82] or from second-order average-Hamiltonian dipolar terms due to which the signal intensities do not decay to zero for long t_1 times, but to a certain offset value resulting in a strong center peak in the dipolar spectrum [149]. Additional smaller splittings can arise from interactions of the carbon with remote protons [150].

Although the distance determination between the two peaks is very precise, the dipolar spectrum can be affected by systematic errors. The largest uncertainty comes from missettings

of the ^1H r.f. field amplitude and from r.f. field inhomogeneity [151]. A relative error of the pulse amplitude of $\mp 10\%$ results in relative error of $\pm 10\%$ of the coupling constant. For higher pulse amplitude missettings the influence on the resulting measurement increases even more. Inhomogeneity of the r.f. field usually results in an overestimation of the coupling constant.

Because the smallest t_1 increment equals the lengths of two R blocks, the maximal widths of the resulting dipolar spectra and with this the maximal dipolar coupling accessible with this method is determined by the spinning frequency. However, modifications of the sequence also allow for smaller t_1 increments and the determination of higher dipolar couplings using moderate spinning speeds. The smallest coupling resolvable in the dipolar spectrum depends on the longest time t_1 over which the R blocks can be applied causing only little sample heating. Here, a coupling of about 0.3 kHz could still be resolved from the dipolar spectrum. Even smaller couplings can sometimes be determined from the time-dependent signal. This, however, is only possible when the respective chemical site exhibits only one dipolar coupling.

The main advantage of the R-PDLF experiment in comparison to the DIPSHIFT method is the higher dipolar resolution. Because dipolar spectra obtained from the R-PDLF sequence are governed by simple two-spin interactions, it is possible to resolve two or more different dipolar couplings from the same chemical site [115,152]. A disadvantage of the R-PDLF experiment is the smaller scaling factor [149].

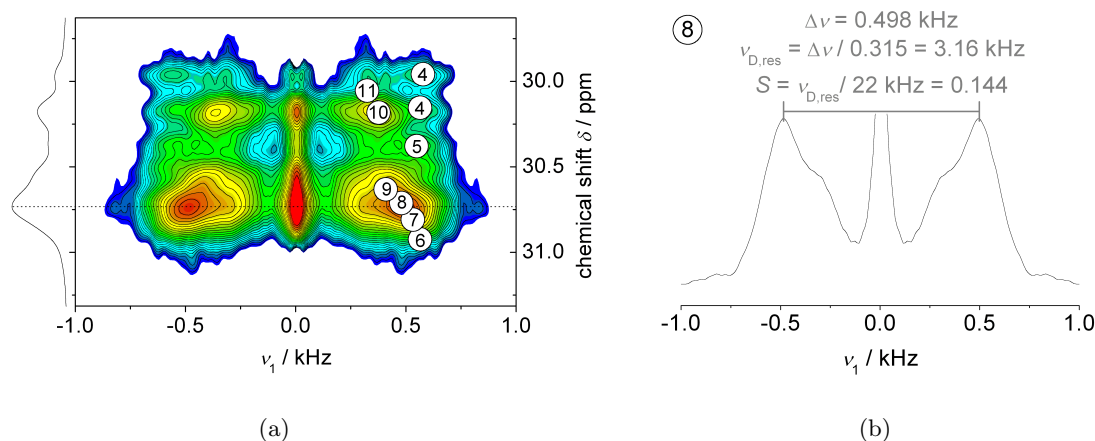


Figure 16: (a) Detail of the 2D R-PDLF spectrum of DMPC at 47°C showing the partly overlapping resonances originating from the lipid alkyl chains. The carbons of the lipid tails and their respective peaks are enumerated along the chain starting at the ester bond with 1 and ending at the tail end with 14 (see Figure 11(b)). The dipolar spectrum (b) is given by the cross-section at the highest peak denoted by the dotted line in (a).

The R-PDLF experiment can well be used for the determination of the small order parameters in lipid bilayers [82,153] or other liquid crystalline systems [115,154]. Here, we present results for a DMPC MLV sample at 47°C . The entire 2D R-PDLF spectrum, dipolar spectra at the peak positions and the t_1 time decay of the respective peak maxima are shown in Figure 62 in the Supplementary Section C.4. In Figure 16, the crowded spectral region containing the partly overlapping resonances of the lipid alkyl chains is shown. The peak assignment was done based

on literature results [61,155]. The resulting order parameters S_{CH} for all the different carbons in the DMPC molecule are given in Figure 17 in the next section.

5.6.3 C–H Order Parameters of DMPC

Using Equation 51 given in Section 4.1, we can calculate the order parameter S_{CH} from the residual dipolar couplings determined by using the recDIPSHIFT or the R-PDLF sequence. We assume here a rigid coupling constant of $\omega_{\text{D}} = 22 \text{ kHz}$ [77,144].

In Figure 17, the results for DMPC measured at 47°C are shown in comparison with some literature data determined at 50°C . The results from the recDIPSHIFT and R-PDLF sequence agree well. Because of the limited resolution of the recDIPSHIFT experiment, we only obtain one averaged coupling constant for all C-H bonds contributing to the main alkyl peak.

The order parameters from literature, especially the values determined from ^2H NMR experiments, are higher than the values measured here. Similar observations were already made before by Warschawski et al. [147]. They explained the higher order parameters S_{CD} compared to S_{CH} by the missing ^1H decoupling during the ^2H experiments, the T_2 anisotropy leading to partial signal relaxation during the sequence and the different timescales for the ^2H and the ^1H - ^{13}C experiment. However, we here determined a larger difference between S_{CH} and S_{CD} than Warschawski et al. Other groups found no or only a very small difference between the order parameters determined from ^{13}C - ^1H dipolar couplings or ^2H quadrupolar couplings [61,156].

As we measured at a slightly lower temperature (47°C), order parameters determined here should be slightly higher than the literature values determined at 50°C . However, this difference is small only amounting to about $\Delta S \approx 0.01$ for $\Delta T = 5^\circ\text{C}$ [34,131]. Therefore, also uncertainties in the temperature determination should only have minor influence. We conclude that additional factors might be responsible for the reduction of our order parameters S_{CH} , for example a beginning sample degradation (see Supplementary Section B). Also the water content (about 50 wt%) cannot be considered as a reason for the different results as it was roughly the same for our measurements and the samples used in literature.

The carbons of the choline group show the smallest order parameters reflecting the high mobility of this group. The highest values are determined for the glycerol group and the upper chain region because the mobility of these segments is most restricted. The order parameters determined for the alkyl chains reflect the mobility gradient in the lipid molecule. For the upper chain region, we measure $S \approx 0.2$ which is a reasonable result as it lies in-between the values for an isotropically mobile segment ($S = 0$) and a rigid chain in all-trans conformation rotating about its long-axis ($S = 0.5$). It includes gauche-trans isomerizations and wobbling motions of the whole molecule occurring additional to the fast rotational reorientations [118]. Towards the chain end, the order parameter decreases to a very small value, because the chain ends nearly perform isotropic motions.

The order parameter profile can also be explained by a packing density argument [118]. Because of defects in the upper acyl chain regions, the tails have different lengths which result in free space in the middle of the bilayer allowing for increased chain mobility. In literature, the order parameters determined for the lipid chains are often interpreted quantitatively. Using specific theoretical models, for example the bilayer thickness, the area per lipid molecule and the chain geometry can be determined [8,34,131,156,157].

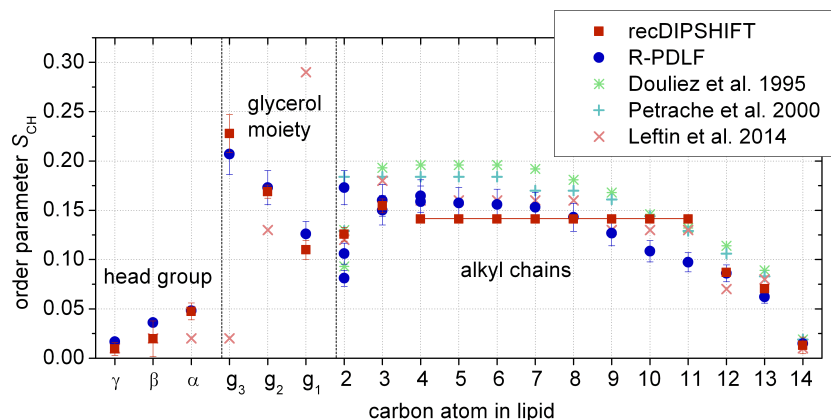


Figure 17: Comparison of order parameters measured for pure DMPC at 47°C using the recDIPSHIFT and the R-PDLF experiment and literature values. Petrache et al. [34] and Douliez et al. [131] determined the order parameters from ^2H NMR measurements and Leftin et al. [156] used the DROSS sequence to measure S_{CH} .

The lipid segments showing nearly isotropic mobility, like the carbons of the choline headgroups or the chain ends, exhibit identical couplings for all respective bonds [140]. However, from the resonances of some carbons situated near the motionally more restricted glycerol backbone or at the upper chain region, two or more different couplings can be detected by the R-PDLF experiment. From the DIPSHIFT experiment however, we only determine one value which represents an averaged coupling constant.

For example, three different order parameters were found for carbon 2. The largest value results from the two C-H bonds of the respective carbon in the sn-1 chain. The two different weaker couplings come from the sn-2 chain, which is bend causing the respective CH_2 group to lay in a plane not perpendicular to the bilayer normal [9, 23, 82, 131].

Also for the g_1 resonance, two order parameters can be found. While one C-H bond shows a high coupling constant similar to the results of other C-H bonds of the glycerol group, the other one is oriented nearly in the magic angle with respect to the bilayer normal, which results in an effective coupling of about zero [61, 82]. Therefore, the respective dipolar spectrum determined by the R-PDLF sequence shows a middle peak of higher relative intensity than for the other spectra.

As already explained above for some examples, the order parameter reacts sensitively on external conditions. For example the lipids in a bilayer in the gel phase show considerable higher dipolar couplings than the lipids in a bilayer in the liquid-crystalline phase. Additionally, molecular motions on the intermediate timescale, appearing in the gel phase, can cause T_2 effects, which can lead to significant signal loss rendering the experiments difficult [23]. For a lipid bilayer in the liquid-crystalline phase, the order parameter determined for the lipid chains decreases with rising temperature [150, 157]. Furthermore, the molecular order depends on the specific type of the molecular system. For example, by introducing one or more double bonds in the lipid alkyl chains the order parameter is decreased. Also, the introduction of a guest molecule in the bilayer can change the lipid order parameters. While, certain molecules like a synthetic cannabinoid

ligand [125], the ras-peptide [126] or oxidized lipids [148] increase the disorder in the lipid alkyl chain region, other molecules like cholesterol [23, 25, 61] or a fluorotelomer alcohol [155] cause an increase of the chain order parameter and enhances the stretching of the chains.

5.6.4 H–H Order Parameters determined by the BaBa-xy16 Experiment

As shown in the previous section, ^1H – ^{13}C dipolar couplings determined from NMR experiments can often be used to probe local order, structure and motional geometries in lipid bilayer systems. However, the methods presented also show limitations, such as a low signal-to-noise ratio associated with the carbon detection and a significant inaccuracy in determining small coupling constants of 1 kHz or below, which is especially disadvantageous for the investigation of highly mobile guest molecules of low concentration in the bilayer. As an alternative, we will therefore introduce Double-Quantum (DQ) NMR methods, which exploit the strong ^1H signal to measure residual ^1H – ^1H dipolar couplings and thus the related order parameter S_{HH} .

Generally, DQ experiments applied under static conditions are well suited and frequently used for the investigation of molecular dynamics in polymer networks or melts yielding a coupling constant of an average monomer unit [142, 158]. To achieve chemical resolution, we here use the Back-to-Back (BaBa) double-quantum recoupling pulse sequence which is applied in combination with MAS [159] and allows for the determination of rather small ^1H – ^1H couplings down to about 100 Hz. Additionally, information on the distribution of the dipolar couplings can be obtained.

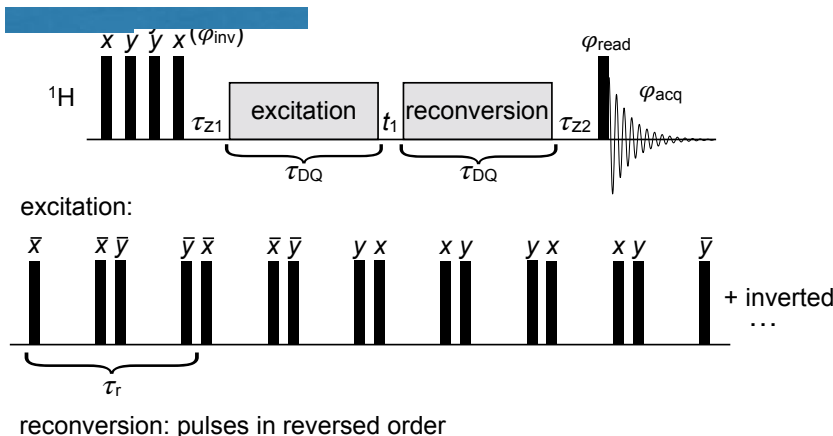


Figure 18: BaBa-xy16 pulse sequence as introduced in ref. [159]. All black bars symbolize 90° pulses. The pulse phases φ_i are varied as described in the text.

Originally, the BaBa (“back-to-back”, referring to pulse placement) experiment was developed by Feike et al. [160]. Later on, Saalwächter et al. added the xy-16 phase cycle known from CPMG (Carr-Purcell Meiboom-Gill)-type and REDOR experiments [161] to achieve a truly broadband BaBa variant, termed BaBa-xy16 [159]. The respective pulse sequence is shown in Figure 18. In the general scheme, we have an excitation sequence creating DQ coherences, an optional t_1 evolution time, and a (mainly just inverted) reconversion sequence which produces measurable magnetization. The excitation and the reconversion units contain a simple two-pulse sequence as the basic building block, the function of which is explained in the Supplementary Section C.5. Due to the specific choice of the pulse phases, additional virtual 180° pulses are included in the

sequence that cancel out offset and chemical-shift effects. The resulting basic four-pulse building block is repeated several times with different pulse phases, so that the complete excitation and the reconversion sequences contain a variable number of 90° pulses and have an equal length τ_{DQ} , which is an integer multiple of the rotation period τ_{r} . Additionally, we have a preparation step containing a spin temperature inversion at the beginning of the total pulse sequence, and in the end there is a read-out pulse before signal acquisition starts during t_2 [159].

As a result, we have a 2D data set with chemical resolution in the direct dimension and information on the recoupled homonuclear dipolar coupling in the indirect dimension. Unlike the simple two-pulse sequence, the BaBa experiment yields a pure DQ Hamiltonian (see Supplementary Section C.5) [142].

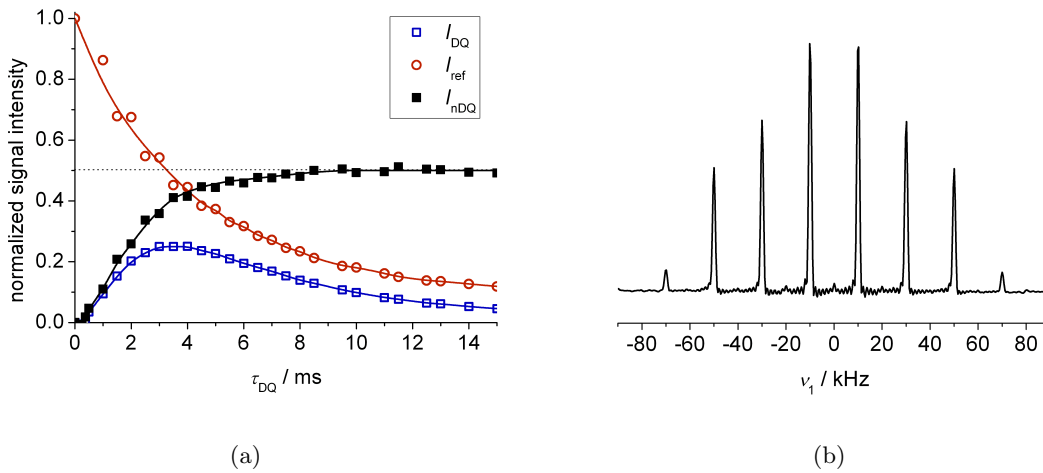


Figure 19: (a) DQ intensity, reference signal and DQ build-up curve determined as exemplary data from a polybutadiene rubber sample. Due to dipolar truncation all resonances of the polymer roughly yield the same build-up curve. (b) Sideband pattern determined as exemplary data from an aromatic compound inserted in a POPC bilayer.

There are essentially two ways to obtain dipolar-coupling information from this experiment. As the first option, DQ build-up curves are recorded by incrementing τ_{DQ} of the excitation and the reconversion blocks while setting the delay time t_1 in-between the two blocks to zero, and as a second possibility, DQ sideband patterns [142, 162] are obtained by fixing τ_{DQ} at a suitable value and incrementing t_1 in small steps $\Delta t_1 \ll \tau_{\text{r}}$, followed by Fourier transformation over this indirect spectral dimension [159]. In both cases, a 4-step DQ selection phase cycle, rotating the excitation (or reconversion) base phase in 90° steps, is applied. Alternation of the receiver phase between $\pm 180^\circ$ yields the DQ signal $I_{\text{DQ}} = \langle \sin \phi_{\text{DQ}}(0) \sin \phi_{\text{DQ}}(t_1) \rangle$. The brackets denote the powder average, $\phi_{\text{DQ}}(t_1)$ is the dipolar phase factor and t_1 is the starting time of the block, which is relevant when $t_1 \neq n\tau_{\text{r}}$.

We first focus on build-up curve analysis. In this case ($\phi_{\text{DQ}}(0) = \phi_{\text{DQ}}(t_1 = 0) = \phi_{\text{DQ}}$), the DQ signal, acquired with receiver alternation, is given by $I_{\text{DQ}} = \langle \sin^2 \phi_{\text{DQ}} \rangle$. The intensities need to be normalized to account for relaxation effects occurring because transverse magnetization is present during the excitation and the reconversion sequence. Therefore, a second signal function

without receiver phase alternation, the reference signal $I_{\text{ref}} = \langle \cos^2 \phi_{\text{DQ}} \rangle$, is recorded. From this intensity, we can calculate the sum $I_{\Sigma\text{MQ}} = I_{\text{DQ}} + I_{\text{ref}}$, which is a type of multi-spin dipolar echo function. The point-by-point normalized DQ build-up curve follows from

$$I_{\text{nDQ}} = \frac{I_{\text{DQ}}}{I_{\Sigma\text{MQ}} - I_{\text{tail}}} = \left\langle \frac{\sin^2 \phi_{\text{DQ}} \cdot R(2\tau_{\text{DQ}})}{(\cos^2 \phi_{\text{DQ}} + \sin^2 \phi_{\text{DQ}}) \cdot R(2\tau_{\text{DQ}})} \right\rangle = \langle \sin^2 \phi_{\text{DQ}} \rangle, \quad (77)$$

which is corrected for motion-related relaxation, pulse sequence imperfections and higher-order dephasing terms (see Figure 19(a)). Potential damping is described by the factor $R(2\tau_{\text{DQ}})$. In the denominator, we subtract the contribution I_{tail} of uncoupled spins showing a slowly relaxing, often exponential tail in I_{ref} . These may be related to isotropically mobile defects in an inhomogeneous system.

The DQ build-up curve I_{nDQ} is theoretically expected to approach a value 0.5 in the long-time limit, which represents a test criterion for successful normalization. However, this plateau value might not be reached in case of very weak dipolar couplings or when relaxation effects cannot be eliminated by normalization for example because of intermediate motions or because of a distribution of couplings coming from different components [142]. On the other hand, experimental data sometimes also shows a small overshoot above 0.5 because of higher coherences occurring in the multi-quantum system [142].

While the build-up curve originating from a single spin pair contains oscillations, a spin ensemble yields a smooth curve. A slow build-up resembles a system with small dipolar couplings and strong interactions cause a fast build-up. To quantify this effect, the dipolar coupling constant is determined using different fit functions that describe the build-up curve. The simplest approach is the second-moment approximation

$$I_{\text{nDQ}}(\tau_{\text{DQ}}) = \langle \sin^2 \phi_{\text{DQ}}(\tau_{\text{DQ}}) \rangle \approx \frac{1}{2} \left\{ 1 - e^{-2\langle \phi_{\text{DQ}}^2(\tau_{\text{DQ}}) \rangle} \right\} \quad (78)$$

with the mean-square phase factor [159]

$$\langle \phi_{\text{DQ}}^2(\tau_{\text{DQ}}) \rangle = \frac{6}{5\pi^2} \nu_{\text{D,res}}^2 \tau_{\text{DQ}}^2. \quad (79)$$

It fits the data well up to an intensity of $I_{\text{nDQ}} \approx 0.45$ [163]. An even better approximation of the experimental data is provided by the ‘‘Abragam-like’’ build-up function

$$I_{\text{nDQ}}(\tau_{\text{DQ}}) = 0.5 \left(1 - \exp\{-0.295 \nu_{\text{D,res}} \tau_{\text{DQ}}\} \right)^{1.5} \times \cos(0.455 \nu_{\text{D,res}} \tau_{\text{DQ}}), \quad (80)$$

which was found empirically by Chassé et al. [163].

Due to inhomogeneities, most samples feature a distribution of coupling constants. The simplest way to take this into account is by introducing a Gaussian distribution function

$$p(\nu'_{\text{D,res}}) = \frac{1}{\sqrt{2\pi\sigma^2}} e^{-\frac{(\nu'_{\text{D,res}} - \nu_{\text{D,res}})^2}{2\sigma^2}} \quad (81)$$

with σ being the standard deviation. For the second-moment approach, the resulting fit function can be calculated analytically. An ‘‘Abragam-like’’ build-up function combined with a coupling

constant distribution (resulting in a mere two-parameter fit) can be implemented numerically with a finite-step integration extending over about $\nu_{D,\text{res}} = \pm 3\sigma$.

The DQ build-up curve analysis is only possible for small coupling constants up to about 1 kHz. Stronger dipolar couplings lead to a very fast increase of the DQ build-up curve which shows in this case only a few data points in the meaningful initial build-up region. The increment of τ_{DQ} can not be set arbitrarily small as it has to be an integer multiple of the rotation period τ_{r} , the minimum value of which is determined by the fastest feasible MAS frequency. Therefore, spinning side-band analysis using an incremented t_1 at fixed τ_{DQ} is preferred for the accurate determination of stronger dipolar couplings.

For this, we choose an excitation time τ_{DQ} beyond the maximum of the normalized DQ build-up curve. and the waiting time t_1 is incremented in steps much smaller than the rotation period. The 2D DQ–SQ correlation spectrum resulting from 2D Fourier transformation shows a spinning sideband pattern in the indirect (DQ) spectral dimension, which reflects the coupling constant of the protons (see Figure 19(b) for an example). Again assuming a Gaussian distribution, $\nu_{D,\text{res}}$ and the distribution width σ can be determined from the sideband pattern on the basis of a fit function developed by K. Saalwächter, which uses a look-up table for the DQ signal intensities determined for different MAS frequencies [142]. The distribution might arise from actual inhomogeneities in the sample, but also from couplings to remote protons or from a bias in the assumed isotropic powder average caused by an anisotropic transversal relaxation [5, 142]. During the fit, the first-order sidebands are neglected as their intensity is influenced by differential relaxation [142].

Like the DIPSHIFT experiment, the BaBa experiment for the determination of spinning sidebands is practically a constant-time experiment during which signal relaxation of some sample components can occur.

6 MD Simulations and Results for Pure Lipid Bilayer Systems

6.1 Introduction

Using computer simulations, molecular systems can be created virtually and their behavior over time can be observed. Time scales and system sizes accessible, depend on the resolution used. The combined application of experiments and simulations can provide meaningful results. On the one hand, simulations can be used to explain experimental results. For example, different molecular configurations can be simulated to find out which one yields results closest to the experimental values. On the other hand, the correctness of simulations can be validated by comparison of specific quantities determined from the experiment and from the simulated trajectories. Because various parameters can be measured with chemical resolution, NMR is one of the most important methods to validate simulations [8]. Simulations of trajectories with time ranges of microseconds to milliseconds using all-atom descriptions are becoming possible nowadays. They represent an important method in addition to experiment and theory. Also for the description of membrane systems, simulations are used commonly [83]. Most widely applied are Molecular Dynamics (MD) and Monte Carlo (MC) simulations.

In this work, we conducted MD simulations, using the software package GROMACS 5.1.4 (GRoningen MACHine for Chemical Simulations) [164]. A basic description of MD simulations in general can be found in References [165, 166]. The atoms are modeled as classical objects that move according to Newton’s laws. A particle with index i is defined by its position \mathbf{r}_i at time zero and its mass m_i . When the potential energy function V describing the system is known, then we can determine the force \mathbf{F}_i on one particle and from this the particle positions after time t using

$$m_i \frac{d^2 \mathbf{r}_i}{dt^2} = \mathbf{F}_i = -\nabla_{\mathbf{r}_i} V(\mathbf{r}_1, \dots, \mathbf{r}_N). \quad (82)$$

The trajectory containing the positions of all interacting particles from an initial state throughout the course of time is calculated numerically by discretization and integration of this equation. Specifically, we use the leap frog algorithm. An integration time step of 2 fs was chosen.

The set of mathematical functions with their corresponding parameters describing the interactions V between and within the molecules is called “force field”. They include forces between bonded atoms associated with bond-stretching and changes of bond angles and dihedrals as well as forces between non-bonded atoms like van der Waals and electrostatic forces. Parameters for these interactions are determined from *ab initio* quantum calculations and they are adjusted empirically to fit experimental results [166]. For this work, we used the force field of Poger et al. [167] to describe the lipid bilayer.

Depending on the information to be extracted, different simulations from low-resolution coarse-grained to atomistic resolution are possible. Here, we use the united atom model, in which all atoms of one methyl or methylene group are treated as a single interaction center at the position of the carbon.

As it is not possible to simulate a sample of macroscopic dimensions, we use a simulation box containing 128 lipids and a few thousands of water molecules, and periodic boundary conditions.

The systems simulated are NpT ensembles, that is the number N of atoms, the pressure p and the temperature T were kept constant while the size of the simulation box of about

$6.5 \times 6.5 \times 10$ nm was flexible. A Nosé-Hoover thermostat was used to keep the temperature stable.

MD simulations are subject to various limitations and therefore results should be interpreted carefully. Firstly, the force field is subject to uncertainties as its parameters are determined so that a specific experimental quantity is predicted [166]. Furthermore, to reliably extract certain quantities, the trajectories need to be long enough which is especially relevant for the determination of NMR relaxation rates, and also the simulation box needs to be large enough so that a converged average value is reached.

The MD simulations used in this work were set-up and run by T. M. Ferreira and analyzed by myself. In Figure 20, a snapshot of the trajectory of a DMPC bilayer in water is shown. In the following, we determine order parameters and relaxation times from these simulated trajectories and compare with results from NMR experiments.

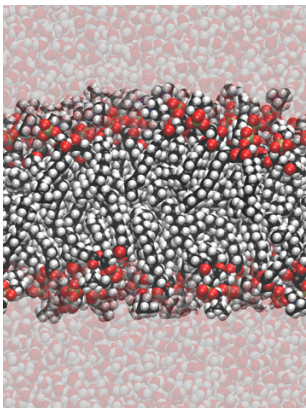


Figure 20: Snapshot of simulated trajectory of a DMPC bilayer in water at a simulation time of 20 ns. The plot was created with VMD. Different colors symbolize different atoms: oxygen = red; carbon = black; hydrogen = white; phosphorous = yellow; nitrogen = blue.

6.2 Lipid Order Parameters Determined from Simulated Trajectories

Firstly, we want to calculate order parameters from the trajectories simulated and compare with experimental results. The Saupe matrix for the connecting vector $\mathbf{r} = (xyz)^T$ between two atoms can be calculated using Equation 48 given in Section 4 which can be rewritten as

$$S_{\alpha\beta} = \frac{1}{2NM} \sum_{m=1}^M \sum_{n=1}^N \left(\frac{3\alpha_{nm}\beta_{nm}}{|\mathbf{r}_{nm}|^2} - \delta_{\alpha\beta} \right) \quad (83)$$

with α and β denoting the three dimensions x , y and z . The index n is counting the time frames and m the molecules in the system.

We firstly calculated the Saupe matrix for a system of a pure DMPC bilayer simulated. As the membrane is oriented in a way that the bilayer normal is aligned parallel to the z -axis, the order parameter S is given by S_{zz} determined from Equation 83. In Figure 21(a), the zz and the xy component of the order tensor is given calculated as the average from all time frames until the time point t plotted on the x -axis. The black line represents the average over all lipids which converges fast to a stable value that is to the order parameter S_{zz} or to zero for the off-diagonal matrix element S_{xy} . However, the results calculated for two individual lipid molecules shown in red and blue that we picked exemplarily, do not in all cases reach a stable value in the given time period. The grey area represents the order parameter range calculated from all individual

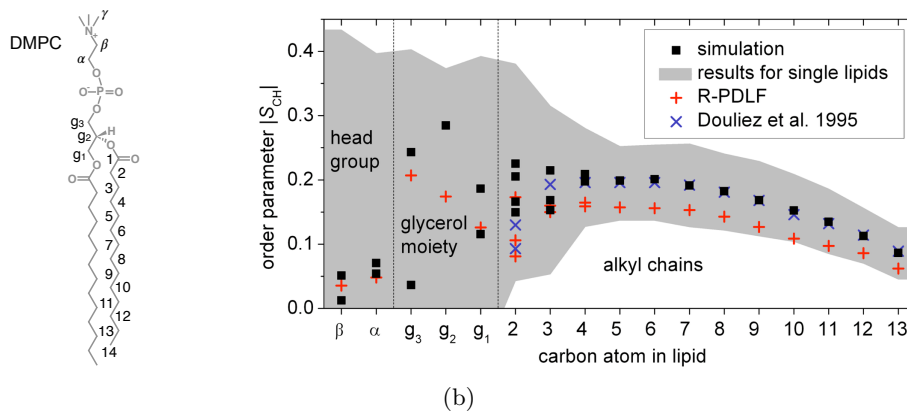
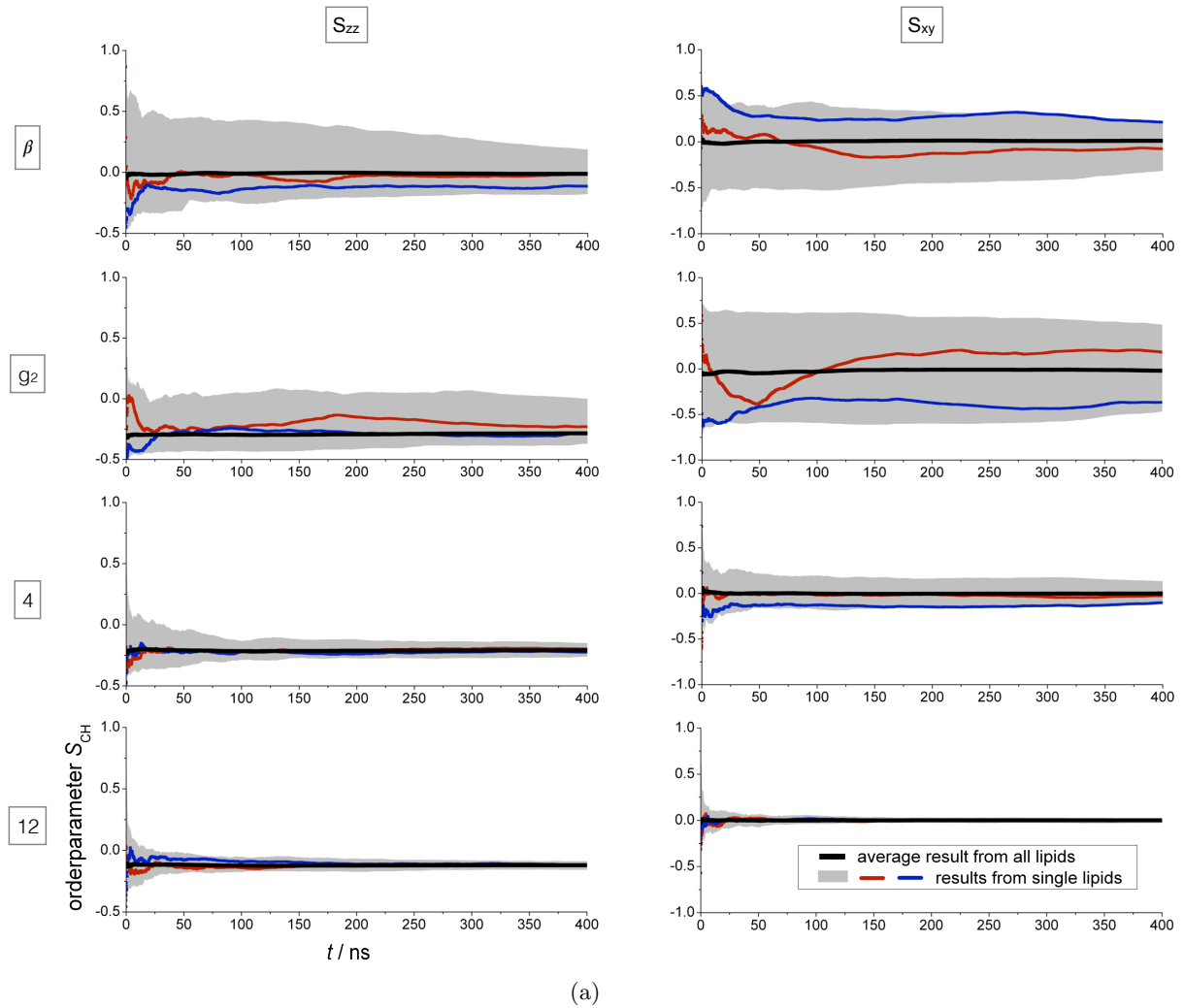


Figure 21: Results from the simulation of a DMPC bilayer in water at 47 °C: (a) order matrix elements calculated from a trajectory of given time length for different C-H bonds of the lipid, and (b) order parameter profile for the whole lipid molecule calculated as average over the entire simulation time of 400 ns and all lipids. For comparison, also order parameters determined from the R-PDLF experiment (see Section 5.6.3) and literature values [131] are shown.

molecules. The upper and the lower boundary are determined from the maximal and minimal value of the 128 values calculated for the individual lipids. Especially, for the choline head group and the glycerol backbone, this range of order parameters is quite large indicating that averaging over one molecule is not enough. For values determined for the middle of the chain and towards the chain end, this behavior improves, that is, an averaging is reached sooner. This observation is in agreement with literature where it was found that order parameters of the glycerol backbone and the choline group are generally less well described by simulations than order parameters of the acyl chains [168].

In Figure 21(b), the results for the order parameter determined from the full time-length simulated for the different lipid segments are shown and compared with values determined from the R-PDLF experiment and from literature. For the alkyl chains the simulation results match well with literature values while our experimentally determined results lie below. Reasons for this were already discussed in Section 5.6.3. Also the temperature of the system simulated and the real sample might not precisely be the same. It could be that the phase transition of the system simulated occurs at a different temperature. Order parameters determined for the choline head group are quite small in both, the experimental and the simulation results. For the glycerol region, the order parameters do not match very well. This is in agreement with literature [61,168] and with the results shown above, that the order parameter from the MD simulations for the headgroup region is least accurate.

6.3 R_1 Relaxation Rates Determined from Simulated Trajectories

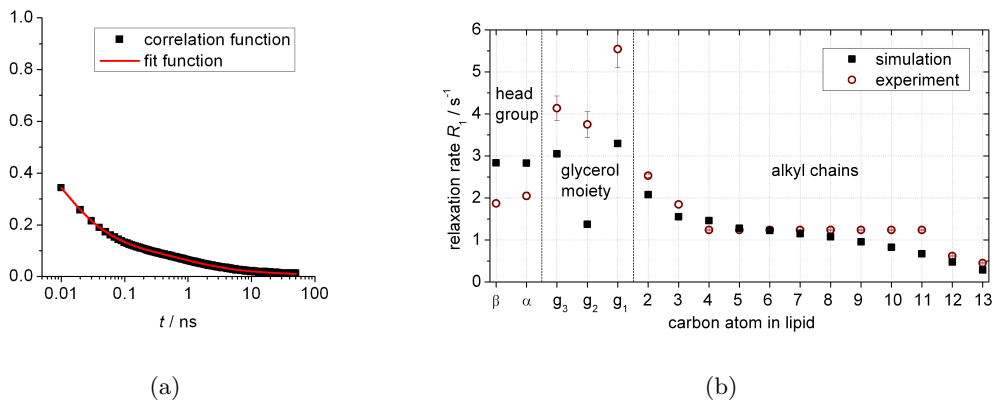


Figure 22: Results from simulations of a DMPC bilayer in water: (a) Correlation function describing the reorientational motion of the C-H bond of carbon 5 which is located in the middle part of the lipid acyl chain; (b) R_1 relaxation rates determined for the different positions in the lipid molecule in comparison with experimentally determined values already shown in Figure 12(b) in Section 5.4.

Besides the order parameter, we also determined R_1 relaxation rates from the simulated systems [83,87]. For this, we calculated the second rank reorientational correlation function given in Equation 53 in Section 4 by using the GROMACS command *rotacf*. As slower motions with correlation times much longer than nanoseconds do not contribute significantly to R_1 , a trajectory of about 200 ns usually is long enough. Subsequently, a multi-exponential decay function was

fitted to the correlation function using the order parameters calculated in the last section as plateau value (see Figure 22(a) for an example). From the fit function, we determined the relaxation rates as explained in Section 5.4.

As it can be seen in Figure 22(b), the resulting R_1 values generally match the experimental data quite well. Similar as for the order parameter, the largest differences between relaxation rates from experiment and simulation occur for the choline group and the glycerol backbone.

7 Lipid Bilayers and Amphiphilic Triblock Copolymers

In the following section, NMR investigations and MD simulations of phospholipid bilayers in interaction with amphiphilic block copolymers will be presented. Numerous studies can be found in literature describing the influence of polymer structure and outer conditions on the interaction with the lipid membranes [13, 60, 169, 170]. Here we consider linear triblock copolymers consisting of a lipophilic middle block in-between two hydrophilic end blocks.

7.1 Amphiphilic Triblock Copolymers

Ploxamers, also known under the commercial names Pluronic or Synperonic, are triblock copolymers composed of a hydrophobic Poly(Propylene Oxide) (PPO) middle block and two hydrophilic Poly(Ethylene Oxide) (PEO) end blocks (see Figure 23(a)). They were investigated intensively in literature with regard to their behavior in water or in interaction with lipid bilayers [171–173].

Pluronics exhibit many properties advantageous for their use in research and their application. They are surface active, nonionic and noncytotoxic. Being synthesized routinely via anionic addition polymerization [171], Pluronics are commercially available with a series of different block lengths which strongly influence the sample properties. Their molecular weights can range from 1100 to 14000 kg/mol and their PEO:PPO weight ratio from 1:9 to 8:2 [173, 174]. Pluronics can occur as liquids, pastes or solids.

Exploiting their interaction potential with lipid membranes, Pluronics find numerous applications, for example in medicine, pharmacy or cosmetics. Hydrophilic Pluronics can help healing wounds caused by thermal burns, frostbite or electrical shock [1, 2]. As one example, the Pluronic P188 incorporates in damaged membranes, restores the membrane integrity and subsequently is squeezed-out again leaving an intact membrane behind [173–175]. Drug delivery systems represent another important field of application. Polymer micelles can allow for drug solubilization and controlled release [176–178]. It was also suggested to use Pluronics for the preparation of sterically stabilized liposomes for drug delivery [13, 66]. Certain Pluronics help to overcome the multidrug resistance of cancer cells. These polymers accelerate the drug permeation through the membrane, impede the action of efflux proteins, like the P-glycoprotein and as a result increase the cytotoxic activity of anticancer agents, like doxorubicin [60, 169, 172, 178–180]. Sensitive cells, however, are only weakly influenced by the Pluronics. The anticancer agent SP1049C developed for the treatment of multi-drug resistant cells contains doxorubicin and the Pluronics L61 and F127 [3].

Properties and phase behavior of the Pluronics in water are drastically influenced by the hydrophobicity of the individual polymer blocks. Due to the additional oxygen atoms in the chain, the PPO block is less hydrophobic than for example an alkyl chain, rendering the entire copolymer water-solvable at low concentrations. At low temperatures, also pure PPO is solvable in water [13, 181]. It gets more unpolar and dehydrates with increasing temperature until the cloud point is reached at about 10–15 °C. At higher temperatures, PPO can be assumed to be hydrophobic as it segregates in water [181]. In contrast, PEO is water solvable over a broad temperature range of 0 - 100 °C [181]. Nevertheless, also the hydrophobicity of PEO rises with increasing temperature which can be explained by the destruction of a hydrogen bond network

between PEO and water or, alternatively, by the preference for more apolar conformations at higher temperatures [7, 171, 182, 183]. An inverse temperature dependence of the Pluronic solubility in water is the overall consequence, that is, with increasing temperature Pluronics become less solvable which results in the self-assembly into a variety of structures [181, 184].

Pluronics with PEO blocks that constitute more than roughly 20% of the molecular weight of the entire copolymer form micelles [181] which have hydrophilic PEO corona and a core mainly containing the hydrophobic PPO blocks but also some PEO units [182]. Due to the gradual change of the polymer hydrophobicity with temperature and partly also due to polydispersity and impurities, the micellization is not a sharp transition, but stretches over a wide temperature or concentration range [171, 173, 181, 182]. Consequently, using different measurement methods, like surface tension measurements, scattering techniques, calorimetry, viscosimetry or diffusion measurements, different values for the cmc are detected varying by up to 10 orders of magnitude [171, 178]. Some Pluronic solutions of higher concentration exhibit a thermoreversible gel transition associated with the aggregation of the micelles and changes of their structure [171, 181, 182]. Also hexagonal, cubic or lamellar liquid-crystalline phases can form in some cases [171, 181, 182, 184, 185]. At higher temperatures, phase separation occurs which causes clouding of the solution [182, 185].

By modification of individual polymer blocks, specific changes of polymer properties can be induced and the interaction of the polymer with other molecules like the lipids in a membrane can be tuned. For example, copolymers containing hyperbranched polyglycerol as hydrophilic block show more pronounced effects on membranes than block copolymers with linear PEO blocks [60]. Also polymers with different hydrophobic middle blocks, like polystyrene (PS) instead of PPO, were investigated in interaction with lipid bilayers [186].

Here, we studied a triblock copolymer, with Poly(Glycerol MonomethAcrylate) (PGMA) blocks replacing the PEO-blocks (see Figure 23(b)) [187] for which we use the short name GP. They were synthesized by the atom transfer radical polymerization technique [187]. Like the Pluronics, also GPs form different structures in water like unimers, unimer-aggregates and micelles which possibly coexist over a wide range of temperatures and concentrations [187].

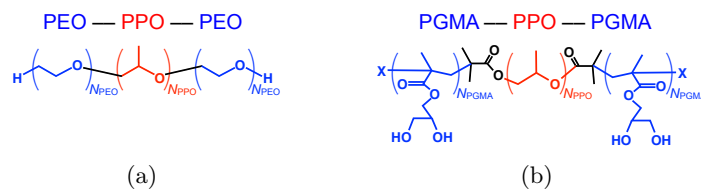


Figure 23: Chemical structures of the amphiphilic triblock copolymers (a) Pluronic and (b) GP. The hydrophilic blocks are depicted in blue and the hydrophobic blocks in red.

7.2 Polymers Interacting with Lipid Bilayers

For the mode of interaction of the triblock copolymers with the lipid membranes different possibilities can be imagined. Due to the hydrophobic effect, the hydrophobic PPO block preferentially penetrates inside the lipid bilayer, while the hydrophilic parts are located at the surface where they interact with the hydrophilic membrane head group layer and are in contact

with water.

Polymers with a very short hydrophobic PPO block can only reach to a short distance into the bilayer core [14]. On the opposite, very long PPO blocks can insert deeply into the membrane and assume there different conformations. For example, they could coil up forming compact cylinders or they could lay in-between the two lipid leaflets as shown in Figures 24(a) and (b), respectively. Investigations from Baekmark et al. on a lipid bilayer system interacting with a PEO-PS-PEO copolymer lead to the conclusion that a PS block, twice as long as the hydrophobic bilayer thickness, most probably does not form a compact structure but is located partly in-between the two bilayer leaflets thereby causing least disturbances of the lipids [186]. Also Rossi et al. found from simulations that longer hydrophobic polymers incorporated in lipid membranes are located preferably close to the center of the membrane [188].

Polymers with hydrophobic PPO blocks of a length exceeding the 3 to 4 nm hydrophobic thickness of the bilayer [33] can assume a membrane-spanning configuration with the two PEO blocks located at opposite sides of the membrane (see Figure 24(a)). From experiments and simulations, a minimal PPO block length of 30 [40,189] or 40 units [13,14,190,191] was determined depending on the specific system used. Polymers with shorter PPO blocks fold to incorporate from one side into the membrane as shown in Figure 24(b).

Additional to the PPO block length, also the lengths of hydrophilic block, the hydrophobicity of the whole polymer and the way of sample preparation influence the way of incorporation [14,16,18,60,191–195]. Many experimental and simulation-based investigations were conducted to determine which configuration is the preferred one. However, a conclusive solution was not found. Depending on the specific sample system, both, the membrane-spanning and the U-form configuration were detected [66,186,190,196] and also transitions are possible [197]. A detailed computational study was done by Rabbel et al. [197] who determined the free energy difference between the transmembrane and the hairpin configuration from Monte-Carlo simulations on a coarse-grained model where they varied the hydrophobicity (which depends on the temperature) and the length of the polymer middle block. When it is too short or when its hydrophobicity is too small then the entire polymer is desorbed from the bilayer. The membrane-spanning configuration is preferred for polymers with middle blocks exhibiting a certain minimum hydrophobicity that are just long enough to span the membrane but would not reach far into the hydrophobic bilayer core in hairpin configuration. The hairpin mode only gets preferred for longer blocks. For long and strongly hydrophobic middle blocks, both configurations exhibit the same free energy, that is they are equally probable.

Furthermore, polymer aggregation inside the membrane is possible [180,191,198,199], which could lead to the formation of defective areas making the membrane more permeable [179]. For example, Frey et al. found lipid-rich, polymer-rich and mixed regions in fluorescence microscopy images of DPPC in mixture with various Pluronics and from their MC simulations using a coarse-grained model, a lipid corralling effect of the polymers was seen [16].

Like the polymer configuration, also the amount of polymer that is incorporated into the membrane depends on the polymer structure and outer conditions. Bryskhe et al. only found a very small miscibility of the lipid soybean lecithin and the Pluronic L121 concluding that the two substances generally form separated phases and only a small amount of the polymer is incorporated in the lipid bilayer independently of the sample preparation method [200]. Also Krylova et al. determined an extremely low affinity of the Pluronic L61 to egg yolk lecithin

vesicles, which nevertheless influences the bilayer properties [179]. Other groups, however, got different results. For a similar system of egg yolk lecithin and L61, Zhirnov et al. determined, that about half of the Pluronic L61 binds to liposomes [201]. Hädicke et al. additionally found out that Pluronics only incorporate effectively in lipid membranes when their cmt value is higher than the lipid phase transition temperature T_m allowing polymer unimers to interact with the membrane in the liquid-crystalline phase [202].

Besides the lipid bilayers with polymers incorporated, also other aggregates like polymer micelles, mixed micelles containing polymers and lipids or bilayer patches can exist [202].

For the GPs, we generally expect similar ways of interaction with the membrane as for the Pluronics. However, also differences can occur because PGMA has a higher propensity to act as hydrogen bond donor and acceptor and additionally is more bulky than PEO and could therefore cause a stronger disturbance of the membrane [11].

As the polymers can associate with the lipid membranes in various ways, they also can have different influence on membrane properties. Pluronics of relatively high hydrophilicity have long PEO blocks that adsorb to the membrane surface and therefore can protect or seal the membrane [13, 18, 190, 203] and sterically stabilize it [190]. In contrast, more hydrophobic polymers with short PEO blocks and a longer PPO middle block tend to increase the membrane permeability and also can accelerate the lipid flip-flop motion possibly because the PPO blocks cause disturbances of the membrane and also because the Pluronics can act as carriers transporting lipids through the membrane [60, 66, 179, 180, 189, 194, 203–206]. On the opposite however, Nawaz et al. claim, that due to hydrophobic interactions with the lipid tails, the PPO block stabilizes the membrane while the short PEO chains cause structural defects [189]. Rabbel et al. concluded from their MC simulations that both copolymers in the transmembrane state and copolymers in U-form can increase or decrease membrane permeability depending on the hydrophilicity of the polymer middle block [197].

As a follow-up of previous work done on lipid bilayer/GP systems [11, 144], we here seek to investigate the specific configuration of different polymers inside a number of phosphatidylcholine membranes with variable bilayer thickness and acyl chain saturation using a combination of NMR techniques and MD simulations.

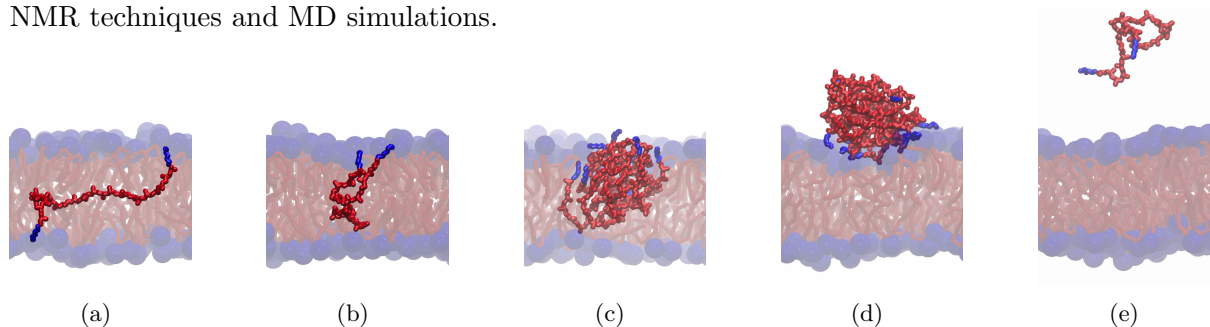


Figure 24: Possible configurations of a polymer in interaction with a lipid bilayer: (a) membrane-spanning configuration with parts of the polymer PPO block being located in-between the bilayer leaflets, (b) U-form configuration with the PPO block coiled up, (c) U-form configuration of a few polymers that form an aggregate in the membrane, (d) polymer aggregate attached to the membrane surface, or (e) single polymer that does not interact with the membrane. The lipid headgroups are represented by blue balls and the acyl chains as red lines. Also for the polymer, the hydrophilic parts are drawn in blue and the hydrophobic parts in red. The color scheme will also be used in the following Figures showing snapshots of simulated trajectories.

7.3 Samples

In this work, we investigated a number of different mixtures of the lipids DPPC, DMPC, DLPC and DOPC and various Pluronics and GPs, characteristics of which are given in Tables 2 and 3. The Pluronics PE3100 (EO₁-PO₁₅-EO₁), PE3500 (EO₁₁-PO₁₆-EO₁₁), PE4300 (EO₆-PO₂₁-EO₆), PE6100 (EO₂-PO₃₀-EO₂) and PE8100 (EO₃-PO₄₀-EO₃) are denoted as given by BASF. The first digit of the number is characteristic for the molecular weight of the polymer PPO block and the second digit multiplied by ten approximately equals the weight fraction of PEO in the entire polymer.

Considering the explanations of the last section, only the polymer PE8100 and possibly also PE6100 have a PPO block long enough to span a lipid membrane. Furthermore, as all the Pluronics investigated are rather hydrophobic, they should not be able to seal or stabilize the membrane but instead increase their permeability. Also due to the high hydrophobicity, Pluronics like PE6100 exhibit a low solubility and a small cmc value. They do not form micelles but “crew-cut” aggregates that can agglomerate and coexist with unimers [205]. For a 20:1 mixture of DMPC and PE6100 with a water content of 50 wt%, we calculate a concentration of $c = 0.071$ mol/L for the polymer in water when we assume that the lipid bilayers form a phase separated from the polymer-in-water phase that is located in-between the bilayers. This concentration lies well above the cmc of PE6100 of $1.1 \cdot 10^{-4}$ mol/L.

polymer	N_{PPO}	N_{PEO}	$M_w / \text{g/mol}$	PD	cmc / mol/L [169]
PE3100	15	1	1000	1.44	N/A
PE3500	16	11	1900	1.59	$5.3 \cdot 10^{-3}$
PE4300	21	6	1750	1.55	$2.2 \cdot 10^{-3}$
PE6100	30	2	2000	1.55	$1.1 \cdot 10^{-4}$
PE8100	40	3	2600	1.50	$2.3 \cdot 10^{-5}$

Table 2: Pluronic samples: the block lengths N_{PPO} and N_{PEO} , which can vary by about monomer unit, and the molecular weight M_w are given by BASF. The polydispersity PD was measured by gel permeation chromatography by M. Jbeily. The cmc values are taken from literature.

Besides the Pluronics, we also investigated the three polymers GP12 (GMA₂₀-PO₁₂-GMA₂₀), GP17 (GMA₂₀-PO₁₇-GMA₂₀) and GP34 (GMA₂₀-PO₃₄-GMA₂₀) in interaction with lipid membranes. These polymers have identical hydrophilic end blocks and a hydrophobic middle block of varying length. While GP34 has a PPO block possibly long enough to span the membrane, GP12 and GP17 are not expected to enter the membrane deeply.

polymer	N_{PPO}	N_{PGMA}	$M_w / \text{g/mol}$	PD
GP12	12	20	7500	1.2
GP17	17	20	7700	1.3
GP34	34	20	8600	N/A

Table 3: GP samples: The polymers were synthesized and characterized by the Physical Chemistry of Polymers Group of the Martin-Luther-University Halle-Wittenberg.

7.4 Polymer and Lipid-Polymer Systems Simulated

For the simulation of the lipid/polymer systems, we used the same set-up for the lipid membrane as described in Section 6.1. Each leaflet of the bilayer consists of 64 lipids and the membrane is surrounded by about 600 water molecules. The force field for the polymer molecules was built in accordance with the force field by A. Goliaei et al. [207] with a slight modification to get PEO blocks terminated by only one proton each. The atactic PPO block of the real samples was modeled to be syndiotactic.

To validate the polymer force field, two systems of a single polymer in water were simulated. With the first system, the molecular dynamics were checked. The polymer PE3500 was chosen because of all Pluronic samples investigated here, it exhibits the highest cmc which makes it easier to produce a solution of unimers experimentally that is comparable with the simulated system. In Figure 25 three snapshots of the simulation are shown. The polymer tumbles isotropically in solution with rapidly changing conformations. As a second system, the considerably bigger Pluronic P85 (EO₂₅-PO₄₀-EO₂₅) in water was investigated with regard to the molecular structure. The size of the polymer coil in solution can be defined by radius of gyration R_g which is given by

$$R_g^2 = \frac{2}{N^2} \sum_{n,m=1}^N \langle (\mathbf{r}_n - \mathbf{r}_m)^2 \rangle. \quad (84)$$

The indices n and m count all atoms of the polymer, N is the total number of atoms in the sample and the vectors $\mathbf{r}_{n,m}$ describe the atom positions. The average over all time steps is taken. From the simulation, a value of $R_g = 1.56$ nm using a trajectory of 240 ns was determined. This value compares well with experimental and simulation results of about 1.4 to 1.8 nm [207, 208].

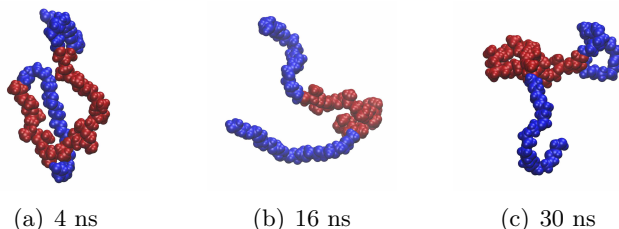


Figure 25: Snapshots from simulation of PE3500 in water at the simulation time indicated.

In the following, the different lipid/polymer systems simulated will be introduced. The lipid (DMPC, DPPC), the polymer (PE3100, PE6100) and the polymer configuration were varied.

Membrane-Spanning: Firstly, a system of six polymers incorporated in membrane-spanning configuration in the lipid bilayer was investigated. The total lipid-to-polymer molar ratio amounts to 21.3 in this case. The system will be referred to as “membrane-spanning” in the following. It was simulated for the three combinations DMPC and PE6100, DMPC and PE3100 and DPPC and PE6100. Only results for the DMPC/PE6100 system are shown in this section since the other systems behave in a similar way.

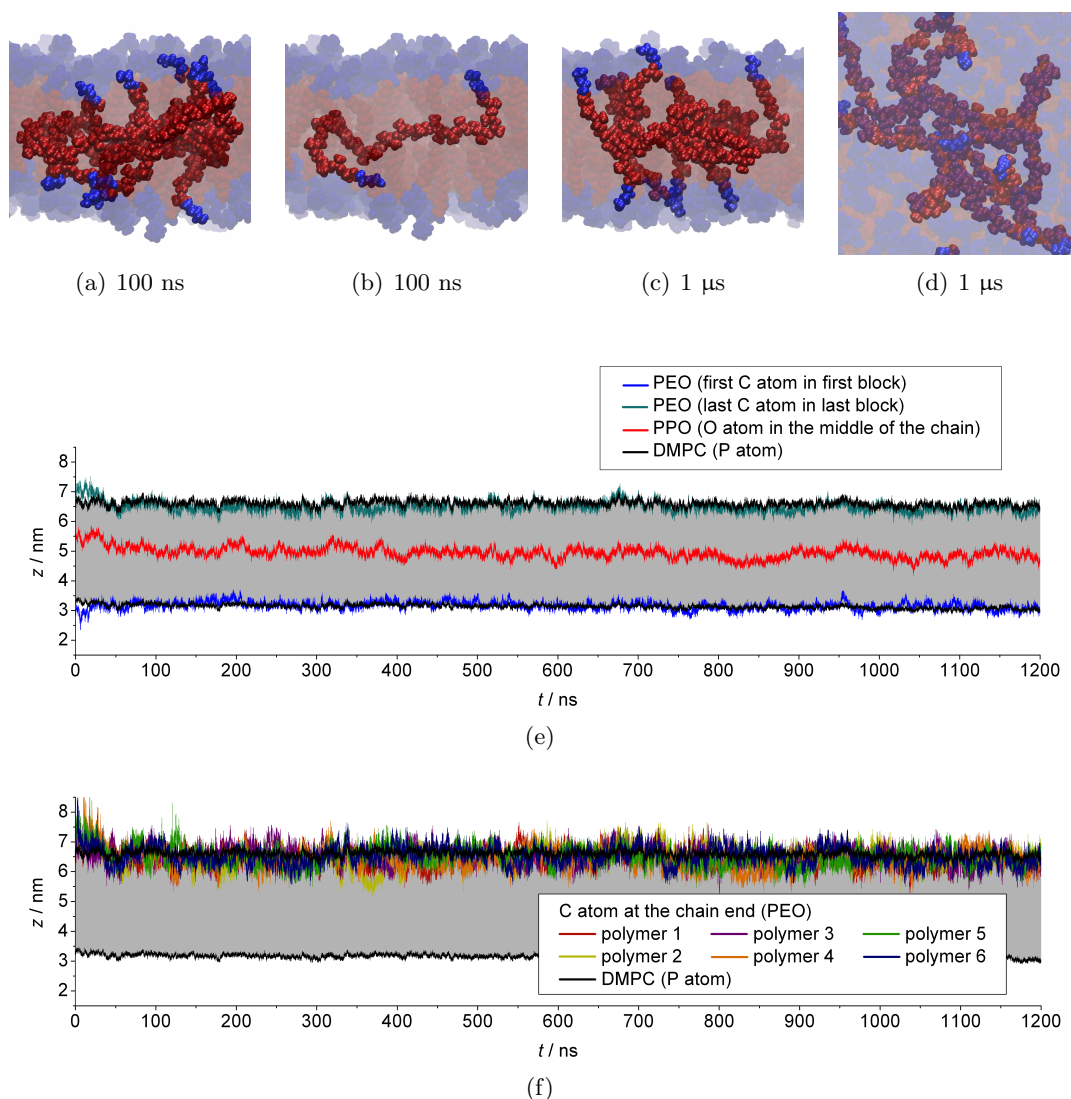


Figure 26: Six polymers PE6100 in membrane-spanning configuration spread homogeneously in a DMPC bilayer: (a), (b) snapshots (side views) taken after a simulation time of 100 ns, whereby only one of the six polymers is shown in (b) so that the membrane-spanning configuration is clearly visible; (c) snapshot (side view) taken after a simulation time of 1 μ s and (d) the corresponding top view; (e) z -coordinates of certain polymer C atoms and an O atom averaged over all polymers together with the position of the lipid bilayer in z -direction represented by the grey area; and (f) z -coordinate of the last C atom at one end of the polymer chain plotted for all polymers separately together with the bilayer position.

For the starting configuration, the polymers were put in the membrane slightly separated from each other, fully stretched and aligned parallel to the bilayer normal. After energy minimization, the polymer chains are partly coiled so that the polymer PEO blocks are situated in the bilayer head group region while the hydrophobic PPO block is incorporated completely into the bilayer acyl chain region. The resulting system after a simulation time of 100 ns and 1 μ s is shown schematically in Figure 26(a) - (d).

To demonstrate that all chains stay in membrane-spanning configuration during the whole

simulation time of 1.2 μs , the time-dependence of the z -coordinate describing the position of certain polymer atoms are plotted together with the average coordinate of the lipid phosphorous defining the edges of the bilayer. More precisely, in Figure 26(e), we can see curves for the z -coordinates of a C-atom at one end of the polymer chain, an O-atom in the chain middle and another C-atom at the other end of the chain. For this, the average over all polymers was taken. In the beginning of the trajectory the polymer chains still seem to be slightly stretched. However, after 50 ns the carbons of the PEO blocks are on a similar position as the lipid phosphorous atoms indicating that the PEO blocks are incorporated in the lipid head group region. The oxygen in the middle of the PPO block stays in the bilayer center during the whole simulation time.

Additionally, in Figure 26(f), the z -coordinates of one chain end are shown for all polymers separately demonstrating that they all behave the same. For the calculation of order parameters and relaxation times given in later Sections, the trajectory was analyzed from $t = 50$ ns onwards.

Single Polymer in U-form: Secondly, a system of a single polymer incorporated in U-form in the lipid bilayer was investigated. It will be referred to as “single polymer in U-form” and was set-up for the mixtures of DMPC and PE6100, and DMPC and PE3100. As both systems showed a similar behavior, we will again only present results for DMPC/PE6100 in this section.

In the initial step, the polymer chain was put on top of the bilayer. It then quickly associated

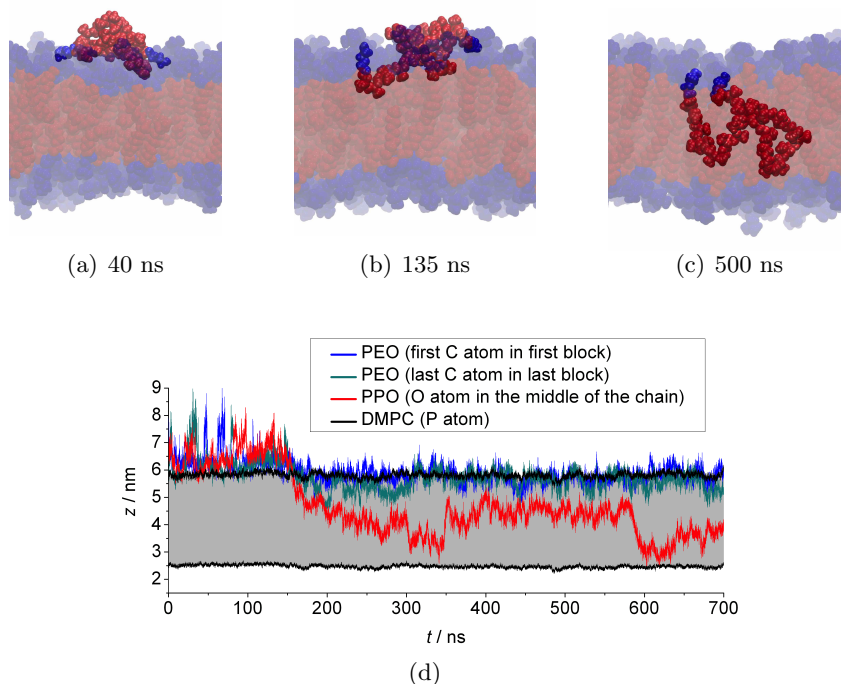


Figure 27: Single polymer PE6100 in interaction with DMPC bilayer: (a)-(c) side view at different simulation times; (d) z -coordinates of certain polymer atoms together with the position of the lipid bilayer (grey area) in z -direction. The polymer, originally placed on top of the membrane, enters the bilayer at about 130 ns and stays deeply incorporated in U-form until the end of the simulation.

with the lipid head groups. After about 130 ns simulation time, the polymer PPO block started to enter the hydrophobic bilayer region and after about 230 ns it was deeply inserted while the two PEO blocks stayed in the headgroup region at the same side of the bilayer. This polymer configuration remained stable until the end of the simulation.

The entire incorporation process is depicted in Figure 27. Snapshots of the system are shown in (a)-(c). In a similar way as already introduced for the “membrane-spanning” system, the polymer position with respect to the bilayer was determined by means of the z -coordinates of three atoms in the polymer chain. The result is depicted in (d) showing in detail the incorporation of the center of the PPO block (represented by the red line) in the lipid bilayer (grey area) over time.

Our observations are compatible with simulation results from literature, where the build-in of a polymer in a membrane is usually described as a two-step process [18, 175, 191, 203]. In the first step, the polymer adsorbs to the membrane surface making contact with lipid head groups and in the second step, the polymer inserts completely into the membrane. This way of incorporation was also confirmed experimentally [198]. For more hydrophilic Pluronics, however, the build-in is expected to take very long, so that the polymer basically stays on top of the membrane.

From the polymer coordinates shown in Figure 27(d), it also can be concluded, that after built-in, the polymer stays in U-form during the rest of the simulation time. Flips of the PEO blocks to the other side of the bilayer do not occur. This behavior is in accordance with literature [191] and can be explained by the high barrier created by the hydrophobic lipid hydrocarbon region.

For comparison with order parameters and relaxation times determined from NMR experiments, the trajectory of the “single polymer in U-form” system was analyzed from 250 ns onwards when the polymer is well incorporated into the lipid bilayer.

Six Polymers in U-form: As a third system, six PE6100 polymers build-in a DMPC bilayer in U-form were investigated. The system will be referred to as “six polymers in U-form”.

Initially, three of the polymers were placed above and three below the bilayer in the water phase. The following incorporation process is depicted in Figure 28. In (a)-(f) snapshots from the simulation are shown and in (g)-(i) the position of certain atoms in the polymer chains with respect to the lipid bilayer can be seen. In the beginning, four polymer molecules associate with each other and with the lipid head groups on top of the bilayer and two polymers attach together to the bottom of the bilayer. Due to the periodic boundary conditions, the polymers can approach the bilayer from both sides. After about 200 ns the two polymer groups start to connect to each other and after about 230 ns the two lower polymers desorb again from the bilayer bottom, so that at 250 ns a single, nearly spherical polymer aggregate is situated on top of the lipid bilayer in contact with the lipid head group region. This aggregate starts entering the bilayer at about 330 ns until it is completely incorporated at about 450 ns. During the polymer build-in, the size of the simulation box increases slightly by about 0.4 nm. Subsequently, the polymers start to separate from each other until they are distributed roughly homogeneously over the whole bilayer. During the entire simulation time, they keep the U-form configuration.

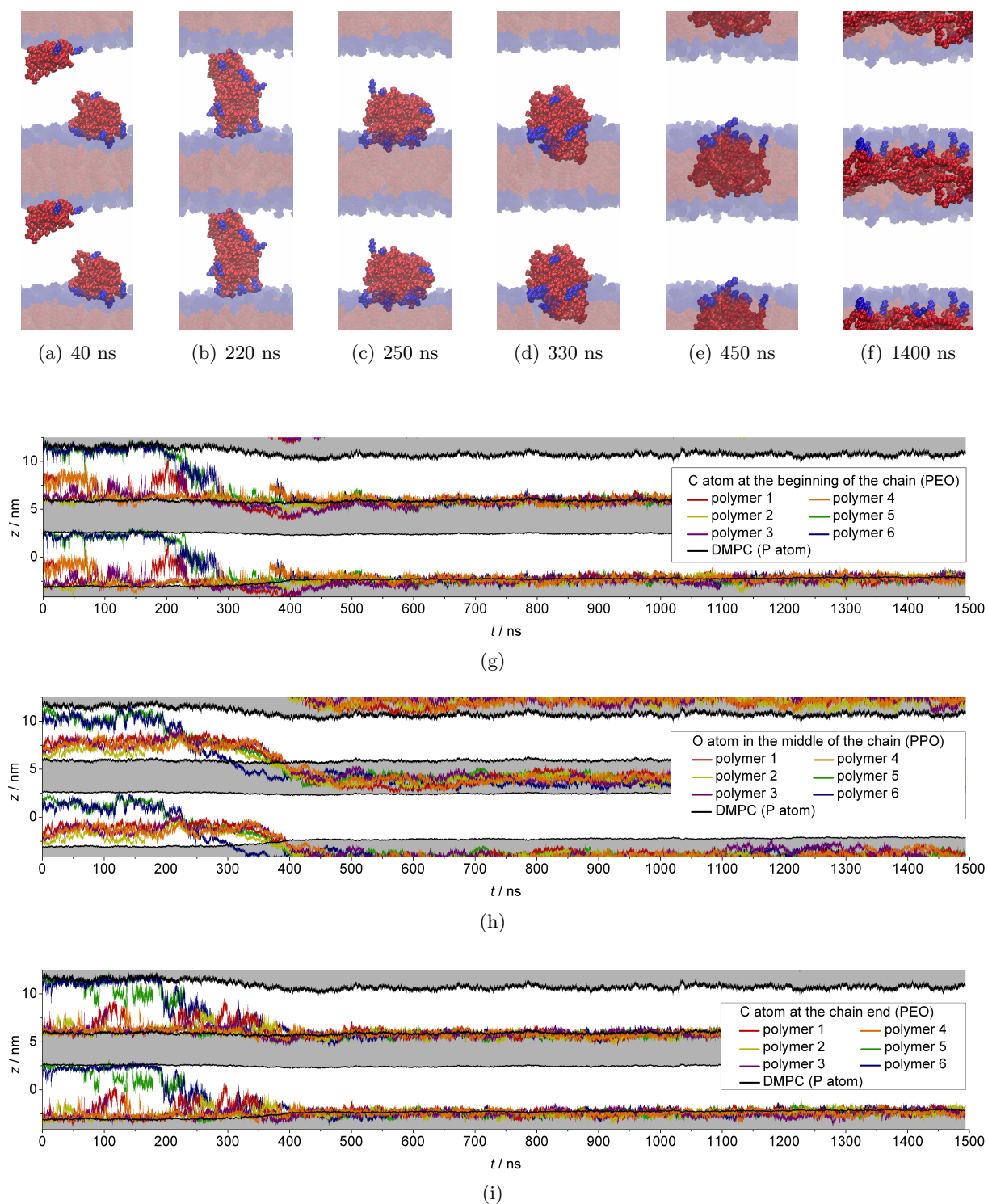


Figure 28: Six PE6100 polymers interacting with DMPC bilayer: (a)-(f) snapshots (side view) at different simulation times; (h)-(i) z -coordinates of two C-atoms on opposite chain ends and the center O-atom of the PPO block in comparison with the position of the lipid bilayer (grey area). The polymers enter the membrane in U-form as an aggregate and subsequently distribute homogeneously over the bilayer.

To investigate the dispersion process in more detail, the average distance in the x - y -plane between the polymer molecules over time was determined. In every time step, the x and y coordinates of a specific C atom were picked for every polymer. The z -components were neglected. Taking the periodic boundary conditions into account, all distances between the six C atoms were determined and averaged. The whole procedure was repeated for another nine carbons along the polymer chain and the total result was then calculated as the average over all ten values. In Figure 29 the time-dependent curve determined for the system is shown in comparison with the curve determined in the same way for the “membrane-spanning” system, for which we expect a homogeneous distribution of the polymers. Accordingly, it can be seen that the average distance between the polymers has a relatively stable value over the entire simulation time. For the “six polymers in U-form” system however, the average distance between the polymers increases after the aggregate incorporated in the membrane indicating that the aggregate dissolves. For simulation times greater than 700 ns, the curve roughly reached the value of the curve of the “membrane-spanning” system indicating that from this time on the polymers are distributed roughly homogeneously over the bilayer.

These observations, however, are not in accordance with results from literature. Using coarse-grained MD simulations, Hezaveh et al. found out that PPO blocks of different Pluronics aggregate in a DMPC bilayer [191]. Also Pembouong et al. concluded from MD simulations which were applied in combination with ^1H NMR experiments that PPO blocks of the Pluronic L64 in membrane form clusters [199].

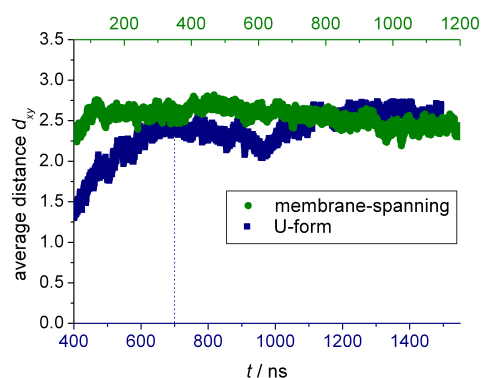


Figure 29: Average lateral distance d_{xy} between the polymer chains calculated as described in the text. The upper time axis belongs to the results from the “membrane-spanning” system shown in green and the downer axis gives the time scale of the “six polymers in U-form” system (results shown in blue). A small d_{xy} as determined for the “six polymers in U-form” system at a simulation time of about 400 ns indicates polymer aggregation. The “membrane-spanning” system, in contrast, exhibits homogeneously distributed polymers over the whole simulation time.

Order parameters and relaxation times for the system “six polymers in U-form” were calculated using the trajectory from 700 ns onwards.

Aggregate on Top of Membrane: The last system investigated consists of an aggregate of six PE6100 polymers on top of a DMPC bilayer. It will be referred to as “aggregate on top of membrane”. To create this system, the polymer molecules were allowed to self-assemble in the water phase. Afterwards the resulting polymer aggregate was placed above the lipid bilayer. It directly attached loosely to the bilayer head group region. In contrast to the previous system, the polymers did not enter deeply into the membrane, but stayed on top of the bilayer during the entire simulation time of 600 ns.

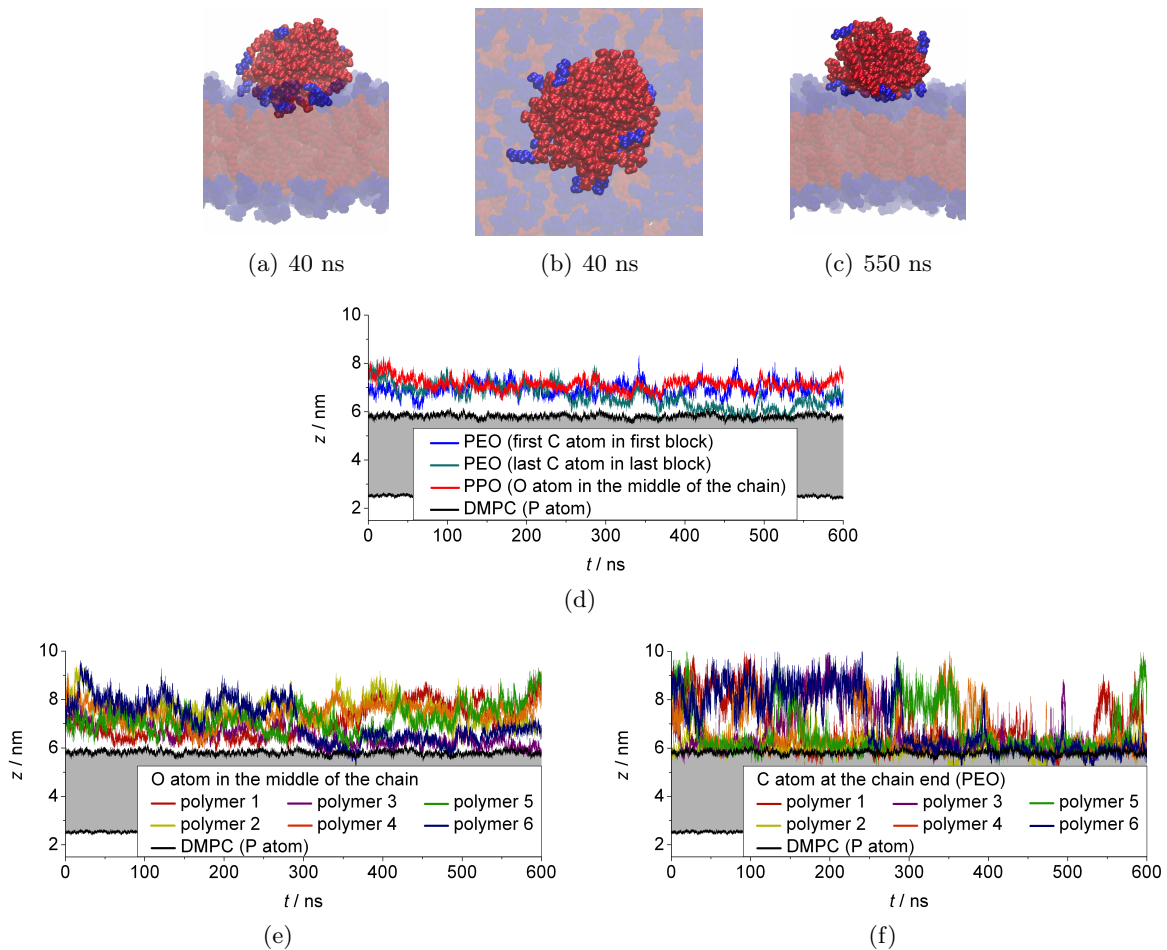


Figure 30: Six polymers PE6100 on top of DMPC bilayer: (a)-(c) snapshots (side views and top view) taken at different simulation times; (d)-(f) z -coordinates of certain polymer atoms, which stay located on top of the lipid bilayer (grey area) for the entire simulation time indicating that the polymers do not enter the lipid bilayer.

The simulation snapshots in Figure 30(a)-(c) show the polymer aggregate which exhibits a roughly spherical form on top of the membrane. In Figure 30(d), it can be seen from the z -coordinates of specific polymer atoms, that during the whole simulation time all polymer chains stay positioned on top of the bilayer. The single PEO blocks only attach temporarily to the lipid head group region while the PPO blocks mostly do not show direct contact with the bilayer (see Figure 30(f) and (e) respectively). However, with regard to the other systems simulated, we believe that the polymer aggregate on top of the bilayer does not resemble a stable state of the system but that the polymers would enter the membrane after an even longer simulation time.

Also in literature, the interaction of polymer micelles with lipid bilayers was investigated. Hezaveh et al. and Adhikari et al. found out that the build-in of a polymer micelle is more complicated and time-consuming than the incorporation of a single polymer molecule into a lipid membrane [175,191] which is in accordance with our results.

Data analysis to compare with NMR results for order parameters and relaxation times was done from a simulation time of 50 ns onwards.

7.5 DSC Results

For a general overview about the phase behavior of the different lipid/polymer systems depending on temperature, we performed Differential Scanning Calorimetry (DSC) measurements. Basically, a calorimeter consists of a sample cell containing the lipid system to be investigated and a reference cell that only accommodates the solvent (water) [7,10]. Both cells are simultaneously heated (upscan) or cooled (downscan) with constant rate. By permanently adjusting the heating power, the temperature difference of the two cells is kept zero at all times during this process. Meanwhile, the differential heat is recorded as function of temperature. It is proportional to heat capacity Δc_p . Deviations from the baseline indicate that a thermally-induced event is happening in the sample system.

For our measurements we used a Microcal VP-DSC to record DSC curves with a heating rate of $1^\circ\text{C}/\text{min}$. At least three up and down scans were performed for each mixture until the curves did not change anymore. For baseline correction, we additionally recorded the DSC curve of pure deuterated water and subtracted it from the DSC curves of our lipid samples. An additional cubic baseline correction was performed for the determination of peak areas.

While we use samples of 50 wt% water for the NMR measurements, the DSC experiments were conducted using distinctly more dilute solutions with a lipid concentration of 1 mmol/L. Nevertheless, the different sample systems should be comparable as complete hydration is present in both cases although the polymer may have an effect on the limit for excess water.

In Figure 31, a typical DSC curve for a phospholipid in water sample is shown. Two peaks are visible. The small and broad peak at lower temperature belongs to the pretransition and the second sharp and strong peak indicates the main phase transition which is a transition of first order. The position of the peak maximum is defined as the phase transition temperature T_m , the peak width $\Delta T_{1/2}$ is a measure for the cooperativity of the transition process and the area underneath the peak represents the enthalpy of transition ΔH . From this, the transition entropy $\Delta S = \frac{\Delta H}{T}$ can be calculated because for first-order phase transitions, the change of free energy equals zero ($\Delta G = \Delta H - T\Delta S = 0$) at the center of the phase transition. For DMPC, the pretransition appears at about 16°C and the main transition at about 24°C (see Figure 31). For the enthalpy of the main phase transition, we determine $\Delta H_m \approx 23\text{kJ}/\text{mol}$ and for the entropy $\Delta S_m \approx 78\text{J}/(\text{mol K})$. All values are in accordance with literature results [9].

It is also known from literature, that samples of pure Pluronics in water show a broad endothermic peak that reflects the process of micellization [171, 184, 202, 209]. The heat of micellization is caused by the dehydration of the PPO block [184]. The peak position defines the cmc. In accordance with this, we measured a DSC curve (see upmost curve in Figure 33(a)) with a very broad endothermic peak stretching from about 20°C to about 60°C for a sample of PE6100 dissolved in deuterated water at a concentration of 1 mmol/L.

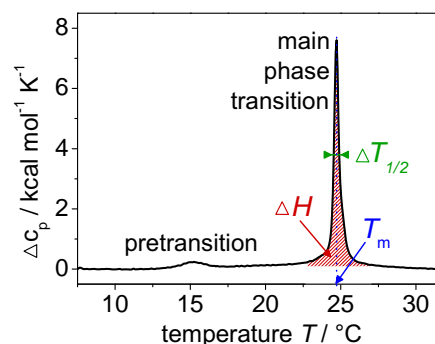


Figure 31: DSC thermogram for DMPC.

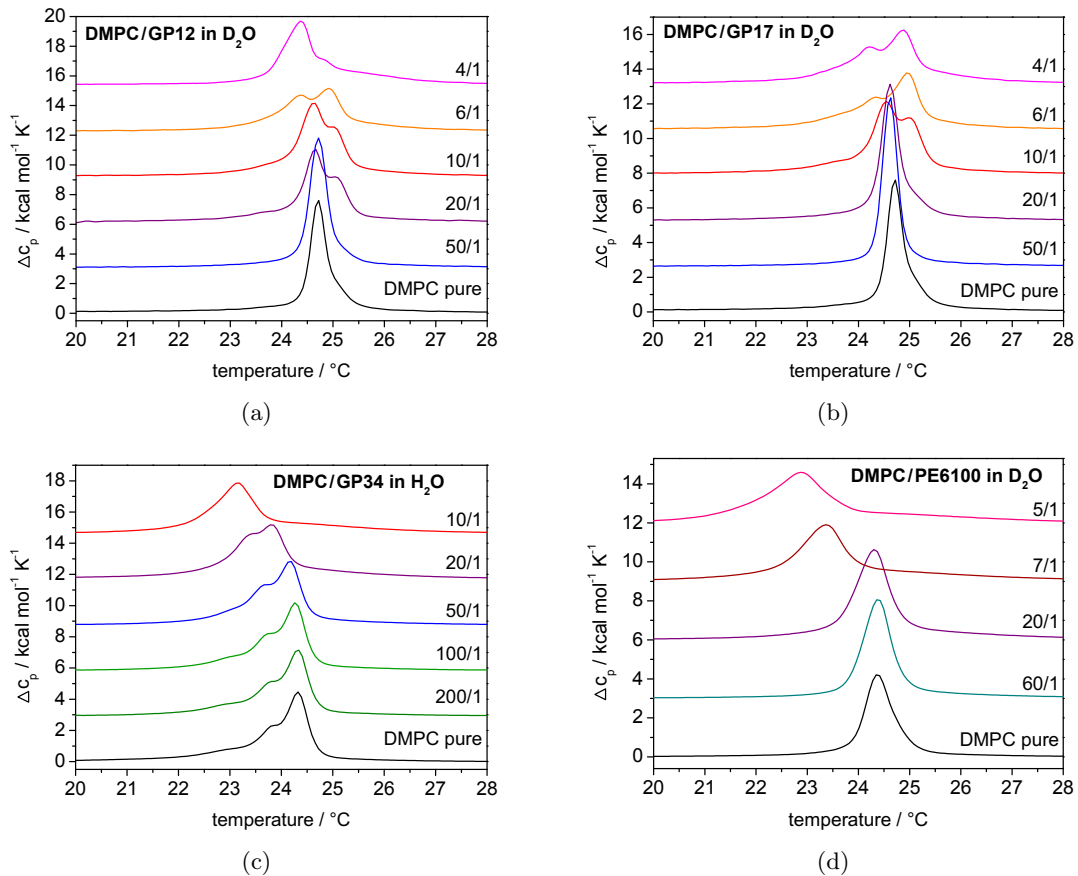


Figure 32: DSC curves recorded for mixtures of different ratios of (a) DMPC/GP12, (b) DMPC/GP17, (c) DMPC/GP34 (data from [11]) and (d) DMPC/PE6100.

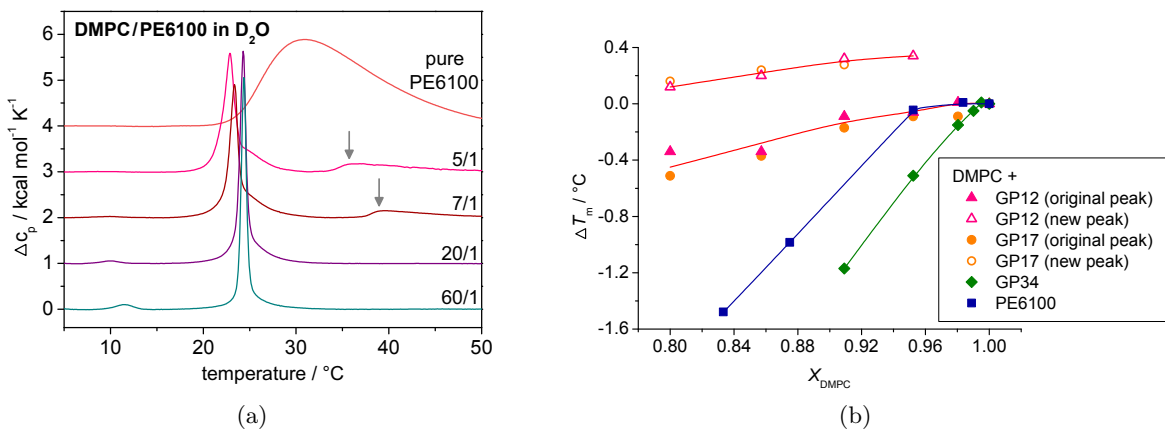


Figure 33: (a) DSC curves of the mixtures of DMPC and PE6100 shown on a larger temperature scale than in Figure 32(d); and (b) temperature difference of the melting peak positions from pure DMPC and from the four triblock copolymer mixtures depending on the molar ratio X_{DMPC} of lipid in the mixture.

Also DSC curves of different lipid/Pluronic mixtures are given in a number of literature sources. As a general result it was found that with rising polymer concentration, the main phase transition broadens [13, 199, 205, 209] while depending on the sample system the melting

temperature T_m decreases [199, 205, 209] or nearly remains constant [13, 205]. For a system of DPPC and L121 (EO₅-PO₆₈-EO₅), mainly separated phases were detected and consequently, the DSC phase transition peaks in the mixture are nearly identical to the ones in the pure samples [200].

Here, we performed DSC measurements for different mixtures of DMPC and the polymers GP12, GP17, GP34 and PE6100. Experiments on the systems DMPC/PE6100 and DMPC/GP34 were partially done by C. Schwieger [11].

From the results shown in Figure 32, we can conclude that all four polymers interact with the lipid membrane because for all sample systems changes of the main phase transition peak can be detected. The DSC curves for the different mixtures of the two systems DMPC/G12 and DMPC/GP17 look similar. With rising polymer content the transition peak broadens, splits into two peaks and gradually shifts to lower temperature. The change of phase transition temperature is shown in Figure 33(b) as a function of the polymer concentration. Also for the mixtures of DMPC and GP34 and DMPC and PE6100, the main phase transition peak broadens with rising polymer content and shifts to lower temperatures. This shift however is more distinct than for the mixtures with GP12 and GP17 (see Figure 33(b)). Additionally, we found for all samples that within the uncertainty limits, the area underneath the main phase transition peak roughly stays the same for all mixing ratios.

Our results generally agree with the literature results described above. For their interpretation, we firstly state that guest molecules can have different influence on the phase transition seen in the DSC curve. Molecules that stabilize the membrane by interacting with the head groups lead to an increase of T_m . An example are the hydrophilic PEO blocks, which additionally cause a dehydration of the membrane leading to a higher packing [210]. The PGMA blocks possibly have an even higher effect on the lipid headgroups than the PEO blocks due to their high capability of forming hydrogen bonds. On the other hand, membrane systems with molecules that disturb the lipid packing by incorporating in hydrophobic region exhibit a lower T_m . As a consequence, a competition of both effects is present in most cases [11]. From the lower melting temperature determined for our systems, we therefore conclude, that the lipid disturbing effect dominates. For the mixtures with GP34 and PE6100 it is larger than for the mixtures with GP12 and GP17, probably because GP34 and PE6100 insert more deeply into the membrane.

Furthermore, the decrease of the melting point temperature can be described as a freezing point depression which arises when the polymers interact more strongly with the membrane in the liquid-crystalline phase than the membrane in the gel phase. In a later section, we will see that also results from other experiments indicate that the block copolymers do not incorporate in the gel phase membrane.

As a general description of all separate features of the DSC curves is cumbersome, the results can also be interpreted using the classification of McElhaney [10]. The systems of DMPC/GP34 and DMPC/PE6100 behave similar to type A systems, which are defined by a decreasing T_m , a increasing $\Delta T_{1/2}$ and a ΔH that stays unchanged with rising guest molecule concentration. Guest molecules of these systems are expected to interact with the upper acyl chain region of the lipid bilayer. The systems DMPC/GP12 and DMPC/GP17 on the other hand can be classified as type B or D showing an additional DSC peak at the main phase transition which is indicative for guest molecules located near the hydrophobic/hydrophilic interface of the bilayer or guest molecules interacting with the lipid head groups at the bilayer surface, respectively.

In Figure 33(a), the DSC curve of the DMPC/PE6100 mixtures is shown on a broader temperature range. Besides the main lipid phase transition, we can see that for high polymer contents an additional broad peak at high temperatures appears, indicated by the grey arrows, probably originating from polymers that are not bound to the membrane but can form micelles instead. As expected, for the 5:1 mixture, the aggregation process starts already at lower temperature than for the 7:1 mixture due to the higher polymer content.

7.6 ^{13}C Spectra

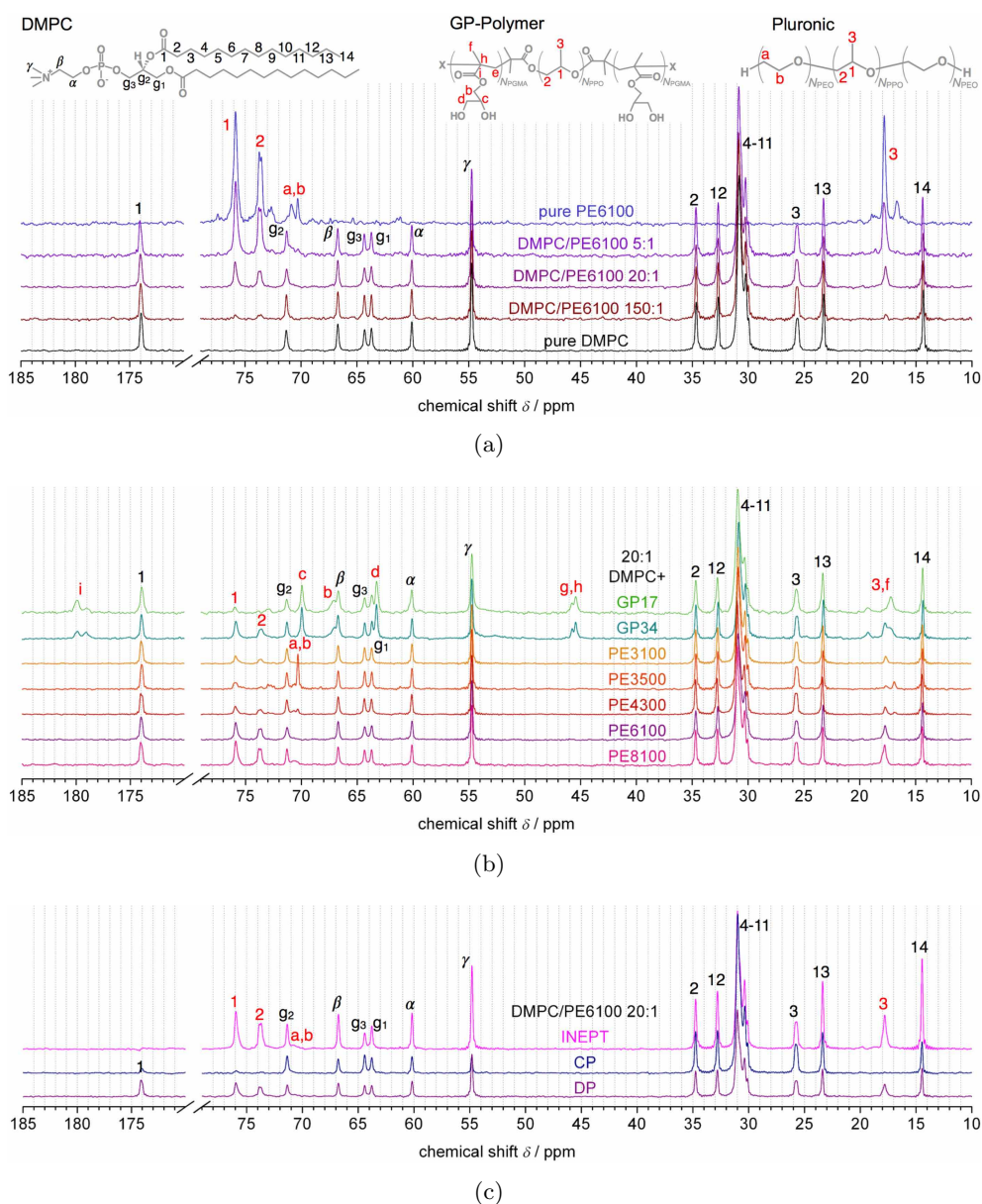


Figure 34: ^{13}C DP MAS spectra of (a) samples of DMPC and PE6100 in different mixing ratios, (b) various DMPC/polymer mixtures of a molar ratio of 20:1 and (c) a DP, a CP and an INEPT spectrum of a DMPC/PE6100 20:1 mixture. All spectra were acquired at temperatures between 35 °C and 40 °C.

In this section, ^{13}C spectra, of the different lipid/copolymer mixtures are presented. In Figure 34(a), DP spectra of mixtures of DMPC and PE6100 of different ratios as well as spectra for the pure lipid and the pure polymer in about 50 wt% deuterated water are shown. DP spectra recorded for mixtures of DMPC with the different polymers are depicted in Figure 34(b). Peak assignment for the polymer peaks was done according to References [119,211].

From slight shifts of the lipid peaks, we can conclude on lipid/polymer interactions [144]. These effects, however, are not very significant.

The polymer peaks of nearly all mixtures are sharp and well resolved, indicating a relative high mobility. This can be further confirmed by comparing the results from CP, INEPT and DP excitation as shown in Figure 34(c) for the 20:1 mixture of DMPC and PE6100. The signals from the polymer PPO block show highest intensity in the INEPT spectrum, are much smaller in the DP spectrum and in the CP spectrum, they are nearly not visible.

Furthermore, it is known from literature, that width and position of the Pluronic signals depend on their aggregation state and on possible interactions with the membrane. In ^{13}C spectra of Pluronics in water acquired under static conditions, the PPO methyl peak of polymers in micelles are shifted downfield by about 0.9 ppm in comparison to unimer resonances. The position of the PEO peaks, however, is the same for unimers and polymers in micelles [212]. For Pluronics incorporated deeply into a lipid bilayer, the PPO methyl peaks are broader than for Pluronics in solution [193]. It is difficult however, to draw quantitative conclusions on the interaction between lipids and polymers from the PPO methyl peaks of our ^{13}C MAS spectra alone. Furthermore, we expect similar peak positions from aggregated polymers and polymers incorporated in lipid bilayers.

While the highly hydrophobic Pluronics PE3100, PE6100 and PE8100 in mixture with DMPC only show one PPO methyl peak, two PPO methyl peaks can be seen in Figure 34(b) for the mixtures DMPC/PE3500 and DMPC/PE4300. Because these two Pluronics have the highest cmc values, the right peak probably originates from unimers dissolved in the water layers in-between the lipid bilayers. For the DMPC/GP mixtures, the polymer PPO methyl peak is rather broad. It is shifted a bit further downfield for DMPC/GP17 than for DMPC/GP34, indicating that more GP17 is dissolved in water than GP34.

7.7 Cross-Relaxation Rates

The NOESY experiment was applied to get information about the location and possibly also the configuration of the copolymers in the membrane. In Figure 35(a) a 2D NOESY spectrum of DMPC/PE6100 in the liquid crystalline phase at a temperature of 40 °C is shown. The assignment of the polymer peaks, which are denoted in red, was done according to literature [184,213]. Peaks from the polymer PEO block cannot be distinguished because in case of the PE6100 polymer this block is quite short and therefore only gives small signal which additionally overlaps with peaks from the lipid headgroup region.

Cross peaks between the resonances of the polymer PPO block and the lipid can clearly be seen reflecting the close contact between the molecules. Especially from the polymer/lipid acyl chain cross peaks, we can conclude that the polymer is not only adsorbed onto the surface but penetrates deeply into the lipid membrane. The relatively small intensity of the cross peaks might be explained by the weak and rather transient contacts in the fluid bilayer. Another possible reason

could be the formation of polymer domains as already suggested in literature [180, 191, 198, 199]. In this case, interaction between polymers and lipids would only occur at the boundaries.

As for the pure lipid samples, we assume that spin diffusion is not relevant for the magnetization exchange in the lipid/polymer systems (see Section 5.5) because like the lipids, also the polymers exhibit high molecular mobility as already explained in the last section.

In general, the NOESY spectra of all lipid/Pluronic mixtures investigated and of the lipid/GP34 mixtures [11]) show similar cross peaks confirming the insertion of the polymer into the lipid bilayer (see Table 4). This result fits to previous investigations from literature showing

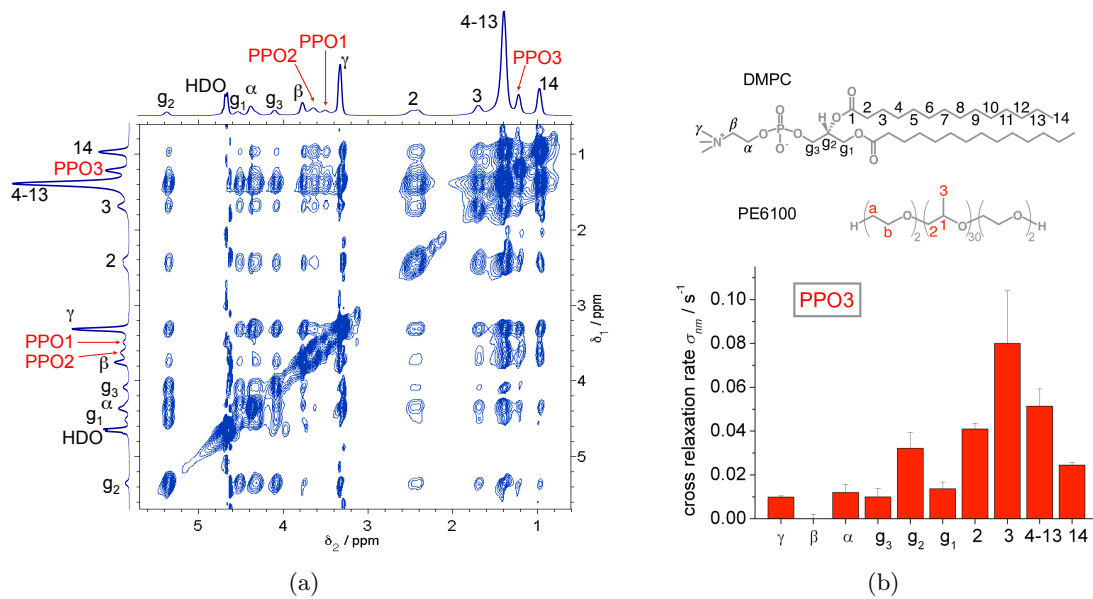


Figure 35: (a) 2D NOESY spectrum of DMPC/PE6100 measured at a temperature of 40°C using a mixing time of $\tau_m = 550$ ms and an MAS frequency of 5 kHz; (b) cross-relaxation rates determined from the cross peaks of the PPO methyl group (PPO3) of the polymer and the lipid resonances using the spin pair approach.

lipid-polymer cross peaks	
yes	no/small
DLPC/GP34 50:1	DLPC/GP17 20:1
DPPC/GP34 50:1	DMPC/GP17 10:1
DMPC/PE3100 20:1	DMPC/Chol/PE6100 60:20:3
DMPC/PE4300 20:1	
DMPC/PE6100 20:1	
DMPC/PE8100 20:1	
DPPC/PE3100 20:1	
DOPC/PE6100 20:1	

Table 4: Summary of results from 2D NOESY spectra.

that hydrophobic Pluronics reach deeply into the bilayer core [13, 203].

However, no lipid-polymer cross peaks could be detected for the mixtures DLPC/GP17, DMPC/GP17 and DMPC/cholesterol/PE6100 with a lipid/cholesterol ratio of 3:1. In these three cases, the polymer is not inserted into the membrane. Instead, it might not interact with the membrane at all or it is adsorbed loosely to the membrane surface.

For the lipid/GP17 mixtures, this lack of strong interaction can probably be explained by the structure of the polymer GP17, more specifically by the ratio of its hydrophilic and hydrophobic molecular blocks. In contrast to these results, we can detect lipid-polymer cross peaks for the mixtures DMPC/PE3100 and DPPC/PE3100. Seemingly the polymer PE3100 is build in the membrane to a significant degree although it even has a slightly shorter PPO block then GP17. However, the hydrophilic PGMA blocks of GP17 are much bigger than the PEO blocks of PE3100, which only consist of about one monomer each. Consequently, the total hydrophilicity of the polymer GP17 is higher and the hydrophilic PGMA blocks might be able to shield the hydrophobic PPO block possibly preventing it from inserting into the membrane. These findings are consistent with literature results suggesting that more hydrophilic Pluronics preferentially interact with the membrane surface [18, 190, 203].

The missing interaction between lipids and polymers found for the DMPC/cholesterol/PE6100 sample can be explained by the ordering of the lipid acyl chains due to cholesterol (see Section 2.4) which results in a more condensed membrane with increased packing density that could hinder the polymer to enter the membrane. A more detailed description of the influence of cholesterol on the lipid/polymer systems will be given in Section 7.10.8.

Besides this qualitative analysis, we also determined cross-relaxation rates for the sample system DMPC/ PE6100 20:1. For this purpose, NOESY spectra were acquired for several mixing times between 1 ms and 1 s. We analyzed the signal of the PPO methyl group, because it shows a suitably isolated peak at about 1.1 ppm, denoted as PPO3 (see Figure 35(a)). The other polymer signals partly overlap with lipid signals and therefore cannot be further considered. Consequently, the full matrix approach could not be used as we could not determine the entire peak volume matrix. Instead, we calculated the cross-relaxation rates from the peak volumes of the PPO3 cross peaks and the respective diagonal peaks only by using the spin pair approach (see Section 5.5). The results are shown in Figure 35(b). The highest cross-relaxation rates, we can see for the lipid acyl chain and especially for the upper chain region indicating that the polymer PPO block reaches into the hydrophobic bilayer core. Also, the cross-relaxation rates for the lipid head group are not zero. They might arise from PPO units close to the PEO blocks which can easily have contact to lipid headgroups facilitated by the high molecular dynamics in the whole system. However, as the spin pair approach is not precise for determining small cross-relaxation rates, it only yields qualitative results which should be interpreted carefully.

In literature, cross-relaxation rates determined from the NOESY experiment on lipid membrane systems exhibiting high mobility and molecular disorder are often interpreted in terms of the contact probability. The highest cross-relaxation rate is taken as an indication of the preferred location of a guest molecule, like ethanol [70], a peptide [214] or aromatic multidrug transporter substrates [124], in the membrane [69]. However, in the case of long polymers in the membrane investigated here, the interpretation of the cross-relaxation rates is more difficult. Therefore we calculated contact probabilities and cross-relaxation rates from the trajectories of the different systems simulated and compared them.

To determine the contact probability for two specific atoms (one from the lipids and one from the polymer), we record their distance r for all combinations and subsequently, sum up the resulting $1/r^6$ for each pair and each time step. To speed up the calculations, we use a cut-off distance of 10 \AA , that is larger distances are not considered. In Figure 37(a)-(c), contact probabilities determined for lipid atoms and the polymer PPO block (average value over all protons from the PPO CH_2 groups) are shown for three different systems simulated. For systems with polymers deeply incorporated into the membrane, we get the highest contact probability between the polymer PPO block and the lipid chain ends irrespective of the way of incorporation (membrane-spanning or U-form), because a significant part of the polymers is located deeply inside the bilayer. For the polymers forming an aggregate on top of the membrane, we naturally get the highest contact probabilities for the lipid headgroup region and in total much smaller values than for the other systems. The experimentally determined cross-relaxation rates displayed in Figure 35(b), however, show a different profile.

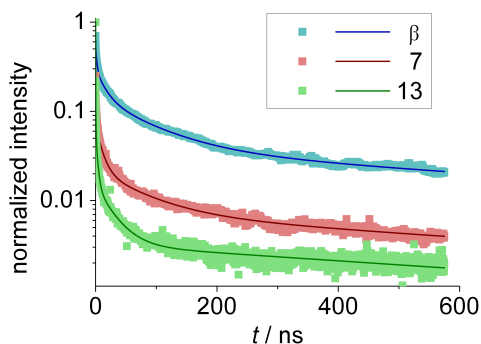


Figure 36: Cross correlation functions determined for proton pairs with one proton coming from the PPO CH_2 groups and the other one from the different lipid segments for the “membrane-spanning” DMPC/PE6100 system. The curves are averages over the whole polymer PPO block interacting with the lipid headgroup (β), the middle of the lipid chains (7) and the lipid chain ends (13) (see Figure 35 for the lipid structure). For the plot, the correlation functions were normalized to start at one.

For their interpretation, we therefore calculate cross-relaxation rates from our trajectories of the different systems simulated. A similar approach was already used in literature to investigate the positioning of ethanol in a lipid bilayer [71]. As, due to the use of the united atom model, the dynamics of the PPO methyl group are not described correctly, we calculate the cross-relaxation rates for protons of the PPO CH_2 groups instead and subsequently take the average over the whole PPO block. For both lipid chains, the cross-relaxation rates are calculated separately and the average is taken. We only consider one proton of each lipid and polymer CH_2 group, because the other proton shows the same behavior. To calculate the cross correlation function from our simulations, we rewrite Equation 73 given in Section 5.5 as

$$C_{ij}(t) = \frac{1}{4\pi KLP} \sum_k^K \sum_l^L \sum_p^P \frac{1}{r_{lp}^3(\tau_k)} \left(\frac{3z_{lp}^2(\tau_k)}{r_{lp}^2(\tau_k)} - 1 \right) \frac{1}{r_{lp}^3(\tau_k + t)} \left(\frac{3z_{lp}^2(\tau_k + t)}{r_{lp}^2(\tau_k + t)} - 1 \right). \quad (85)$$

The sums are taken over all protons contributing to one resonance, that is all protons with the same chemical shift of one lipid or polymer molecule and all the protons of the different molecules. The total numbers of contributing lipid or polymer protons of the entire system are denoted as L or P . Division by LP yields the correlation function on a per-proton basis. Additionally, we average over all time steps τ_k available with a total number of K . Because for

longer time steps t , the average is taken over a smaller number K of values, we only calculate the correlation function for half of our simulated trajectory. As explained in Section 5.5, the correlation function subsequently is described by a fit function given as the sum of exponentials $C_{ij}(t) = \sum_n a_n e^{-t/\tau_n}$. We use fixed parameters τ_n varying from 10^{-2} to 10^3 s in steps of $10^{0.1}$ and determine the prefactors a_n by fit. As we can see in Figure 36, for long times t , all correlation functions show an identical decay originating from the lateral diffusion of lipids and polymers. The cross relaxation rates are then calculated using to Equation 75 in Section 5.5. Because they are dominated by the terms containing long τ_n , it is important to determine the respective a_n precisely that describe the tail of the correlation function.

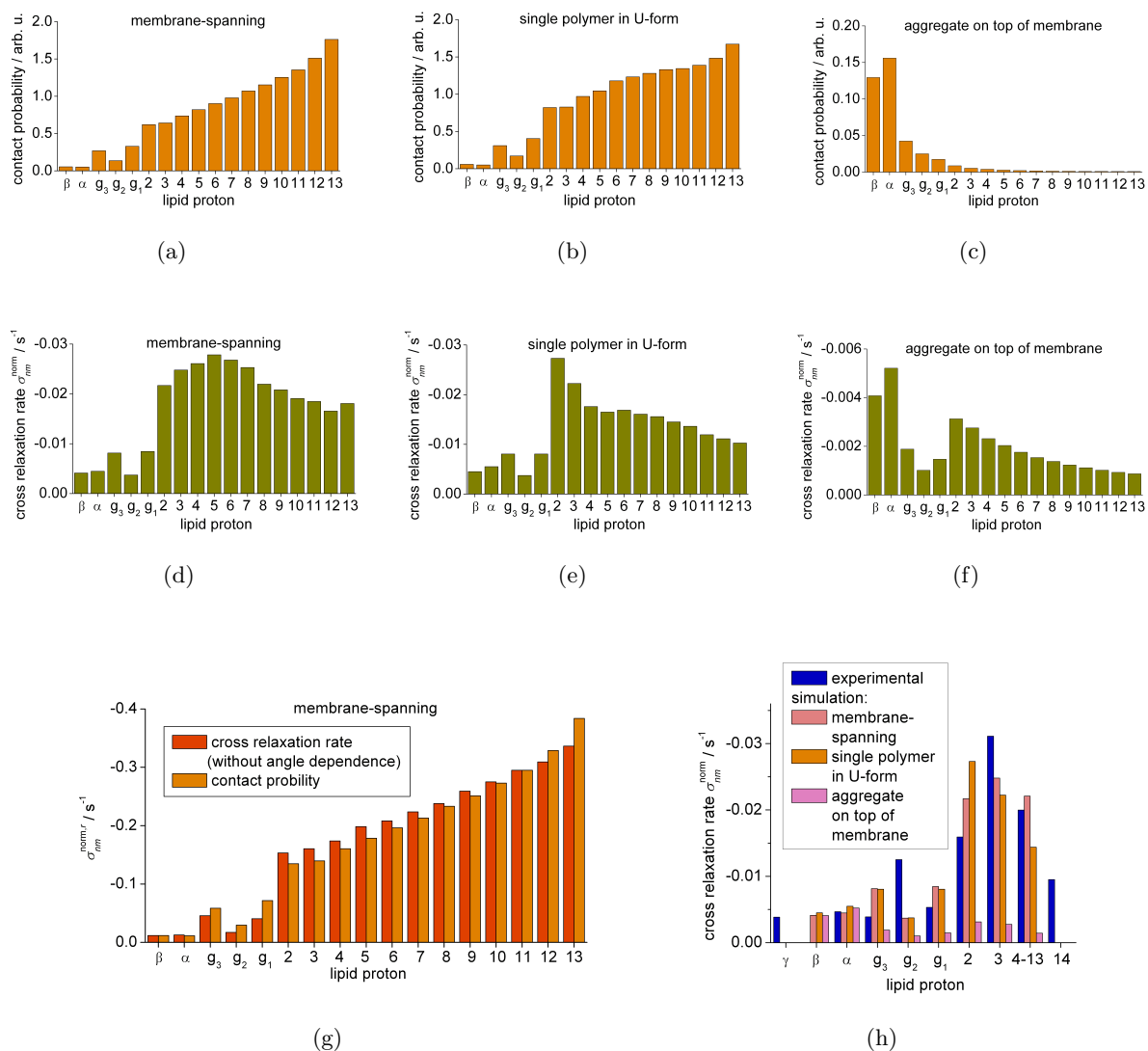


Figure 37: Results for different DMPC/PE6100 systems: (a)-(c) contact probabilities determined from the different systems simulated; (d)-(f) cross-relaxation rates of the respective systems; (g) comparison of contact probabilities and relaxation rates determined from the cross correlation function omitting the angular dependence (see Equation 86); (h) cross-relaxation rates per proton determined from experiments and from simulations.

In Figure 37(d)-(f), the resulting cross-relaxation rates, calculated on a per-proton-basis, are shown for three different systems. The cross relaxation rates determined for the systems with PE6100 incorporated deeply into the membrane show a maximum at the upper acyl chain region of the lipids. The profile of the cross relaxation rates therefore is different than the profile of the contact probabilities. Cross-relaxation rates determined for the system “aggregate on top of membrane” are considerably smaller and very roughly show the same behavior as the respective contact probabilities.

For a better understanding of the differences between the contact probabilities and the cross relaxation rates, we calculated the cross relaxation rates a second time omitting the angular dependence of Equation 73 (Section 5.5). As a result, we get the correlation function

$$C_{ij}(t) = \frac{1}{4\pi KLP} \sum_k^K \sum_l^L \sum_p^P \frac{1}{r_{lp}^3(\tau_k)} \frac{1}{r_{lp}^3(\tau_k + t)} \quad (86)$$

from which we calculate the cross-relaxation rates in the same way as described above. The results for the “membrane-spanning” system are shown in Figure 37(g) in comparison to the contact probabilities calculated before which were normalized to roughly give the same intensities. It can be seen that the profiles of the contact probabilities and the cross-relaxation rates without angular dependence along the lipid molecule match quite well. Therefore, we conclude that the experimentally determined cross-relaxation rates cannot just be interpreted in terms of contact probabilities for our lipid/polymer systems but that the correlation times describing the reorientational motions of the connecting vectors also influence these cross-relaxation rates significantly.

In Figure 37(h), the cross-relaxation rates determined from experiment and simulation are shown in comparison. For this, the experimental values already shown in Figure 35(b) were normalized by division by the number of contributing protons and multiplied by a factor of 0.6 to get a good match of the experimental and simulation results. This additional factor might arise because only about half of the polymers available gets incorporated into the membrane. The experimentally determined values match best with the simulation results from the ‘membrane-spanning’ system. However, also the results from the “single polymer in U-form” system look quite similar, so that a safe conclusion on the polymer configuration in the membrane cannot be drawn. Also both configurations might occur.

7.8 Order Parameter S_{CH} of Lipid Molecules

The R-PDLF and the recDIPSHIFT experiment were performed to determine heteronuclear dipolar coupling constants of the lipids in mixture with triblock copolymers and from this conclude on molecular order and dynamics. As an interaction between lipid and polymer molecules was clearly proven in the previous sections, it could be imagined that the polymers alter the lipid packing or influence lipid headgroup dynamics.

In literature, different results for the influence of the polymer on the lipid packing can be found. While more hydrophobic Pluronics apparently increase the bilayer rigidity and the lipid order parameters [16, 189, 190, 192], more hydrophilic Pluronics rather seem to lower the lipid ordering [191, 194]. However, also hydrophobic Pluronics were found to disturb the lipid

packing [18,194,203,206]. Yet other sources claim that lipid dynamics and packing are unchanged by the polymers [18,186].

From our results shown in Figure 38, we can conclude that within the experimental error the lipid order parameters are the same for the different lipid/Pluronic mixtures and identical to the results from the pure lipid sample. Increasing the polymer concentration did not result in any changes and also for the mixtures of DMPC and GP34, it was found that the polymer does not influence the lipid order parameters [144]

An analysis of the polymer resonances from the ^{13}C detected SLF experiments was not successful. Despite we have proven that the polymer is inserted deeply into the membrane, anisotropic motions of the polymers in the membrane cannot be detected. Instead, the residual heteronuclear dipolar couplings of the copolymer seem to be highly averaged. In the recDIPSHIFT curves, a modulation is hardly visible and the dipolar spectrum acquired using the R-PDLF experiment only shows an intense middle peak and broad rather shallow peaks at the sides that hint to a distribution of couplings (see Figure 67 in the Supplementary Section E.2).

For comparison, the lipid order parameters were calculated from the simulated trajectories of all different systems (see Figure 39(a)). In accordance with the experimental results, the lipid order parameters are not influenced by the presence of the polymer. In Figure 39(b), additionally the order parameters calculated for the lipid acyl chains from the upper and the lower bilayer leaflet are shown separately. While for the system of pure DMPC, we find identical order parameters for the upper and the lower leaflet, a difference can be seen for the system with six polymers incorporated in U-form in the upper leaflet. In this case, the lipids in the upper leaflet show a higher order parameter than the lipids in the lower leaflet or in the pure DMPC system. However, this effect of lipid ordering is not strong and also can be explained by the relatively high polymer concentration in this leaflet, which probably would not occur in real samples.

Generally, we can conclude from experimental and simulation results, that the block copolymers do not influence the lipid packing or their geometry of motions. The most likely explanation is that the polymer incorporates in the membrane in the least disturbing way and adapts to the lipid dynamics [186]. Also the formation of polymer aggregates could be a reason as in this case lipid-polymer interactions would only occur at the aggregate borders. However, our simulations have shown that also polymers homogeneously distributed over the membrane do not have much influence on the lipid ordering (see Figure 39(a)).

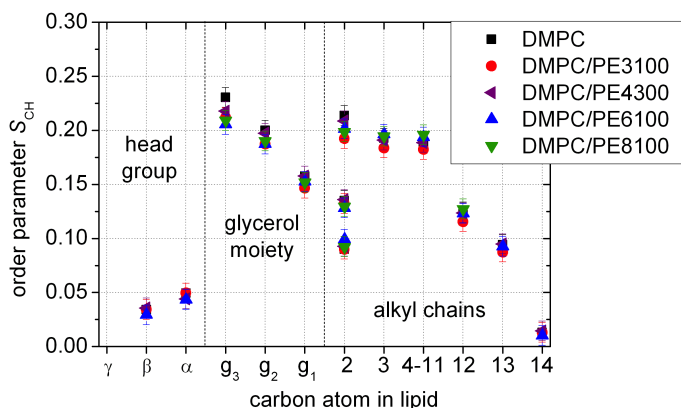


Figure 38: Order parameters determined from the R-PDLF experiment for a number of lipid/polymer samples with a mixing ratio of 20:1 at 40 °C. For the alkyl chain peak containing many overlapping resonances, we only determined one averaged value for the order parameter.

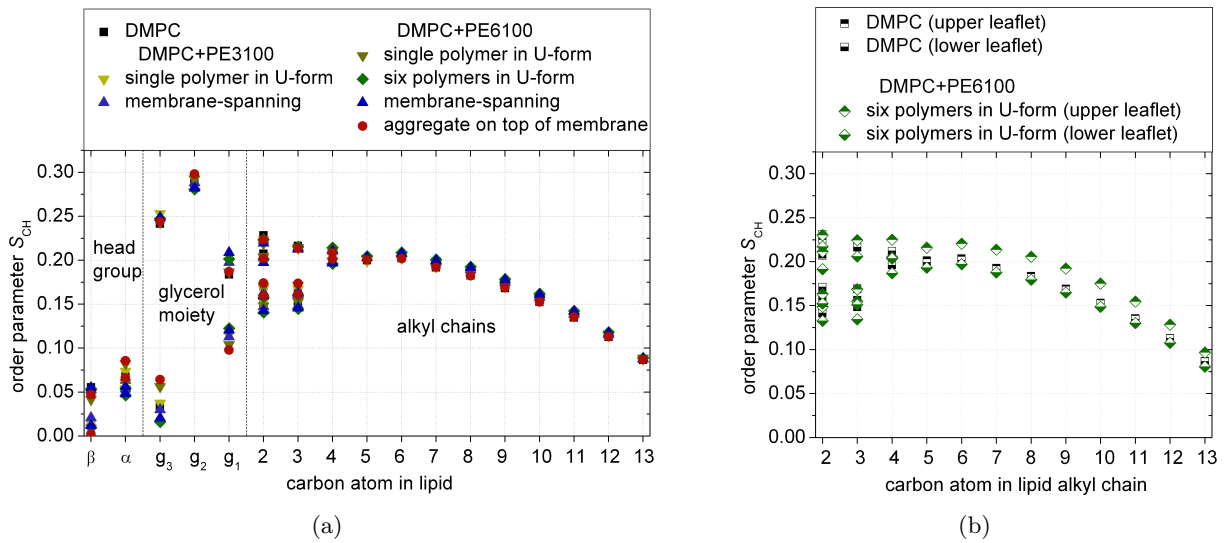


Figure 39: DMPC order parameters from MD simulation (a) for the different systems, and (b) for the upper and lower leaflet separately calculated for two different systems.

7.9 Relaxation Rates R_1 of Lipid Molecules

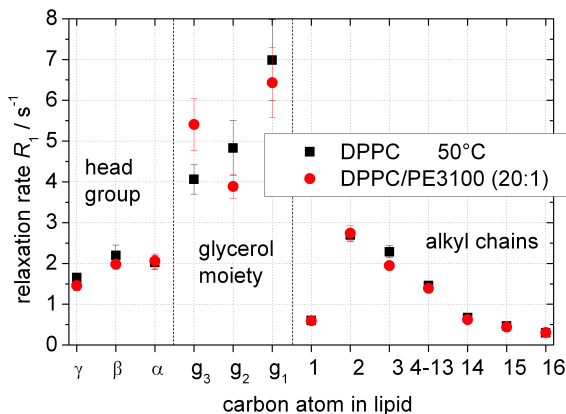
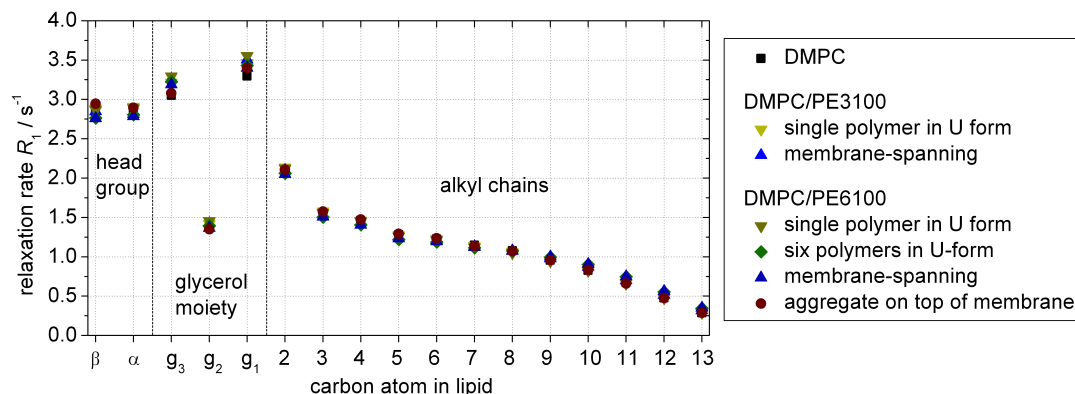


Figure 40: R_1 relaxation rates determined from the SATREC experiment for a pure DPPC sample and a 20:1 mixture of DPPC and PE3100 at 50 °C.

Like the lipid order parameters S_{CH} , also the R_1 relaxation rates of the lipid molecules are not influenced by the polymers. In Figure 40, the results for a pure DPPC sample and for a mixture with the Pluronic PE3100 determined at 50 °C using the SATREC experiment are shown in comparison. Within the uncertainty limit, the relaxation rates of both samples are the same. Also for other samples, for example DPPC and DPPC/GP34, nearly identical relaxation rates were found for the lipids.

In the same way, the relaxation rates of the lipids determined from the trajectories of the MD simulations are quite similar for all the different systems. The results are shown in Figure 41.

Summarizing the results from experiments and simulations for the lipids, we can conclude that the fast lipid dynamics are generally not influenced by the polymer as neither the order parameter nor the relaxation rates show any changes.

Figure 41: Relaxation Rates R_1 determined from the MD simulations.

7.10 Polymer Configuration and Dynamics

From the results of the R-PDLF and the recDIPSHIFT sequence, we concluded that the polymers in mixture with the lipids show a highly averaged heteronuclear dipolar coupling that is too small to be determined by these experiments (see Section 7.8). Additionally, a wide distribution of couplings might be present. To nevertheless detect anisotropic polymer motions, we use the BaBa-xy16 sequence which allows for the measurement of small homonuclear ^1H - ^1H residual couplings (see Section 5.6.4). This approach for the investigation of lipid/polymer systems was already introduced in References [96, 144]. Additionally, polymer order parameters were determined from the simulated trajectories and compared for the different systems.

7.10.1 Analysis of the DQ build-up curve

Using the BaBa-xy16 sequence, we recorded DQ build-up curves. Like for the NOESY experiment, we analyzed the PPO methyl peak because of all the polymer signals it is resolved best. The DQ and the reference intensities were determined by integration. A baseline correction was not necessary.

For samples of pure polymer in deuterated water at a concentration of 50 wt% (GP34 and PE6100), we did not measure any build-up of DQ intensity which is an indication for isotropic molecular mobility. Seemingly, the polymers are quite mobile although they are expected to form aggregates at such a high concentration.

The individual steps of data analysis for experiments conducted on the lipid/polymer samples are shown in Figure 42 using as an example the results of a 20:1 mixture of DMPC and PE6100. In part (a), on the very left we can see that for small DQ evolution times τ_{DQ} of less than 2 ms, the DQ intensity first increases very strongly and then decreases again. This is due to an overlap of the polymer peak with the foot of the large signal of the motionally more restricted lipid acyl chain (see the spectrum at the top of Figure 35(a) in Section 7.7), causing the large initial peak in the DQ build-up curve. However, the lipid signal relaxes fast, so that for τ_{DQ} exceeding 1 or 2 ms, the polymer peak can be separated clearly and the intensity is not influenced by the lipid molecule anymore, but shows a slow increase of the DQ intensity which is characteristic of the mobile polymer. For all data analyses, one can therefore just neglect the intensities measured

during the first 1 or 2 ms.

Besides the molecular segments that show anisotropic mobility leading to a build-up of DQ intensity, there is also a fraction of nuclei exhibiting isotropic mobility. The contribution I_{tail} of these uncoupled spins was determined by a bi-exponential fit to the intensity difference $I_{\text{ref}} - I_{\text{DQ}}$ (see Figure 42(b)) which is generally the best way to identify signal contributions arising from isotropically mobile moieties [215]. As there is some uncertainty about the starting point from which data should be used for fitting, we chose six different starting points and took the average result from all of them. Consequently, we also calculated six different build-up functions in the next step, which all reached the plateau value of 0.5 at slightly different times and which we all analyzed separately.

The origin of the isotropically mobile fraction can be attributed to PPO methyl groups within chains that are not incorporated in the membrane but instead exhibit a high mobility in water where they exist as unimers or in form of some aggregates, for example small micelles with a radius of only a few tens of nanometers [187]. However, also polymers that only attach loosely to the membrane surface or even polymers that fold into a hairpin upon membrane incorporation could exhibit isotropically mobile parts of the PPO block in the middle of the bilayer. A third possibility is the formation of polymer domains within the membrane [180, 191, 198, 199]. While polymer dynamics are anisotropic at the lipid/polymer border, there could be much less motional restriction for polymers within the domain.

The signal fraction f_a of the anisotropically mobile PPO methyl groups is determined from

$$f_a = \frac{I_{\text{ref}}(0) + I_{\text{DQ}}(0) - I_{\text{tail}}(0)}{I_{\text{ref}}(0) + I_{\text{DQ}}(0)}. \quad (87)$$

For this, the sum intensity at a DQ evolution time of zero $I_{\text{ref}}(0) + I_{\text{DQ}}(0)$ was determined by back extrapolation based upon a single-exponential, a bi-exponential or a stretched exponential fit, to the difference of sum and tail intensities. For this sample, we obtain $f_a = 0.46 \pm 0.05$. It reflects the fraction of polymer that is deeply inserted into the lipid bilayer therefore showing anisotropic, restricted dynamics which result in a coupling constant different from zero.

In the next step, we analyzed the normalized DQ build-up curve shown in Figure 42(c). In the long-time limit, it reaches a plateau value of 0.5. Although the DQ build-up curve of an isolated methyl group is theoretically only expected to rise to 0.33 [216], we measure a higher value, due to the influence of additional couplings to remote protons and dipolar truncation. The residual dipolar coupling constant is determined using the fit function of the second moment approach given in Equation 78 in Section 5.6.4. To get stable end results that are comparable and an estimation of the statistical error for all the different samples investigated, we performed the fit to the DQ build-up curves for three different fit intervals (starting value at 1, 1.5 and 2 ms) and took the average value of all the 18 fits as the result. Additionally, we performed each experiment about two or three times to check for reproducibility.

For the DMPC/PE6100 20:1 mixture, a coupling constant of $\nu_{\text{D,res}} = (153 \pm 30)$ Hz and a distribution width of $\sigma = (53 \pm 15)$ Hz were determined. We also tried the fit using the Abragam-like function given in Equation 80 in Section 5.6.4. It yields the same value for the coupling constant $\nu_{\text{D,res}} = (153 \pm 30)$ Hz and a significantly higher distribution width of $\sigma = (111 \pm 15)$ Hz. The same tendencies were found for all samples. However, due to the missing initial slope, a

stable fit could not be reached in all cases by using the Abragam-like function. Therefore, we will only present results from fits using the second moment approach.

For calculating the order parameter S of the polymer backbone (rather than a specific H–H internuclear vector) from the residual dipolar coupling measured for the methyl groups of the PPO block, one can use a reference coupling of about $\nu_{D,\text{ref}} = 6.3$ kHz as estimated for polymers with similar local spin configuration [142,217]. The resulting order parameter of $S_{\text{HH}} = 0.023$ is rather small. To calculate this order parameter theoretically, the polymer can be modeled as a freely fluctuating Gaussian chain of contour length R_{max} subtended between two fixed points at a distance R . Classical arguments yield $S = \frac{3}{5} \frac{R^2}{R_{\text{max}}^2}$ [158,218]. Assuming that the polymer has the membrane-spanning configuration, we can take R to be the hydrophobic membrane thickness of 2.54 nm [219]. With $R_{\text{max}} = 12.2$ nm for the fully stretched PPO block [198], we obtain an order parameter of $S = 0.026$ which is indeed very close to the experimental value.

However, according to the results of the last sections, it is more probable to assume that the polymer is not just moving freely between two fix points given by the membrane headgroup region, but is adapting to the lipid chains instead. This explanation is also supported by the MD simulation results shown in the following section.

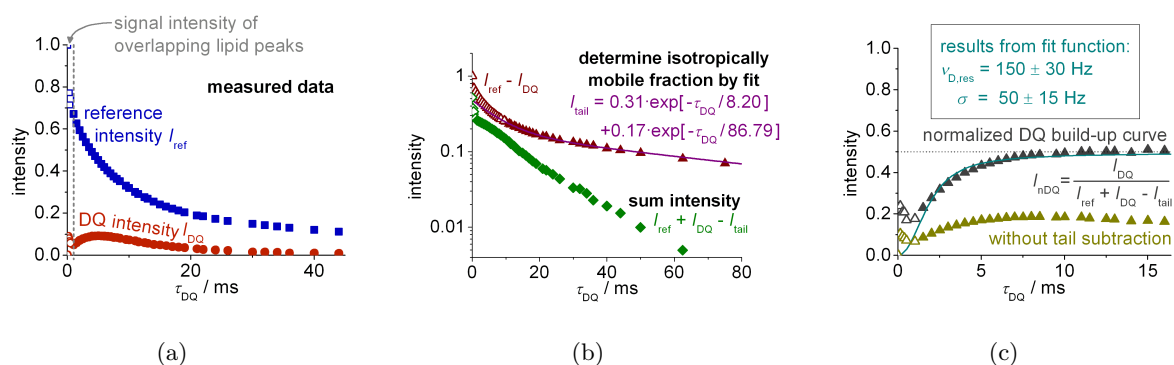


Figure 42: Results from a DQ experiment on DMPC/PE6100 20:1 at about 40 °C using a MAS frequency of 8 kHz. The DQ evolution time was incremented between 0 and 1000 rotor periods with $\tau_{\text{DQ}} = n\tau_{\text{R}}$, $n = 1, 2, 3, \dots$ for small τ_{DQ} and $\tau_{\text{DQ}} = 4n\tau_{\text{R}}$ for larger τ_{DQ} to avoid intensity reduction due to higher-order effects [159]. (a) Measured DQ and reference intensities; (b) tail fraction determined from $I_{\text{ref}} - I_{\text{DQ}}$ and sum intensity; (c) normalized DQ build-up curve and results from a fit based upon Equation 78 given in Section 5.6.4

7.10.2 Order Parameters Determined from MD Simulations

As it is not possible to conclude on the polymer configuration in the membrane from the averaged dipolar coupling constant of the PPO methyl groups alone, we will, in a next step, compare our experimental results to the respective order parameters of the polymer PPO block calculated from the trajectories of the different lipid/polymer systems simulated.

Specifically, we determine the order parameter S_{CC} for the C–C bond between the methyl and methine group (see Figure 43 at the lower right). To compare S_{CC} with the experimentally determined order parameter S of the polymer backbone, we need to consider a factor of 0.5 which accounts for the fast reorientations about the polymer backbone. From the residual

dipolar couplings $\nu_{D,\text{res}}$ measured, we consequently determine the order parameter as $|S_{CC}| = \nu_{D,\text{res}}/12.6 \text{ kHz}$.

Besides the calculation of a mean order parameter describing the whole PPO block, simulation results also allow for the examination of each PO segment separately. Furthermore, the entire order tensor can be calculated for a detailed investigation of the average chain orientation.

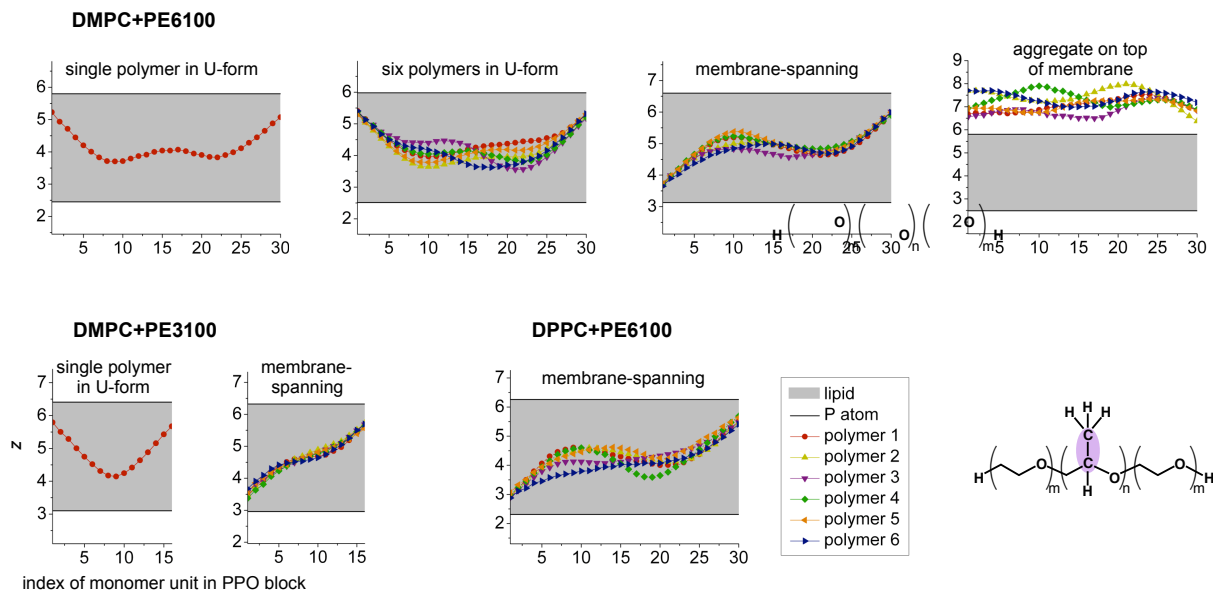


Figure 43: Position of the polymer PPO block in the membrane determined from the simulated trajectories of the respective systems as the time-averaged z -coordinate of the C-C bond between the methyl and methine group for each monomer of the PPO block. For systems containing more than one polymer, also the average over all polymers was taken.

In a first step, we will have a look on the general location of the polymer chains in the membrane. For the different systems investigated, Figure 43 shows the averaged positions of all the individual PO monomers with respect to the z -direction. For this, the z coordinate of the center of each HC-CH₃ bond in the PPO block was picked and the average over all time steps and all polymers was calculated. As a result, it was found that except for the different symmetry for the folded and the transmembrane configuration (chain ends at the same side of the bilayer or on the opposite sides), the polymer PPO blocks of all systems are arranged in a similar way inside the bilayer. The chain center in average is situated in the middle of the bilayer lying perpendicular to the membrane normal, that is over time it temporarily enters the upper or lower leaflet or it stays in-between the leaflets. The chain ends reach in direction of the lipid head group region and are partly aligned parallel to the lipid tails.

As already noted in Section 7.4, the polymers in the system 'aggregate on top of membrane' show a different behavior. On average no connection between the PPO blocks and the bilayer is visible.

Firestone et al. had concluded that a polymer can anchor the membrane most effectively when its length is similar to the hydrophobic bilayer thickness, that is, about 40 units [13]. In contrast, we see here that a PPO block of even 15 units is actually too long to span the membrane just parallel to the bilayer normal.

In Figure 44, results for the order tensor elements and the averaged order parameters of the PPO HC-CH₃ bonds for the different systems simulated are shown. To explain the relation of chain localization/orientation and the order tensor, we consider a single PPO block in (a) and the average over the PPO blocks of all six polymers in (b) for the 'membrane-spanning' system. The ends of the PPO block are roughly aligned with the lipid tails thus in average oriented parallel to the z axis. Therefore, they show a similar order tensor as the lipid chains. The off-diagonal elements S_{xy} , S_{xz} and S_{yz} are zero due to the averaging caused by fast reorientational motions about the polymer backbone. However, because of the high level of scatter visible in Figure 44(a), this can hardly be recognized. The mean values over all six polymers are closer to zero (see Figure 44(b)). The diagonal matrix element S_{zz} is similar to the order parameter determined for the upper chain region of the lipids $S_{zz} \approx -0.2$ (see Section 5.6.3). As expected for an order tensor describing uniaxial motions, the other two diagonal components amount to $S_{xx} = S_{yy} = -0.5 S_{zz} \approx 0.1$.

On average, the middle of the PPO block is situated in the bilayer center. Here, the motional geometry of the chain is generally the same as for the block ends but the orientation is changed. Due to fast reorientations about the polymer backbone, the off-diagonal elements of the order tensor are zero. For a chain that is aligned parallel to x axis, the diagonal elements amount to $S_{xx} \approx -0.2 = -2S_{yy} = -2S_{zz}$ which, for example, can be seen for the monomer units 18 to 22 in Figure 44(a). However, in general the polymer chain assumes a random orientation in the x - y plane. Therefore, we consider an averaged value of $0.5(S_{xx} + S_{yy}) \approx -0.5$ which is shown in Figure 44(b).

In Figure 44(c), results for the order parameter S_{zz} of the PPO HC-CH₃ bonds are shown for all the different systems simulated. The order parameters of the polymer PE3500 dissolved in water are nearly zero, as expected for an isotropically mobile chain. Also the PE6100 polymers in the aggregate located on top of the membrane show an order parameter close to zero indicating their high dynamics. Only for one chain end, a slightly negative order parameter is determined probably originating from polymer chain ends partially attached to the bilayer.

For the systems with the polymer PE6100 deeply incorporated in a lipid bilayer, we find nearly identical profiles of S_{zz} independently of the actual polymer configuration (membrane-spanning or U-form). Also the total average order parameter, calculated as the average of the absolute order parameters of the single PO units, is similar for all the systems and amounts to $|S_{CC}| \approx 0.1$. Thus, it is not possible to conclude from the order parameter whether the polymer spans the membrane or whether both ends reach out at the same side of the membrane.

In Table 5, order parameters $|S_{CC}|$ determined from the experiments are shown for comparison. They are about one order of magnitude smaller than the results from the simulations. However, it is not surprising to find these differences because the experimentally determined order parameter is subject to a number of uncertainties. Most relevant is here the error of the rigid coupling constant arising from couplings to remote protons. But also the average order parameters determined from the MD simulations are not very precise because the end results are very small. As additional motions, like lateral diffusion on the vesicle surface or bilayer undulations, which are not covered by the simulation, do not have a significant influence on the lipid order parameters, they are also not expected to be relevant for the order parameters of the individual polymer segments which are quite similar to the ones of the lipid tails.

The distribution of couplings determined from the experiments can be explained by the

different order parameters for different positions along the chain determined from the MD simulation. However, it is difficult to determine the coupling distribution from the simulation results quantitatively. Histograms calculated for the absolute order parameters $|S_{CC}|$ (see Figure 44(f)) show strong fluctuations which probably could only be diminished by recording trajectories over considerable longer times. Nevertheless, we determined the distribution widths σ_S from these plots. The results amount to about one third or one half of the the average order parameter and in this sense roughly match the experimentally determined values.

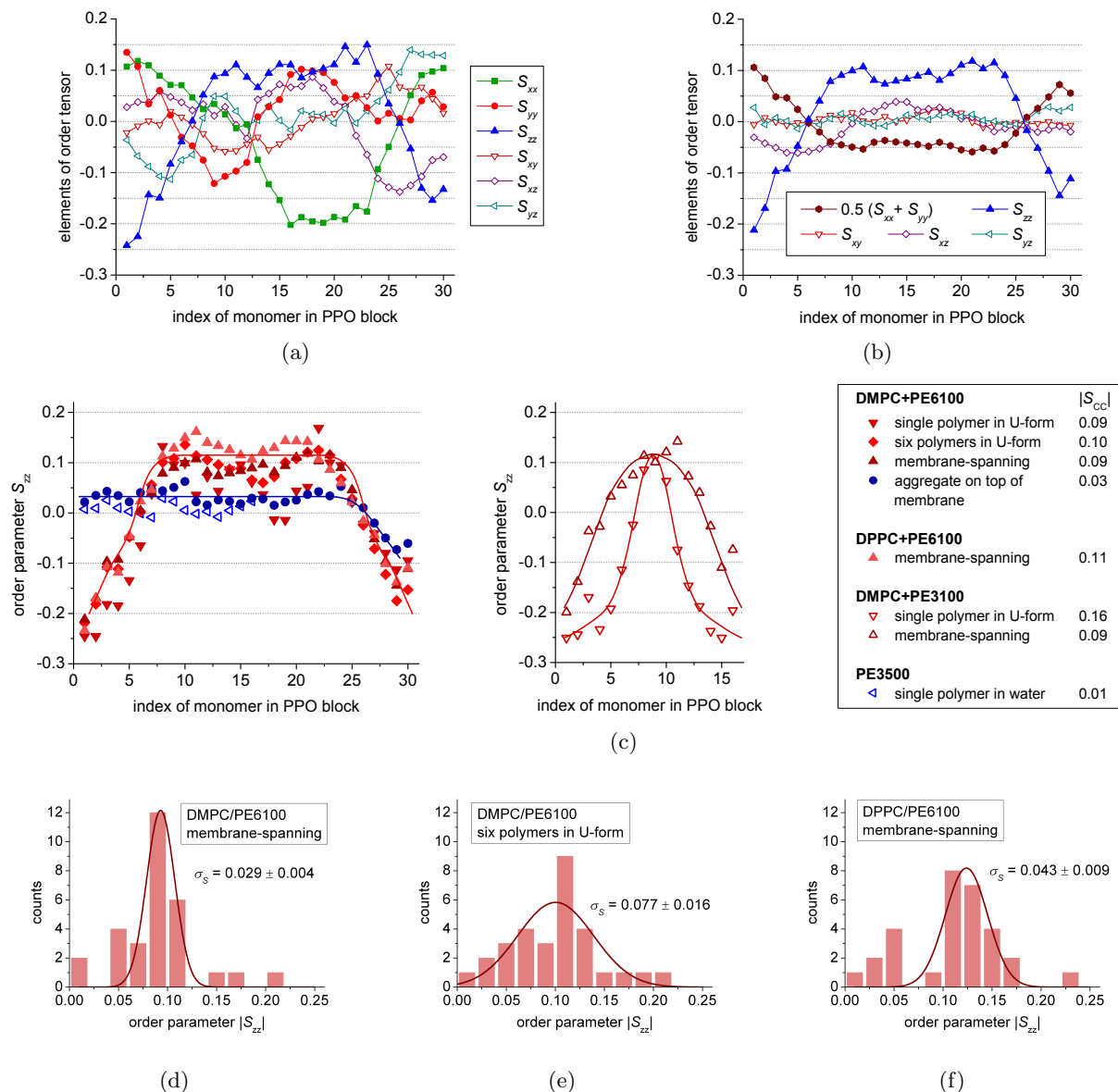


Figure 44: (a), (b) Elements of the order tensor determined for all HC-CH₃ bonds in the polymer PPO block for the 'membrane-spanning' system, in (a) the results for one polymer and in (b) average results over all six polymers are shown; (c) order parameters S_{zz} of the HC-CH₃ bonds in the polymer PPO block; and (d)-(f) results from (c) for the respective systems plotted as a histogram which allows for the determination of the order parameter distribution σ_S .

sample	S_{CC}
DMPC/PE6100	0.012 ± 0.003
DMPC/PE3100	0.018 ± 0.003
DPPC/PE6100	0.012 ± 0.003
PE3500	0

Table 5: Order parameters of the HC-CH₃ bond determined from the experimental results for the homonuclear dipolar coupling of the PPO methyl group.

From the experiments and from the simulations, we obtained roughly the same order parameter for PE6100 in DMPC and for PE6100 in DPPC in the membrane-spanning configuration (see Table 5 and Figure 44(c)). A stronger stretching of the polymer in the slightly thicker DPPC membrane cannot be observed.

Also for PE3100 incorporated in a DMPC bilayer in membrane-spanning configuration, we determine roughly the same average order parameter of $|S_{CC}| = 0.1$ as for PE6100 in DMPC from the simulations (see Figure 44(c)). A PE3100 polymer incorporated in the bilayer in U-form, however, yields a average order parameter for the PPO block that is about 1.8 times larger. As can be seen from Table 5, also the experimentally determined order parameter for the DMPC/PE3100 mixture is about 1.5 times larger than the order parameter for the DMPC/PE6100 mixture possibly indicating that for PE3100 in a DMPC membrane, the U-form configuration is preferred.

7.10.3 Relaxation Rates R_1 of Polymers

Using the ‘‘Torchia-like’’ pulse sequence (see Section 5.4), we determined $R_1(^{13}\text{C})$ relaxation rates for a sample of pure polymer in water and for lipid/polymer mixtures. The experimental results are compared with relaxation rates determined for the respective carbon atoms from the systems simulated.

Firstly, we investigated a solution of PE3500 in deuterated water at a concentration of 0.01 mol/L. This polymer was chosen because it has the highest cmc value compared to the other Pluronics investigated and therefore allows for the preparation of a sample containing polymer unimers like the simulated system used for comparison on the one hand, and simultaneously exhibits a polymer amount sufficiently high for an acceptable signal-to-noise ratio in the NMR experiment on the other hand. The concentration chosen slightly exceeds the cmc value of $5.3 \cdot 10^{-3}$ mol/L given in Table 2 in Section 7.3. Therefore, polymer unimers and micelles probably coexist in the sample and both contribute to the measurement. However, as cmc values can only be determined with an uncertainty of several orders of magnitude, it is not clear whether micelles are present or whether polymer unimers are dominating. From literature, it is known that different relaxation rates for the polymer PPO block are determined for samples of polymer unimers and samples with polymer micelles [213]. However, in our experiment, a single exponential decay of the signal intensity was measured (see Figure 45(a)) and consequently a single relaxation time was determined for each polymer peak. Possibly different relaxation times from different components could not be distinguished.

The resulting relaxation rates are given in Table 6. The CH_3 group of PPO exhibits the slowest relaxation arising from the lower dipolar coupling that is averaged by the fast three-site jump motions. For the PPO- CH_2 group a higher relaxation rate is detected than for the CH group, because of the contribution of two protons. Similar results were already found in literature for solutions of pure PPO [119].

To compare with results from MD simulations, relaxation rates were determined for the system of a single PE3500 polymer in water assuming that only the dipolar coupling influences the ^{13}C relaxation [119]. As the dynamics of methyl group are not described well by the united-atom model, the corresponding relaxation rates were disregarded. The results for the other chemical sites are shown in Table 7. Similar to the experimental results, we get values of $R_1 \approx 2\text{ s}^{-1}$ for the PPO CH_2 group and $R_1 \approx 1\text{ s}^{-1}$ for the PEO CH_2 group and the for the PPO CH group. The good agreement of results from experiment and simulation confirm that polymer dynamics relevant to R_1 were simulated correctly.

In the next step, we measured relaxation times of PE6100 in DMPC in a 1:14 mixture at about 30°C . Again only a single exponential decay of the polymer signal intensities was detected (see Figure 45(b)) although two different polymer fractions are present: polymer that is bound to the membrane and isotropically mobile polymer that is assumed to diffuse freely in the surrounding water phase. The relaxation rates determined from the PPO resonances are shown in Table 6. For the PEO blocks, we could not get any results due to the partial overlap of the PEO resonance with lipid peaks and because the PEO resonance is only very small (see Figure 34(a) in Section 7.6). The relaxation rates of the polymer PE6100 in interaction with the lipid bilayer are about double as high as the rates of the pure polymer PE3500 in water indicating a stronger restriction the polymer dynamics in the membrane.

For comparison, we determined the relaxation rates for all the lipid/polymer systems simulated. The results are summarized in Table 7. For all the systems of polymers that are deeply incorporated into the lipid bilayer, we obtain similar results of $R_1 \approx 3.6\text{ s}^{-1}$ for the PPO CH_2 group and $R_1 \approx 2\text{ s}^{-1}$ for the PEO CH_2 group and the PPO CH group. The exact polymer configuration in the membrane or the polymer concentration in the range investigated does not show an influence. Also the length of the polymer PPO block (PE3100 and PE6100) and of the lipid acyl chains (DMPC and DPPC) does not make a difference. Even higher relaxation rates are determined for the polymers forming an aggregate on top of the membrane. As for the pure Pluronic in water also for the lipid/water systems, the simulation results resemble the experimental values quite well. Only for the PPO CH group the experimentally determined value is a bit higher than the value from the MD simulations. But this difference is not very significant. We conclude that most polymers in the mixture are incorporated into the bilayer or interact with its surface.

In Figure 46, the results for the polymer R_1 relaxation rates, determined from the simulation of the 'membrane-spanning' system, are shown for all the individual C-H bonds investigated separately. While the relaxation rates of the PEO blocks decrease towards the chain end because of the increasing mobility, the relaxation rates of the PPO monomers are roughly constant over the entire block, only slightly increasing towards the block ends. From the R_1 profile along the polymer chain, we conclude that the relaxation rate R_1 is sensitive to the molecular motions present. Relaxation rates of the individual polymer C-H bonds in the different systems simulated are shown in the Appendix D.

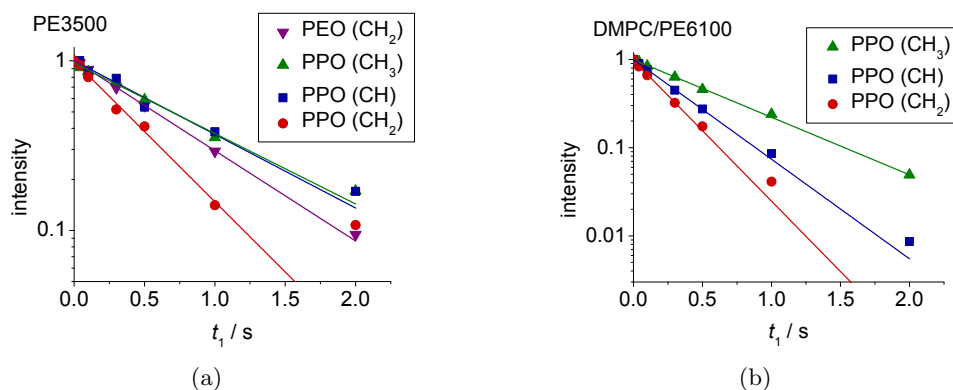


Figure 45: Signal decay recorded with the 'Torchia-like' experiment for (a) PE3500 in water with $c > \text{cmc}$ and (b) DMPC/PE6100 14:1 at about 30°C

sample	R_1 / s^{-1}			
	PEO (CH_2)	PPO (CH_2)	PPO (CH)	PPO (CH_3)
PE3500 in water	1.23 ± 0.02	1.91 ± 0.18	1.00 ± 0.10	0.96 ± 0.05
DMPC/PE6100 14:1		3.68 ± 0.15	2.60 ± 0.04	1.50 ± 0.04

Table 6: R_1 relaxation rates determined for the different polymer resonances using the "Torchia-like" pulse sequence at about 30°C . The errors are taken from the fit to the peak intensity decay.

system	R_1 / s^{-1}		
	PEO (CH_2)	PPO (CH_2)	PPO (CH)
PE3500			
single polymer in water	0.85	2.05	1.07
DMPC/PE6100			
single polymer in U-form	1.81	3.79	2.12
six polymers in U-form	1.74	3.59	2.05
membrane-spanning	1.73	3.57	2.03
aggregate on top of membrane	1.37	4.17	2.27
DPPC/PE6100			
membrane-spanning	1.71	3.37	1.93
DMPC/PE3100			
single polymer in U-form	1.81	3.54	2.01
membrane-spanning	1.84	3.54	2.01

Table 7: R_1 relaxation rates determined from MD simulations.

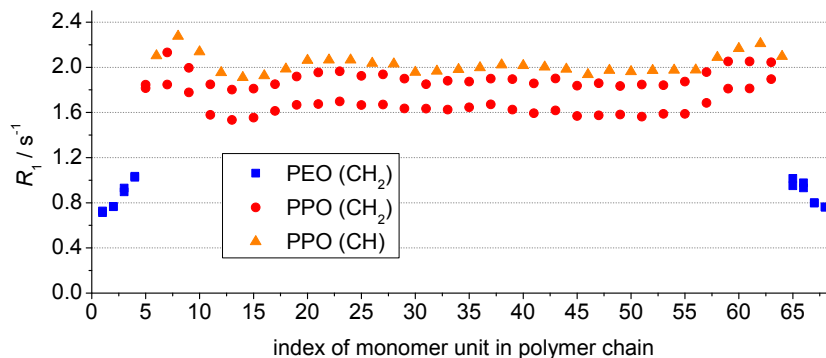


Figure 46: R_1 relaxation rates determined from MD simulation results of the membrane-spanning system. Here the results for every C-H bond in the polymer are shown separately.

Considering the multi-exponential fit to the correlation function, we conclude that the relaxation rates determined from the simulation are influenced significantly by molecular motions with rates considerably higher than the Larmor frequency, but they also contain contributions with correlation times near the T_1 minimum.

Summarizing the results from this section, we can say that the R_1 relaxation rates calculated from the simulations match the experimentally determined values quite well. However, a conclusion on the polymer configuration in the membrane cannot be drawn from the R_1 relaxation rates.

7.10.4 Comparison of Different Sample Preparation Methods

From literature, it is known that the way of sample preparation decisively influences the interaction between polymer and lipid bilayer and consequently the membrane properties like the permeability. When liposomes were formed in presence of the polymers then these polymers are incorporated deeply into the membrane and presumably the membrane-spanning configuration is preferred. In case that liposomes were prepared first and mixed with polymer solution subsequently, the polymer probably only interacts with the membrane surface or enters the membrane from one side in U-form configuration [18, 192–194].

way of preparation	f_a	$\nu_{D,res}$ / Hz	σ / Hz
normal	0.46 ± 0.05	153 ± 30	53 ± 15
separated	0.61 ± 0.05	163 ± 30	64 ± 15

Table 8: Results from the BaBa-xy16 experiment for a 20:1 mixture of DMPC and PE6100 at 40 °C.

For most of our experiments, lipid and copolymer of the desired ratio were codissolved in methanol/chloroform. Subsequently, the solvent was evaporated and the remaining powder was hydrated by adding 50 wt% of deuterated water. The resulting lipid bilayers should contain polymers that are built-in to a large extent. In the next step, we applied a freeze-thaw-vortex cycle for a few times to achieve a homogeneous mixture. This is necessary to achieve reproducible

results. However, the cooling of the bilayers might lead to a temporary 'squeeze-out' of the polymer from the membrane into the water layers in-between the lipid bilayers, because according to several literature sources, Pluronics do not incorporate into gel phase membranes [196, 220]. After increasing the temperature again, the polymer enters the bilayer when the fluid phase is reached. We will refer to the whole procedure as the 'normal' way of sample preparation.

For comparison, we prepared a sample of lipid and copolymer hydrated separately with 50 wt% of water and subsequently mixed together. Again, the vortex-freeze-thaw cycle was applied. We expect, that the polymer firstly interacts with the membrane surface and only after a while enters the membrane. Additionally, it should only interact with the outermost layer of the MLV in the beginning [66].

DQ build-up curves were recorded and analyzed for both samples at different temperatures. The results for 40 °C are shown in Table 8 exemplarily. While the dipolar coupling of the polymer PPO block and the coupling distribution width are the same within the uncertainty limits, the 'separately' prepared sample shows a somewhat higher fraction of polymer with anisotropic mobility than the 'normal' sample which is in contrast to our expectations. A reason might be that due to its high hydrophobicity, the polymer PE6100 enters the membrane very fast so that it does not matter in which step the two substances are mixed. However, the different preparation methods could influence the liposome structure.

With the experiment described in the following, we wanted to find out whether the polymer fraction showing isotropic mobility is located in the water phase around the MLVs or trapped within the vesicles. Two 20:1 mixtures of DLPC and PE6100 were prepared in the 'normal' way with 50 wt% water added to the first sample and about double the amount to the second sample. After the freeze-thaw-vortex cycle, we removed the excess water from second sample before measurements. From comparison of the peak intensities in the proton spectra of the two samples, we can see that the polymer content in the second sample is slightly reduced. This difference, however, is not very large and only amounts to a few percent. Also, the results from the BaBa-xy16 experiment are similar for both samples. We conclude that only very few polymer molecules are dissolved in the water phase surrounding the MLVs. Most of the isotropically mobile polymers are moving within the water layers between the lipid bilayers or are attached to the membrane surfaces, which corresponds to our findings from the R_1 measurements.

Accordingly, we also achieved nearly identical results for samples prepared with different amounts deuterated water (50, 60 and 85 wt%).

7.10.5 Influence of the Polymer Architecture

Influence of Hydrophobic Block: Firstly, we want to investigate the influence of the length of the PPO middle block. From the BaBa-xy16 experiment, we generally determine for our samples a decreasing fraction f_a of polymers showing anisotropic dynamics with increasing PPO block length (see Table 9). As can be seen in Figure 47(a), for a roughly constant PEO block length, f_a depends nearly linearly on the PPO block length. One possible explanation could be that a longer PPO block needs less stretching when built into the membrane and therefore has more motional freedom and exhibits more segments with an order parameter of zero. However, results from the MD simulations indicated that lipids and polymers exhibit a similar order which leads to the conclusion that the polymer fraction exhibiting isotropic mobility mainly originates

from polymers that are not inserted deeply into the membrane. We conclude that polymers with a shorter PPO block can build into the membrane more easily taking f_a as the amount of polymer inserted into the membrane.

From literature, it is known that the cmc and the cmt value of Pluronics is decreasing with increasing PPO block length for PEO blocks of constant length [171,202] (see Table 2 in Section 7.3). Consequently, the unimer concentration in the water phase decreases, so that less single chains are available that can be inserted into the membrane [178]. Assuming that the micelles cannot enter the membrane so easily, the block-length-dependence of the cmc therefore supports our experimental findings.

Furthermore, we know from literature that for Pluronics with identical N_{PEO}/N_{PPO} ratio, there are more limitations for the bigger polymers to enter the membrane which however also stay more stable inside the membrane when once built-in [174]. Similarly, Hezaveh et al. found from coarse-grained MD simulations that due to aggregation and entanglements of the hydrophobic middle blocks, the polymers with longer PPO blocks need longer or do not manage at all to enter the membrane in a given time [191]. Both of these literature findings are in agreement with our results.

From the fraction f_a of anisotropically mobile polymer and the lipid-polymer mixing ratio $X:1$, we determined the molar fraction of PPO monomers in the membrane:

$$X_{\text{PPO units}} = f_a N_{\text{PPO}} / (X + f_a N_{\text{PPO}}) \quad (88)$$

With rising PPO block length, the fraction $X_{\text{PPO units}}$ increases (see Table 9), that is the amount of PPO monomers in the membrane increases and consequently their effect on membrane properties. These findings are in agreement with many different results from literature. For example, it was found that polymers with longer PPO blocks cause a stronger decrease of the main lipid phase transition temperature [202], accelerate the lipid flip-flop motion more strongly [60] and increase the membrane permeability [60,194] more than polymers with shorter PPO blocks.

The two GP polymers GP17 and GP34 exhibit identical hydrophilic blocks and hydrophobic PPO middle blocks of differing length. While a membrane-bound fraction of about 0.2 can be measured for GP34 in mixture with DMPC, the polymer GP17 with the smaller PPO block does not show a higher anisotropic fraction, but in contrast a DQ build-up of the PPO methyl peak was not detected at all (see Table 10) which means that the respective dipolar coupling constant is very small or zero. The same result is obtained for a mixture of DLPC and GP17. In accordance with our DSC results (see Section 7.5), we conclude that GP17 only attaches loosely to the membrane surface where, according to the MD simulations (see Section 7.10.2), it probably exhibits nearly isotropic mobility. This explanation was also already proposed by literature [18,190,203]. Furthermore, also the NOESY experiment confirms the missing incorporation of the polymer GP17 into the membrane. For a mixture of the copolymer GP12 and DPPC, DMPC or DLPC we would expect similar results as this polymer has an even shorter PPO block and therefore is less likely to incorporate deeply into the membrane. Also literature results confirm that polymers with a hydrophobic block that is too short in comparison to the hydrophilic blocks only adsorb weakly to the membrane surface while more hydrophobic polymers enter more deeply into the membrane [14,197,203].

For the Pluronics with a PPO block length of 20, 30 and 40 monomers in mixture DMPC,

we determine dipolar coupling constants that are identical within the uncertainty limit ($\nu_{D,\text{res}} \approx 150$ kHz). Seemingly, these polymers are long enough to easily span the membrane. Only for the lipid/PE3100 mixtures, we detect a dipolar coupling of $\nu_{D,\text{res}} \approx 220$ kHz that is significantly higher. The reason might be the enhanced stretching of this polymer. However, because the dipolar coupling does not increase gradually with decreasing PPO block length but shows a sudden jump at about 15 units, also a different polymer configuration (U-form instead of membrane-spanning) could be the explanation (see Section 7.10.2). For all samples, we find $\sigma/\nu_{D,\text{res}} \approx 0.3$. For the mixtures with DLPC, we found similar results as for the mixtures with DMPC.

For PE6100 in DOPC slightly higher couplings were determined than for PE8100 in DOPC which can be explained by the higher hydrophobic thickness of the DOPC membrane in comparison with DMPC. Therefore the polymer block length has a stronger impact.

sample	f_a	$X_{\text{PPO units}}$	$\nu_{D,\text{res}} / \text{Hz}$	σ / Hz
DMPC/PE3100	0.72 ± 0.05	0.35 ± 0.05	232 ± 30	88 ± 15
DMPC/PE4300	0.61 ± 0.05	0.37 ± 0.05	149 ± 30	45 ± 15
DMPC/PE6100	0.46 ± 0.05	0.41 ± 0.05	153 ± 30	53 ± 15
DMPC/PE8100	0.34 ± 0.05	0.40 ± 0.05	135 ± 30	39 ± 15
DLPC/PE3100	0.54 ± 0.05	0.29 ± 0.05	215 ± 30	69 ± 10
DLPC/PE6100	0.49 ± 0.05	0.42 ± 0.05	143 ± 30	44 ± 10
DOPC/PE6100	0.70 ± 0.05	0.51 ± 0.05	245 ± 30	80 ± 10
DOPC/PE8100	0.57 ± 0.05	0.53 ± 0.05	176 ± 30	55 ± 10

Table 9: Results from the BaBa-xy16 experiment showing the influence of the PPO block length. Measurements on the mixtures with DMPC and DLPC were conducted at 40 °C and measurements on the mixtures with DOPC at 30 °C. The molar lipid-to-polymer ratio was 20:1 in all cases. The mole fraction $X_{\text{PPO units}}$ of PPO monomers relative to the lipid molecules in the bilayer was calculated from Equation 88 assuming f_a to be the fraction of polymer built into the membrane.

Influence of Hydrophilic Block: Length and structure of the hydrophilic block also influence the amount of polymer that is incorporated in the lipid membrane. Here, we generally find that polymers with bigger hydrophilic blocks incorporate in the membrane to a lesser extend than polymers with smaller hydrophilic blocks when the hydrophobic PPO block stays the same.

In Table 10, results for the mixtures of DMPC and the polymer PE3100, PE3500 and GP17, which all have a PPO block of 30 monomers, are compared. The highest anisotropic fraction was measured for PE3100, which only contains two PEO units. PE3500 has longer PEO blocks of about ten monomers each and accordingly, less polymer molecules are built-in the membrane. As already shown before, the polymer GP17 with its bulky PGMA end blocks does not insert into the membrane at all. In the same way, the polymer GP34 incorporates into the lipid membrane to a lesser extend than the polymer PE6100 which has smaller hydrophilic blocks (see downer

part of Table 10).

Additionally, it is already known from literature that Pluronics with longer PEO blocks incorporate less efficiently into lipid membranes than Pluronics with smaller PEO blocks [14, 16, 60, 191, 195]. This behavior can be explained by the cmc of the polymers which is rising slightly with increasing PEO block length. Consequently less polymers are available for getting incorporated in the membrane [171, 178, 185]. Furthermore, the bulky hydrophilic blocks can shield the hydrophobic PPO blocks preventing them from entering the membrane. Therefore, the polymers might only incorporate into the membrane after a very long time or stay as micelles in the surrounding water [18, 203]. Additionally, it was found in experiments [202] and in simulations [197], that for Pluronics with PEO end blocks exceeding a certain, relatively large number of EO monomers, the exact block length does not make a further difference for the lipid/polymer interaction.

In Table 10, we can see that the dipolar coupling constant of the hydrophobic PPO block is not influenced by the length and structure of the hydrophilic blocks. The bulkiness of the hydrophilic blocks should have an impact on the possibility to switch between transmembrane and U-form configuration [197]. In our experiments, however, we could not detect any effect.

sample	f_a	$\nu_{D,res} / \text{Hz}$	σ / Hz
DMPC/GP17	0	-	-
DMPC/PE3500	0.21 ± 0.05	232 ± 30	83 ± 15
DMPC/PE3100	0.72 ± 0.05	223 ± 30	88 ± 15
DMPC/GP34 (Anja)	0.18 ± 0.05	130 ± 30	45 ± 15
DMPC/PE6100	0.46 ± 0.05	153 ± 30	53 ± 15

Table 10: Results from the BaBa-xy16 experiment applied at 40 °C showing the influence of structure and length of the hydrophilic polymer block.

Influence of the Total Polymer Hydrophilicity:

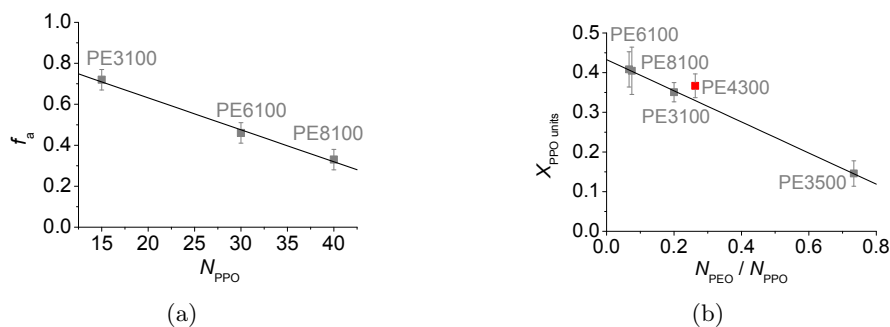


Figure 47: Results from the BaBa-xy16 experiment: (a) fraction f_a of polymer that shows anisotropic mobility which assumingly corresponds to the fraction of polymer that is incorporated in the lipid membrane; and (b) mole fraction $X_{PPO \text{ units}}$ of PPO monomers relative to the lipid molecules in the bilayer for different 20:1 DMPC/Pluronic mixtures measured at a temperature of 40 °C.

For a summarizing illustration of the influence of the hydrophilic and the hydrophobic blocks, we plotted the fraction $X_{\text{PPO units}}$ of PPO unimers in the membrane against the ratio of the polymer block length $N_{\text{PEO}}/N_{\text{PPO}}$. In the resulting graph (see Figure 47(b)), we basically see a linear decrease of $X_{\text{PPO units}}$ with increasing $N_{\text{PEO}}/N_{\text{PPO}}$, that is the PPO content in the membrane is decreasing with increasing polymer hydrophilicity which agrees well with results from literature [16, 174].

7.10.6 Temperature Dependence

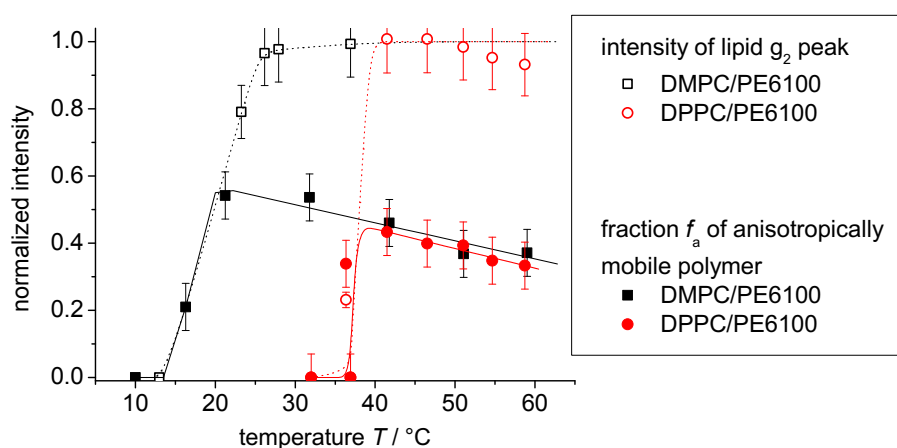


Figure 48: Temperature dependence of lipid and polymer components changing with the lipid phase transition. The open symbols represent the intensity of the lipid g_2 peak in the proton spectrum. The data points were normalized such that they reach unity at temperatures above the phase transition temperature because there all lipid molecules are assumed to be mobile and contribute to the signal. The filled symbols represent the fraction of anisotropically mobile polymer determined by the BaBa-xy16 experiment. Results for the mixture with DMPC are shown in black and for the mixture with DPPC in red. The lines are given as guides to the eye.

To get a better understanding of the lipid/polymer interaction and detect possible influences of the lipid mobility, we performed temperature-dependent measurements. As already explained in Section 5.2 on the example of a pure lipid sample, we acquired ^1H spectra at several temperatures and determined the intensity of g_2 resonance originating from the lipid glycerol backbone. The results are shown in Figure 48 as open symbols. In the phase transition region the peak intensity increases from zero to its maximum value due to the rising number of mobile lipid molecules. We normalized the data points in a way that they reach an intensity of one for high temperatures above the phase transition temperature because we assume that at these temperatures all lipid molecules are mobile and contribute to the signal.

The phase transition temperatures of the two mixtures lies slightly below the ones of the pure lipids. However, due to the temperature gradient over the sample and possible sample heating during the experiments, we refrain from determining this relatively small difference quantitatively. Like for the pure lipid samples, we checked the temperature calibration using the intrinsic water peak. The broader temperature range determined for the phase transition of the DMPC/PE6100 mixture compared to the phase transition range of the DPPC/PE6100 mixture can most probably

just be explained by the two different ways of sample preparation used (sample directly in the rotor between two spacers vs. sample in an additional insert) resulting in a different temperature gradient over the sample.

The fraction of anisotropically mobile polymer determined from the BaBa-xy16 experiment, that is the fraction of polymer incorporated in the membrane, is shown in Figure 48 for different temperatures as filled symbols. As the order in which the data points were collected did not make any difference, we conclude that all processes detected here are reversible and fast.

Firstly, we can see that there is slightly more polymer in the DMPC than in the DPPC bilayer. This difference, however, is not very big and will be explained in the next section in more detail.

When decreasing the temperature below the phase transition temperature, then the fraction of anisotropically mobile polymer gets smaller until it is not detectable anymore when the lipid bilayer is in the gel phase. We conclude that in this phase, the polymer is excluded from the membrane. Similar results also can be found in literature. While Firestone et al. claim that for their systems the Pluronics are not incorporated in the bilayer at low temperatures because of the improved water-solubility of the PPO block [13], others groups found that Pluronics generally do not incorporate in a lipid bilayer in the gel phase and that the water-solubility of the PPO block does not play a crucial role [196, 220]. The latter is in accordance with the results from our experiments. The tighter packing of the ordered lipid chains in the gel phase results in an expulsion of the polymer from the membrane [202]. Further literature results that confirm our findings come from measurements on systems of Pluronics in interaction with lipid monolayers. Compression of the layer leads to the 'squeeze-out' of the Pluronic when a certain pressure is reached and the other way around, the Pluronic only incorporates into the membrane when its pressure is below a certain value [15, 16].

The change of f_a at the phase transition temperature can be seen as one more proof that f_a corresponds to the fraction of polymer that is incorporated into the membrane. When it would contain signal from polymer attached to the membrane surface or from polymer forming aggregates in the water phase, then it would not decrease to zero when the temperature is lowered beneath the phase transition temperature because with this neither the lipid headgroup dynamics nor the water phase change strongly [220].

At temperatures above the phase transition temperature, the fraction of anisotropically mobile polymer decreases with rising temperature. This could be because there is indeed less polymer in the membrane at higher temperature keeping the assumption that f_a corresponds to the fraction of polymer in the membrane or because the PPO block becomes more mobile with rising temperature so that more segments contribute to the signal fraction of the mobile polymer blocks. A maximum number of polymers inserted into the membrane at the phase transition temperature can be explained by the fact that at this temperature the bilayer is exceptionally permeable [221, 222] and therefore allows for strong Pluronic-lipid interactions and consequently an effective incorporation of the Pluronics in the membrane [202, 209]. The increased membrane permeability is also combined with an enhanced flip-flop motion of the lipids at the phase transition temperature [223]. Therefore, also a polymer PEO block might switch more easily from one side of the membrane to the other so that a polymer could assume more easily the transmembrane configuration after entering the membrane.

However, a number of sources from literature also state that with rising temperature the

amount of polymer absorbed in the membrane is increasing because the bilayer gets more fluid (the absolute lipid order parameters decrease [34, 131, 157]) and the polymer become more hydrophobic which both should stimulate the interaction of the lipid chains and the polymer PPO block [196, 204, 220]. Others have concluded that with rising polymer hydrophobicity the binding strength of polymer and lipid bilayer is increasing and the polymer gets built-in the membrane more deeply [197].

Further influence might come from the self-assembly of the polymers. From literature results, it can be concluded that the amount of Pluronics in the membrane depends on the polymer cmc [169, 178]. With rising temperature, the cmc decreases and consequently less polymer unimers are available for the incorporation into the lipid bilayer.

The dipolar coupling of $\nu_{D,\text{res}} = (150 \pm 30)$ Hz and distribution width of $\sigma = (55 \pm 10)$ Hz determined for the anisotropically mobile fraction roughly stay the same over the whole temperature range.

7.10.7 Variation of the Lipid Molecules

In a next step, the influence of the lipid type on the lipid-polymer interaction will be investigated. While some literature sources state that the composition of the lipid membrane does not influence the effect of the Pluronic on membrane properties, like the permeability [60], others found that the incorporation of Pluronics in the membrane depends on the specific lipid structure, for example the saturation degree of the acyl chains [174].

sample	f_a	$\nu_{D,\text{res}} / \text{Hz}$	σ / Hz	$D_{c,\text{pure lipid}} / \text{\AA}$
DLPC/PE6100	0.49 ± 0.05	143 ± 30	44 ± 15	20.8
DMPC/PE6100	0.46 ± 0.05	153 ± 30	53 ± 15	24.8
DPPC/PE6100	0.43 ± 0.05	145 ± 30	54 ± 15	28.5

Table 11: Results from the BaBa-xy16 experiment demonstrating the influence of the lipid bilayer thickness measured at about 40 °C (the DPPC bilayer is just in the fluid phase) and literature results for the hydrocarbon thicknesses $D_{c,\text{pure lipid}}$ of the pure lipid bilayers determined at 50 °C.

Results from the DQ experiment for the Pluronics PE6100 in lipid membranes of DLPC, DMPC and DPPC that exhibit different hydrocarbon thicknesses are shown in Table 11. For the mixtures with PE6100, the fraction of anisotropically mobile polymer, that is the fraction of polymer incorporated, slightly decreases with increasing membrane thickness. This difference, however, is only very small. A possible explanation might be the higher stability of thicker membranes which reduces the membrane-polymer interaction [11].

Besides the illustration of the results for the different membranes determined at one specific temperature, also the results from a reduced temperature $T_{\text{red}} = T - T_m$ that depends on the main lipid phase transition temperature could be compared. From the temperature dependence shown in Figure 48 in Section 7.10.6, we can see that f_a at any fixed temperature difference T_{red} is bigger by about 0.05 for DMPC than for DPPC for the mixtures with PE6100.

The residual dipolar couplings and the distribution width are quite similar for the three mixtures. An enhanced stretching of the PPO blocks in the thicker membranes was not observed which is in accordance with results from MD simulations showing the same order parameters for the mixtures DPPC/PE6100 und DMPC/PE6100 (see Section 7.10.2). From, this we conclude that the PPO block of PE6100 with 30 units is long enough to easily span also the thickest membrane formed by DPPC.

Next, we want to investigate the influence of lipid chain saturation on the lipid/polymer interaction. For this, we compare results from the BaBa-xy16 sequence for the mixtures DOPC/PE6100 and DMPC/PE6100, shown in Table 12. DOPC has two unsaturated acyl chains which show a higher mobility than the saturated chains of DMPC. Additionally, DOPC exhibits a higher hydrocarbon thickness of $D_C = 27.1 \text{ \AA}$ than DMPC ($D_C = 26.2 \text{ \AA}$) [224]. For the mixture with DOPC, we determine a higher incorporated polymer fraction than for the mixture with DMPC. This finding is in accordance with literature results from Wu et al. who conducted studies on monolayers of DOPC and DPPC in interaction with the Pluronic P188 which incorporates in the DOPC monolayer already at a higher pressure than in the DPPC monolayer [174]. Reason for this behavior is probably the lower chain order in the bilayer with the unsaturated chain [8] which results in a reduced packing density that generally allows for an easier incorporation of guest molecules into the membrane [44, 190]. Order parameters for the different lipid segments are shown in Figure 65 in the Supplementary Section E.1.

In comparison to the results for the mixtures of a lipid with saturated chains and a polymer, we measure a distinctly higher dipolar coupling of about 245 kHz for the polymer PPO block in the mixture with DOPC. At first sight, this result seems to be contradictory as the lipid chains in the DOPC bilayer show lower order parameters and so should the polymer which adapts to the lipid geometry and dynamics. However, the total order parameter and thus the dipolar coupling of the PPO block is influenced more strongly by the way of polymer incorporation into the membrane than the exact order parameters of the individual PPO segments.

Additionally, we need to keep in mind that in this case, the way of sample preparation also could influence the measurement results strongly. While PE6100 is “squeezed-out” from the membrane at the phase transition temperature, there is no phase transition of DOPC and consequently the polymer stays in the membrane. This might influence the polymer configuration and lead to a preferred deeper incorporation of the polymer in the membrane.

sample	f_a	$\nu_{D,res} / \text{Hz}$	σ / Hz
DOPC/PE6100	0.70 ± 0.05	245 ± 30	80 ± 15
DMPC/PE6100	0.54 ± 0.05	155 ± 30	57 ± 15

Table 12: Results from BaBa-xy16 experiment at 30 °C showing the influence of saturation of the lipid chains.

7.10.8 Addition of Cholesterol

Additional to the lipid/polymer systems, we also investigated mixtures of lipid, polymer and cholesterol. Cholesterol causes an ordering of the lipid acyl chains which possibly influences the interaction of lipid and polymer molecules.

Using the R-PDLF experiment, we determined higher lipid order parameters S_{CH} for DMPC/Chol/PE6100 than for DMPC/PE6100 mixtures which confirms the increased ordering of the lipid chains in the second sample (for exemplary data see Figure 66 in the Supplementary Section E.1).

sample	f_a	$\nu_{D,res} / \text{Hz}$	σ / Hz
DMPC/Chol/PE6100 60:20:3	0	-	-
DMPC/Chol/PE6100 120:20:6	0.26 ± 0.05	136 ± 30	48 ± 15
DMPC/PE6100 20:1	0.46 ± 0.05	153 ± 30	53 ± 15

Table 13: Results from the BaBa-xy16 experiment conducted at 40 °C showing the influence of cholesterol on the lipid/polymer mixtures.

Results from the BaBa-xy16 experiment reflecting the behavior of the polymer PPO block are shown in Table 13. The higher the cholesterol concentration in the sample, the smaller is the anisotropic fraction f_a , that is, the less polymer is incorporated into the membrane. For the sample with the highest cholesterol concentration (molar ratio DMPC/Chol is 3:1), a build-up of the DQ signal is not detected, indicating that the polymer is not inserted into the membrane.

Our findings agree well with literature results. From monolayer studies, it was found that Pluronics only incorporate in membranes with reduced packing density [15,16,174]. As we increase the lipid packing density with the addition of cholesterol, a lower incorporation efficiency for the polymer is expected. Also from results of coarse-grained MD simulation, it was concluded that Pluronics interact preferentially with membranes exhibiting reduced integrity [175]. Furthermore, specific lipid/cholesterol/Pluronic samples are described in several publications qualitatively confirming our results that Pluronics interact less with lipid bilayers containing cholesterol in higher concentrations [201,204]. Accordingly, the addition of cholesterol also reduces the effect of Pluronics on membrane properties, for example the membrane permeability [66]. In contrast to that, also an opposing effect was found in monolayer studies of lipid/cholesterol/Pluronic systems. For monolayers under low pressure and/or Pluronics with long PEO blocks, Chang et al. found a preferred interaction of the copolymers with lipid/cholesterol membranes probably due to the formation of hydrogen bonds between the PEO blocks and the cholesterol hydroxy group [195]. However, as the Pluronic PE6100 investigated here only exhibits short PEO blocks, this effect is only weak.

From the results given in Table 13, it can be seen that the presence of cholesterol in the membrane does not have a significant influence on the dipolar coupling constant determined for the polymer PPO block. This is in agreement with the results presented in Section 7.10.6, showing that the total order parameter of the PPO block is not very sensitive to changes of the lipid order.

7.10.9 Concentration Dependences

In this section, we discuss the influence of the molar ratio of lipid to polymer on their interaction. In Figure 49(a), the fraction f_a of anisotropically mobile polymer determined from the BaBa-xy16 experiment for mixtures of different polymer concentration are shown. On the x -axis, the molar fraction $X_{\text{DMPC}} = X/(X + 1)$ of lipid molecules of the DMPC/PE6100 $X:1$ mixtures is plotted. With increasing polymer concentration in the sample, we measure an f_a that first decreases approximately linearly and then stays constant.

For an alternative plot of the same data, we again assume f_a to be the fraction of polymer that is built-in the membrane. In Figure 49(b), the molar fraction $X_{\text{POL,in}} = f_a/(X + f_a)$ of polymer in the membranes is plotted versus the molar fraction $X_{\text{POL,tot}} = 1/(X + 1)$ of polymer in the entire sample. It can be seen that the amount of polymer in the membrane generally increases with rising polymer concentration. When more polymer is available then also more polymer penetrates the membrane. A saturation limit does not seem to be reached for the concentrations used.

Qualitatively, our findings fit to literature results showing that the amount of Pluronic bound to the membrane and with this their influence on membrane properties increases with rising polymer concentration in the sample [179]. It also was found in literature that the amount of polymer built-in the lipid membrane depends on the polymer concentration relative to the polymer cmc, more precisely, Pluronic influence membrane properties most efficiently when their concentration equals the cmc [169, 178, 225]. For our mixtures, however, the polymer concentration exceeds the cmc in all cases.

For all mixtures a similar dipolar coupling constant of $\nu_{\text{D,res}} = (150 \pm 20)$ Hz and a distribution width of $\sigma = (53 \pm 10)$ Hz were determined indicating that the configuration of the polymers incorporated in the membrane is similar for all the different mixtures.

The lipid order parameters S_{CH} determined by using the R-PDLF experiment are equal within the uncertainty range for all the different mixtures. We therefore assume that also at the high polymer concentrations, the lipid bilayer structure is undisturbed.

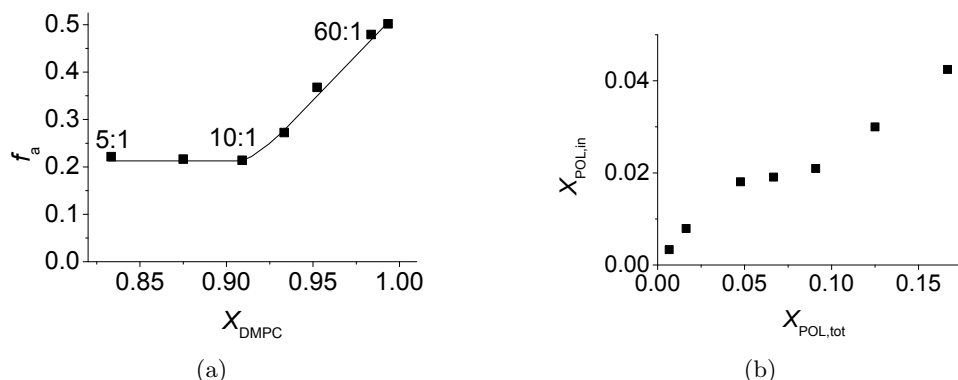


Figure 49: Results from the BaBa-xy16 experiment for mixtures of DMPC and PE6100 for different ratios measured at 50°C : (a) polymer fraction f_a showing anisotropic mobility depending on the lipid fraction X_{DMPC} of the mixtures; (b) total polymer fraction $X_{\text{POL,tot}}$ in the mixture vs. polymer fraction $X_{\text{POL,in}}$ in the membrane.

7.11 Summary of Results for the Lipid/Polymer Systems

It was the aim of this part of the thesis to get a detailed understanding of the interaction of amphiphilic triblock copolymers with lipid membranes. For the polymers to be investigated experimentally, we chose various Pluronics and GPs which contain PGMA instead of PEO end blocks. Additionally, lipid bilayer systems including Pluronics of different configurations were simulated. Order parameters and relaxation rates determined from the simulations for the lipids and for the polymers generally agree well with experimental results.

From experiments and simulations, we can conclude that all polymers interact with the lipid membranes. The most hydrophilic polymers GP12 and GP17, only interact with the membrane surface as can be seen from the DSC curves, the 2D NOESY spectrum and the BaBa-xy16 experiment. For all other polymers, we can prove that at least a part of the polymers incorporates deeply into the membrane. In these cases, cross-peaks between resonances from the polymer PPO block and the lipid tails appear in the 2D NOESY spectrum and a build-up curve for the PPO methyl resonance can be measured with the BaBa-xy16 experiment. Also from the systems simulated, we observed the Pluronics penetrate into the membrane. While a single Pluronic PE6100 enters the membrane after about 130 nm simulation time a polymer aggregate needs considerably longer.

The increased relaxation rates measured for the membrane/polymer systems as compared to the relaxation rates of the pure polymer in water indicate a restriction of the mobility of polymers that are incorporated in the bilayer.

From the simulations, we determined very small order parameters for polymers that are not incorporated in the lipid bilayer. Polymer chains that are deeply incorporated in lipid bilayer are on average aligned with the lipid tails near the upper chain region where the individual chain segments show similar order parameters as the lipid tails. In the center of the bilayer, the polymer middle part on average lies perpendicular to the bilayer normal between the bilayer leaflets. However, neither from the polymer order parameters or the R_1 relaxation rates, nor from the cross relaxation rates determined from the NOESY experiment, we could draw conclusions on the polymer configuration in the membrane, as the transmembrane and the U-form configuration are basically symmetric, yielding the same results. We assume that the shorter polymer PE3100 enters the membrane in U-form while for the longer PE6100 both configurations are possible.

From the BaBa-xy16 experiment, we find a fraction of polymer showing isotropic mobility, which we attribute to polymers dissolved in the water layers between the membranes, and a second component that exhibits restricted mobility probably due to the incorporation of the respective polymer PPO middle blocks into the membrane. With rising total hydrophilicity of the polymer (decreasing PPO block length, increasing size of the hydrophilic blocks), the amount of PPO units in the membrane decreases. Furthermore, the amount of polymer that enters the membrane depends on the membrane fluidity. The polymers generally only penetrate lipid bilayers in the liquid-crystalline phase and do not incorporate into a lipid bilayer in gel phase. In comparison to pure lipid bilayers, a smaller amount of polymers enters membranes containing cholesterol additionally.

Self-assembly of the polymers inside the membrane could not be detected. On the contrary, from simulations we find, that the polymers of an aggregate in the membrane separate after about 150 ns simulation time.

Furthermore, we found that lipid order and fast dynamics are not significantly influenced by the polymers as neither the lipid order parameters S_{CH} nor the lipid relaxation rates R_1 change appreciably.

8 Systems of Lipid Bilayers and Anion Transporters

Controlled molecular permeation through lipid membranes is essential for many biological processes, for example for the propagation of a nerve signal [7]. Because the hydrophobic core of a lipid bilayer effectively prevents the passage of ions and polar molecules [7, 30], the cell membrane is a natural barrier for a number of small molecules. However, there exist different mechanisms to transfer molecules from one side of the membrane to the other. For example, proteins can provide membrane-spanning hydrophilic channels for molecules to pass through or they can act as pumps [30]. Furthermore, certain molecules can be transported by membrane soluble carriers or by exocytosis and endocytosis [7].

In this part of the thesis, we investigate how synthetic molecules are capable of transporting ions over a lipid membrane. Specifically, we study a series of partially fluorinated anion transporters containing urea and thiourea groups [226, 227]. These mobile carriers are able to bind a target anion, like chloride, from water without involving the counteraction, pass through the membrane and release the anion on the other side [227, 228]. Here, we investigate the interaction of the carrier molecules with the lipid membrane without adding the anions. We applied the NOESY experiment to determine the average position of the molecules in the membrane.

8.1 Samples and ^1H Spectra

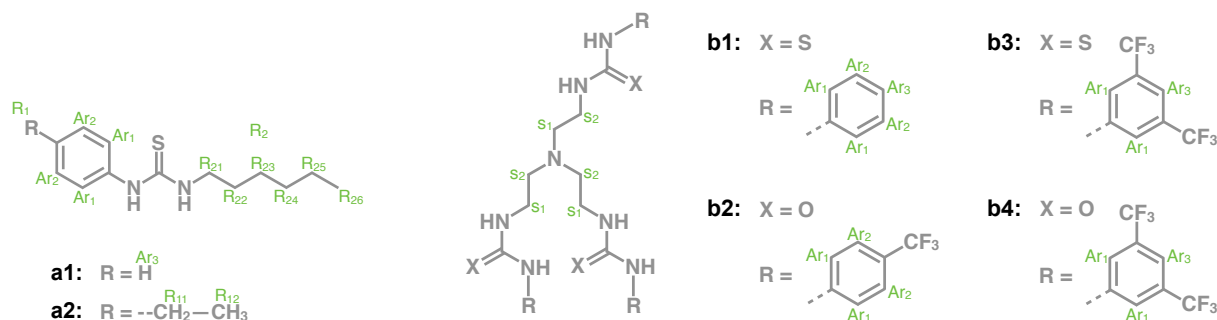


Figure 50: Molecular structures of ureas and thioureas that were investigated in interaction with lipid bilayers.

Firstly, we investigated two different 1-hexyl-3-phenylthiourea molecules, the structures of which are shown in Figure 50 on the left. It was shown that the positioning of the phenylthiourea binding unit within a linear carbon chain strongly influences the transport activity through a membrane [227]. Secondly, a series of fluorinated tripodal anion transporters containing urea and thiourea groups (see Figure 50 on the right) was studied. Also for these molecules it was proven before that they are capable of transporting anions through a lipid bilayer [226]. With rising degree of fluorination, their lipophilicity is increased and their transport activity enhanced [226]. All anion transporters were investigated in a 1:10 mixture with fully hydrated POPC. The resulting proton spectra are shown in Figure 51. The signals originating from the aromatic rings of the anion transporters are well separated from the rest and will be used in the following for the analysis of cross-relaxation rates.

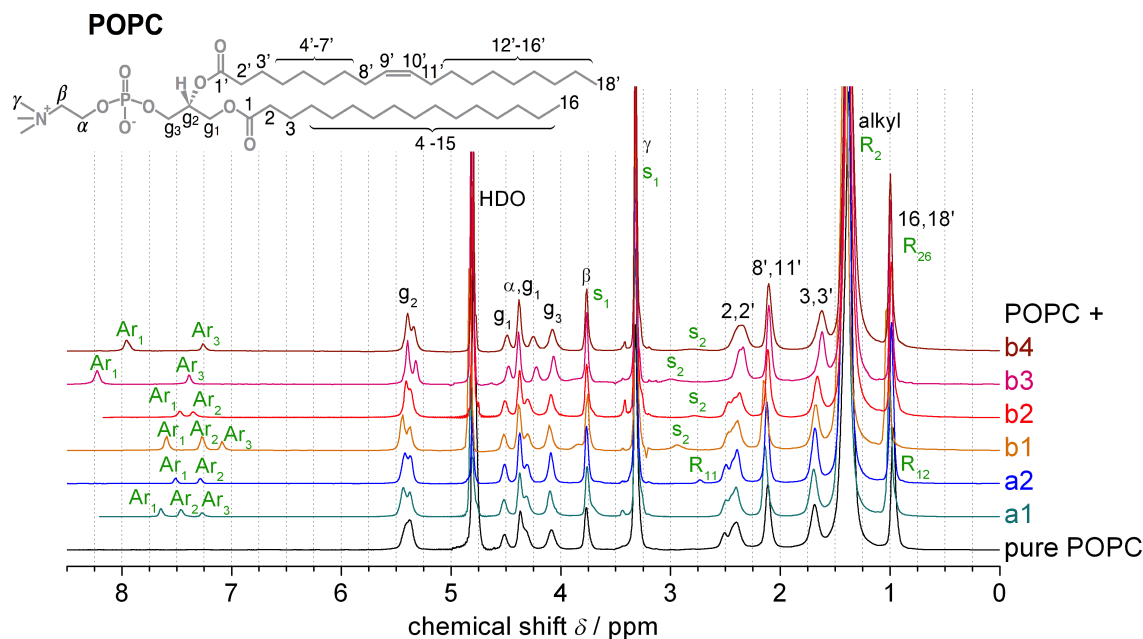


Figure 51: ^1H MAS spectra of POPC in a 10:1 mixture with different anion transporters (see Figure 50) acquired at a temperature of 25 °C.

8.2 Results from the NOESY Experiment

To probe the most favorable location of the carrier molecules in the membrane, we acquired two-dimensional ^1H - ^1H NOESY spectra under MAS. Cross peaks between the lipid signals and the resonances from the aromatic protons of the carrier molecules could be resolved well proving that the anion transporters penetrate deeply into the membrane. For a quantitative analysis, we performed the NOESY experiment for different mixing times between 1 ms and 1 s and additionally measured $T_1(^1\text{H})$ relaxation times using the SATREC experiment. Cross-relaxation rates were determined subsequently using the full matrix approach as described in Section 5.5. This most elaborate approach was used because of all the analysis methods, it yields the most reliable results for small cross-relaxation rates which are expected for carrier molecules that do not stay permanently inside the membrane. Partially, the cross peaks between the resonances of the carrier molecules and the lipids are very small and consequently the peak volumes are difficult to determine. For the resulting cross-relaxation rates shown in Figure 52, we therefore estimate an uncertainty of about 20%. To allow for better comparison, all cross-relaxation rates were normalized with regard to the number of contributing protons.

For all samples, the highest cross-relaxation rates were found between the aromatic protons of the anion transporters and the glycerol backbone and upper chain region of the lipids, possibly indicating that the carrier molecules are most frequently located in this region of the bilayer. Comparison with literature shows that this is a rather common result. In interaction with lipid bilayers, a number of different molecules, for example ethanol [70], aromatic multidrug transporter substrates [124] or a cannabinoid ligand [125], were found with the highest probability at the lipid/water interface near the glycerol backbone and the upper acyl chain region by using the NOESY experiment. Also for the amphiphilic triblock copolymers in interaction with

lipid membranes, we determined the highest relaxation rates from cross peaks between the polymer signals and resonances from the upper chain region of the lipids. However, in this case, the highest cross-relaxation rates did not indicate the preferred location of the polymer in the membrane but rather arose from the slower reorientational motions of the respective lipid-polymer interconnecting H-H vectors. Consequently, it cannot be concluded with certainty that the aromatic rings of the anion transporter preferentially locate in the glycerol backbone-upper acyl chain region of the lipid bilayer. Instead, the reason for the high cross-relaxation rates could also be the smaller mobility of these lipid segments. Generally, cross-relaxation rates can only be interpreted in terms of contact probabilities or molecular distributions when the guest molecules on their own perform fast isotropic reorientational motions, which is unknown here and most probably depends on the molecule size.

Although, the cross-relaxation rate profiles look rather similar for all samples investigated, the total values show differences depending on the precise structure of the anion transporters. For the aromatic rings in the POPC/a1 sample, we generally find smaller cross-relaxation rates than for the aromatic rings in the POPC/a2 sample which can be explained by the higher lipophilicity of a2 causing a higher attraction to the lipid bilayer [227]. From the results of the tripodal anion transporters (b1-b4) in POPC, we conclude that higher cross-relaxation rates can be determined for molecules containing more fluorinated groups. Also in this case the lipophilicity of the molecules is enhanced with increasing degree of fluorination, causing a stronger interaction with the membrane [226]. For the samples POPC/b3 and POPC/b4, we obtain similar results for the cross-relaxation rates. The substitution of the oxygen in the urea group by sulfur in the thiourea group does not seem to have much influence on the interaction of the anion transporter with the membrane, although it is known from literature that it should influence the lipophilicity of the molecule [226].

In summary, we can say that the highest cross-relaxation rates were generally found between the aromatic protons of the anion transporters and the protons of the lipid upper acyl chains. More lipophilic molecules show a stronger interaction with the membrane and consequently exhibit higher cross-relaxation rates.

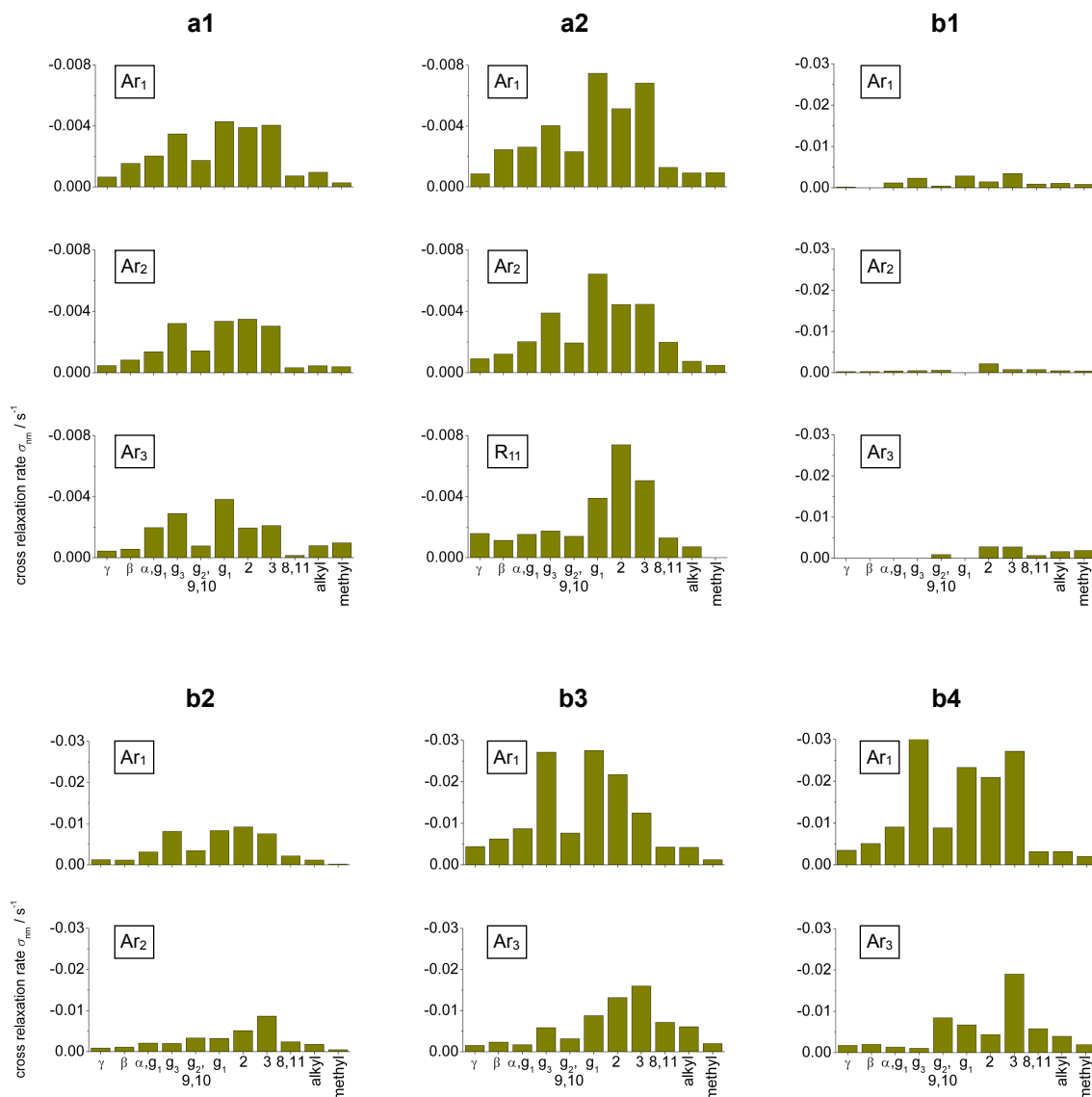


Figure 52: Cross relaxation rates determined for 10:1 mixtures of POPC and the respective carrier molecule from the NOESY experiment at 25 °C using 10 kHz MAS. To avoid peak broadening due to magnetic field drift, a ^2H lock was applied. All cross-relaxation rates were normalized by the number of protons in the molecule. The uncertainty is estimated to be about 20%. The cross-relaxation rates determined for the mixtures with the anion transporters a1 and a2 are significantly smaller than the cross-relaxation rates of the mixtures with the anion transporters b1 to b4. Therefore, a different scale of the y -axis was used.

9 X-shaped Bolapolyphiles in Interaction with Lipid Bilayers

In this section, we turn on polyphilic rigid molecules, specifically X-shaped bolapolyphiles. In interaction with lipid membranes, rigid molecules generally can develop a variety of different structures, for example, they can self-assemble and form pores [74, 203] or cause membrane compartmentalization [229]. As a result, phase transitions can change and the membrane can be stabilized or destabilized [229].

Bolaamphiphiles form a specific class of amphiphilic molecules. They consist of a hydrophobic middle part with two hydrophilic head groups at both ends. Bolaamphiphiles can assemble into monolayered membranes and also incorporate in lipid bilayers [230]. Here, we investigated bolapolyphiles which exhibit both, stiff and flexible hydrophobic units. By varying the specific chemical structure of the individual molecular regions, we seek to investigate their influence on the lipid bilayer-bolapolyphile interaction. These results were published in two papers [5, 6].

9.1 Sample Systems and Previous Results

In this work, we studied two different X-shaped bolapolyphilic molecules in interaction with DPPC and DOPC bilayers. The structure of the bolapolyphiles is shown in Figure 53. Generally, they consist of a stiff rod-like aromatic core, which is terminated by two identical hydrophilic end

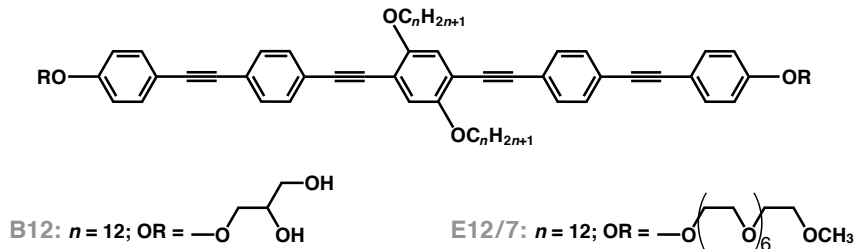


Figure 53: Chemical structures of the X-shaped bolapolyphiles investigated.

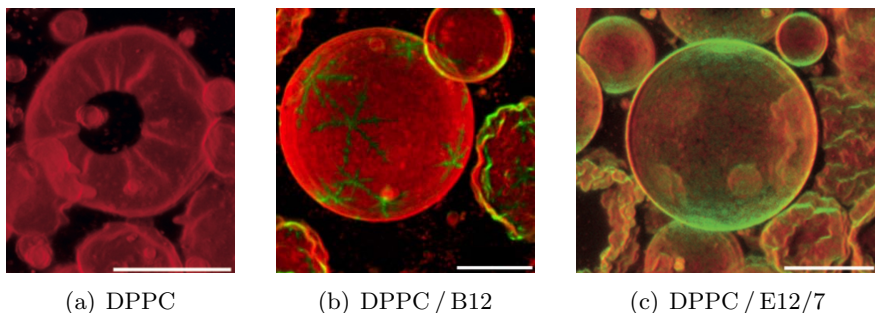


Figure 54: Confocal fluorescence images taken at room temperature (22 °C). The mixtures were prepared with a lipid/bolapolyphile molar ratio of 10:1. The autofluorescence of the bolapolyphiles is shown in green and the red fluorescence comes from a dye label added to the lipids. The scale bars correspond to a length of 20 μm (taken from [5]).

groups. Additionally, flexible aliphatic side chains are attached to the center of the core. The length of the rigid core of about 3 nm is comparable to the thickness of the lipid bilayer [4, 231]. There are a number of molecules available, that exhibit this general structure but differ in lengths and type of the side chains and the head group [5, 229].

We firstly have chosen the bolapolyphile B12 which has glycerol head groups capable of hydrogen bonding, and side chains of twelve carbons [5]. As B12 mainly consists of hydrophobic units, it is not water-soluble. Instead, it forms crystals, with the phenyl rings performing 180° flips and the side chains showing a certain, although restricted mobility [144].

The bolapolyphile E12/7 is the second molecule we investigated [5]. As for B12 its side chains contain twelve carbons each. The head group of E12/7 consists of a chain of seven ethylene oxide units, which are incapable of acting as hydrogen-bond donor.

The chemical synthesis of X-shaped bolapolyphiles was done at the Institute of Chemistry in the framework of different projects in the DFG-funded research unit FOR 1145. In the following, results for two different sample systems will be presented and compared.

DPPC / B12 System: Mixtures of DPPC, B12 and water were investigated by a number of different techniques revealing an inhomogeneous system which shows a rather complex and concentration dependent phase behavior. Using DSC, numerous phase transitions were detected [4]. Confocal fluorescence images of giant unilamellar vesicles in the gel phase revealed supramolecular snowflake-like structures formed by B12-rich phases (see Figure 54(b)) suggesting a certain regular packing structure of the individual B12 molecules [5]. These structures can be stabilized by hydrogen bonds between the head groups of the bolapolyphiles and between the head groups of the lipids and the bolapolyphiles. The transmembrane orientation of the B12 molecules was deduced from infrared spectroscopy and fluorescence anisotropy experiments [4].

Taking together various results from X-ray diffraction and NMR measurements, a honeycomb structure as shown in Figure 55 was suggested [5, 232]. The honeycomb walls are formed by the rod-like π - π -stacked backbones of the B12 molecules and honey cells accommodate the alkyl side chains as well as confined lipids. The glycerol head groups of B12 are aligned along the upper and lower edges of the honeycombs.

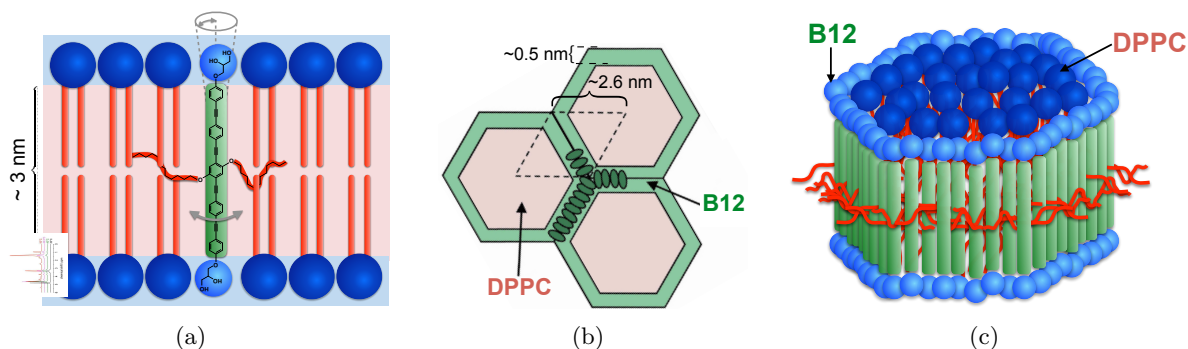


Figure 55: Schematic plot of the honeycomb structure formed in a DPPC / B12 system [5].

DPPC / E12/7 System: For the system of DPPC and the bolapolyphile E12/7, macroscopically segregated domains cannot be seen in the images of fluorescence microscopy (see Figure 54(c)). Because of the reduced capability of E12/7 for hydrogen bonding, it does not form dense supramolecular structures [5]. In the DSC thermogram, only one peak corresponding to the main lipid phase transition is visible [6]. Like the B12 molecule in the lipid bilayer, also E12/7 is oriented approximately transmembrane [5].

9.2 ^1H Spectra

DPPC / B12 System: As already explained in Section 5.2, valuable information on molecular mobility can be extracted from ^1H line shapes. Therefore, we acquired ^1H spectra for a number of temperatures between 25 °C and 80 °C for a pure DPPC sample and for a 4:1 and a 10:1 mixture of DPPC and B12 to study phase behavior and transitions of the sample systems on a molecular level [5,6]. Measurements and data analysis for the DPPC sample and the 4:1 mixture were done by A. Achilles [144].

In Figure 56(a) three ^1H spectra are shown exemplarily. The peak intensities were determined by integration over the peaks after a baseline correction was performed. To make the resulting intensities comparable to each other, they were divided by the lipid mass in the sample and the number of protons contributing to the peak. Furthermore, the same number of scans was used for all experiments and Curie correction was applied. Subsequently, all intensities were normalized in a way that the intensity of the g_2 peak of the pure DPPC sample at 50 °C reached one. Due to this procedure, all peak intensities are proportional to the fraction of mobile molecules in the sample.

In Figure 56(b) the resulting temperature dependent signal intensities for the g_2 peak and the aliphatic region from the lipid, and the aromatic protons of B12 are shown, along with the DSC curves. At temperatures below the main phase transition temperature of pure DPPC, for all mixtures, mainly a broad peak arising from the rather immobile lipid molecules is visible. Only head group resonances can be distinguished (see Figure 56(a)).

With rising temperature, pure DPPC shows a well defined phase transition, characterized by a sharp increase of the g_2 and alkyl chain signal intensities. However, for the 4:1 and the 10:1 mixture of DPPC and B12 only about 20 % and 50 % of the lipid molecules becomes mobile at the main phase transition temperature, respectively. The remaining lipids are probably located in the B12-enriched phase where they are immobilized within the honeycomb cells formed by B12. Accordingly, also the signals of the well-packed aromatic cores of B12 are not detectable at this temperature.

The first additional peak in the DSC curve can be seen at 60 °C for the 4:1 mixture and at 55 °C for the 10:1 mixture pointing to another phase transition which, however, cannot be correlated to any specific changes of the ^1H signal intensities. An explanation was found by help of ^{13}C spectra recorded for the 4:1 mixture. From a position switch of an aromatic signal of B12 at about this temperature, we concluded on a change in the π - π packing [6]. With increasing temperature, the lipid signals slowly grow further and also small B12 signals appear. The peaks of the aromatic rings of B12 appear between 7 and 8 ppm well separated from the lipid resonances.

The next DSC peak appears at about 67 °C and 62 °C for the 4:1 and the 10:1 mixture respectively. Because we observe the most rapid increase of the lipid signal intensity in the ^1H

spectrum in this temperature range, it is attributed to the phase transition of the lipid molecules confined by B12. Meanwhile, the signal intensity of the aromatic protons of B12 is small and just slowly increases to its maximum in the temperature range of the third DSC peak which appears at 75 °C for 4:1 and at 67 °C for the 10:1 mixture, respectively. Therefore, we can conclude that this transition is associated with the mobilization of the aromatic cores of B12 which goes along with the dissolution of the supramolecular structure. The temperature difference of about 5 °C of all the additional DSC peaks of the two different mixtures can possibly be explained by different structure or size of the macroscopic domains.

Above all phase transitions at a temperature of $T \geq 75$ °C, all peaks reached maximum intensity within the error margin of about 10 %, confirming that a homogeneous mixture with fully mobilized molecules is reached [5].

In conclusion, we can say that we were able to assign the phase transitions detected by DSC to the different components in the system by help of the ^1H and ^{13}C spectra.

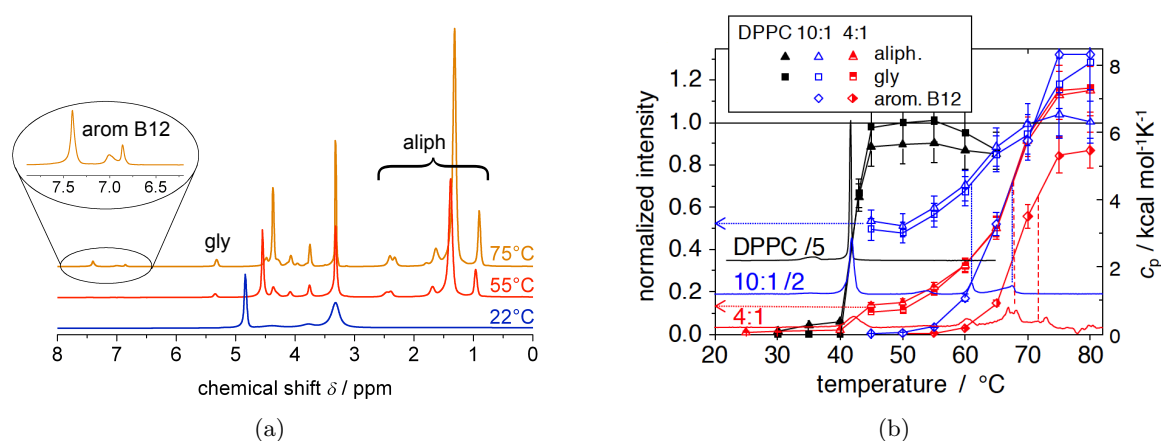


Figure 56: MAS ^1H NMR data of hydrated pure DPPC and two mixtures of DPPC and B12. (a) Exemplary quantitative ^1H spectra of a 10:1 mixture DPPC/B12 taken at three different temperatures. (b) Integrals of different spectral regions depending on temperature overlaid with scaled DSC traces (right vertical scale) (from [6]). The data for the pure DPPC sample and the 4:1 mixture of DPPC and B12 was measured and analyzed by A. Achilles [144]. The DSC curves were provided by B.-D. Lechner [4].

DPPC / E12/7 System: In Figure 57, a DSC curve measured by B.-D. Lechner and normalized ^1H peak integrals for a 4:1 mixture of DPPC and E12/7 are depicted. At the main phase transition temperature, the lipid signals rise to maximum intensity which means that, within the uncertainty limits, all lipids become mobile at this temperature. The phase transition of the lipid molecules is also reflected by the peak in the DSC curve. However, only small signals from the aromatic protons of E12/7 can be detected in the ^1H spectrum that also increase only very slowly with rising temperature. At 75 °C, the peak intensities reached about 10 % of the expected maximum intensity. It was thus concluded that E12/7 forms π -stacked, rigid domains, presumably filaments with a width in the nanometer range, that randomly pervade the DPPC membranes and are too small to be seen in the fluorescence measurements [5, 6]. These fibrils do not melt/disintegrate within the temperature range studied by DSC [6]. Instead the E12/7 molecules stay immobilized to the highest temperature measured of 75 °C. A further confirmation of the fibril hypothesis is

given by the lack of corrugation of the DPPC / E12/7 GUVs shown in the fluorescence microscopy images in Figure 54(c). While the pure DPPC in the gel phase exhibits somewhat crumpled GUVs (see Figure 54(a)), the vesicles formed by DPPC in mixture with E12/7 are round and smooth, suggesting that the E12/7 fibrils separate small patches of DPPC along line defects.

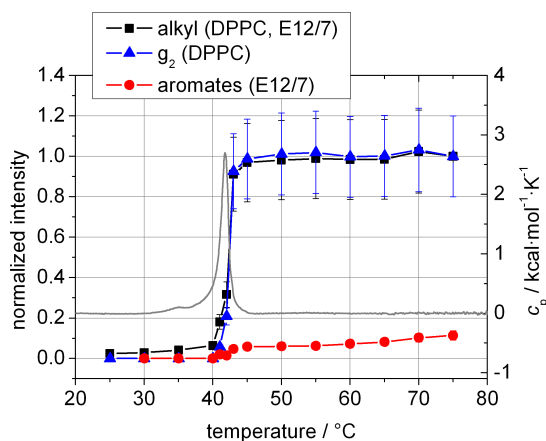


Figure 57: Intensities determined from the ^1H spectrum of the mixture DPPC / E12/7 4:1 of two different lipid peaks and the aromate peaks of E12/7 depending on the temperature together with the DSC curve.

Generally, the different behavior of the B12 and the E12/7 bolapolyphiles in the DPPC membrane can probably be explained by their different capabilities to form hydrogen bonds that can stabilize the molecular aggregate structures.

9.3 ^1H - ^{13}C Dipolar Couplings from the DIPSHIFT Experiment

Order and motional geometry of the X-shaped molecules and the lipid bilayers were determined from dipolar couplings measured using different NMR pulse sequences. To cover the wide range of heteronuclear coupling constants of the more rigid bolapolyphiles and the mobile lipids, we performed DIPSHIFT and recDIPSHIFT experiments.

DPPC / B12 System: The experiments for the 4:1 mixture of DPPC and B12 were acquired and analyzed by A. Achilles for different temperatures. By help of a fit function, the dipolar coupling constants were determined from the resulting modulation curves (as explained in Section 5.6.1) and the respective order parameter was calculated. Here, we will only summarize the results shortly. For a detailed description see References [6, 144]. The 10:1 mixture yields too small ^{13}C signals from B12 to analyze their intensities in the DIPSHIFT experiment.

As for the lipid resonances, it is noted that in the homogeneous mixing phase at 75°C , a variation in the order parameters S_{CH} was not detectable, indicating that the lipid membrane remained unchanged upon bolapolyphile addition, at least on the fast timescale probed by S_{CH} . Probably due to the transmembrane configuration of the B12 molecules, the motional freedom of the lipid molecules is not influenced.

The order parameter S_{CH} of the B12 molecules in the lipid bilayer was determined for a number of different temperatures. At 45°C and 55°C , the sample system is phase-separated and the B12 molecules exhibit a similar type of motion as in the crystal, that is, they perform 180°

two-site jumps about their molecular long-axis and additional wobbling motions which result in an order parameter of $S_{CH} \approx 0.6$ for aromatic ring carbons with directly bonded protons and $S_{CH} \approx 1$ for quaternary ring carbons.

At a temperature of $T = 75^\circ\text{C}$, the supramolecular structure is dissolved and the B12 aromatic rings perform uniaxial rotations about the molecular long axis, again with additional wobbling motions. Consequently, for all B12 resonances an order parameter of $S_{CH} \approx 0.1 - 0.2$ was determined.

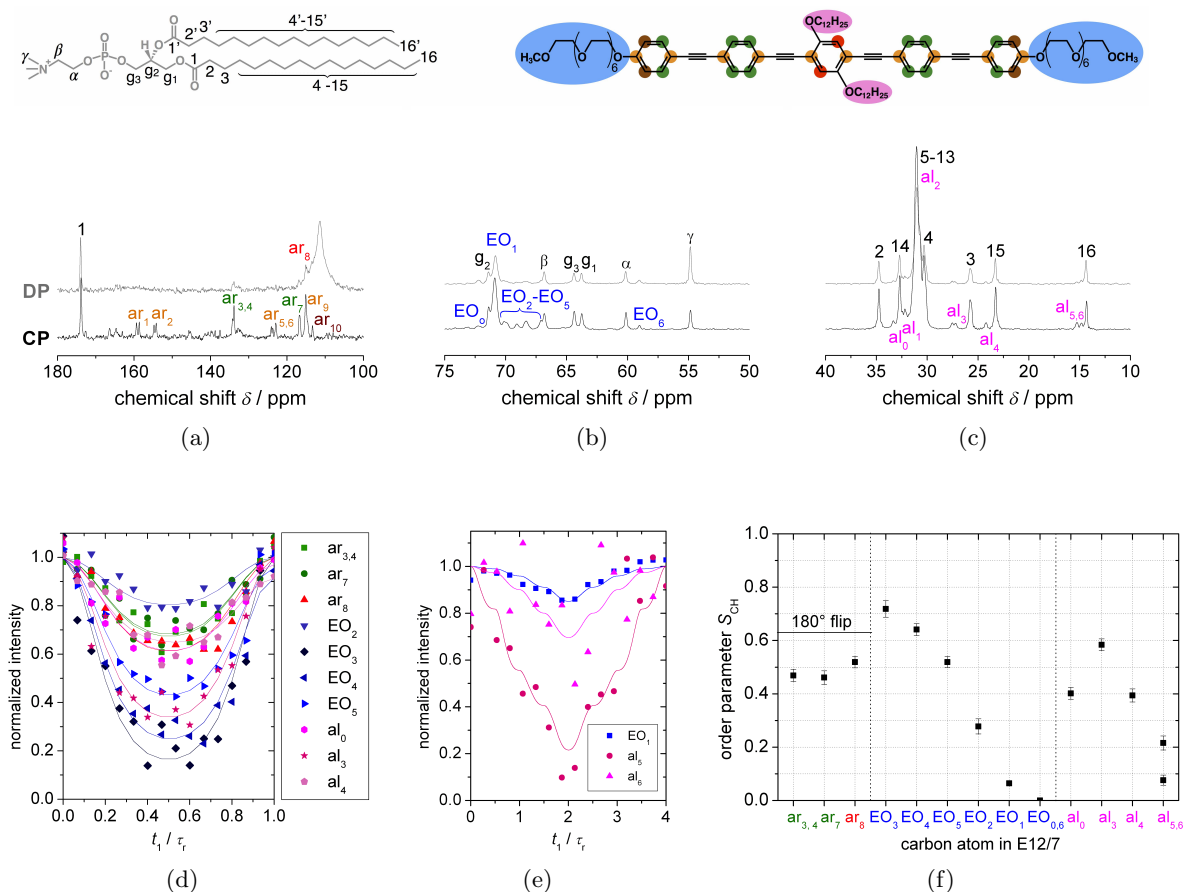


Figure 58: (a)-(c) Details of the ^{13}C spectra measured with DP (grey) and CP (black) excitation at 50°C for a 4:1 mixture of DPPC and E12/7. Resonances originate from (a) the aromatic rings of E12/7, (b) the head group regions and (c) the aliphatic chains. Signals from the lipid are denoted in black and the resonances originating from E12/7 are marked according to the color scheme shown in the molecular structure above. Under the same experimental conditions, modulation curves reflecting the dipolar coupling constant were recorded using (d) the DIPSHIFT and (e) the recDIPSHIFT pulse sequence. In (f) the resulting order parameters for E12/7 are shown. The order parameter of $S_{CH} = 0.63$ that is expected for aromatic rings performing 180° flips is shown as a dotted line [84, 144].

DPPC / E12/7 System: In Figure 58, ^{13}C spectra and S_{CH} order parameters determined from a 4:1 mixture of DPPC and the bolapolyphile E12/7 are shown. Comparing the results from the DP and CP excitation scheme in (a)-(c), we find higher peak intensities from E12/7, especially for the aromatic rings, in the CP spectrum. Due to motional restrictions, dipolar couplings of E12/7 are relatively high and therefore can mainly be measured with the DIPSHIFT experiment. The recDIPSHIFT experiment was only used to determine the smaller couplings on the chain ends. The resulting order parameters are shown in Figure 58(f). For peaks that have too low intensity or partly overlap with other peaks and for quaternary ring carbons, we did not determine a dipolar coupling.

The aromatic rings of E12/7 show a slightly lower order parameter of $S_{\text{CH}} \approx 0.5$ in DPPC than the aromatic rings of B12. We therefore conclude on molecular dynamics with higher motional amplitude occurring due to a somehow less defined π - π packing structure. For the EO head groups we determined increasing mobility and accordingly decreasing order parameters towards the chain ends. Generally, the EO head groups are more mobile than the glycerol head groups of B12, probably because of the lack of hydrogen bonds [6].

A similar mobility gradient was detected for the aliphatic side chains. Furthermore, the spectrum contained two signals (denoted as $\text{al}_{5,6}$) originating from methyl groups of the alkyl side chains of E12/7 and accordingly two different order parameters were determined. The two signals possibly can be explained by two different packing modes for the two lateral alkyl chains of the E12/7 in the fibrillar structure (realized, e.g., in a double strand). However, it is also possible that the additional signal arises from a more ordered minority fraction of the lipid in interaction with the E12/7. Generally, the ^{13}C NMR results reflect the restricted motions of E12/7 in the membrane and therefore confirm the small peak intensities measured in the ^1H spectrum.

9.4 ^1H - ^1H Dipolar Couplings from DQ Sideband Spectra

DPPC / B12 System: To study the wobbling motion of the B12 molecules in the membrane more in detail, order parameters S_{HH} were determined using DQ sideband measurements [5, 6]. We here investigated the protons in the *para*-substituted phenyl rings. Their internuclear vector points along the long axis of the molecule and is thus not affected by the fast uniaxial rotational motion but only by the additional fluctuations of the molecular long axis. The DQ sideband spectrum (see Figure 59(a)) was acquired using the BaBa-xy16 pulse sequence as described in Section 5.6.4. The individual sidebands were integrated to determine their intensity. Small shoulders appearing on the left side of the peaks, which possibly correspond to additional couplings, were omitted. For the two, theoretically identical, sidebands on opposing positions relative to the center of the spectrum, the average value of the two intensities was taken and their difference was considered as error during the fit. For calculating the order parameter, we used a reference coupling of $\nu_{\text{D, res}} \approx (8300 \pm 400)$ Hz determined from the average distance $r \approx 2.44\text{\AA}$ of two aromatic ring protons. The measurements were conducted for both mixtures of DPPC and B12 over a temperature range of $65 - 80^\circ\text{C}$, in which the aromatic ^1H signals of B12 can be resolved. As can be seen in Figure 59(b), the resulting dipolar couplings or order parameters S_{HH} , alternatively, show a relatively large distribution. Possibly, this comes from inhomogeneities in the sample, like local concentration fluctuations, that even exist at high temperatures ($T = 80^\circ\text{C}$)

at which the system is characterized as a homogeneous mixture. With increasing temperature, the order parameter decreases slightly indicating a small increase of the motional amplitude of the wobbling motion. The most important outcome of this measurement, however, can be deduced from a comparison of the results of the two mixtures. The order parameter of B12 is lower in the 10:1 mixture than in the 4:1 mixture, suggesting smaller-amplitude motions of B12 when its concentration in the membrane is higher, probably due to crowding effects. Depending on the assumed motional model (rotation on or within a cone), the mean tilt angle of the molecules with respect to the membrane normal can be estimated to be about 20° – 30° and 35° – 45° for the 1:4 and 1:10 mixtures, respectively [84]. This result can probably be explained as an crowding effect of the B12 molecules. In the 1:4 sample, they restrict the molecular dynamics of each other more strongly than in the 1:10 sample. Additionally, we determined a broader distribution width of dipolar couplings for the 10:1 mixture than for the 4:1 sample.

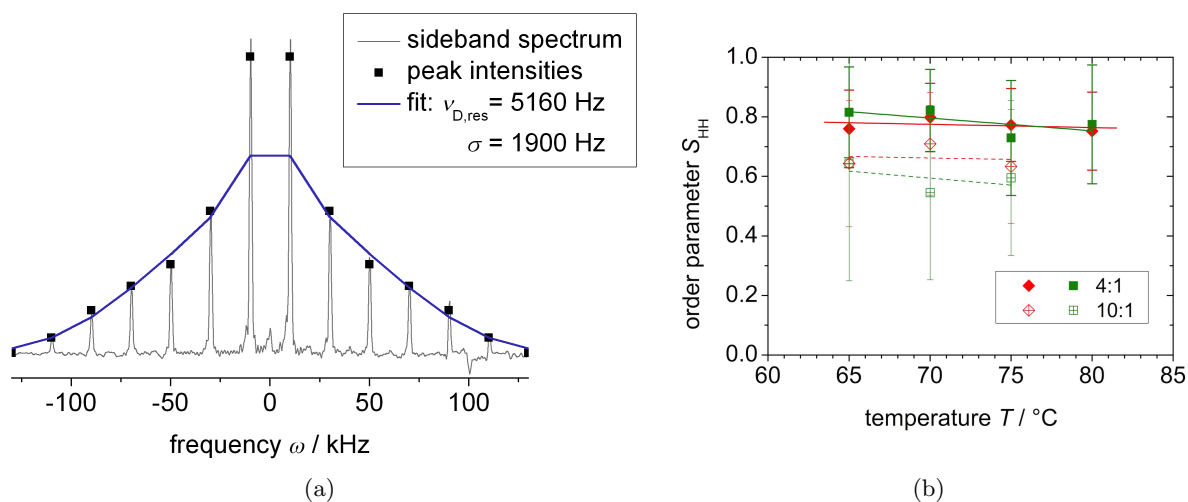


Figure 59: (a) DQ spinning sideband pattern determined using the BaBa-xy16 pulse sequence for an aromate resonance of B12 in a 1:10 mixture with DPPC at 75 °C. We used a MAS frequency of 10 kHz a DQ evolution time of $\tau_{\text{DQ}} = 4\tau_r$ and acquired spectra for 512 t_1 times incremented in steps of $\Delta t_1 = 2.5 \mu\text{s}$. The blue line represents the fit function from which we obtained the ^1H – ^1H dipolar coupling and its distribution width; (b) Order parameters S_{HH} determined from the DQ sidebands for 4:1 and 10:1 mixtures of DPPC and B12 evaluated for two aromate signals each as a function of temperature. The error bars indicate the dipolar distribution width σ from the fit; the actual experimental error is smaller and apparent from the deviations from the trend lines (adapted from Reference [6]).

10 Summary

In this work, the interaction of a number of different amphiphilic and polyphilic molecules in interaction with lipid model membranes was characterized by different solid-state NMR techniques. Spectral distinction between the lipid and the guest molecules was reached by the usage of MAS. Already simple ^1H and ^{13}C spectra contain information on sample composition and molecular mobility and for example allow for the observation of phase transitions. R_1 relaxation rates were determined to study molecular dynamics more in detail. Being influenced mainly by dipolar interactions, they depend on the order parameter as well as on correlation times of bond reorientational motions. The 2D NOESY experiment was used to prove the deep insertion of the guest molecules into the membrane and to qualitatively probe their average location. Using dipolar NMR methods, structure or packing and dynamics of the lipid molecules as well as the interacting guest molecules was described. From the DIPSHIFT, the R-PDLF and the BaBa-xy16 experiment, we determined residual dipolar couplings for specific resonances from which dynamic order parameters were calculated. Furthermore, DSC curves were recorded to investigate the phase transition behavior of the lipid/guest molecule systems. The lipid/triblock copolymer systems were additionally modeled by MD simulations.

Triblock Copolymers: The main part of this thesis deals with lipid bilayers in interaction with amphiphilic triblock copolymers that contain a hydrophobic PPO middle block between two hydrophilic end blocks. Results from the NOESY and the BaBa-xy16 experiment and from DSC measurements confirmed the interaction of all polymers investigated with the lipid bilayers. While in some cases the polymers only interact with the membrane surface, for other systems, for example for DMPC/PE6100, the deep insertion of the polymer into the membrane was proven directly by cross peaks between resonances of the lipid tails and the polymer in the 2D NOESY spectrum. Relaxation rates R_1 determined for Pluronics in mixture with lipids are about two times larger than relaxation rates of pure Pluronics dissolved in water at a small concentration indicating a more restricted mobility of the polymers in the first system probably due to the incorporation into the lipid bilayer or the interaction with the membrane surface.

For a more detailed interpretation of our experimental findings, we performed MD simulations. Their validity was confirmed by the good agreement of the experimental and the simulation results for the order parameters and R_1 relaxation rates of the lipids and the polymers in the pure aqueous systems and in mixture. Also the radius of gyration calculated for a simulated system of a Pluronic in water matches well with literature values. A number of different lipid/polymer systems with varying type of lipid, polymer PPO block length and polymer configuration inside the membrane (membrane-spanning vs. U-form) was simulated. A single PE6100 polymer initially placed on top of a lipid bilayer enters the membrane significantly faster than a polymer aggregate containing three or six polymers. In contrast to literature results, we found that the polymers of an aggregate inside the membrane separate from each other after some time.

The configuration of the polymer PPO block inside the membrane was characterized more in detail. MD simulations show that the ends of the PPO block are roughly aligned parallel to the lipid tails exhibiting similar order parameters and the middle part of the PPO block in average lies in-between the bilayer leaflets. As this general behavior of the polymer chains is found for transmembrane polymers as well as for polymers that enter the bilayer in U-form, these

two configurations are hard to distinguish on the basis of the results of our NMR experiments. Order parameters, NOESY cross-relaxation rates and R_1 relaxation rates are roughly the same for both systems. However, from this, we can also conclude that the influence of the polymers on membrane properties is probably rather similar for the membrane-spanning and for the U-form configuration. One could imagine that two polymers in membrane-spanning configuration, or two polymers incorporated into the membrane in U-form from two sides, basically form the same system influencing membrane properties, like its permeability, in a similar way. Only for the Pluronic PE3100 with its rather short PPO block of 15 units, we find slightly enhanced order parameters which according to MD simulations indicate a U-form configuration.

By comparison of results from experiments and simulations, we discovered that in case of the lipid/polymer systems, the cross relaxation rates determined from the NOESY sequence do not correspond to contact probabilities, that is, they do not indicate the preferred position of the polymer in the membrane. For the mixture DMPC/PE6100, the highest cross relaxation rates were determined for resonances between the PPO block and the upper chain region of the lipids. However, from the simulated trajectories of the same system with the polymers spanning the membrane or with a polymer incorporated in the membrane in U-form configuration, the highest contact probabilities were determined for the lipid tail ends, because the largest part of the polymer PPO block in average lies in the middle of the bilayer. We therefore calculated cross correlation functions from the simulated trajectories in a next step. Besides the distance dependence, these correlation functions also include the angle between the interconnecting vector of the two protons investigated and the bilayer normal, which also influences the dipolar coupling and consequently the cross peak intensities. The resulting cross-relaxation rates determined from these correlation functions match well with the experimental results confirming that the polymers are deeply inserted into the membrane and do not only reach into the membrane up to the upper lipid acyl chain region.

From experiments as well as from simulations, it was found that the neither the order parameters nor the R_1 relaxation rates of the lipids are changed due to the incorporation of the polymer in the membrane. We conclude that the lipid ordering and dynamics on timescales relevant for R_1 are not affected. The polymer does not disturb the lipid molecules but rather adapts their structure.

Besides the determination of residual dipolar couplings for the polymers, we were also able to quantify the amount of polymer incorporated in the membrane vs. the amount of polymer dissolved in the water phase between the bilayers by using the BaBa-xy16 experiment. We conducted the experiment on number of different samples, thereby systematically varying the molecular structures and outer conditions.

From alteration of the polymer block lengths, we found that the molar fraction of PPO units inside the membrane decreases with increasing total polymer hydrophilicity, that is with decreasing PPO block length or increasing volume of the hydrophilic blocks. Results of the BaBa-xy16 experiment as well as of the NOESY experiment show that polymers with high hydrophilicity generally do not enter deeply into the membrane but only interact with the surface.

From the higher anisotropic fraction and the higher residual dipolar coupling found for PE6100 in DOPC than for PE6100 in DMPC, we conclude that the polymers incorporate more efficiently into bilayers containing lipids with unsaturated chains than into bilayers of fully saturated lipids. This might be explainable by the higher disorder in the bilayers with the

unsaturated chains. However, also the differences in sample preparation could have an influence. While the DMPC/PE6100 system is cooled below the main phase transition temperature several times, DOPC does not show a phase transition in the accessible temperature range. When the sample temperature is decreased below the main phase transition temperature of the lipids, then the molar fraction of PPO units inside the membrane is reduced to zero. We conclude that the polymer is “squeezed-out” from the membrane at the transition to the gel phase probably due to the increase of lipid packing density and the decrease of molecular mobility.

Also the addition of cholesterol to the lipid/polymer mixtures results in an ordering of the lipid acyl chains. As a consequence we measure an decreasing amount of polymer incorporated in the membrane with increasing cholesterol concentration. Therefore, we generally conclude that the fluidity of the membrane strongly influences its interaction with the polymer.

Anion Transporters: In a second part of the thesis, we investigated a series of partially fluorinated anion transporters containing urea and thiourea groups and aromatic rings in mixture with POPC membranes. Applying the NOESY experiment, we have proven the interaction of these molecules with the membrane. The strongest interactions were found between the aromatic protons of the anion transporters and the upper acyl chain region and the glycerol backbone of the lipids possibly indicating their preferential location in the membrane. However, due to the anisotropy of the system, the cross-relaxation rates might not directly reflect the contact probability. Molecules showing a higher degree of fluorination generally show stronger interactions with the membrane due to their enhanced lipophilicity.

Bolapolyphiles: Lastly, we investigated two different kinds of X-shaped bolapolyphiles in interaction with lipid membranes. The complex phase behavior of the DPPC / B12 mixture was assigned to the different components of the system by help of ^1H and ^{13}C spectra. From the dipolar couplings determined for the B12 molecules in the membrane, we conclude that these molecules perform 180° two-site jumps about their molecular long-axis at temperatures $T < 75^\circ\text{C}$ and uniaxial rotation at temperatures above 75°C , and additional wobbling motions. The lipids in the DPPC / E12/7 system were found to show a main phase transition as in pure lipid bilayers while the E12/7 molecules stay rather immobilized over the whole temperature range ($25 - 75^\circ\text{C}$) investigated presumably forming rigid filaments with a width in the nanometer range.

A Spin State Representation by Wave Functions

Using Equation 5 given in Section 3.1, we can describe the state of a nuclear spin as a superposition of the $(2I + 1)$ eigenfunctions $|\psi_j\rangle = |I, m_j\rangle$ enumerated here by the index j . A spin superposition state can be imagined as a lack of knowledge of the actual spin state. Instead, from the corresponding coefficients c_j a certain probability for the spin to be in state $|I, m_j\rangle$ can be calculated.

As an example, the wave function for a spin with $I = 1/2$ is shown here in Dirac notation and as a vector with complex components

$$|\psi\rangle = c_\alpha |\alpha\rangle + c_\beta |\beta\rangle = \begin{pmatrix} c_\alpha \\ c_\beta \end{pmatrix} \quad (89)$$

with the eigenstates or Zeeman basis eigenvectors being defined as

$$|\alpha\rangle = \left| \frac{1}{2}, \frac{1}{2} \right\rangle = \begin{pmatrix} 1 \\ 0 \end{pmatrix} \quad \text{and} \quad |\beta\rangle = \left| \frac{1}{2}, -\frac{1}{2} \right\rangle = \begin{pmatrix} 0 \\ 1 \end{pmatrix}. \quad (90)$$

The spin operators for \hat{I}_x , \hat{I}_y and \hat{I}_z are given by the Pauli matrices. Together with the unity operator, they represent the basis functions for describing a two-state system.

$$\begin{aligned} \hat{I}_x &= \frac{1}{2} (|\alpha\rangle \langle\beta| + |\beta\rangle \langle\alpha|) = \frac{1}{2} \begin{pmatrix} 0 & 1 \\ 1 & 0 \end{pmatrix} & \hat{I}_y &= \frac{1}{2i} (|\alpha\rangle \langle\beta| - |\beta\rangle \langle\alpha|) = \frac{1}{2i} \begin{pmatrix} 0 & 1 \\ -1 & 0 \end{pmatrix} \\ \hat{I}_z &= \frac{1}{2} (|\alpha\rangle \langle\alpha| - |\beta\rangle \langle\beta|) = \frac{1}{2} \begin{pmatrix} 1 & 0 \\ 0 & -1 \end{pmatrix} & \frac{1}{2}\hat{1} &= \frac{1}{2} (|\alpha\rangle \langle\alpha| + |\beta\rangle \langle\beta|) = \frac{1}{2} \begin{pmatrix} 1 & 0 \\ 0 & 1 \end{pmatrix} \end{aligned}$$

Again the Dirac notation as well as the matrix representation is given. These hermitian operators fulfill the relations $\hat{I}_x^2 + \hat{I}_y^2 + \hat{I}_z^2 = \hat{I}^2$ and $[\hat{I}_i, \hat{I}_j] = 2i\epsilon_{ijk}\hat{I}_k$, with $i, j, k = x, y, z$ and ϵ_{ijk} being the Levi-Civita symbol. With \hat{I}_x and \hat{I}_y , the shift operators \hat{I}_\pm can be defined by

$$\hat{I}_\pm = \hat{I}_x \pm i\hat{I}_y. \quad (91)$$

Because of $\hat{I}_z |\alpha\rangle = +\frac{1}{2} |\alpha\rangle$ and $\hat{I}_z |\beta\rangle = -\frac{1}{2} |\beta\rangle$, it can be concluded that a spin in state $|\alpha\rangle / |\beta\rangle$ is represented by a vector with a positive / negative z -component and completely undefined x - and y -components. Accordingly, the functions $|\alpha\rangle$ and $|\beta\rangle$ are associated with the 'spin-up' and the 'spin-down' state, respectively.

The construction of a wave function for more complex systems is carried out in an analogous manner. For example, for a spin with $I = 1$, we have three eigenstates of angular momentum along the z -axis. Also coupled spins can be described as a single quantum system using only one wave function. For a system of two interacting spin-1/2 nuclei, for example a $^{13}\text{C}-^1\text{H}$ spin pair, such a wave function can be written as a superposition of four orthonormal eigenfunctions:

$$|\Psi\rangle = c_{\alpha\alpha} |\alpha\alpha\rangle + c_{\alpha\beta} |\alpha\beta\rangle + c_{\beta\alpha} |\beta\alpha\rangle + c_{\beta\beta} |\beta\beta\rangle \quad (92)$$

These eigenfunctions, also called (Zeeman) product states, display the eigenstate of spin 1 in the

first digit and the eigenstate of spin 2 in the second digit, for example $|\alpha\beta\rangle \equiv |\alpha\rangle^{\text{spin } 1} |\beta\rangle^{\text{spin } 2}$. The matrix representation of such a product state is calculated from the direct product of the matrix representations of the individual states of the two spins.

Generally, the state $|\Psi\rangle$ of a spin system is a superposition of the states $|\psi_j\rangle = |I, m_j\rangle$ and therefore not an eigenstate of \hat{I}_z or the Zeeman Hamiltonian \hat{H}_0 . Using the Schrödinger equation and the Zeeman Hamiltonian, given in Equation 10 and 13 in Section 3.1, respectively, the time development of such a general spin state under influence of an external magnetic field can be calculated to be

$$|\Psi(t)\rangle = \exp\left[-i\omega_0 t \hat{I}_z\right] |\Psi(0)\rangle. \quad (93)$$

For the state of a single spin with $I = 1/2$ it follows that

$$|\Psi(t)\rangle = c_\alpha(0)e^{-\frac{i}{2}\omega_0 t} |\alpha\rangle + c_\beta(0)e^{\frac{i}{2}\omega_0 t} |\beta\rangle. \quad (94)$$

A spin with a state being equal to a pure Hamiltonian eigenstate ($|\Psi(t)\rangle = |\alpha\rangle$ or $|\Psi(t)\rangle = |\beta\rangle$) will remain in that state over time and, as long as the Hamiltonian stays constant, only accumulate a complex phase factor. For a spin showing a general superposition state, however, the contributions of $|\alpha\rangle$ and $|\beta\rangle$ to the total state will oscillate with the Larmor frequency ω_0 during time. From a classical point of view, one can imagine that when a sample is brought into the magnetic field a torque is applied to the nuclear magnetic moments. This leads to a so-called precession movement of the magnetic moments about the direction of the external magnetic field with the precession frequency given by the Larmor frequency.

B Experimental Details

B.1 Sample Preparation

For the preparation of all lipid sample systems, we used commercial lipids delivered as dry powders. Usually, an amount of about 10–30 mg lipid is enough to ensure a reasonable signal-to-noise ratio also for the less sensitive ^{13}C measurements at natural abundance. The lipids were mixed with about 50 wt% of deuterated water which leads to the spontaneous formation of MLVs. The water content is high enough to fully hydrate the lipid molecules which means that structure and dynamics of the lipid bilayer are nearly independent of water content, hence adding more water would not change the spectra or other results. The samples were frozen, heated to a temperature above the melting point, and treated with a vortex mixer several times until homogeneous suspensions were achieved.

The lipid/guest molecule mixtures were prepared by co-dissolving all molecules in a chloroform/methanol solution. After evaporating the solvent, the samples were rehydrated with 50 wt% of D_2O and the freeze-thaw-vortex cycle was applied. The resulting samples were either directly filled in ZrO_2 MAS rotors, positioned between two teflon spacers or they were filled in an insert first which was inserted into the rotor subsequently.

Sample preparation for the DSC measurements was done in a similar way, however, more dilute samples with a lipid concentration of 1 mmol/L were used. Instead of applying the freeze-thaw-vortex cycle, the samples were only vortexed and additionally sonicated. Nevertheless, the samples were cooled to a temperature below the main phase transition temperature several times because a number of DSC up- and down- scans were run.

For all samples, we need to keep in mind that after some time, the lipid molecules in water begin to degrade. Oxidation of phospholipids with unsaturated chains and hydrolysis can occur. In the last case, the ester bonds of the glycerol backbone get broken and free fatty acids and lysophospholipids are produced which destabilize the bilayer [233]. To ensure that intact lipid samples were used for all measurements, we only used the samples for a few months, stored them in the freezer and checked the NMR spectra of the samples as lipid degradation can be detected from additional signals in the ^{13}C spectrum [144].

B.2 NMR Measurements

Temperature regulation for the NMR measurements is achieved by a stream of heated or cooled air. Significant heating from sample rotation and r.f. irradiation must be considered in the temperature calibration and the use of long recycle delays, respectively [100]. The temperature calibration was done with lead nitrate [234] or methanol [235] and tested by using the well-known phase transition temperatures of pure lipid samples. Also the chemical shift of the water peak can be used for temperature calibration [82, 100]. All in all, a temperature accuracy $\Delta T = \pm 1\text{ K}$ was achieved.

For most NMR measurements, a Bruker Avance III spectrometer operating at 400 MHz ^1H Larmor frequency and a 4 mm MAS WVT double- or triple-resonance probe were used. Only the measurements on the lipid/anion transporter systems were carried out on a Varian spectrometer operating at a ^1H Larmor frequency of 600 MHz using a 3.2 mm MAS double resonance probe. Typically, we applied ^1H 90° pulses with a length of $3\ \mu\text{s}$ and ^{13}C 90° pulses of $3.5\ \mu\text{s}$. For the

acquisition of ^{13}C spectra, a minimum recycle delay of $d_1 = 5$ s was necessary to compensate for sample warming due to the heteronuclear decoupling for which we used the SPINAL-64 sequence with a decoupling power of 50 kHz. While a few scans (4-16) were enough to obtain a ^1H spectrum with a good signal-to-noise ratio, several hundred scans (128-1024) were needed for a ^{13}C spectrum. The chemical shift axis of proton spectra were referenced by setting the γ peak on 3.32 ppm and the carbon spectra were referenced by help of an alanin sample, the COO resonance of which was set to 177.87 ppm [236].

C Description of NMR Experiments and Data Analysis

C.1 Determination of the Peak Volume Matrix from a 2D NOESY Spectrum

For a quantitative description of two-dimensional NOESY spectra, the peak intensities need to be determined and collected in the peak volume matrix \mathbf{A} . However, reliable results can only be obtained when the peaks are well resolved and not too small. In a two-dimensional spectrum, the peak intensities are given by the peak volumes which are determined here simply by drawing a rectangle around every peak and summing up the amplitudes of all points within. Additionally, a baseline correction is performed. This is especially important for small peaks and resonances that are in the neighborhood of bigger ones and partly overlapping. The base area is determined from the average signal intensity on all four edges of the rectangle and subtracted from the peak intensity. For weak resonances, the intensity on a specific location within the rectangle can be lower than the base area. In this case, these data points are omitted in the calculation of the sum.

As a measurement with $\tau_{\text{mix}} = 0$ is not very precise [107], we determine the peak volume matrix $\mathbf{A}(0)$ using the sequence with a very small mixing time of $\tau_{\text{mix}} = 1$ ms. Due to some artifacts, small cross peaks can appear in the resulting spectrum. However, for the volume matrix $\mathbf{A}(0)$ only peak volumes of diagonal peaks are considered and all other matrix elements are set to zero.

Although, theoretically all volume matrices describing peak intensities in NOESY spectra are symmetric, experimentally determined intensities a_{nm} and a_{mn} of opposite cross peaks might differ. Especially for small or partly overlapping peaks uncertainties in the determination of peak volumes can occur. Therefore, a symmetric volume matrix was created by taking the average intensity for opposing peaks or by choosing the intensity of the peak that was resolved better in cases where a difference was visible. Such a differing resolution within one spectrum is caused by the different time increments chosen in t_1 and t_2 dimension. While a small t_2 increment can easily be chosen, a small t_1 increment renders the acquisition of the two-dimensional spectrum time consuming.

C.2 Relaxation Rate Matrix of POPC

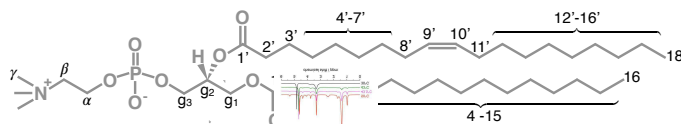


Figure 60: Chemical structure of POPC.

Using the full-matrix approach, the cross-relaxation rates of POPC at 25 °C was determined from the NOESY experiment (see Figure 13 in Section 5.5). All peak volumes determined from 2D spectra acquired for different mixing times and the respective fit function are shown in Figure 61.

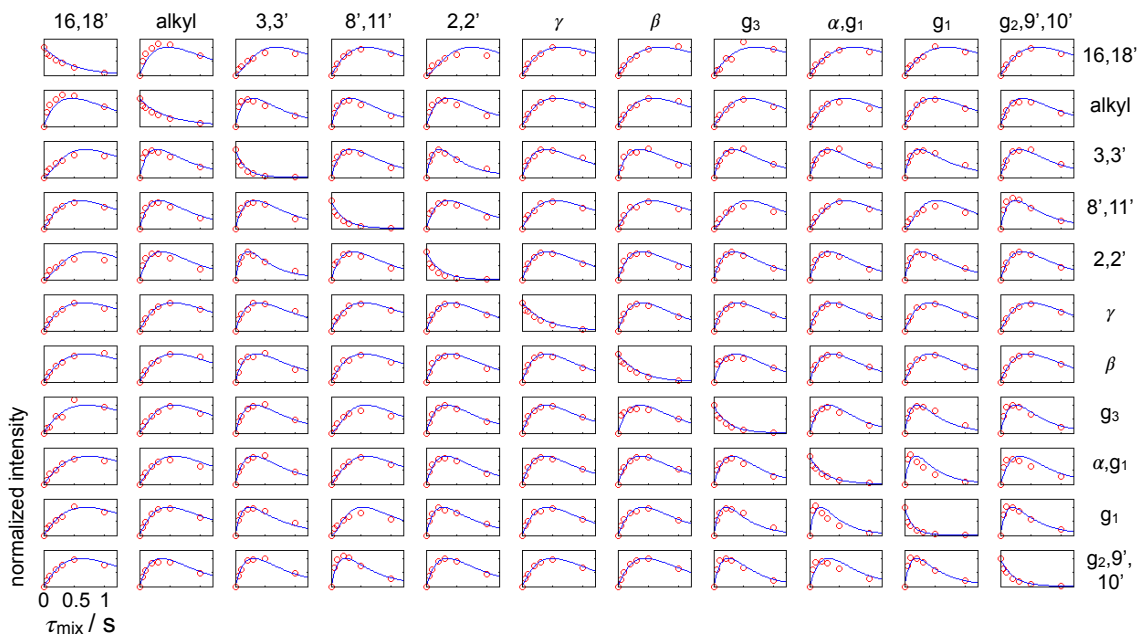


Figure 61: Peak volumes determined from 2D NOESY spectra that were acquired for different mixing times for POPC at 25 °C. The blue lines represent the fit function that was used to determine the cross relaxation rate matrix.

As a result, we obtain the cross relaxation matrix:

$$\mathbf{R} = \begin{pmatrix} & 16, 18' & \text{alkyl} & 3, 3' & 8', 11' & 2, 2' & \gamma & \beta & g_3 & \alpha, g_1 & g_1 & g_2, 9', 10' \\ 16, 18' & 2.333 & -0.157 & -0.014 & -0.068 & -0.011 & -0.022 & -0.021 & -0.033 & -0.026 & -0.034 & -0.057 \\ \text{alkyl} & -0.998 & 2.525 & -2.787 & -2.370 & -1.633 & -0.213 & -0.217 & -0.306 & -0.304 & -0.625 & -1.718 \\ 3, 3' & -0.007 & -0.210 & 6.153 & -0.160 & -0.600 & -0.046 & -0.072 & -0.151 & -0.170 & -0.303 & -0.191 \\ 8', 11' & -0.041 & -0.221 & -0.198 & 4.853 & -0.144 & -0.021 & -0.023 & -0.008 & -0.025 & -0.000 & -0.478 \\ 2, 2' & -0.006 & -0.140 & -0.684 & -0.132 & 4.7025 & -0.050 & -0.071 & -0.186 & -0.192 & -0.312 & -0.167 \\ \gamma & -0.032 & -0.048 & -0.138 & -0.052 & -0.132 & 2.598 & -0.335 & -0.273 & -0.348 & -0.199 & -0.093 \\ \beta & -0.007 & -0.011 & -0.048 & -0.013 & -0.041 & -0.074 & 2.887 & -0.096 & -0.092 & -0.058 & -0.033 \\ g_3 & -0.008 & -0.011 & -0.072 & -0.003 & -0.078 & -0.043 & -0.069 & 4.348 & -0.250 & -0.849 & -0.352 \\ \alpha, g_1 & -0.012 & -0.021 & -0.157 & -0.019 & -0.155 & -0.107 & -0.128 & -0.484 & 4.249 & -3.005 & -0.265 \\ g_1 & -0.0051 & -0.014 & -0.089 & -0.000 & -0.080 & -0.020 & -0.026 & -0.524 & -0.956 & 7.986 & -0.326 \\ g_2, 9', 10' & -0.025 & -0.120 & -0.176 & -0.358 & -0.136 & -0.029 & -0.045 & -0.683 & -0.265 & -1.027 & 4.998 \end{pmatrix}$$

The largest cross-relaxation rates are determined for resonances of segments that are spatially close to each other. Resonances of segments with larger distances yield smaller cross-relaxation rates that exhibit a bigger error.

C.3 Analytical Fit Functions for DIPSHIFT Curves

In this section, analytical fit functions $I(t_1)$ for the DIPSHIFT curves are introduced, which enable us to determine the dipolar coupling from the experimental data [143, 144]. However, during the determination of an order parameter from the dipolar coupling, we need to consider the pre-averaging introduced by assuming a certain motional geometry. A DIPSHIFT curve resembles an FID signal only influenced by dipolar interactions. For its description the angular frequency ω_{CH} is needed which in turn depends on the dipolar coupling constant d , the MAS frequency ω_r , the initial rotor phase γ and two additional Euler angles α and β which transform the dipolar tensor components given in the principal axis frame to the tensor components in

the laboratory frame. With this, the accumulated phase during the evolution period can be calculated from

$$\phi(t_1) = \int_0^{t_1} \omega_{\text{CH}}(t) dt \quad (95)$$

and the DIPSHIFT curve results from the cosine of the phase ϕ . As the molecules in a liposome dispersion are oriented randomly, the powder average over the angles α , β and γ (denoted by the angle brackets) needs to be taken which is done numerically.

For a CH group, we have

$$I(t_1)/I(0) = \langle \cos \phi(t_1) \rangle, \quad (96)$$

with

$$\phi(t_1) = d_{\text{CH}} \left[\frac{1}{4\omega_r} \sin^2 \beta (\sin(2\gamma + 2\omega_r t_1) - \sin(2\gamma)) - \frac{1}{\sqrt{2}\omega_r} \sin(2\beta) (\sin(\gamma + \omega_r t_1) - \sin(\gamma)) \right].$$

Because of the axial symmetry of the dipolar tensor in this simple case, the Euler angle α does not appear.

In a CH₂ group, the two C-H bonds are characterized by two dipolar tensors exhibiting different principal axis systems. Assuming the dipolar coupling constant to be the same for each bond, we can calculate the DIPSHIFT curve from

$$I(t_1)/I(0) = \langle \cos \phi_1(t_1) \cos \phi_2(t_1) \rangle = \langle 0.5 \cos(\phi_1(t_1) - \phi_2(t_1)) + 0.5 \cos(\phi_1(t_1) + \phi_2(t_1)) \rangle \quad (97)$$

with

$$\begin{aligned} \phi_{1,2}(t_1) = & d_{\text{CH}} \left[\frac{1}{6} \cos(2\alpha) (\cos^2 \beta + 1) \pm \frac{\sqrt{2}}{3} \cos \alpha \sin \beta \cos \beta \right] \cos(2\omega_r t_1 + 2\gamma) \\ & + d_{\text{CH}} \left[\mp \frac{\sqrt{2}}{3} \sin \alpha \sin \beta - \frac{2}{3} \cos \alpha \sin \alpha \cos \beta \right] \sin(2\omega_r t_1 + 2\gamma) \\ & + d_{\text{CH}} \left[\frac{\sqrt{2}}{3} \cos(2\alpha) \cos \beta \sin \beta \mp \frac{2}{3} \cos \alpha \cos(2\beta) \right] \cos(\omega_r t_1 + \gamma) \\ & + d_{\text{CH}} \left[-\frac{2}{3} \sqrt{2} \cos \alpha \sin \alpha \sin \beta \pm \frac{2}{3} \cos \beta \sin \alpha \right] \sin(\omega_r t_1 + \gamma). \end{aligned}$$

For a CH₂ group performing fast uniaxial reorientations, we have a more simple result because the two dipolar tensors are aligned parallel to each other due to the motional averaging. Additionally assuming the same coupling constant for the interaction of both spin pairs, we have $\phi_1 = \phi_2 = \phi$, and from this it follows

$$I(t_1)/I(0) = \frac{1}{2} + \frac{1}{2} \langle \cos(2\phi(t_1)) \rangle. \quad (98)$$

The DIPSHIFT curve of a CH₃ group can be calculated using a similar approach. Because the protons of a methyl group perform fast motions about a threefold symmetry axis, the dipolar interaction of the three C-H spin pairs can be described by three identical tensors. Therefore, we

have identical phases $\phi_1 = \phi_2 = \phi_3 = \phi$ and from this:

$$I(t_1)/I(0) = \langle \cos^3 \phi(t_1) \rangle \quad (99)$$

For describing the modulation curves determined with the recDIPSHIFT experiment, similar fit functions can be applied. However, as a consequence of the additional 180° pulses, the accumulated phase ϕ is N times enhanced and can be calculated from

$$\phi(t_1) = \int_0^{t_1} (-1)^m \omega_{\text{CH}}(t) dt \quad (100)$$

with $m = \text{int} \{2t/\tau_r\}$ being the number of half rotor periods that fit in a given time period t . The resulting recDIPSHIFT curves show a greater modulation depth than the respective DIPSHIFT curves.

C.4 Results from the R-PDLF Experiment for DMPC

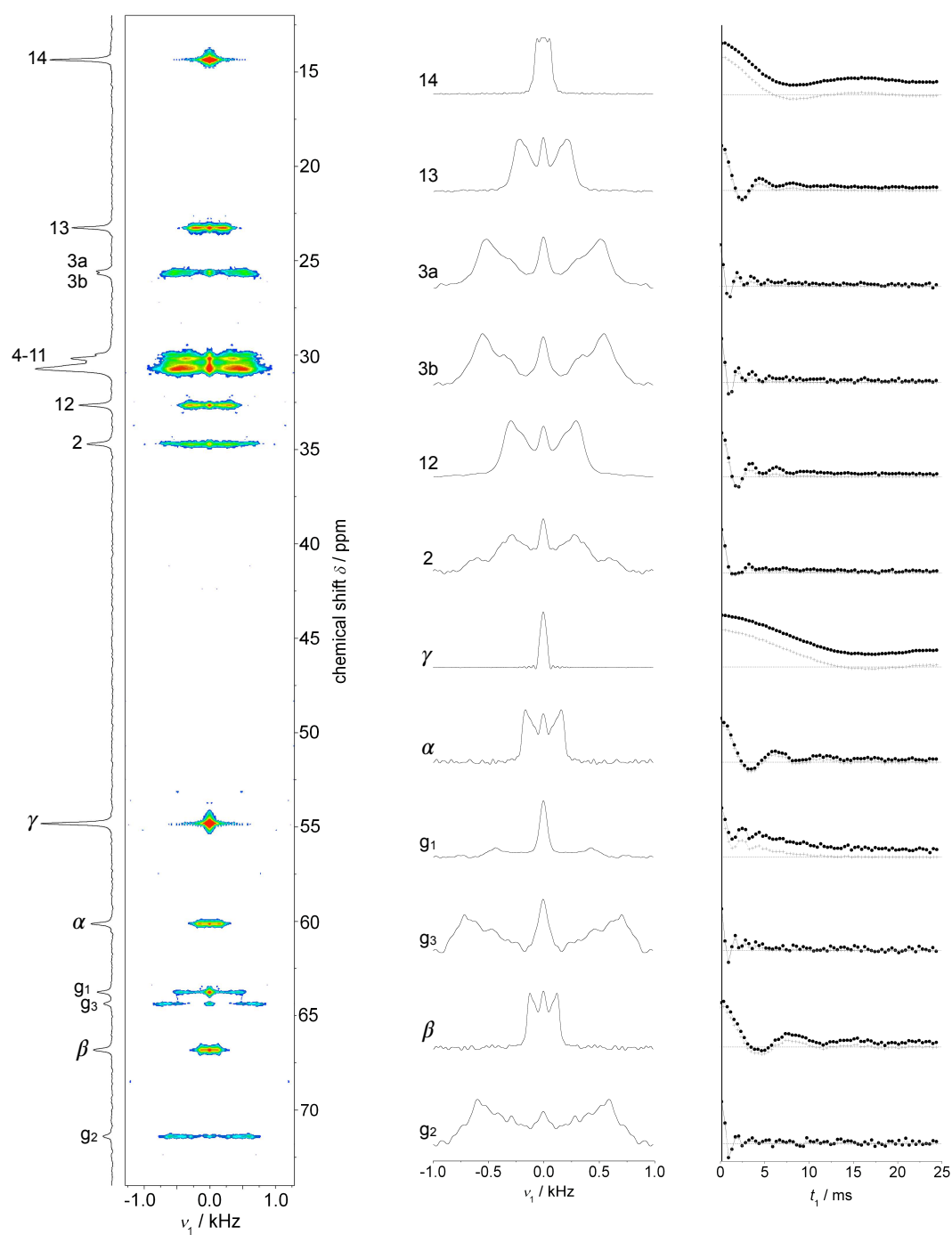


Figure 62: Results from the R-PDLF experiment for DMPC at 47 °C. An MAS frequency of 5.15 kHz was used and the t_1 time was incremented in steps of $10.79 \mu\text{s} \times 18 \times 2$. The 2D spectrum is shown on the left. On the right, the time dependent signal decay of the respective peak maxima are depicted. The measured curves (black symbols) were corrected for the offset and multiplied by an exponential window function. From the resulting time-depending curves (grey symbols) we determined the dipolar spectra, which are shown in the middle.

C.5 The Basic DQ Experiment

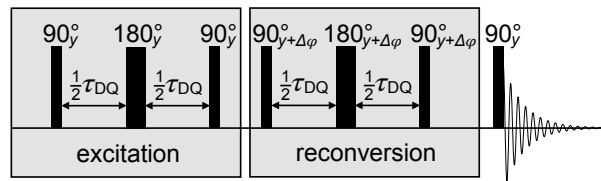


Figure 63: Basic DQ pulse sequence

The most simple experiment to excite DQ coherences consists of two 90° pulses with the same phase separated by an evolution time of the length τ_{DQ} during which the system evolves under the influence of homonuclear dipolar couplings [142]. An additional 180° pulse is placed in the middle of the evolution time to refocus signal dephasing caused by the chemical shift interaction (see Figure 63)

To understand the mechanism of action of this pulse sequence, we firstly assume an ensemble of spin pairs with the two individual spins denoted by $\hat{\mathbf{I}}_1$ and $\hat{\mathbf{I}}_2$. Normally, we would need to consider the Hamiltonian describing homonuclear dipolar couplings given in Equation 43 in Section 3.4.2. However, for simplicity, we here use a Hamiltonian

$$\hat{H}_{\text{D}} = \omega_{\text{D,eff}} \left(3\hat{I}_{1z}\hat{I}_{2z} \right) \quad (101)$$

assuming that the coupling is weak compared to the distance of the resonance frequencies of the interacting spins in the spectrum [237]. This simpler Hamiltonian allows for the application of the product operator formalism. Starting from thermal equilibrium, we obtain:

$$\begin{aligned} \hat{I}_{1z} + \hat{I}_{2z} &\xrightarrow{90_y^\circ} \hat{I}_{1x} + \hat{I}_{2x} \\ &\xrightarrow{\hat{H}_{\text{D}}\tau_{\text{DQ}}} (\hat{I}_{1x} + \hat{I}_{2x}) \cos(\phi_{\text{DQ}}) + 2(\hat{I}_{1y}\hat{I}_{2z} + \hat{I}_{2y}\hat{I}_{1z}) \sin(\phi_{\text{DQ}}) \\ &\xrightarrow{90_y^\circ} -(\hat{I}_{1z} + \hat{I}_{2z}) \cos(\phi_{\text{DQ}}) + 2(\hat{I}_{1y}\hat{I}_{2x} + \hat{I}_{2y}\hat{I}_{1x}) \sin(\phi_{\text{DQ}}) \\ &= -(\hat{I}_{1z} + \hat{I}_{2z}) \cos(\phi_{\text{DQ}}) - 2i(\hat{I}_{1+}\hat{I}_{2+} - \hat{I}_{2-}\hat{I}_{1-}) \sin(\phi_{\text{DQ}}) \end{aligned}$$

The last term corresponds to the DQ coherence [142]. The phase $\phi_{\text{DQ}} = 1.5\omega_{\text{D,eff}}\tau_{\text{DQ}}$ is specific for the homonuclear dipolar interaction. It contains the effective residual dipolar coupling $\omega_{\text{D,eff}}$ and the evolution period τ_{DQ} . The same result can be obtained in a single step by using an average DQ Hamiltonian:

$$\begin{aligned} \hat{H}_{\text{DQ}} &= \omega_{\text{D,eff}} \left(\hat{I}_{1x}\hat{I}_{2x} - \hat{I}_{1y}\hat{I}_{2y} \right) \\ &= \omega_{\text{D,eff}} \left(\hat{I}_{1+}\hat{I}_{2+} + \hat{I}_{1-}\hat{I}_{2-} \right) \end{aligned} \quad (102)$$

As the DQ term cannot be measured directly, it needs to be converted into z -magnetization using a reconversion sequence, which contains the same sequence of pulses as the excitation part, but they are applied with a phase shift of $\Delta\varphi$ which is varied in a 4-step-cycle. The effect of this reconversion sequence is described by the DQ Hamiltonian, the sign of which varies with $\Delta\varphi$. It

results in

$$\xrightarrow{\text{reconversion}} \underbrace{(\hat{I}_{1z} + \hat{I}_{2z}) \cos^2 \phi_{\text{DQ}}}_{\text{reference term}} \pm \underbrace{(\hat{I}_{1z} + \hat{I}_{2z}) \sin^2 \phi_{\text{DQ}}}_{\text{DQ term}}. \quad (103)$$

We obtain a positive sign in front of the DQ term when a $\Delta\varphi = \pm 90^\circ$ is applied and negative sign is achieved using $\Delta\varphi = 0$ or $\Delta\varphi = \pm 180^\circ$. The following 90° read-out pulse rotates the z magnetization in the transverse plane where it can be detected subsequently applying an appropriate receiver phase cycle. Using a constant receiver phase, we pick the $\cos^2 \phi_{\text{DQ}}$ - (or reference-) term, and with alternating receiver phase the $\sin^2 \phi_{\text{DQ}}$ - (DQ-) term is selected.

Also coherences of higher order can be excited by the sequence. However, they only influence the signal at long excitation times.

D Results from MD Simulations of Lipid/Polymer Systems

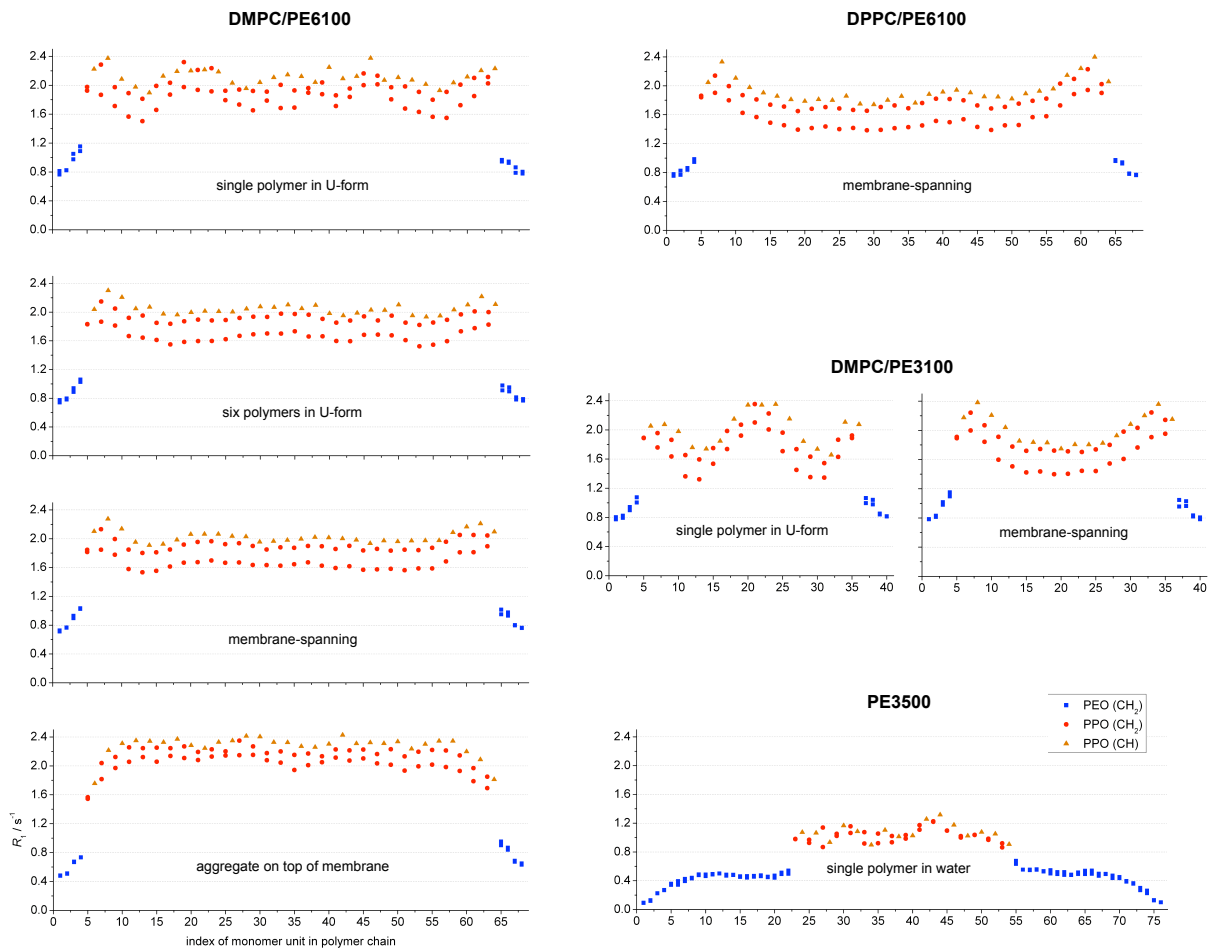


Figure 64: R_1 relaxation rates determined for the different systems simulated. The results for every C-H bond in the polymer are shown separately.

E Results from NMR Experiments on Lipid/Polymer Systems

E.1 Lipid Order Parameters

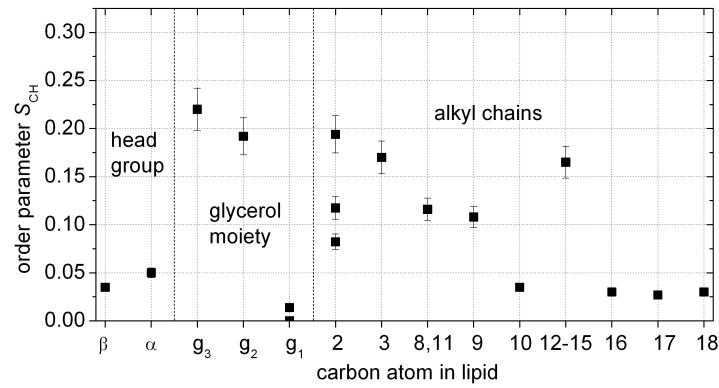
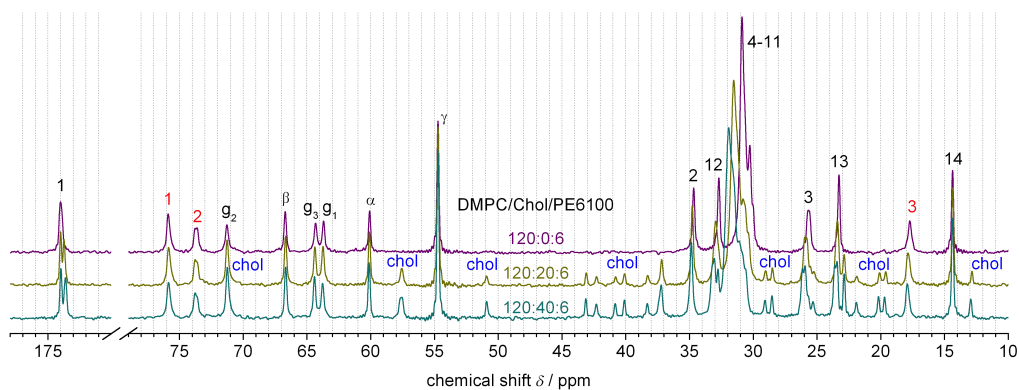
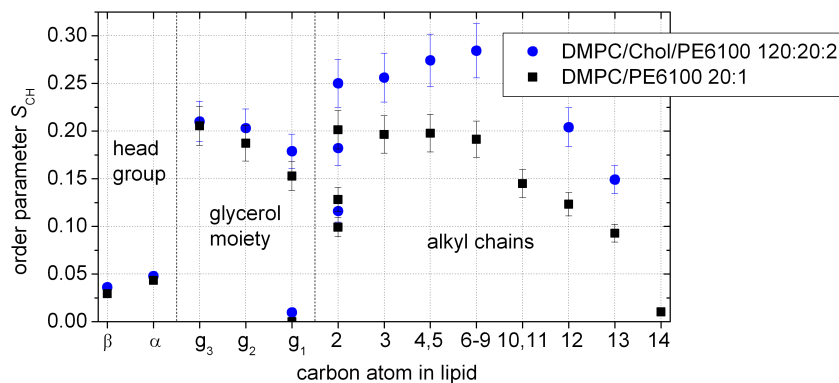


Figure 65: Lipid order parameters S_{CH} determined from the R-PDLF experiment for the mixture DOPC/PE6100 20:1 at 30 °C.



(a)



(b)

Figure 66: (a) DP spectra; and (b) lipid order parameters S_{CH} determined from the R-PDLF experiment for different mixtures of DMPC, cholesterol and PE6100.

E.2 Results from the R-PDLF Experiment for a Polymer Resonance

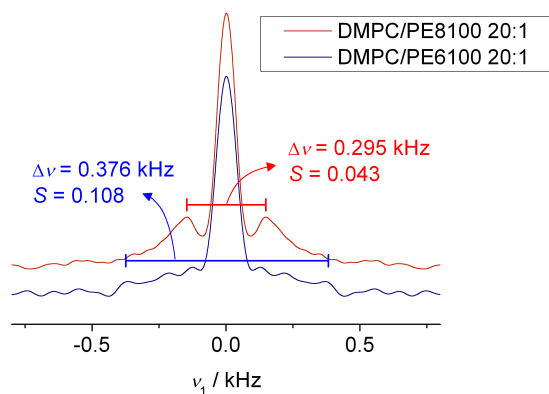


Figure 67: Dipolar spectrum determined by the R-PDLF experiment for the PPO CH resonance for two different DMPC/Pluronic mixtures at 40 °C. Especially for the sample DMPC/PE6100 a distinct dipolar splitting is hardly recognizable as the lines are quite broad and the isotropic contribution in the center dominates. The order parameters estimated here are in a similar range as the order parameters determined from the MD simulations.

References

- [1] Edlich, R. F., Schmolka, I. R., Prusak, M. P., and Edgerton, M. T. (1973) The Molecular Basis for Toxicity of Surfactants in Surgical Wounds. 1. EO:PO Block Polymers. *J. Surg. Res.*, **14**, 277–284.
- [2] Lee, R. C., River, L. P., Pan, F.-S., Ji, L., and Wollmann, R. L. (1992) Surfactant-induced sealing of electroporabilized skeletal muscle membranes *in vivo*. *Proc. Natl. Acad. Sci. USA*, **89**, 4524–4528.
- [3] Danson, S., Ferry, D., Alakhov, V., Margison, J., Kerr, D., Jowle, D., Brampton, M., Halbert, G., and Ranson, M. (2004) Phase I dose escalation and pharmacokinetic study of pluronic polymer-bound doxorubicin (SP1049C) in patients with advanced cancer. *Br. J. Cancer*, **90**, 2085–2091.
- [4] Lechner, B.-D., Ebert, H., Prehm, M., Werner, S., Meister, A., Hause, G., Beerlink, A., Saalwächter, K., Bacia, K., Tschierske, C., and Blume, A. (2015) Temperature-Dependent In-Plane Structure Formation of an X-Shaped Bolapolyphile within Lipid Bilayers. *Langmuir*, **31**, 2839–2850.
- [5] Werner, S., Ebert, H., Lechner, B.-D., Lange, F., Achilles, A., Bärenwald, R., Poppe, S., Blume, A., Saalwächter, K., Tschierske, C., and Bacia, K. (2015) Dendritic domains with hexagonal symmetry formed by X-shaped bolapolyphiles in lipid membranes. *Chem. Eur. J.*, **21**, 8840–8850.
- [6] Achilles, A., Bärenwald, R., Lechner, B.-D., Werner, S., Ebert, H., Tschierske, C., Blume, A., Bacia, K., and Saalwächter, K. (2016) Self-Assembly of X-Shaped Bolapolyphiles in Lipid Membranes: Solid-State NMR Investigations. *Langmuir*, **32**, 673–682.
- [7] Evans, D. F. and Wennerström, H. (1999) *The Colloidal Domain. Where Physics, Chemistry, Biology and Technology Meets*. Wiley-VCH, Hoboken, 2nd edn.
- [8] Leftin, A. and Brown, M. F. (2011) An NMR database for simulations of membrane dynamics. *Biochim. Biophys. Acta*, **1808**, 818–839.
- [9] Marsh, D. (2013) *Handbook of Lipid Bilayers*. CRC Press, Boca Raton, Fl., 2nd edn.
- [10] McElhaney, R. N. (1982) The use of differential scanning calorimetry and differential thermal analysis in studies of model and biological membranes. *Chem. Phys. Lipids*, **30**, 229–259.
- [11] Schwieger, C., Achilles, A., Scholz, S., Rüger, J., Bacia, K., Saalwächter, K., Kressler, J., and Blume, A. (2014) Binding of Amphiphilic and Triphilic Block Copolymers to Lipid Model Membranes: The Role of Perfluorinated Moieties. *Soft Matter*.
- [12] Somerharju, P. J., Virtanen, J. A., Eklund, K. K., Vainio, P., and Kinnunen, P. K. J. (1985) 1-Palmitoyl-2-pyrenedecanoyl Glycerophospholipids as Membrane Probes: Evidence for Regular Distribution in Liquid-Crystalline Phosphatidylcholine Bilayers. *Biochemistry*, **24**, 2773–2781.
- [13] Firestone, M. A., Wolf, A. C., and Seifert, S. (2003) Small-Angle X-ray Scattering Study of the Interaction of Poly(ethylene oxide)-*b*-Poly(propylene oxide)-*b*-Poly(ethylene oxide) Triblock Copolymers with Lipid Bilayers. *Biomacromolecules*, **4**, 1539–1549.

- [14] Lee, B. and Firestone, M. A. (2008) Electron Density Mapping of Triblock Copolymers Associated with Model Biomembranes: Insights into Conformational States and Effect on Bilayer Structure. *Biomacromolecules*, **9**, 1541–1550.
- [15] Frey, S. L. and Lee, K. Y. C. (2007) Temperature Dependence of Poloxamer Insertion Into and Squeeze-Out from Lipid Monolayers. *Langmuir*, **23**, 2631–2637.
- [16] Frey, S. L., Zhang, D., Carignano, M. A., Szleifer, I., and Lee, K. Y. C. (2007) Effects of block copolymer's architecture on its association with lipid membranes: Experiments and simulations. *J. Chem. Phys.*, **127**, 114904.
- [17] Amado, E., Kerth, A., Blume, A., and Kressler, J. (2008) Infrared Reflection Absorption Spectroscopy Coupled with Brewster Angle Microscopy for Studying Interactions of Amphiphilic Triblock Copolymers with Phospholipid Monolayers. *Langmuir*, **24**, 10041–10053.
- [18] Cheng, C.-Y., Wang, J.-Y., Kausik, R., Lee, K. Y. C., and Han, S. (2012) Nature of Interactions between PEO-PPO-PEO Triblock Copolymers and Lipid Membranes: (II) Role of Hydration Dynamics Revealed by Dynamic Nuclear Polarization. *Biomacromolecules*, **13**, 2624–2633.
- [19] Auger, M. (2000) Biological Membrane Structure By Solid-State NMR. *Curr. Issues Mol. Biol.*, **2**, 119–124.
- [20] Gawrisch, K., Eldho, N. V., and Polozov, I. V. (2002) Novel NMR tools to study structure and dynamics of biomembranes. *Chem. Phys. Lipids*, **116**, 135–151.
- [21] Chapman, D. and Penkett, S. A. (1966) Nuclear Magnetic Resonance Spectroscopic Studies of the Interaction of Phospholipids with Cholesterol. *Nature*, **211**, 1304–1305.
- [22] Seelig, J. (1977) Deuterium magnetic resonance: theory and application to lipid membranes. *Q. Rev. Biophys.*, **10**, 353–418.
- [23] Davis, J. H. (1983) The Description of Membrane Lipid Conformation, Order and Dynamics by ^2H -NMR. *Biochim. Biophys. Acta*, **737**, 117–171.
- [24] de Kruijff, B., Rietveld, A., and Cullis, P. R. (1980) ^{31}P -NMR studies on membrane phospholipids in microsomes, rat liver slices and intact perfused rat liver. *Biochim. Biophys. Acta*, **600**, 343–357.
- [25] Forbes, J., Bowers, J., Shan, X., Moran, L., Oldfield, E., and Moscarello, M. A. (1988) Some New Developments in Solid-state Nuclear Magnetic Resonance Spectroscopic Studies of Lipids and Biological Membranes, including the Effects of Cholesterol in Model and Natural Systems. *J. Chem. Soc., Faraday Trans. 1*, **84**, 3821–3849.
- [26] Winter, R. and Noll, F. (1998) *Methoden der Biophysikalischen Chemie*. B. G. Teubner.
- [27] Kressler, J. (June 7, 2013), personal communication.
- [28] Tanford, C. (1978) The hydrophobic effect and the organization of living matter. *Science*, **200**, 1012–1018.
- [29] Singer, S. J. and Nicolson, G. L. (1972) The Fluid Mosaic Model of the Structure of Cell Membranes. *Science*, **175**, 720–731.

- [30] Bamberg, E., Benz, R., Läuger, P., and Stark, G. (1974) Ionentransport durch biologische Membranen. *Chem. i. u. Zeit*, **8**, 33–43.
- [31] Israelachvili, J. N., Mitchell, D. J., and Ninham, B. W. (1976) Theory of Self-Assembly of Hydrocarbon Amphiphiles into Micelles and Bilayers. *J. Chem. Soc., Faraday Trans. 2*, **72**, 1525–1568.
- [32] van Meer, G., Voelker, D. R., and Feigenson, G. W. (2008) Membrane lipids: where they are and how they behave. *Nat. Rev. Mol. Cell Biol.*, **9**, 112–124.
- [33] Kučerka, N., Nieh, M.-P., and Katsaras, J. (2011) Fluid phase lipid areas and bilayer thicknesses of commonly used phosphatidylcholines as a function of temperature. *Biochim. Biophys. Acta*, **1808**, 2761–2771.
- [34] Petrache, H. I., Dodd, S. W., and Brown, M. F. (2000) Area per Lipid and Acyl Length Distributions in Fluid Phosphatidylcholines Determined by ^2H NMR Spectroscopy. *Biophys. J.*, **79**, 3172–3192.
- [35] Worcester, D. L. and Franks, N. P. (1976) Structural Analysis of Hydrated Egg Lecithin and Cholesterol Bilayers, II. Neutron Diffraction. *J. Mol. Biol.*, **100**, 359–378.
- [36] Büldt, G., Gally, H. U., Seelig, A., and Seelig, J. (1978) Neutron diffraction studies on selectively deuterated phospholipid bilayers. *Nature*, **271**, 182–184.
- [37] Rudakova, M. and Filippov, A. (2005) Water Transbilayer Diffusion in Macroscopically Oriented Lipid Bilayers as Studied by Pulsed Field Gradient NMR. *Appl. Magn. Reson.*, **29**, 451–457.
- [38] Wästerby, P., Orädd, G., and Lindblom, G. (2002) Anisotropic water diffusion in macroscopically oriented lipid bilayers studied by pulsed magnetic field gradient NMR. *J. Magn. Reson.*, **157**, 156–159.
- [39] Sanders, C. R. and Schwonek, J. P. (1992) Characterization of Magnetically Orientable Bilayers in Mixtures of Dihexanoylphosphatidylcholine and Dimyristoylphosphatidylcholine by Solid-State NMR. *Biochemistry*, **31**, 8898–8905.
- [40] Soong, R., Nieh, M.-P., Nicholson, E., Katsaras, J., and Macdonald, P. M. (2010) Bicellar Mixtures Containing Pluronic F68: Morphology and Lateral Diffusion from Combined SANS and PFG NMR Studies. *Langmuir*, **26**, 2630–2638.
- [41] Macdonald, P. M., Saleem, Q., lai, A., and Morales, H. H. (2013) NMR methods for measuring lateral diffusion in membranes. *Chem. Phys. Lipids*, **166**, 31–44.
- [42] Chrai, S. S., Murari, R., and Ahmad, I. (2002) Liposomes: A Review, Part I: Manufacturing Issues. *Pharm. Technol.*, pp. 28–34.
- [43] Walde, P., Cosentino, K., Engel, H., and Stano, P. (2010) Giant Vesicles: Preparations and Applications. *ChemBioChem*, **11**, 848–865.
- [44] Rand, R. P. and Parsegian, V. A. (1989) Hydration forces between phospholipid bilayers. *Biochim. Biophys. Acta*, **988**, 351–376.
- [45] Janiak, M. J., Small, D. M., and Shipley, G. G. (1979) Temperature and Compositional Dependence of the Structure of Hydrated Dimyristoyl Lecithin. *J. Biol. Chem.*, **254**, 6068–6078.

- [46] Tardieu, A., Luzzati, V., and Reman, F. C. (1973) Structure and Polymorphism of the Hydrocarbon Chains of Lipids: A Study of Lecithin-Water Phases. *J. Mol. Biol.*, **75**, 711–733.
- [47] Matsuki, H., Kusube, M., Hata, T., and Kaneshina, S. (2002) Barotropic and Thermotropic Phase Behavior of Bilayer Membranes Composed of Phospholipids Containing *Cis* Double Bond in the *sn*-2 Acyl Chain. Winter, R. (ed.), *Advances in High Pressure Biosciences and Biotechnology II*, pp. 199–203, Springer, Berlin, Heidelberg.
- [48] Pietzsch, J. (2004) Mind the Membrane. *Horizon Symposia: A Living Frontier*. Nature publishing group, pp. 1–4.
- [49] Edidin, M. (2003) Lipids on the frontier: a century of cell-membrane bilayers. *Nature Rev. Mol. Cell Biol.*, **4**, 414–418.
- [50] Gorter, E. and Grendel, F. (1925) On bimolecular layers of lipoids on the chromocytes of the blood. *J. Exp. Med.*, **41**, 439–443.
- [51] Engelman, D. M. (2005) Membranes are more mosaic than fluid. *Nature*, **438**, 578–580.
- [52] Goñi, F. M. (2014) The basic structure and dynamics of cell membranes: An update of the Singer–Nicolson model. *Biochim. Biophys. Acta*, **1838**, 1467–1476.
- [53] Nicolson, G. L. (2014) The Fluid-Mosaic Model of Membrane Structure: Still relevant to understanding the structure, function and dynamics of biological membranes after more than 40 years. *Biochim. Biophys. Acta*, **1838**, 1451–1466.
- [54] Zelenka, P. S. (1984) Lens lipids. *Curr. Eye Res.*, **3**, 1337–1359.
- [55] Doyle, D. A., Cabral, J. M., Pfuetzner, R. A., Kuo, A., Gulbis, J. M., Cohen, S. L., Chait, B. T., and MacKinnon, R. (1998) The Structure of the Potassium Channel: Molecular Basis of K^+ Conduction and Selectivity. *Science*, **280**, 69–77.
- [56] Shai, Y. (1999) Mechanism of the binding, insertion and destabilization of phospholipid bilayer membranes by α -helical antimicrobial and cell non-selective membrane-lytic peptides. *Biochim. Biophys. Acta*, **1462**, 55–70.
- [57] Simons, K. and Ikonen, E. (1997) Functional rafts in cell membranes. *Nature*, **387**, 569–572.
- [58] Toppozini, L., Meinhardt, S., Armstrong, C. L., Yamani, Z., Kučerka, N., Schmid, F., and Rheinstädter, M. C. (2014) Structure of Cholesterol in Lipid Rafts. *Phys. Rev. Lett.*, **113**, 1–5.
- [59] Seddon, A. M., Casey, D., Law, R. V., Gee, A., Templer, R. H., and Ces, O. (2009) Drug interactions with lipid membranes. *Chem. Soc. Rev.*, **38**, 2509–2519.
- [60] Demina, T., Grozdova, I., Krylova, O. O., Zhirnov, A., Istratov, V., Frey, H., Kautz, H., and Melik-Nubarov, N. S. (2005) Relationship between the Structure of Amphiphilic Copolymers and Their Ability To Disturb Lipid Bilayers. *Biochemistry*, **44**, 4042–4054.
- [61] Ferreira, T. M., Coreta-Gomes, F., Ollila, O. H. S., Moreno, M. J., Vaz, W. L. C., and Topgaard, D. (2013) Cholesterol and POPC segmental order parameters in lipid membranes: solid state 1H - ^{13}C NMR and MD simulation studies. *Phys. Chem. Chem. Phys.*, **15**, 1976–1989.

- [62] Guernevé, C. L. and Auger, M. (1995) New Approach to Study Fast and Slow Motions in Lipid Bilayers: Application to Dimyristoylphosphatidylcholine-Cholesterol Interactions. *Biophys. J.*, **68**, 1952–1959.
- [63] Marsh, D. and Smith, I. C. P. (1973) An interacting spin label study of the fluidizing and condensing effects of cholesterol on lecithin bilayers. *Biochim. Biophys. Acta*, **298**, 133–144.
- [64] Krause, M. R. and Regen, S. L. (2014) The Structural Role of Cholesterol in Cell Membranes: From Condensed Bilayers to Lipid Rafts. *Acc. Chem. Res.*, **47**, 3512–3521.
- [65] Ipsen, J. H., Mouritsen, O. G., and Bloom, M. (1990) Relationships between lipid membrane area, hydrophobic thickness, and acyl-chain orientational order. The effects of cholesterol. *Biophys. J.*, **57**, 405–412.
- [66] Jamshaid, M., Farr, S. J., Kearney, P., and Kellaway, I. W. (1988) Poloxamer sorption on liposomes: comparison with polystyrene latex and influence on solute efflux. *Int. J. Pharm.*, **48**, 125–131.
- [67] El-Sayed, M. Y., Guion, T. A., and Fayer, M. D. (1986) Effect of Cholesterol on Viscoelastic Properties of Dipalmitoylphosphatidylcholine Multibilayers As Measured by a Laser-Induced Ultrasonic Probe. *Biochemistry*, **25**, 4825–4832.
- [68] Ipsen, J. H., Karlström, G., Mouritsen, O. G., Wennerström, H., and Zuckermann, M. J. (1987) Phase equilibria in the phosphatidylcholine-cholesterol system. *Biochim. Biophys. Acta*, **905**, 162–172.
- [69] Scheidt, H. and Huster, D. (2008) The interaction of small molecules with phospholipid membranes studied by ^1H NOESY NMR under magic-angle spinning. *Acta Pharmacol. Sin.*, **29**, 35–49.
- [70] Holte, L. L. and Gawrisch, K. (1997) Determining Ethanol Distribution in Phospholipid Multilayers with MAS-NOESY Spectra. *Biochemistry*, **36**, 4669–4674.
- [71] Feller, S. E., Brown, C. A., Nizza, D. T., and Gawrisch, K. (2002) Nuclear Overhauser Enhancement Spectroscopy Cross-Relaxation Rates and Ethanol Distribution across Membranes. *Biophys. J.*, **82**, 1396–1404.
- [72] Ulmius, J., Lindblom, G., Wennerström, H., Johansson, L. B.-A., Fontell, K., Söderman, O., and Arvidson, G. (1982) Molecular Organization in the Liquid-Crystalline Phases of Lecithin-Sodium Cholate-Water Systems Studied by Nuclear Magnetic Resonance. *Biochemistry*, **21**, 1553–1560.
- [73] Wang, T., Widanapathirana, L., Zhao, Y., and Hong, M. (2012) Aggregation and Dynamics of Oligocholate Transporters in Phospholipid Bilayers Revealed by Solid-State NMR Spectroscopy. *Langmuir*, **28**, 17071–17078.
- [74] Sakai, N. and Matile, S. (2013) Synthetic Ion Channels. *Langmuir*, **29**, 9031–9040.
- [75] Theisgen, S., Scheidt, H. A., Magalhães, A., Bonagamba, T. J., and Huster, D. (2010) A solid-state NMR study of the structure and dynamics of the myristoylated N-terminus of the guanylate cyclase-activating protein-2. *Biochim. Biophys. Acta*, **1798**, 266–274.
- [76] Hong, M., Zhang, Y., and Hu, F. (2012) Membrane Protein Structure and Dynamics from NMR Spectroscopy. *Annu. Rev. Phys. Chem.*, **63**, 1–24.

- [77] Levitt, M. H. (2008) *Spin Dynamics*. John Wiley & Sons, Ltd, Chichester, 2nd edn.
- [78] Duer, M. (2004) *Introduction to Solid-State NMR Spectroscopy*. Blackwell Publishing Ltd, Oxford.
- [79] Sørensen, O. W., Eich, G. W., Levitt, M. H., Bodenhausen, G., and Ernst, R. R. (1983) Product Operator Formalism for the Description of NMR Pulse Experiments. *Progr. NMR Spectrosc.*, **16**, 163–192.
- [80] <https://www.bruker.com/products/mr/nmr/magnets/magnets/aeon-1ghz/overview.html>. February 27, 2018.
- [81] de Kruijff, B., Cullis, P. R., Verkleij, A. J., Hope, M. J., van Echteld, C. J. A., and Taraschi, T. F. (1985) Lipid Polymorphism and Membrane Function. Martonosi, A. N. (ed.), *The Enzymes of Biological Membranes*, Springer, Boston, MA.
- [82] Dvinskikh, S. V., Castro, V., and Sandström, D. (2005) Efficient solid-state NMR methods for measuring heteronuclear dipolar couplings in unoriented lipid membrane systems. *Phys. Chem. Chem. Phys.*, **7**, 607–613.
- [83] Pastor, R. W., Venable, R. M., and Feller, S. E. (2002) Lipid Bilayers, NMR Relaxation, and Computer Simulations. *Acc. Chem. Res.*, **35**, 438–446.
- [84] Reichert, D. and Saalwächter, K. (2008) Dipolar Coupling: Molecular-Level Mobility. Harris, R. K. and Wasylishen, R. (eds.), *Encyclopedia of Magnetic Resonance*, John Wiley: Chichester.
- [85] Lipari, G. and Szabo, A. (1982) Model-Free Approach to the Interpretation of Nuclear Magnetic Resonance Relaxation In Macromolecules. 1. Theory and Range of Validity. *J. Am. Chem. Soc.*, **104**, 4546–4559.
- [86] Brown, M. F., Ribeiro, A. A., and Williams, G. D. (1983) New view of lipid bilayer dynamics from ^2H and ^{13}C NMR relaxation time measurements. *Proc. Natl. Acad. Sci. USA*, **80**, 4325–4329.
- [87] Ferreira, T. M., Ollila, O. H. S., Pigliapochi, R., Dabkowska, A. P., and Topgaard, D. (2015) Model-free estimation of the effective correlation time for C–H bond reorientation in amphiphilic bilayers: ^1H – ^{13}C solid-state NMR and MD simulations. *J. Chem. Phys.*, **142**.
- [88] Lee, A. G., Birdsall, N. J. M., Levine, Y. K., and Metcalfe, J. C. (1972) High Resolution Proton Relaxation Studies of Lecithins. *Biochim. Biophys. Acta*, **255**, 43–56.
- [89] Sefcik, M. D., Schaefer, J., Stejskal, E. O., Ellena, J. F., Dodd, S. W., and Brown, M. F. (1983) Lipid bilayer dynamics and rhodopsin-lipid interactions: new approach using high-resolution solid-state ^{13}C NMR. *Biochem. Biophys. Res. Commun.*, **114**, 1048–1055.
- [90] Dolainsky, C., Möps, A., and Bayerl, T. M. (1993) Transverse relaxation in supported and nonsupported phospholipid model membranes and the influence of ultraslow motions: A ^{31}P -NMR study. *J. Chem. Phys.*, **98**, 1712–1720.
- [91] Althoff, G., Stauch, O., Vilfan, M., Frezzato, D., Moro, G. J., Hauser, P., Schubert, R., and Kothe, G. (2002) Transverse Nuclear Spin Relaxation Studies of Viscoelastic Properties of Membrane Vesicles. II. Experimental Results. *J. Phys. Chem. B*, **106**, 5517–5526.

- [92] Bloom, M. and Sternin, E. (1987) Transverse Nuclear Spin Relaxation in Phospholipid Bilayer Membranes. *Biochemistry*, **26**, 2101–2105.
- [93] Lindblom, G. and Orädd, G. (2009) Lipid lateral diffusion and membrane heterogeneity. *Biochim. Biophys. Acta*, **1788**, 234–244.
- [94] Schmidt-Rohr, K. and Spiess, H. W. (1994) *Multidimensional Solid-State NMR and Polymers*. Academic Press.
- [95] Williamson, P. T. F. (2009) Solid-State NMR for the Analysis of High-Affinity Ligand/Receptor Interactions. *Concepts in Magn. Reson. Part A*, **34A**, 144–172.
- [96] Bärenwald, R., Achilles, A., Lange, F., Ferreira, T. M., and Saalwächter, K. (2016) Applications of Solid-State NMR Spectroscopy for the Study of Lipid Membranes with Polyphilic Guest (Macro)Molecules. *Polymers*, **8**, 439.
- [97] <https://ir.bruker.com/investors/press-releases/press-release-details/2015/bruker-introduces-novel-solid-state-nmr-probe-with-ultra-high-spinning-frequency/default.aspx>. March 01, 2018.
- [98] Bennett, A. E., Rienstra, C. M., Auger, M., Lakshmi, K. V., and Griffin, R. G. (1995) Heteronuclear decoupling in rotating solids. *J. Chem. Phys.*, **103**, 6951–6958.
- [99] Fung, B. M., Khittrin, A. K., and Ermolaev, K. (2000) An improved broadband decoupling sequence for liquid crystals and solids. *J. Magn. Reson.*, **142**, 97–101.
- [100] Dvinskikh, S. V., Castro, V., and Sandström, D. (2004) Heating caused by radiofrequency irradiation and sample rotation in ^{13}C magic angle spinning NMR studies of lipid bilayers. *Magn. Reson. Chem.*, **42**, 875–881.
- [101] Bielecki, A., Kolbert, A. C., and Levitt, M. H. (1989) Frequency-Switched Pulse Sequences: Homonuclear Decoupling and Dilute Spin NMR in Solids. *Chem. Phys. Lett.*, **155**, 341–346.
- [102] Lee, M. and Goldburg, W. I. (1965) Nuclear-Magnetic-Resonance Line Narrowing by a Rotating rf Field. *Phys. Rev. A*, **140**, 1261–1271.
- [103] Vinogradov, E., Madhu, P. K., and Vega, S. (1999) High-resolution proton solid-state NMR spectroscopy by phase-modulated Lee-Goldburg experiment. *Chem. Phys. Lett.*, **314**, 443–450.
- [104] Forbes, J., Husted, C., and Oldfield, E. (1988) High-Field, High-Resolution Proton "Magic-Angle" Sample-Spinning Nuclear Magnetic Resonance Spectroscopic Studies of Gel and Liquid Crystalline Lipid Bilayers and the Effects of Cholesterol. *J. Am. Chem. Soc.*, **110**, 1059–1065.
- [105] Davis, J. H., Auger, M., and Hodges, R. S. (1995) High Resolution ^1H Nuclear Magnetic Resonance of a Transmembrane Peptide. *Biophys. J.*, **69**, 1917–1932.
- [106] Birdsall, N. J. M., Feeney, J., Lee, A. G., Levine, Y. K., and Metcalfe, J. C. (1972) Dipalmitoyl-lecithin: Assignment of the ^1H and ^{13}C Nuclear Magnetic Resonance Spectra, and Conformational Studies. *J. Chem. Soc., Perkin Trans. 2*, **0**, 1441–1445.
- [107] Huster, D., Arnold, K., and Gawrisch, K. (1999) Investigation of Lipid Organization in Biological Membranes by Two-Dimensional Nuclear Overhauser Enhancement Spectroscopy. *J. Phys. Chem. B*, **103**, 243–251.

- [108] Tonelli, A. E. (1989) *NMR Spectroscopy and Polymer Microstructure: The Conformational Connection*. VCH.
- [109] Peersen, O. B., Wu, X., Kustanovich, I., and Smith, S. O. (1993) Variable-Amplitude Cross-Polarization MAS NMR. *J. Magn. Reson. A*, **104**, 334–339.
- [110] Metz, G., Wu, X., and Smith, S. O. (1994) Ramped-Amplitude Cross Polarization in Magic-Angle-Spinning NMR. *J. Magn. Reson. A*, **110**, 219–227.
- [111] Gross, J. D., Costa, P. R., Dubacq, J.-P., Warschawski, D. E., Lirsac, P.-N., Devaux, P. F., and Griffin, R. G. (1995) Multidimensional NMR in Lipid Systems. Coherence Transfer through J Couplings under MAS. *J. Magn. Reson. B*, **106**, 187–190.
- [112] Burum, D. P. and Ernst, R. R. (1980) Net Polarization Transfer via a *J*-Ordered State for Signal Enhancement of Low-Sensitivity Nuclei. *J. Magn. Reson.*, **39**, 163–168.
- [113] Morris, G. A. and Freeman, R. (1979) Enhancement of Nuclear Magnetic Resonance Signals by Polarization Transfer. *J. Am. Chem. Soc.*, **101**, 760–762.
- [114] Lux, P., Brunet, F., Desvaux, H., and Virlet, J. (1993) Determination of the Structure of Alkoxysilane Polymers in Solution by Natural Abundance Two Dimensional ^{29}Si - ^{29}Si INEPT DQF COSY NMR. *Magn. Reson. Chem.*, **31**, 623–631.
- [115] Dvinskikh, S. V., Zimmermann, H., Maliniak, A., and Sandström, D. (2004) Measurements of motionally averaged heteronuclear dipolar couplings in MAS NMR using R-type recoupling. *J. Magn. Reson.*, **168**, 194–201.
- [116] Nowacka, A., Mohr, P. C., Norrman, J., Martin, R. W., and Topgaard, D. (2010) Polarization Transfer Solid-State NMR for Studying Surfactant Phase Behavior. *Langmuir*, **26**, 16848–16856.
- [117] Warschawski, D. E. and Devaux, P. F. (2000) Polarization Transfer in Lipid Membranes. *J. Magn. Reson.*, **145**, 367–372.
- [118] Brown, M. F. and Williams, G. D. (1985) Membrane NMR: a dynamic research area. *J. Biochem. Biophys. Methods*, **11**, 71–81.
- [119] Heatley, F. (1975) Molecular motion in polyisobutylene and poly(propylene oxide) studied by ^{13}C nuclear magnetic relaxation. *Polymer*, **16**, 493–496.
- [120] Wittebort, R. J. and Szabo, A. (1978) Theory of NMR relaxation in macromolecules: Restricted diffusion and jump models for multiple internal rotations in amino acid side chains. *J. Chem. Phys.*, **69**, 1722–1736.
- [121] Gawrisch, K., Gaede, H. C., Mihailescu, M., and White, S. H. (2007) Hydration of POPC bilayers studied by ^1H -PFG-MAS-NOESY and neutron diffraction. *Eur. Biophys. J.*, **36**, 281–291.
- [122] Scheidt, H. A., Pampel, A., Nissler, L., Gebhardt, R., and Huster, D. (2004) Investigation of the membrane localization and distribution of flavonoids by high-resolution magic angle spinning NMR spectroscopy. *Biochim. Biophys. Acta*, **1663**, 97–107.
- [123] Gaede, H. C., Yau, W.-M., and Gawrisch, K. (2005) Electrostatic Contributions to Indole-Lipid Interactions. *J. Phys. Chem. B*, **109**, 13014–13023.

- [124] Siarheyeva, A., Lopez, J. J., and Glaubitz, C. (2006) Localization of Multidrug Transporter Substrates within Model Membranes. *Biochemistry*, **45**, 6203–6211.
- [125] Kimura, T., Cheng, K., Rice, K. C., and Gawrisch, K. (2009) Location, Structure and Dynamics of the Synthetic Cannabinoid Ligand CP-55,940 in Lipid Bilayers. *Biophys. J.*, **96**, 4916–4924.
- [126] Huster, D., Vogel, A., Katzka, C., Scheidt, H. A., Binder, H., Dante, S., Gutberlet, T., Zschörnig, O., Waldmann, H., and Arnold, K. (2003) Membrane Insertion of a Lipidated Ras Peptide Studied by FTIR, Solid-State NMR, and Neutron Diffraction Spectroscopy. *J. Am. Chem. Soc.*, **125**, 4070–4079.
- [127] Huster, D. and Gawrisch, K. (1999) NOESY NMR Crosspeaks between Lipid Headgroups and Hydrocarbon Chains: Spin Diffusion or Molecular Disorder? *J. Am. Chem. Soc.*, **121**, 1992–1993.
- [128] Jeener, J., Meier, B. H., Bachmann, P., and Ernst, R. R. (1979) Investigation of exchange processes by two-dimensional NMR spectroscopy. *J. Chem. Phys.*, **71**, 4546–4553.
- [129] Feller, S. E., Huster, D., and Gawrisch, K. (1999) Interpretation of NOESY Cross-Relaxation Rates from Molecular Dynamics Simulation of a Lipid Bilayer. *J. Am. Chem. Soc.*, **121**, 8963–8964.
- [130] Brüschweiler, R. and Wright, P. E. (1994) Water self-diffusion model for protein-water NMR cross relaxation. *Chem. Phys. Lett.*, **229**, 75–81.
- [131] Douliez, J.-P., Léonard, A., and Dufourc, E. J. (1995) Restatement of Order Parameters in Biomembranes: Calculation of C-C Bond Order Parameters from C-D Quadrupolar Splittings. *Biophys. J.*, **68**, 1727–1739.
- [132] Bloom, M., Davis, J. H., and Mackay, A. L. (1981) Direct Determination of the Oriented Sample NMR Spectrum from the Powder Spectrum for Systems with Local Axial Symmetry. *Chem. Phys. Lett.*, **80**, 198–202.
- [133] Shi, X., Yarger, J. L., and Holland, G. P. (2013) ^2H - ^{13}C HETCOR MAS NMR for indirect detection of ^2H quadrupole patterns and spin-lattice relaxation rates. *J. Magn. Reson.*, **226**, 1–12.
- [134] Shi, X. and Rienstra, C. M. (2016) Site-Specific Internal Motions in GB1 Protein Microcrystals Revealed by 3D ^2H - ^{13}C - ^{13}C Solid-State NMR Spectroscopy. *J. Am. Chem. Soc.*, **138**, 4105–4119.
- [135] Gullion, T. and Schaefer, J. (1989) Rotational-Echo Double-Resonance NMR. *J. Magn. Reson.*, **81**, 196–200.
- [136] Levitt, M. H. (2002) Symmetry-based pulse sequences in magic-angle spinning solid-state nmr. Grant, D. M. and Harris, R. K. (eds.), *Encyc. Nucl. Magn. Reson.*, vol. 9, pp. 165–196, John Wiley & Sons.
- [137] Munowitz, M. G., Griffin, R. G., Bodenhausen, G., and Huang, T. H. (1981) Two-Dimensional Rotational Spin-Echo Nuclear Magnetic Resonance in Solids: Correlation of Chemical Shift and Dipolar Interactions. *J. Am. Chem. Soc.*, **103**, 2529–2533.

- [138] Hong, M., Gross, J. D., and Griffin, R. G. (1997) Site-Resolved Determination of Peptide Torsion Angle ϕ from the Relative Orientations of Backbone N–H and C–H Bonds by Solid-State NMR. *J. Phys. Chem. B*, **101**, 5869–5874.
- [139] deAzevedo, E. R., Saalwächter, K., Pascui, O., de Souza, A. A., Bonagamba, T. J., and Reichert, D. (2008) Intermediate motions as studied by solid-state separated local field NMR experiments. *J. Chem. Phys.*, **128**.
- [140] Gross, J. D., Warschawski, D. E., and Griffin, R. G. (1997) Dipolar Recoupling in MAS NMR: A Probe for Segmental Order in Lipid Bilayers. *J. Am. Chem. Soc.*, **119**, 796–802.
- [141] Cobo, M. F., Achilles, A., Reichert, D., deAzevedo, E. R., and Saalwächter, K. (2012) Recoupled separated-local-field experiments and applications to study intermediate-regime molecular motions. *J. Magn. Reson.*, **221**, 85–96.
- [142] Saalwächter, K. (2013) Robust NMR Approaches for the Determination of Homonuclear Dipole–Dipole Coupling Constants in Studies of Solid Materials and Biomolecules. *ChemPhysChem*, **14**, 3000–3014.
- [143] Hackel, C., Zinkevich, T., Belton, P., Achilles, A., Reichert, D., and Krushelnitsky, A. (2012) The trehalose coating effect on the internal protein dynamics. *Phys. Chem. Chem. Phys.*, **14**, 2727–2734.
- [144] Achilles, A. (2014), Charakterisierung der Wechselwirkung amphiphiler und polyphiler Moleküle mit Modellmembranen mittels Festkörper-NMR. Doctoral thesis.
- [145] Kurz, R., Cobo, M. F., deAzevedo, E. R., Sommer, M., Wicklein, A., Thelakkat, M., Hempel, G., and Saalwächter, K. (2013) Avoiding Bias Effects in NMR Experiments for Heteronuclear Dipole-Dipole Coupling Determinations: Principles and Application to Organic Semiconductor Materials. *ChemPhysChem*, **14**, 3146–3155.
- [146] Middleton, D. A., Hughes, E., and Madine, J. (2004) Screening Molecular Associations with Lipid Membranes Using Natural Abundance ^{13}C Cross-Polarization Magic-Angle Spinning NMR and Principal Component Analysis. *J. Am. Chem. Soc.*, **126**, 9478–9479.
- [147] Warschawski, D. E. and Devaux, P. F. (2005) Order parameters of unsaturated phospholipids in membranes and the effect of cholesterol: a ^1H - ^{13}C solid-state nmr study at natural abundance. *Eur. Biophys. J. Biophys. Lett.*, **34**, 987–996.
- [148] Ferreira, T. M., Sood, R., Bärenwald, R., Carlström, G., Topgaard, D., Saalwächter, K., Kinnunen, P. K. J., and Ollila, O. H. S. (2016) Acyl Chain Disorder and Azelaoyl Orientation in Lipid Membranes Containing Oxidized Lipids. *Langmuir*, **32**, 6524–6533.
- [149] Gansmüller, A., Simorre, J.-P., and Hediger, S. (2013) Windowed R-PDLF recoupling: A flexible and reliable tool to characterize molecular dynamics. *J. Magn. Reson.*, **234**, 154–164.
- [150] Yamamoto, K., Soong, R., and Ramamoorthy, A. (2009) Comprehensive Analysis of Lipid Dynamics Variation with Lipid Composition and Hydration of Bicelles Using Nuclear Magnetic Resonance (NMR) Spectroscopy. *Langmuir*, **25**, 7010–7018.
- [151] Schanda, P., Meier, B. H., and Ernst, M. (2011) Accurate measurement of one-bond H-X heteronuclear dipolar couplings in MAS solid-state NMR. *J. Magn. Reson.*, **210**, 246–259.

- [152] Caldarelli, S., Hong, M., Emsley, L., and Pines, A. (1996) Measurement of Carbon-Proton Dipolar Couplings in Liquid Crystals by Local Dipolar Field NMR Spectroscopy. *J. Phys. Chem.*, **100**, 18696–18701.
- [153] Leal, C., Sandström, D., Nevsten, P., and Topgaard, D. (2008) Local and translational dynamics in DNA-lipid assemblies monitored by solid-state and diffusion NMR. *Biochim. Biophys. Acta*, **1778**, 214–228.
- [154] Ferreira, T. M., Medronho, B., Martin, R. W., and Topgaard, D. (2008) Segmental order parameters in a nonionic surfactant lamellar phase studied with ^1H - ^{13}C solid-state NMR. *Phys. Chem. Chem. Phys.*, **10**, 6033–6038.
- [155] Jbeily, M., Bärenwald, R., Kressler, J., Saalwächter, K., and Ferreira, T. M. (2018) Cholesterol-like effects of a fluorotelomer alcohol incorporated in phospholipid membranes. *Sci. Rep.*, **8**, 2154.
- [156] Leftin, A., Molugu, T. R., Job, C., Beyer, K., and Brown, M. F. (2014) Area per Lipid and Cholesterol Interactions in Membranes from Separated Local-Field ^{13}C NMR Spectroscopy. *Biophys. J.*, **107**, 2274–2286.
- [157] Seelig, A. and Seelig, J. (1974) The Dynamic Structure of Fatty Acyl Chains in a Phospholipid Bilayer Measured by Deuterium Magnetic Resonance. *Biochemistry*, **13**, 4839–4845.
- [158] Saalwächter, K. (2007) Proton Multiple-Quantum NMR for the Study of Chain Dynamics and Structural Constraints in Polymeric Soft Materials. *Progr. NMR Spectrosc.*, **51**, 1–35.
- [159] Saalwächter, K., Lange, F., Matyjaszewski, K., Huang, C.-F., and Graf, R. (2011) BaBaxxy16: Robust and broadband homonuclear DQ recoupling for applications in rigid and soft solids up to the highest MAS frequencies. *J. Magn. Reson.*, **212**, 204–215.
- [160] Feike, M., Demco, D. E., Graf, R., Gottwald, J., Hafner, S., and Spiess, H. W. (1996) Broadband Multiple-Quantum NMR Spectroscopy. *J. Magn. Reson.*, **122**, 214–221.
- [161] Gullion, T., Baker, D. B., and Conradi, M. S. (1990) New, Compensated Carr-Purcell Sequences. *J. Magn. Reson.*, **89**, 479–484.
- [162] Geen, H., Titman, J. J., Gottwald, J., and Spiess, H. W. (1995) Spinning Sidebands in the Fast-MAS Multiple-Quantum Spectra of Protons in Solids. *J. Magn. Reson. A*, **114**, 264–267.
- [163] Chassé, W., Valentín, J. L., Genesky, G. D., Cohen, C., and Saalwächter, K. (2011) Precise dipolar coupling constant distribution analysis in proton multiple-quantum NMR of elastomers. *J. Chem. Phys.*, **134**, 044907.
- [164] Lindahl, E., Hess, B., and van der Spoel, D. (2001) GROMACS 3.0: a package for molecular simulation and trajectory analysis. *J. Mol. Mod.*, **7**, 306–317.
- [165] Haile, J. M. (1992) *Molecular Dynamics Simulation*. John Wiley & Sons, Inc, New York.
- [166] Berendsen, H. J. C. (2007) *Simulating the Physical World*. Cambridge University Press.
- [167] Poger, D., van Gunsteren, W. F., and Mark, A. E. (2009) A New Force Field for Simulating Phosphatidylcholine Bilayers. *J. Comput. Chem.*, **31**, 1117–1125.

- [168] Ollila, O. H. S. and Pabst, G. (2016) Atomistic resolution structure and dynamics of lipid bilayers in simulations and experiments. *Biochim. Biophys. Acta*, **1858**, 2512–2528.
- [169] Batrakova, E., Lee, S., Li, S., Venne, A., Alakhov, V., and Kabanov, A. (1999) Fundamental Relationships Between the Composition of Pluronic Block Copolymers and Their Hypersensitization Effect in MDR Cancer Cells. *Pharmaceut. Res.*, **16**, 1373–1379.
- [170] Amado, E. and Kressler, J. (2011) Interactions of amphiphilic block copolymers with lipid model membranes. *Curr. Opin. Colloid Interface Sci.*, **16**, 491–498.
- [171] Alexandridis, P. and Hatton, T. A. (1995) Poly(ethylene oxide)–poly(propylene oxide)–poly(ethylene oxide) block copolymer surfactants in aqueous solutions and at interfaces: thermodynamics, structure, dynamics, and modeling. *Colloids Surf. A*, **96**, 1–46.
- [172] Kabanov, A. V., Batrakova, E. V., and Alakhov, V. (2002) Pluronic[®] block copolymers for overcoming drug resistance in cancer. *Adv. Drug Deliv. Rev.*, **54**, 759–779.
- [173] Maskarinec, S. A., Wu, G., and Lee, K. Y. S. (2005) Membrane Sealing by Polymers. *Ann. N.Y. Acad. Sci.*, **1066**, 310–320.
- [174] Wu, G., Frey, S. L., Maskarinec, S. A., and Lee, K. Y. C. (2006) Triblock Copolymer as an Effective Membrane-Sealing Material. *MRS Bulletin*, **31**, 532–535.
- [175] Adhikari, U., Goliaei, A., Tsereteli, L., and Berkowitz, M. L. (2016) Properties of Poloxamer Molecules and Poloxamer Micelles Dissolved in Water and Next to Lipid Bilayers: Results from Computer Simulations. *J. Phys. Chem. B*, **120**, 5823–5830.
- [176] Kabanov, A. V., Batrakova, E. V., Melik-Nubarov, N. S., Fedoseev, N. A., Dorodnich, T. Y., Alakhov, V. Y., Chekhonin, V. P., Nazarova, I. R., and Kabanov, V. A. (1992) A new class of drug carriers: micelles of poly(oxyethylene)-poly(oxypropylene) block copolymers as microcontainers for drug targeting from blood in brain. *J. Control. Release*, **22**, 141–158.
- [177] Chiappetta, D. A. and Sosnik, A. (2007) Poly(ethylene oxide)–poly(propylene oxide) block copolymer micelles as drug delivery agents: Improved hydrosolubility, stability and bioavailability of drugs. *Eur. J. Pharm. Biopharm.*, **66**, 303–317.
- [178] Kabanov, A. V., Batrakova, E. V., and Alakhov, V. Y. (2002) Pluronic[®] block copolymers as novel polymer therapeutics for drug and gene delivery. *J. Control. Release*, **82**, 189–212.
- [179] Krylova, O. O., Melik-Nubarov, N. S., Badun, G. A., Ksenofontov, A. L., Menger, F. M., and Yaroslavov, A. A. (2003) Pluronic L61 Accelerates Flip-Flop and Transbilayer Doxorubicin Permeation. *Chem. Eur. J.*, **9**, 3930–3936.
- [180] Krylova, O. O. and Pohl, P. (2004) Ionophoric Activity of Pluronic Block Copolymers. *Biochemistry*, **43**, 3696–3703.
- [181] Mortensen, K. (1996) Structural studies of aqueous solutions of PEO–PPO–PEO triblock copolymers, their micellar aggregates and mesophases; a small-angle neutron scattering study. *J. Phys.: Condens. Matter*, **8**, A103–A124.
- [182] Almgren, M., Brown, W., and Hvidt, S. (1995) Self-aggregation and phase behavior of poly(ethylene oxide)-poly(propylene oxide)-poly(ethylene oxide) block copolymers in aqueous solution. *Colloid Polym. Sci.*, **273**, 2–15.

- [183] Karlström, G. (1985) A New Model for Upper and Lower Critical Solution Temperatures in Poly(ethylene oxide) Solutions. *J. Phys. Chem.*, **89**, 4962–4964.
- [184] Wanka, G., Hoffmann, H., and Ulbricht, W. (1994) Phase Diagrams and Aggregation Behavior of Poly(oxyethylene)-Poly(oxypropylene)-Poly(oxyethylene) Triblock Copolymers in Aqueous Solutions. *Macromolecules*, **27**, 4145–4159.
- [185] Fusco, S., Borzacchiello, A., and Netti, P. A. (2006) Perspectives on: PEO-PPO-PEO Triblock Copolymers and their Biomedical Applications. *J. Bioact. Compat. Polym.*, **21**, 149–164.
- [186] Baekmark, T. R., Pedersen, S., Jørgensen, K., and Mouritsen, O. G. (1997) The Effects of Ethylene Oxide Containing Lipopolymers and Tri-Block Copolymers on Lipid Bilayers of Dipalmitoylphosphatidylcholine. *Biophys. J.*, **73**, 1479–1491.
- [187] Amado, E., Augsten, C., Mäder, K., Blume, A., and Kressler, J. (2006) Amphiphilic Water Soluble Triblock Copolymers Based on Poly(2,3-dihydroxypropyl methacrylate) and Poly(propylene oxide): Synthesis by Atom Transfer Radical Polymerization and Micellization in Aqueous Solutions. *Macromolecules*, **39**, 9486–9496.
- [188] Rossi, G., Barnoud, J., and Monticelli, L. (2014) Polystyrene Nanoparticles Perturb Lipid Membranes. *J. Phys. Chem. Lett.*, **5**, 241–246.
- [189] Nawaz, S., Redhead, M., Mantovani, G., Alexander, C., Bosquillon, C., and Carbone, P. (2012) Interactions of PEO-PPO-PEO block copolymers with lipid membranes: a computational and experimental study linking membrane lysis with polymer structure. *Soft Matter*, **8**, 6744–6754.
- [190] Liang, X., Mao, G., and Ng, K. Y. S. (2005) Effect of chain lengths of PEO-PPO-PEO on small unilamellar liposome morphology and stability: an AFM investigation. *J. Colloid Interf. Sci.*, **285**, 360–372.
- [191] Hezaveh, S., Samanta, S., Nicola, A. D., Milano, G., and Roccatano, D. (2012) Understanding the Interaction of Block Copolymers with DMPC Lipid Bilayer Using Coarse-Grained Molecular Dynamics Simulations. *J. Phys. Chem. B*, **116**, 14333–14345.
- [192] Kostarelos, K., Luckham, P. F., and Tadros, T. F. (1997) Addition of (Tri-) Block Copolymers to Phospholipid Vesicles: A Study of the Molecular Morphology and Structure by Using Hydrophobic Dye Molecules as Bilayer Probes. *J. Colloid Interf. Sci.*, **191**, 341–348.
- [193] Kostarelos, K., Kipps, M., Tadros, T. F., and Luckham, P. F. (1998) Molecular structure and conformation in phospholipid vesicles sterically stabilized by (tri)-block copolymers investigated by multi-nuclear magnetic resonance techniques. *Colloids Surf. A*, **136**, 1–9.
- [194] Kintali, S. R., Varshney, G. K., and Das, K. (2017) Effect of three pluronic polymers on the transport of an organic cation across a POPG bilayer studied by Second Harmonic spectroscopy. *Chem. Phys. Lett.*, **684**, 267–272.
- [195] Chang, L.-C., Chang, Y.-Y., and Gau, C.-S. (2008) Interfacial properties of Pluronics and the interactions between Pluronics and cholesterol/DPPC mixed monolayers. *J. Colloid Interf. Sci.*, **322**, 263–273.

- [196] Wu, G. and Lee, K. Y. C. (2009) Interaction of Poloxamers with Liposomes: An Isothermal Titration Calorimetry Study. *J. Phys. Chem. B*, **113**, 15522–15531.
- [197] Rabbel, H., Werner, M., and Sommer, J.-U. (2015) Interactions of Amphiphilic Triblock Copolymers with Lipid Membranes: Modes of Interaction and Effect on Permeability Examined by Generic Monte Carlo Simulations. *Macromolecules*, **48**, 4724–4732.
- [198] Amado, E., Kerth, A., Blume, A., and Kressler, J. (2009) Phospholipid crystalline clusters induced by adsorption of novel amphiphilic triblock copolymers to monolayers. *Soft Matter*, **5**, 669–675.
- [199] Pembouong, G., Morellet, N., Kral, T., Hof, M., Scherman, D., Bureau, M.-F., and Mignet, N. (2011) A comprehensive study in triblock copolymer membrane interaction. *J. Control. Release*, **151**, 57–64.
- [200] Bryskhe, K., Schillén, K., Löfroth, J.-E., and Olsson, U. (2001) Lipid-block copolymer immiscibility. *Phys. Chem. Chem. Phys.*, **3**, 1303–1309.
- [201] Zhirnov, A. E., Demina, T. V., Krylova, O. O., Grozdova, I. D., and Melik-Nubarov, N. S. (2005) Lipid composition determines interaction of liposome membranes with Pluronic L61. *Biochim. Biophys. Acta*, **1720**, 73–83.
- [202] Hädicke, A. and Blume, A. (2015) Interactions of Pluronic block copolymers with lipid vesicles depend on lipid phase and Pluronic aggregation state. *Colloid Polym. Sci.*, **293**, 267–276.
- [203] Wang, J.-Y., Marks, J., and Lee, K. Y. C. (2012) Nature of Interaction between PEO-PPO-PEO Triblock Copolymers and Lipid Membranes: (I) Effect of Polymer Hydrophobicity on Its Ability to Protect Liposomes from Peroxidation. *Biomacromolecules*, **13**, 2616–2623.
- [204] Johnsson, M., Silvander, M., Karlsson, G., and Edwards, K. (1999) Effect of PEO-PPO-PEO Triblock Copolymers on Structure and Stability of Phosphatidylcholine Liposomes. *Langmuir*, **15**, 6314–6325.
- [205] Chieng, Y. Y. and Chen, S. B. (2009) Interaction and Complexation of Phospholipid Vesicles and Triblock Copolymers. *J. Phys. Chem. B*, **113**, 14934–14942.
- [206] Yaroslavov, A. A., Melik-Nubarov, N. S., and Menger, F. M. (2006) Polymer-Induced Flip-Flop in Biomembranes. *Acc. Chem. Res.*, **39**, 702–710.
- [207] Goliaei, A., Lau, E. Y., Adhikari, U., Schwegler, E., and Berkowitz, M. L. (2016) Behavior of P85 and P188 Poloxamer Molecules: Computer Simulations Using United-Atom Force-Field. *J. Phys. Chem. B*, **120**, 8631–8641.
- [208] Hammouda, B. (2010) SANS from Pluronic P85 in d-water. *Eur. Polym. J.*, **46**, 2275–2281.
- [209] Castile, J. D., Taylor, K. M. G., and Buckton, G. (2001) The influence of incubation temperature and surfactant concentration on the interaction between dimyristoylphosphatidylcholine liposomes and poloxamer surfactants. *Int. J. Pharm.*, **221**, 197–209.
- [210] Yamazaki, M., Ohshika, M., Kashiwagi, N., and Asano, T. (1992) Phase transitions of phospholipid vesicles under osmotic stress and in the presence of ethylene glycol. *Biophys. Chem.*, **43**, 29–37.

- [211] Amado, E. (2010), Triblock Copolymers of Poly(2,3-dihydroxypropyl methacrylate) and Poly(propylene oxide): Synthesis, Behavior in Aqueous Solution and at the Air-Water Interface, and Interactions with Model Lipid Membranes. Doctoral thesis.
- [212] Almgren, M., v. Stam, J., and Lindblad, C. (1991) Aggregation of Poly(ethylene oxide)-Poly(propylene oxide)-Poly(ethylene oxide) Triblock Copolymers in the Presence of Sodium Dodecyl Sulfate in Aqueous Solution. *J. Phys. Chem.*, **95**, 5677–5684.
- [213] Cau, F. and Lacelle, S. (1996) ^1H NMR Relaxation Studies of the Micellization of a Poly(ethylene oxide)-Poly(propylene oxide)-Poly(ethylene oxide) Triblock Copolymer in Aqueous Solution. *Macromolecules*, **29**, 170–178.
- [214] Huster, D., Yao, X., and Hong, M. (2002) Membrane Protein Topology Probed by ^1H Spin Diffusion from Lipids Using Solid-State NMR Spectroscopy. *J. Am. Chem. Soc.*, **124**, 874–883.
- [215] Saalwächter, K., Klüppel, M., Luo, H., and Schneider, H. (2004) Chain Order in Filled SBR Elastomers: a Proton Multiple-Quantum NMR Study. *Appl. Magn. Reson.*, **27**, 401–417.
- [216] Saalwächter, K. (2002) Methyl groups as local probes for polymer dynamics as investigated by ^1H double-quantum magic-angle spinning NMR spectroscopy. *Chem. Phys. Lett.*, **362**, 331–340.
- [217] Saalwächter, K., Herrero, B., and López-Manchado, M. A. (2005) Chain Order and Cross-Link Density of Elastomers As Investigated by Proton Multiple-Quantum NMR. *Macromolecules*, **38**, 9650–9660.
- [218] Kuhn, W. and Grün, F. (1942) Beziehungen zwischen elastischen Konstanten und Dehnungsdoppelbrechung hochelastischer Stoffe. *Kolloid-Z.*, **101**, 248–271.
- [219] Kučerka, N., Liu, Y., Chu, N., Petrache, H. I., Tristram-Nagle, S., and Nagle, J. F. (2005) Structure of Fully Hydrated Fluid Phase DMPC and DLPC Lipid Bilayers Using X-Ray Scattering from Oriented Multilamellar Arrays and from Unilamellar Vesicles. *Biophys. J.*, **88**, 2626–2637.
- [220] Wu, G., Khant, H. A., Chiu, W., and Lee, K. Y. C. (2009) Effects of bilayer phases on phospholipid-ploxamer interactions. *Soft Matter*, **5**, 1496–1503.
- [221] Papahadjopoulos, D., Jacobson, K., Nir, S., and Isac, T. (1973) Phase transitions in phospholipid vesicles. Fluorescence polarization and permeability measurements concerning the effect of temperature and cholesterol. *Biochim. Biophys. Acta*, **311**, 330–348.
- [222] Blicher, A., Wodzinska, K., Fidorra, M., Winterhalter, M., and Heimburg, T. (2009) The Temperature Dependence of Lipid Membrane Permeability, its Quantized Nature, and the Influence of Anesthetics. *Biophys. J.*, **96**, 4581–4591.
- [223] John, K., Schreiber, S., Kubelt, J., Herrmann, A., and Müller, P. (2002) Transbilayer Movement of Phospholipids at the Main Phase Transition of Lipid Membranes: Implications for Rapid Flip-Flop in Biological Membranes. *Biophys. J.*, **83**, 3315–3323.
- [224] Nagle, J. F. and Tristram-Nagle, S. (2000) Structure of lipid bilayers. *Biochim. Biophys. Acta*, **1469**, 159–195.

- [225] Kayes, J. B. and Rawlins, D. A. (1979) Adsorption characteristics of certain polyoxyethylene-polyoxypropylene block co-polymers on polystyrene latex. *Colloid. Polym. Sci.*, **257**, 622–629.
- [226] Busschaert, N., Wenzel, M., Light, M. E., Iglesias-Hernández, P., Pérez-Tomás, R., and Gale, P. A. (2011) Structure - Activity Relationships in Tripodal Transmembrane Anion Transporters: The Effect of Fluorination. *J. Am. Chem. Soc.*, **133**, 14136–14148.
- [227] Valkenier, H., Haynes, C. J. E., Herniman, J., Gale, P. A., and Davis, A. P. (2014) Lipophilic balance - a new design principle for transmembrane anion carriers. *Chem. Sci.*, **5**, 1128–1134.
- [228] Busschaert, N. and Gale, P. A. (2013) Small-Molecule Lipid-Bilayer Anion Transporters for Biological Applications. *Angew. Chem. Int. Ed.*, **52**, 1374–1382.
- [229] Poppe, S., Poppe, M., Ebert, H., Prehm, M., Chen, C., Liu, F., Werner, S., Bacia, K., and Tschierske, C. (2017) Effects of Lateral and Terminal Chains of X-Shaped Bolaamphiphiles with Oligo(phenylene ethynylene) Cores on Self-Assembly Behaviour. Part 1: Transition between Amphiphilic and Polyphilic Self-Assembly in the Bulk. *Polymers*, **9**, 471.
- [230] Fuhrhop, J.-H. and Wang, T. (2004) Bolaamphiphiles. *Chem. Rev.*, **104**, 2901–2937.
- [231] Lewis, B. A. and Engelman, D. M. (1983) Lipid Bilayer Thickness Varies Linearly with Acyl Chain Length in Fluid Phosphatidylcholine Vesicles. *J. Mol. Biol.*, **166**, 211–217.
- [232] Werner, S., Ebenhan, J., Poppe, M., Poppe, S., Ebert, H., Tschierske, C., and Bacia, K. (2017) Effects of Lateral and Terminal Chains of X-Shaped Bolaamphiphiles with Oligo(phenylene ethynylene) Cores on Self-Assembly Behavior. Part 2: Domain Formation by Self-Assembly in Lipid Bilayer Membranes. *Polymers*, **9**, 476.
- [233] Grit, M. and Crommelin, D. J. A. (1993) Chemical stability of liposomes: implications for their physical stability. *Chem. Phys. Lipids*, **64**, 3–18.
- [234] Bielecki, A. and Burum, D. P. (1995) Temperature Dependence of ^{207}Pb MAS Spectra of Solid Lead Nitrate. An Accurate, Sensitive Thermometer for Variable-Temperature MAS. *J. Magn. Reson. A*, **116**, 215–220.
- [235] Ammann, C., Meier, P., and Merbach, A. E. (1982) A Simple Multinuclear NMR Thermometer. *J. Magn. Reson.*, **46**, 319–321.
- [236] Wishart, D. S., Bigam, C. G., Holm, A., Hodges, R. S., and Sykes, B. D. (1995) ^1H , ^{13}C and ^{15}N random coil NMR chemical shifts of the common amino acids. I. Investigations of nearest-neighbor effects. *J. Biomol. NMR*, **5**, 67–81.
- [237] Schäler, K. (2012), Low-field NMR Studies of Structure and Dynamics in Semicrystalline Polymers. Doctoral thesis.

Danksagung

An dieser Stelle möchte ich mich bei allen Personen bedanken, deren freundliche Unterstützung zum Gelingen dieser Arbeit beigetragen hat.

Zuerst möchte ich Prof. Kay Saalwächter für die Überlassung des Themas und die Betreuung der Arbeit danken. Besonders dankbar bin ich auch für die vielen Möglichkeiten an nationalen und internationalen Konferenzen teilnehmen zu können.

Großer Dank geht auch an Tiago M. Ferreira für seine vielfältige fachliche Beratung sowohl im Hinblick auf die Lipidproben und die NMR-Experimente als auch bezüglich der MD-Simulationen und der Entwicklung von Auswertprogrammen. Durch die ausgiebigen Diskussionen entstanden viele neue Ideen. Außerdem bedanke ich mich für das Aufsetzen der MD-Simulationen und das Korrekturlesen dieser Arbeit.

Für ihre Vorarbeit, die Einführung in die Forschung an Lipidmembranen, die Erklärung der verschiedenen NMR-Methoden und der Probenpräparation danke ich herzlich Anja Achilles.

Die Untersuchungen an den Lipid/Blockcopolymer- und den Lipid/Bolapolyphil-Mischungen wurden in Zusammenarbeit mit verschiedenen Fachgruppen der Chemie im Rahmen der Forschergruppe FOR 1145 durchgeführt. Hier danke ich an erster Stelle meinem Mentor Prof. Blume für seine unkomplizierte Unterstützung und die vielen guten Ratschläge und Ideen. Bei der Fachgruppe von Prof. Blume, insbesondere bei Christian Schwieger, bedanke ich mich für die DSC-Ergebnisse und für die Hilfestellung bei der Durchführung und Auswertung von DSC-Experimenten. Für die Bereitstellung der Polymerproben und ihrer Charakterisierung bedanke ich mich bei Mark Jbeily.

Phil Williamson und seiner Arbeitsgruppe danke ich für den netten Aufenthalt an der University of Southampton, wo ich das Projekt zu den Aniontransportmolekülen durchgeführt habe.

Außerdem danke ich allen Mitgliedern der Fachgruppe NMR, für die gute Zusammenarbeit und die stets vorhandene Hilfsbereitschaft. Günter Hempel danke ich für das Korrekturlesen und für seine Hilfestellung bei Rechnungen zur Korrelationsfunktion. Bei meinem Büroteam Anna Naumova und Ricardo Kurz bedanke ich mich für die gute Verpflegung und für die Diskussion jeglicher fachlicher Probleme.

Weiterer Dank geht an meine Eltern für ihre Unterstützung.

Lebenslauf

Persönliche Daten

Name: Ruth Bärenwald
Geburtsdatum: 28.09.1987
Geburtsort: Dessau
Staatsangehörigkeit: deutsch
Familienstand: ledig

Schulausbildung

8/1994 - 7/1998 Grundschule Dessau-Ziebigk
8/1998 - 7/2000 Sekundarschule Kühnau Dessau (Förderstufe)
8/2000 - 7/2004 Fürst-Franz-Gymnasium Dessau
8/2004 - 6/2007 Gymnasium Philanthropinum Dessau

Studium

10/2007 - 10/2010 Bachelorstudium der Physik an der MLU Halle-Wittenberg
05.08.2010 Abschluss der Bachelorarbeit zum Thema: *Untersuchung der Ketten-
dynamik der semikristallinen Polymere PCL und PE mit Hilfe von ¹H-
Niederfeld-Festkörper-NMR*

10/2010 - 12/2012: Masterstudium der Physik an der MLU Halle-Wittenberg
12.12.2012: Abschluss der Masterarbeit zum Thema: *Untersuchung der Ketten-
dynamik in Polyethylen-Kristalliten mit Hilfe von Festkörper-NMR*

ab 2013 Promotion an der MLU Halle-Wittenberg

Halle (Saale), den 07.05.2018

Ruth Bärenwald

Publikationsliste

1. Werner, S., Ebert, H., Lechner, B.-D., Lange, F., Achilles, A., Bärenwald, R., Poppe, S., Blume, A., Saalwächter, K., Tschierske, C., and Bacia, K. (2015) Dendritic domains with hexagonal symmetry formed by X-shaped bolapolyphiles in lipid membranes. *Chem. Eur. J.*, **21**, 8840–8850
2. Achilles, A., Bärenwald, R., Lechner, B.-D., Werner, S., Ebert, H., Tschierske, C., Blume, A., Bacia, K., and Saalwächter, K. (2016) Self-Assembly of X-Shaped Bolapolyphiles in Lipid Membranes: Solid-State NMR Investigations. *Langmuir*, **32**, 673–682
3. Ferreira, T. M., Sood, R., Bärenwald, R., Carlström, G., Topgaard, D., Saalwächter, K., Kinnunen, P. K. J., and Ollila, O. H. S. (2016) Acyl Chain Disorder and Azelaoyl Orientation in Lipid Membranes Containing Oxidized Lipids. *Langmuir*, **32**, 6524–6533
4. Bärenwald, R., Achilles, A., Lange, F., Ferreira, T. M., and Saalwächter, K. (2016) Applications of Solid-State NMR Spectroscopy for the Study of Lipid Membranes with Polyphilic Guest (Macro)Molecules. *Polymers*, **8**, 439
5. Jbeily, M., Bärenwald, R., Kressler, J., Saalwächter, K., and Ferreira, T. M. (2018) Cholesterol-like effects of a fluorotelomer alcohol incorporated in phospholipid membranes. *Sci. Rep.*, **8**, 2154

Eidesstattliche Erklärung

Hiermit versichere ich, dass ich die vorliegende Arbeit selbständig und ohne fremde Hilfe verfasst und dabei nur die von mir angegebenen Quellen und Hilfsmittel benutzt habe. Die den benutzten Werken wörtlich oder inhaltlich entnommenen Stellen habe ich als solche kenntlich gemacht.

Die vorliegende Dissertation habe ich weder in der gegenwärtigen noch in einer anderen Fassung einer anderen wissenschaftlichen Einrichtung vorgelegt. Weiterhin bestätige ich hiermit, keine anderweitigen Promotionsversuche unternommen zu haben.

Halle (Saale), den 07.05.2018

Ruth Bärenwald